

A SOFT X-RAY EMISSION ENDSTATION FOR THE  
CANADIAN LIGHT SOURCE

A Thesis Submitted to the  
College of Graduate Studies and Research  
in Partial Fulfillment of the Requirements  
for the degree of Doctor of Philosophy  
in the Department of Physics and Engineering Physics  
University of Saskatchewan  
Saskatoon

By  
David Muir

©David Muir, October/2013. All rights reserved.

# PERMISSION TO USE

In presenting this thesis in partial fulfilment of the requirements for a Postgraduate degree from the University of Saskatchewan, I agree that the Libraries of this University may make it freely available for inspection. I further agree that permission for copying of this thesis in any manner, in whole or in part, for scholarly purposes may be granted by the professor or professors who supervised my thesis work or, in their absence, by the Head of the Department or the Dean of the College in which my thesis work was done. It is understood that any copying or publication or use of this thesis or parts thereof for financial gain shall not be allowed without my written permission. It is also understood that due recognition shall be given to me and to the University of Saskatchewan in any scholarly use which may be made of any material in my thesis.

Requests for permission to copy or to make other use of material in this thesis in whole or part should be addressed to:

Head of the Department of Physics and Engineering Physics  
116 Science Place  
University of Saskatchewan  
Saskatoon, Saskatchewan  
Canada  
S7N 5E2

# ABSTRACT

Based on a previously completed design for a soft X-ray (50-1100 eV) emission spectrometer, an endstation was constructed for the Resonant Elastic and Inelastic X-ray Scattering (REIXS) beamline at the CLS. The optical design employed techniques and software tools developed in-house using ray-tracing and diffraction grating efficiency calculations to analyze and compare existing designs and to propose a new design with superior performance. This design employs Rowland circle geometry to achieve a theoretical resolving power in excess of 2,500 in our range of interest. In addition, a novel optical design for a larger extremely high resolution spectrometer has been completed to provide theoretical resolving powers exceeding 10,000 throughout the higher end of the spectrum. To accommodate this optical design a completely new mechanical design was required, involving significant mechanical, electrical, vacuum and software engineering. Countless custom fabricated parts were required along with numerous off-the-shelf secondary instruments and systems. All told, this entirely student-managed project has cost over \$1.5M and taken over 5 years. Construction is finally complete and the endstation is currently being commissioned. Necessary design changes made during the mechanical design process resulting in the selection of a more suitable, but lower resolution, detector. This reduced the theoretical maximum resolving power to 1,800 for the first order gratings and roughly 5,000 for the third order gratings. Commissioning is still underway, but first order resolutions in the range of 1,000 - 2,000 have been recorded as have third order resolutions exceeding 4,000. Publication quality data has been collecting by members of this research group and invited external users have successfully grown and measured samples here. Two of the optical elements required rework and upon their delivery the system commissioning will be completed and peer-reviewed access will begin.

# ACKNOWLEDGEMENTS

To be clear from the beginning, no one person could possibly complete a project of such magnitude and from the very beginning it has been a team effort. The members of that team have changed over time and one of my significant contributions has been to manage the project and keep it on track in spite of ever changing contributors. I am very proud of my contribution and what has been accomplished. In preparing this document, I found looking back over the incredible number and variety of problems that I have encountered and overcome nearly breath taking. Even more impressive were the humbling levels of experience, skill and intelligence that I have found in the people that I have had the great privilege to work with and learn from over the course of this project. Any time a group of people is working on solving problems such as those encountered in this project, any attempt to assign individual credit for the solutions that are eventually implemented is bound to fail. Inspiration, ideas and specific solutions came not only from myself but from everyone mentioned here. The remainder of this document will focus on what has been accomplished and how. With a few outstanding exceptions, no further attempt will be made to give credit for individual effort. I want it to be clear that I am not attempting to take credit for anyone else's work. On the flip side, no attempt will be made to assign blame for the issues encountered either. This was a team effort!

I would like to gratefully acknowledge the support and guidance of my thesis supervisor, Dr. Alexander Moewes and my supervisor at the CLS, Dr. Feizhou He.

The encouragement, camaraderie and input of all the members of the Beamteam has been greatly appreciated. I would like to give special thanks to Mark Boots, whose contribution to this project was significant and invaluable. Robert Green was more involved than most, but everyone on the group has been pressed into service or provided invaluable feedback at one point or another, and they are John McLeod, Teak Boyko, Adrian Hunt, Neil Johnson, Tyrel Kerpan, Israel Pèrez, Eamon McDermott, Regan Wilks, Tyler Shendruk, Mikhail Yablonskikh, Tor Pedersen, Janay McNaughton, Trent Hamilton and Sam Leitch.

I will attempt to list all the people that made a contribution to this project here, but they are so numerous that an omission is almost certain, my apologies in advance:

Drew Bertwistle, Mike McKibben, Daniela Tanase Broten, Tony Wilson, Denis Beauregard, Johannes Vogt, Wade Dolton, John Swirsky, Terry Johnson, Elder Matias, Tom Ellis, Rob Blyth, Siyue Chen, Glenn Judkins, Mark Li, Alex Sitnikov, David Loken, Andrew Lockwood, Glenn Pegg, Carl Jansen, Doug Starnes, Ryan Lautner, Larry Weibe, Ed Unrau, Bryan Schmiedge, Harley Berndt, Noel Craddock, Jeff Wetzell, Gordon Blair, Mark Besse, Brian Yates, Alan Duffy, Dylan Maxwell, Joe Hanrahan, Andrew Brown, Randy Mackenzie, Ben Boyachek, Reg Aupperle, James Morgan, Carl Finlay and Erich Bach.

On a personal note, I would like to thank my family for their support, both financial and moral, which has been without limits throughout my life. Finally, I would like to especially thank Jennifer, who has been by my side throughout the course of this degree and the last. This course was made a great deal easier by her loving company and persistent encouragement.

This project was supported by funding from the National Science and Engineering Research Council (NSERC) and the Canada Research Chair program.

# CONTENTS

<b>Permission to Use</b>	<b>i</b>
<b>Abstract</b>	<b>ii</b>
<b>Acknowledgements</b>	<b>iii</b>
<b>Contents</b>	<b>v</b>
<b>List of Tables</b>	<b>viii</b>
<b>List of Figures</b>	<b>ix</b>
<b>List of Abbreviations</b>	<b>xii</b>
<b>I Background</b>	<b>1</b>
<b>1 Introduction</b>	<b>2</b>
1.1 Document Layout . . . . .	3
1.2 A Note On Units . . . . .	4
<b>2 Instrumentation Theory</b>	<b>5</b>
2.1 Synchrotrons & X-ray Science . . . . .	5
2.1.1 Synchrotron Radiation . . . . .	6
2.1.2 A Third Generation Light Source . . . . .	8
2.1.3 Sources . . . . .	12
2.2 The REIXS Beamline . . . . .	16
2.2.1 Primary Optics . . . . .	18
2.2.2 Monochromator . . . . .	19
2.2.3 Secondary Optics & Endstation Switching . . . . .	20
2.2.4 Performance . . . . .	21
2.3 Diffraction Gratings . . . . .	25
2.3.1 Variable Line Spacing . . . . .	29
2.3.2 Grating Efficiency . . . . .	30
2.4 Detectors . . . . .	33
2.4.1 MCP Operating Principle . . . . .	33
2.5 Vacuum Systems . . . . .	37
2.5.1 Levels of Vacuum . . . . .	37
2.5.2 Vacuum System Design . . . . .	39
2.5.3 Vacuum Hardware & Instrumentation . . . . .	46
<b>3 Spectroscopic Techniques</b>	<b>60</b>

3.1	Soft X-ray Spectroscopy . . . . .	60
3.2	X-ray Absorption Spectroscopy . . . . .	64
3.2.1	Total Electron Yield . . . . .	66
3.2.2	Total and Partial Fluorescence Yield . . . . .	67
3.3	X-ray Emission Spectroscopy . . . . .	68
3.3.1	Resonant Inelastic X-Ray Scattering . . . . .	69
3.4	Theoretical Interpretation . . . . .	70
3.5	Other Techniques . . . . .	71
3.5.1	Kinetic Electron Excitation . . . . .	71
3.5.2	Cylindrical Mirror Analyzer . . . . .	72
<b>II</b>	<b>The Project</b>	<b>74</b>
<b>4</b>	<b>The Design</b>	<b>75</b>
4.1	Optical Design . . . . .	75
4.1.1	A Rowland Circle Spectrometer . . . . .	75
4.1.2	High Resolution Third Order Gratings . . . . .	77
4.1.3	VLS Spectrometer . . . . .	78
4.2	Mechanical Design . . . . .	81
4.2.1	Sample Chamber . . . . .	82
4.2.2	Grating Chamber . . . . .	87
4.2.3	Detector Chamber . . . . .	90
4.3	Sample Preparation System . . . . .	92
<b>5</b>	<b>Construction &amp; Commissioning</b>	<b>94</b>
5.1	Procurement . . . . .	94
5.1.1	Diffraction Gratings . . . . .	95
5.2	Assembly . . . . .	102
5.2.1	Main Frame . . . . .	102
5.2.2	Sample Chamber . . . . .	103
5.2.3	Grating Chamber & Optics . . . . .	109
5.2.4	Detector Chamber . . . . .	113
5.3	Commissioning . . . . .	122
5.3.1	Initial Alignment . . . . .	122
5.3.2	Motion Modeling and Control Calibration . . . . .	123
5.3.3	Initial Testing . . . . .	130
5.3.4	Flux and Beam Alignment . . . . .	139
5.3.5	Stray Light and Photoelectron Noise . . . . .	144
5.3.6	Image Linearity . . . . .	149
5.3.7	Thermal Stability . . . . .	152
5.4	System Integration and User Interface . . . . .	156
<b>6</b>	<b>Results</b>	<b>164</b>
6.1	X-ray Absorption Measurements . . . . .	164

6.2	Emission Reference Standards . . . . .	167
6.2.1	Relative Performance Considerations . . . . .	167
6.2.2	Non-Resonant Emission . . . . .	168
6.2.3	Resonant Emission . . . . .	172
6.3	Performance . . . . .	173
6.3.1	Resolving Power . . . . .	174
6.3.2	Efficiency and Flux . . . . .	179
<b>III Conclusion</b>		<b>182</b>
<b>7</b>	<b>Conclusion</b>	<b>183</b>
7.1	The Design . . . . .	183
7.2	Construction and Commissioning . . . . .	183
7.3	Performance . . . . .	184
7.4	Future Development . . . . .	184
<b>References</b>		<b>186</b>
<b>IV Appendix</b>		<b>191</b>
<b>A</b>	<b>Resolving Power Measurements</b>	<b>192</b>
A.1	LEG Measurements . . . . .	193
A.2	Impurity Grating Measurements . . . . .	194
A.3	MEG Measurements . . . . .	195
A.4	HRMEG Measurements . . . . .	196
<b>B</b>	<b>Submitted Publications With Data From the REIXS XES Spectrometer</b>	<b>197</b>

# LIST OF TABLES

2.1	REIXS beamline design goals . . . . .	22
2.2	Outgassing rates for baked metals . . . . .	43
2.3	Outgassing rates for unbaked metals . . . . .	43
2.4	Outgassing rates for non-metals . . . . .	44
4.1	Designed grating specifications . . . . .	76
4.2	Designed high resolution grating specifications . . . . .	78
5.1	Grating metrology data . . . . .	96
5.2	Grating AFM measurements . . . . .	97
5.3	Gasket hardness test results . . . . .	115
6.1	Spectrometer count rate for various oxides . . . . .	172
A.1	LEG resolving power measurements, 25 $\mu\text{m}$ exit slit. . . . .	193
A.2	LEG resolving power measurements, 50 $\mu\text{m}$ exit slit. . . . .	193
A.3	LEG resolving power measurements, 100 $\mu\text{m}$ exit slit. . . . .	193
A.4	Impurity grating resolving power measurements, 25 $\mu\text{m}$ exit slit. . . . .	194
A.5	Impurity grating resolving power measurements, 50 $\mu\text{m}$ exit slit. . . . .	194
A.6	Impurity grating resolving power measurements, 100 $\mu\text{m}$ exit slit. . . . .	194
A.7	MEG resolving power measurements, 25 $\mu\text{m}$ exit slit. . . . .	195
A.8	MEG resolving power measurements, 50 $\mu\text{m}$ exit slit. . . . .	195
A.9	MEG resolving power measurements, 100 $\mu\text{m}$ exit slit. . . . .	195
A.10	HRMEG resolving power measurements, 25 $\mu\text{m}$ exit slit. . . . .	196

# LIST OF FIGURES

2.1	SR emission pattern . . . . .	8
2.2	Diagram of the key parts of a the CLS . . . . .	9
2.3	CLS booster ring . . . . .	10
2.4	CLS RF cavity . . . . .	10
2.5	Schematic of a DBA SR cell . . . . .	11
2.6	The two chicaned IDs for the REIXS and SM beamlines . . . . .	12
2.7	Comparison of SR sources . . . . .	12
2.8	Schematic of an EPU . . . . .	16
2.9	Electron paths through an EPU . . . . .	17
2.10	REIXS beamline plan drawing . . . . .	18
2.11	REIXS beamline elevation drawing . . . . .	19
2.12	REIXS beamline optical layout . . . . .	20
2.13	REIXS bellows branches . . . . .	21
2.14	REIXS flux curves . . . . .	22
2.15	Beam spot behavior . . . . .	24
2.16	N <sub>2</sub> gas phase absorption . . . . .	24
2.17	Optical element coordinate system . . . . .	25
2.18	The Rowland circle . . . . .	28
2.19	A blazed grating profile . . . . .	32
2.20	MCP detector system schematic . . . . .	34
2.21	The custom MCP detector head . . . . .	35
2.22	MCP operating principle . . . . .	35
2.23	An image formed by an MCP . . . . .	36
2.24	Vacuum level characteristics . . . . .	37
2.25	Vented fastener design . . . . .	41
2.26	SEM images of surface preparation techniques . . . . .	45
2.27	Schematic diagram of scroll pump operation . . . . .	50
2.28	Diagram of a turbomolecular pump . . . . .	52
2.29	Schematic diagram of a diode ion pump . . . . .	53
2.30	Schematic diagram of a thermocouple gauge . . . . .	56
2.31	Schematic diagrams of hot and cold cathode gauges . . . . .	56
2.32	Diagram of a residual gas analyzer . . . . .	58
3.1	X-ray absorption process . . . . .	61
3.2	Fluorescent emission process . . . . .	62
3.3	Fluorescence yields . . . . .	63
3.4	Auger emission process . . . . .	63
3.5	An example of an XAS Spectra . . . . .	65
3.6	An example of a RIXS spectra . . . . .	69
4.1	Calculated grating performance . . . . .	77

4.2	Calculated high resolution grating performance . . . . .	78
4.3	VLS CCD image . . . . .	79
4.4	The proposed VLS spectrometer design . . . . .	80
4.5	Rendering of the complete endstation CAD model . . . . .	81
4.6	Cut-away rendering of the endstation CAD model . . . . .	83
4.7	Sample chamber photo . . . . .	84
4.8	The sample holder . . . . .	85
4.9	Sample chamber and load lock drawing . . . . .	86
4.10	Entrance Slit and CEM mount . . . . .	87
4.11	The grating chamber . . . . .	88
4.12	Physik Instrumente M-840 hexapod . . . . .	89
4.13	Detector chamber cut-away drawing . . . . .	91
4.14	Detector chamber rear flange . . . . .	92
5.1	Initial grating AFM measurements at the SSSC . . . . .	96
5.2	LEG efficiency measurements and calculations . . . . .	98
5.3	Impurity Grating efficiency measurements and calculations . . . . .	98
5.4	MEG efficiency measurements and calculations . . . . .	99
5.5	HEG efficiency measurements and calculations . . . . .	99
5.6	AFM measurements from CXRO of the re-ruled HEG . . . . .	100
5.7	AFM images of second HEG ruling attempt . . . . .	101
5.8	The main endstation frame . . . . .	102
5.9	The main spectrometer frame after installation . . . . .	103
5.10	The assembled sample arm . . . . .	104
5.11	Sample mount and custom heater coil . . . . .	105
5.12	RSXS/SGM style sample holder . . . . .	106
5.13	Sample chamber, load lock and sample arm. . . . .	107
5.14	Sample Z stage in place, model vs. actual . . . . .	108
5.15	First measurement, with CMA . . . . .	108
5.16	Entrance slit installation . . . . .	109
5.17	Grating kinematic mount . . . . .	110
5.18	Grating after mounting . . . . .	111
5.19	Original grating mount flange design . . . . .	112
5.20	Detector modification for dual incident directions . . . . .	116
5.21	Ballscrew isolation bellows with internal pressure . . . . .	116
5.22	RGA measurements of the detector . . . . .	118
5.23	Contaminated v-rail bearing . . . . .	118
5.24	The preamplifier electronics . . . . .	119
5.25	The original and final detector carriages . . . . .	120
5.26	The first detector mount modification . . . . .	121
5.27	Installation of the detector chamber . . . . .	121
5.28	FaroArm survey . . . . .	124
5.29	Equivalent grating alignments . . . . .	126
5.30	A grating incidence angle scan . . . . .	127
5.31	Lift-stage frame-angle relation . . . . .	129

5.32	First recorded emission line . . . . .	131
5.33	Noise pulse on preamplifier signal on motor move . . . . .	132
5.34	Noise seen in preamplifier output signal from motor drivers . . . . .	133
5.35	Noise seen on preamplifier signal from limit switch cables . . . . .	133
5.36	UHV high voltage filter PCB installed on the MCP . . . . .	135
5.37	X-Y image and noise pulse from the failing detector . . . . .	135
5.38	Observed damage to the MCP and filter PCB . . . . .	136
5.39	MCP grounded enclosure model . . . . .	137
5.40	MCP installed in grounded enclosure . . . . .	138
5.41	Results of refocusing the beamline . . . . .	141
5.42	SiO <sub>2</sub> O K-edge with and without an entrance slit . . . . .	143
5.43	Elastic peaks with and without an entrance slit . . . . .	143
5.44	Results of refocusing the beamline . . . . .	144
5.45	Secondary electron cloud from an elastic peak . . . . .	145
5.46	Localized noise in relation to detector geometry . . . . .	146
5.47	HRMEG diffraction space scan . . . . .	147
5.48	Drawings of the added photon masks . . . . .	148
5.49	Detector image linearity test . . . . .	150
5.50	Image linearity versus top plate bias voltage . . . . .	151
5.51	Energy calibration instability . . . . .	153
5.52	Energy calibration drift cycle . . . . .	153
5.53	Calibration drift with hutch temperature . . . . .	154
5.54	Calibration drift with stabilized hutch temperature . . . . .	156
5.55	The REIXS XES endstation P&ID . . . . .	158
5.56	The REIXS XES endstation EDM screen . . . . .	159
5.57	An Acquaman experiment setup screen . . . . .	161
5.58	The Acquaman data browser . . . . .	162
5.59	The Acquaman workflow screen . . . . .	163
6.1	Mn & MnO <sub>2</sub> K-edge XAS . . . . .	165
6.2	<i>h</i> -BN N K-edge XAS . . . . .	166
6.3	B <sub>2</sub> O <sub>3</sub> O K-edge XAS . . . . .	166
6.4	<i>h</i> -BN B K-edge XES . . . . .	169
6.5	<i>h</i> -BN N K-edge XES . . . . .	170
6.6	O K-edge XES for various oxides . . . . .	171
6.7	FeO Fe L-edge RIXS series . . . . .	173
6.8	Impurity grating vs. MEG resolution . . . . .	174
6.9	An elastic peak used to determine the resolving power . . . . .	175
6.10	Measured resolving power of the REIXS XES spectrometer . . . . .	176
6.11	SiO <sub>2</sub> Si L-edge XES with various exit slit sizes . . . . .	177
6.12	Resolving power variation with slit size . . . . .	178
6.13	Elastic Peak widths for different gratings . . . . .	179
6.14	Resolution Contributions . . . . .	180
6.15	Relative grating flux . . . . .	181

## LIST OF ABBREVIATIONS

AFM	Atomic Force Microscope
AHU	Air Handling Unit
ALS	Advanced Light Source
BL	Beamline
CEM	Channel Electron Multiplier
CF	Conflat (vacuum flange)
CLS	Canadian Light Source
CCD	Charge Coupled Device
CXRO	Center for X-ray Optics
DOS	Density of States
EPU	Elliptically Polarized Undulator
EXAFS	Extended X-ray Absorption Fine Structure
HRHEG	High Resolution High Energy Grating
HRMEG	High Resolution Medium Energy Grating
HV	High Vacuum or High Voltage
IMP	Impurity grating
LEED	Low Energy Electron Diffraction
LEG	Low Energy Grating
MEG	Medium Energy Grating
MCP	Micro-Channel Plate
NEG	Non-Evaporative Getter
NEXAFS	Near Edge X-ray Absorption Fine Structure
pDOS	Partial Density of States
PGM	Plane Grating Monochromator
RAE	Resistive Anode Encoder
RP	Resolving Power
RGA	Residual Gas Analyzer
RHEED	Reflection High Energy Electron Diffraction
REIXS	Resonant Elastic and Inelastic X-ray Scattering beamline
RF	Radio Frequency
RSXS	Resonant Soft X-ray Scattering endstation
TSP	Titanium Sublimation Pump
SDD	Silicon Drift Detector
SR	Storage Ring or Synchrotron Radiation
UHV	Ultra High Vacuum
VLS	Variable Line Spaced
XANES	X-ray Absorption Near Edge Structure
XAS	X-ray Absorption Spectroscopy
XEOL	X-ray Excited Optical Luminescence
XES	X-ray Emission Spectroscopy or the XES endstation
XMCD	X-ray Magnetic Circular Dichroism

# Part I

## Background

# CHAPTER 1

## INTRODUCTION

The focus of this thesis project was the construction and commissioning of the soft X-ray emission endstation that is now in operation on the Resonant Elastic and Inelastic X-ray Scattering (REIXS) beamline at the Canadian Light Source (CLS). Soft X-ray Emission Spectroscopy (XES) is a unique tool in the field of condensed matter physics and this endstation will facilitate a wide range of experiments that would be otherwise unavailable at the CLS. The goal of this document is to present the features and scientific potential of this instrument and to, as concisely as possible, summarize the construction and commissioning process. The hope is that, in the process of doing so, the remarkable amount of effort that went in to designing this system and devising novel solutions to the complex problems encountered becomes clear without the need to monotonously cover the details of every single issue.

For interest's sake, in addition to the main body of the discussion centered on the XES spectrometer, sections will be dedicated to the auxiliary instrumentation that has been implemented on the endstation and the associated sample preparation system and the added scientific potential that results. Finally, the plans for future expansion of this system, including another novel, complimentary spectrometer design will be presented.

This has been a challenging thesis to write. The majority of the innovative science that is the backbone of this project was completed as part of a previous degree's work and is documented elsewhere. Taking the optical design for a soft X-ray emission spectrometer described therein and turning it in to a functioning endstation is what this project eventually evolved in to. The numerous challenges, complications and setbacks involved in that project made it all consuming and the pure science initially conducted on the endstation that was to be a part of this project did not end up fitting within its scope. The goal of this document

is to showcase the impressive scientific instrument that was created during the course of this project. It is not the goal of this document to be a catalog of all the issues faced along the way, but it would not be complete without touching on a few of the most significant. Furthermore, it is believed that members of the scientific community would do well to spend as much time documenting and publishing their failures as they do their successes. For future researchers following in their footsteps, the latter are likely to be more useful than the former.

The work herein is closely tied to two previously completed theses<sup>1,2</sup> and one recently published paper<sup>3</sup>. Every effort will be made to avoid unnecessary duplication of the information presented in those works but, for completeness, some of that material will be summarized here. For further detail and background on this project, refer to those works as well.

## 1.1 Document Layout

This document is comprised of four parts, the first two make up the main body followed by a conclusion and appendix. The first part serves as an introduction and theoretical grounding including sections on the systems, equipment and techniques available on the REIXS XES endstation. This includes an overview of the synchrotron and beamline that supplies light to the endstation, the theory behind the optics that are the heart of the endstation, the detectors used to collect and analyze the light emitted by the sample, and the vacuum systems required to work with soft X-rays and air sensitive equipment and samples. Part I is concluded with a brief introduction to the science behind the measurements that the endstation is capable of.

Part II discusses the project itself, beginning with a review of the optical design previously completed and an in depth walk-through of the mechanical design developed to realize that optical design and the required supporting systems. This is followed by an overview of the procurement process, a detailed look at the assembly and commissioning of the REIXS XES endstation, and its integration into the Canadian Light Source. Part II concludes with a look at some early results from the ongoing commissioning of this instrument.

Appendix A contains the raw measurement data used to calculate the resolving power of the spectrometer. Appendix B contains a list of submitted publications containing measure-

ments from the REIXS XES endstation.

## 1.2 A Note On Units

No effort has been made to consistently use S.I. units in this document. While they are the preferred system of units of the author, they are not the standard system of units for vacuum hardware and attempting to soft-convert to S.I. simply for the sake of consistency only breeds confusion. A perfect example is the common form of the empirical formula for conductance found in Section 2.5.3. With pumping speeds typically quoted in S.I. and vacuum hardware dimensions measured in imperial, the common formula  $C = 78 \frac{D^3}{L}$  gives the conductance in litres per second for a tube with dimensions in inches.

# CHAPTER 2

## INSTRUMENTATION THEORY

### 2.1 Synchrotrons & X-ray Science

Within two decades of Röntgen's 1895 discovery of X-rays, work by the likes of Barkla, von Laue, Bragg and Moseley had made it very clear that X-rays are a powerful tool for the investigation of the nature of matter. The significance of this work was recognized almost immediately as is evidenced by the fact that so many of the early Nobel prizes went to those mentioned above including the very first Nobel Prize in Physics which went to Wilhelm Conrad Röntgen himself.

As early as the 1920's physicists began considering particle accelerators as possible sources of X-rays for experimentation<sup>4</sup>, although X-rays resulting from what is now commonly known as synchrotron radiation were not observed until 1947 by scientists at GE who identified it as a source of energy loss in their 70 MeV electron synchrotron<sup>5</sup>. This synchrotron radiation occurs when high energy electrons are accelerated by the magnetic fields used to maintain their circular path within an accelerator. In 1956, the first experiments dedicated to the study of this new source of radiation were conducted by Tomboulion and Hartman<sup>6</sup> and by 1961 a program was underway using a synchrotron modified to allow this new source of X-rays to be used for experimentation.

Over the next two decades, synchrotron radiation experiments increased in popularity as more and more accelerator facilities designed for particle physics began to grant access to synchrotron radiation experimenters. The development of constant energy storage rings designed to be filled by a synchrotron, also a product particle physics research, turned out to be a great boon for users of synchrotron radiation as they were quickly proven to be a far superior X-ray source. This quickly led to the second generation of synchrotron radiation

science with the construction of purpose built storage rings dedicated to the generation of synchrotron radiation. Some of these facilities also began to include additional devices inserted into the storage rings which were made up of magnetic structures specifically designed for the production of more intense radiation.

The technology of synchrotron radiation has continued to develop with a third generation of sources coming online in the 1990's that featured storage rings that were carefully engineered to provide electron beam characteristics optimized for the production of high brilliance (i.e. high phase space density) photons. In addition, they were designed with long straight sections between the storage ring bending magnets to take full advantage of insertion devices.

The latest synchrotrons, the Canadian Light Source included among them, are sometimes loosely termed 3.5 generation facilities<sup>4</sup> and feature higher stored beam energies, further improved brilliance and more advanced insertion device technologies such as in-vacuum, small gap undulators and super-conducting wigglers.

### 2.1.1 Synchrotron Radiation

Synchrotron radiation arises from the fundamental principle that accelerating charged particles emit electromagnetic radiation. Synchrotron radiation is a relativistic effect resulting from very high energy charged particles (typically electrons) being accelerated along curved or sinusoidal trajectories by magnetic fields. Two main relativistic effects impact the production of radiation by a synchrotron: Lorentz contraction and the relativistic Doppler effect<sup>7</sup>.

The electrons themselves are the source of the emitted radiation and from the perspective of the experimenter they are approaching at relativistic velocities. This gives rise to a relativistic doppler shift:

$$\lambda = \frac{\lambda'}{\gamma(1 + \beta)}$$

taking  $\beta = v/c \sim 1$  this becomes:

$$\lambda \approx \frac{\lambda'}{2\gamma} \tag{2.1}$$

resulting in a shift in wavelength on the order  $1/\gamma$  of the emitted radiation in the laboratory reference frame. Here,  $\gamma$  is the Lorentz factor given by:

$$\gamma = \frac{1}{\sqrt{1 - \frac{v^2}{c^2}}} = E/E_0 \quad (2.2)$$

where  $v$  is the electron velocity,  $E$  is the storage ring energy, and  $E_0$  is the electron rest mass (0.511 MeV).

The frequency of emitted radiation from the periodic magnetic structures that make up insertion devices is related to the period of the field variation ( $\lambda_u$ ). As a result, Lorentz contraction plays a significant role in that the apparent contracted length of those structures ( $\lambda_u/\gamma$ ), as witnessed by the relativistic electrons, is significantly smaller than their physical size.

With modern synchrotron storage rings ranging in energy from 1.5-8.0 GeV,  $\gamma$  can be significant and with these effects combined the produced wavelengths are reduced by a factor of  $1/2\gamma^2$ . As a result, insertion devices with periods of several centimeters can produce radiation on the order of nanometers (hundreds or thousands of electron volts).

The Lorentz transformation also significantly affects the apparent radiated power density distribution as seen in the laboratory frame. The geometry of the familiar dipole radiation pattern (Figure 2.1a) is also subjected to Lorentz contraction from the point of view of the experimenter. This results in the elongation and effective collimation of the emitted radiation (Figure 2.1b), which has an emission angle on the order of  $1/\gamma$ . This effect leads to the a very high brilliance which is one of the most attractive properties of synchrotron radiation<sup>8</sup>:

$$\text{Brilliance} = \frac{(\text{Photon Flux})}{I} \frac{1}{\sigma_x \sigma_y \sigma'_x \sigma'_y BW} \quad (2.3)$$

where  $I$  is the electron current in the storage ring,  $\sigma_x \sigma_y$  is the transverse source area,  $\sigma'_x \sigma'_y$  is the emitted solid angle, and  $BW$  is the spectral band width. Hence, brilliance is the phase space photon flux density<sup>7</sup> (i.e. photons per unit area per unit solid angle), and high brilliance means that extremely high monochromatic flux density at the sample is achievable.

Three other commonly used terms are worth defining at this point as well. Brightness is similar to brilliance, but decoupled from the source size:

$$\text{Brightness} = \frac{(\text{Photon Flux})}{I} \frac{1}{\sigma'_x \sigma'_y BW} \quad (2.4)$$

with the same definitions as above. Flux usually refers to the photons per unit time per unit area delivered by a source or beamline, but it is often used (sometimes as spectral flux<sup>9</sup>) to simply mean photons per second delivered. Intensity (or sometime spectral intensity) is often used differently in the context of spectroscopy than in other fields of physics, and usually refers to the photons per unit time or signal strength collected by a detector during an experiment. The last two definitions are rather loose and they often end up being used interchangeably. The difference between the two is usually not significant in the context of most discussions.

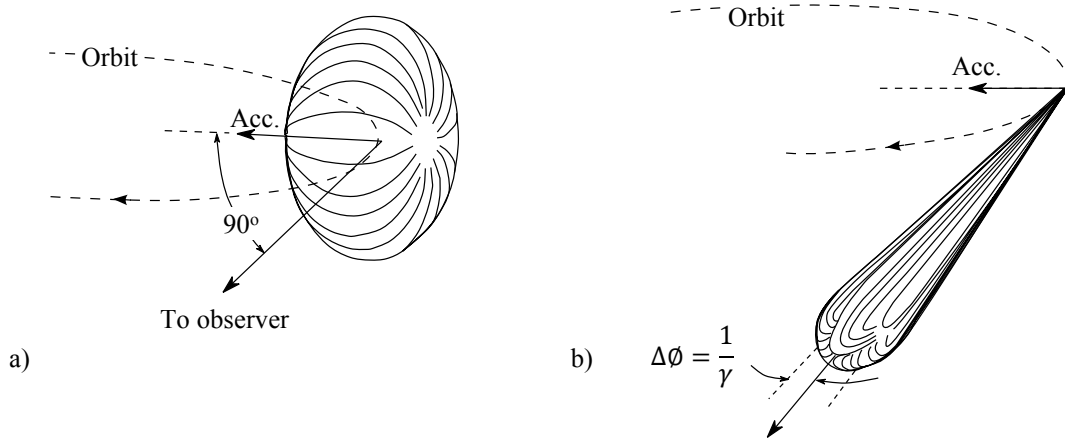


**Figure 2.1:** As the relativistic limit is approached, the emission pattern shifts from the familiar dipole envelop to a narrow angular distribution<sup>10</sup>.

### 2.1.2 A Third Generation Light Source

The Canadian Light Source (CLS) is an advanced, compact, third generation synchrotron light source. As already noted, improved beam characteristics and the implementation of new insertion device technologies at facilities such as the CLS has led some to label them as third-and-a-half generation facilities<sup>4</sup>, but this somewhat awkward distinction is rarely heard. The facility, located on the campus of the University of Saskatchewan in Saskatoon took advantage of the infrastructure from the existent Saskatchewan Accelerator Laboratory to economically provide Canada with its first synchrotron light source, which began serving the scientific

community in 2005. With the construction of a third phase of beamlines well underway, the CLS already provides a wide range of experimental techniques and its capabilities continue to grow.

Regardless of the designation, second, third and third-and-a-half generation facilities share a common basic structure. A brief walk-through of the principle components of a synchrotron will follow. The general information is common to most facilities, but the specific details given here relate to the CLS.

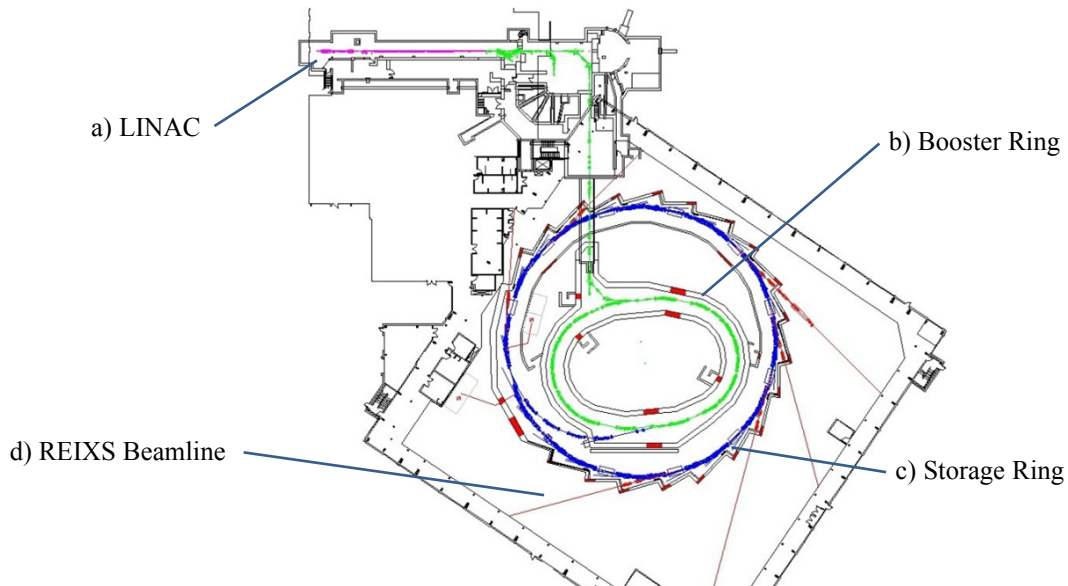


**Figure 2.2:** The basic layout of the key parts of the CLS. Electron produced by the LINAC (a) are accelerated by the Booster Ring (b) and then stored in the Storage Ring (c) where they are used to generate light that is conditioned by the beamlines (d) and delivered to the experimenters working on the Endstations<sup>11</sup>.

The electrons that will eventually generate synchrotron light are produced by a high power electron gun that feeds the linear accelerator (LINAC) that was the heart of the Saskatchewan Accelerator Laboratory (Figure 2.2a). The LINAC uses pulsed RF to ramp the electrons up to 200 MeV and bunch the electrons together.

These bunches are fed via the LINAC-to-Booster (LTB) transfer line up to the Booster Ring (Figure 2.2b) that sits inside the main storage ring. Technically speaking, the 103 m Booster Ring is the *synchrotron* proper. The RF cavity frequency must be ramped up *in synch* with the accelerating electrons, since they reach sufficiently high velocity that the change in their relativistic mass would otherwise cause them to fall out of phase and be

scattered out of orbit. After orbiting in the Booster Ring 1.5 million times in 0.6 seconds, the electrons reach the storage ring energy of 2.9 GeV.



**Figure 2.3:** A section of the CLS booster ring. The (blue) dipole bending magnets guide the electrons around the booster ring and the (green) quadrupole magnets are used for focusing<sup>12</sup>.

At this point, the electron bunches are transferred to the Storage Ring (SR) via the Booster to Storage Ring (BTS) transfer line. Each such injection to the SR contains up to 10 mA of current in ideal operating conditions and several injections are required to reach the full operating current of the Storage Ring which is currently 250 mA with plans to go to 350 mA and eventually 500 mA. Once in the SR, the electrons orbit continuously for up to 12 hours. The energy lost as the electrons pass through the SR magnetic lattice and insertion devices is replenished by a super conducting RF cavity (see Figure 2.4)<sup>13</sup>.

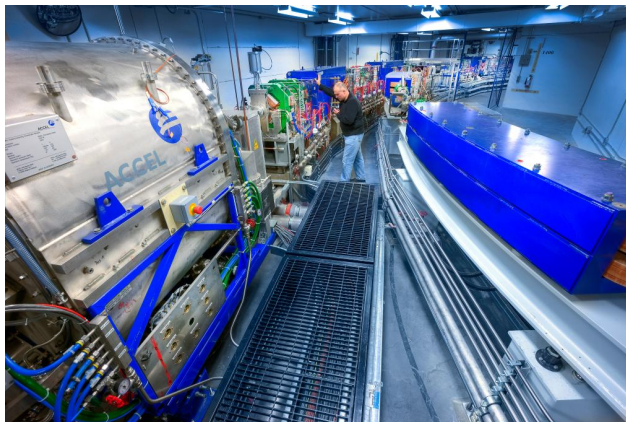


**Figure 2.4:** The CLS RF Cavity in the storage ring (left) and the booster-to-storage ring transfer Line (right)<sup>11</sup>.

The Canadian Light Source’s 171 m circumference storage ring is a lattice of 12 straight sections. One section is use for the RF cavity, one for the injection branch and a third is reserved for the addition of the second RF cavity that will be required to reach the final designed ring current of 500 mA<sup>14</sup>. The remaining 9 straight sections accommodate insertion devices to provide photons to beamlines. Each straight is sandwiched between two double bend achromat bending magnet cells, which can also be used as photon sources, and contains a series of quadrupole and sextupole permanent magnets as well as adjustable electromagnetic corrector coils to focus and steer the electron beam<sup>15</sup>.

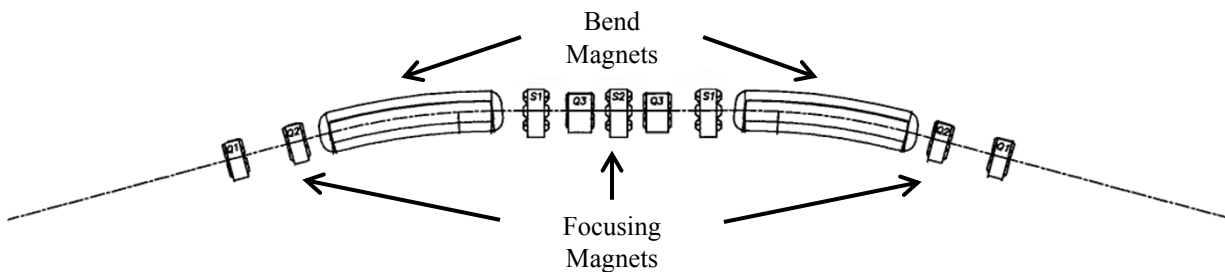


**Figure 2.5:** Schematic of a full double bend achromat storage ring cell<sup>16</sup>.

The CLS is one of the first facilities to use a chicane arrangement to place two separate insertion devices in a single straight section (Figure 2.6)<sup>14</sup>. By shifting the electron beam path slightly before each insertion device, the two resulting photon beams have sufficient angular separation to service two separate beamlines. This arrangement allows the CLS to support a more competitive number of insertion device beamlines despite the fact that it has a smaller storage ring than many newer facilities.

Due to the extremely short mean free path of electrons in air, the entire accelerator from the electron gun to the storage ring must be operated under vacuum. The use of a superconducting RF cavity makes excellent vacuum (typically  $1 \times 10^{-8}$  torr or better) in the storage ring even more critical. A combination of pumping technologies, including some advanced NEG coated straight sections, are used but vacuum is primarily maintained by hundreds of ion pumps at regular intervals throughout the system. For more details on the complexities of designing and operating vacuum systems, see Section 2.5.



**Figure 2.6:** The two EPUs for the Spectromicroscopy (10ID-1) and REIXS (10ID-2) beamlines share one chicaned straight section.

### 2.1.3 Sources

There are three broad types of devices in modern synchrotron storage rings that generate photons for beamlines. Bending magnets, wigglers and undulators are the heart of any third generation light source. The light from each type of device has unique characteristics.

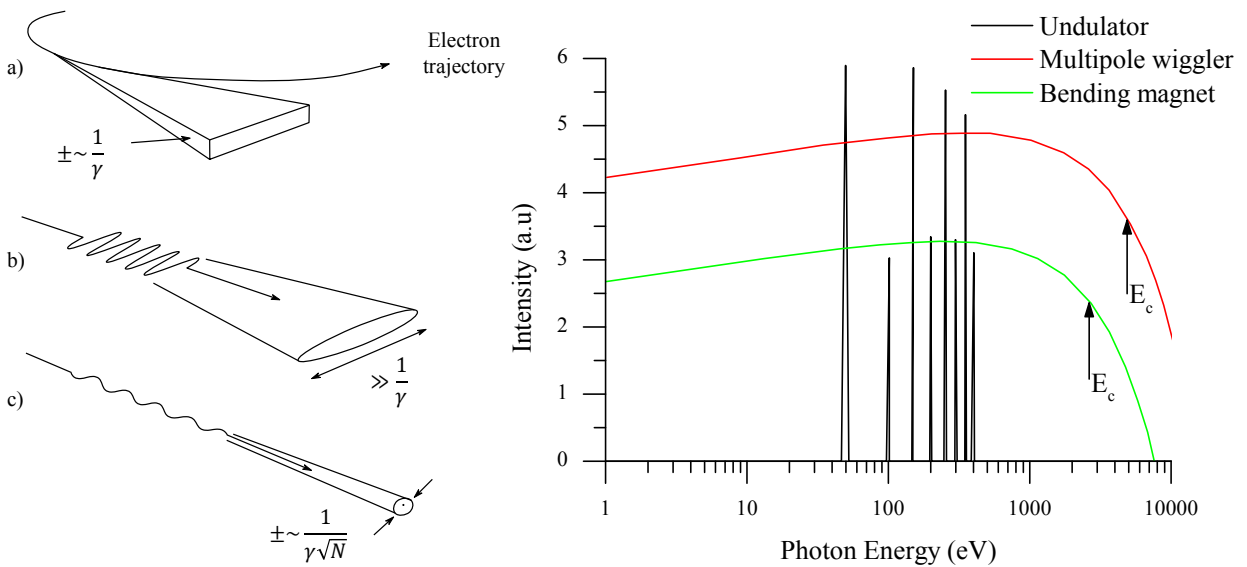


**Figure 2.7:** A comparison of the general character of different common synchrotron radiation sources. Left: the spatial emission patterns of (a) a bending magnet, (b) a wiggler, and (c) an undulator. Right: typical spectral distributions<sup>7</sup>.

## Bending Magnets

The original SR sources were the bending magnets that are used to create the desired electron trajectory within the synchrotron ring (or storage ring). The emitted radiation is generally a source of energy loss in the ring and is far less intense than that produced by insertion devices, but it can still be effectively harnessed for many types of less photon-hungry experimental techniques. Since the demands of the storage ring lattice determine the specifications of the bending magnets, beamline designers must work with the light given. Bending magnet radiation is emitted in a broad horizontal fan as the electrons pass around the bend in a smooth, broad energy distribution (Figure 2.7). The location of the center of this energy distribution, known as the critical energy ( $E_c$ ), depends on the ring energy ( $E$ ) and bending magnet field strength ( $B$ ) as<sup>17</sup>:

$$E_c = \frac{3e\hbar B\gamma^2}{2m} \quad (2.5)$$

where  $e$  and  $m$  are the electron mass and charge respectively and  $\gamma$  is the Lorentz factor discussed earlier. By collecting the physical constants, the critical energy can be conveniently expressed as

$$E_c(\text{keV}) = 0.6650E^2(\text{GeV})B(\text{T}) \quad (2.6)$$

## Wigglers & Undulators

Wigglers and undulators have significant advantages over bending magnets as SR sources. While distinctly different devices, the line separating them can be, at times, unclear. Both devices use an array of magnets in a storage ring straight section to cause the electron beam to undergo a series of sinusoidal oscillations generating significantly more light than a single curve though a bending magnet. One of the key values that describes this path taken is the unitless deflection parameter  $K$  given by<sup>7</sup>:

$$K = \frac{Be\lambda_u}{mc2\pi} = 93.36B_0(\text{T})\lambda_u(\text{m}) \quad (2.7)$$

where  $B_0$  is the peak vertical magnetic field in the insertion device and  $\lambda_u$  is the period of the magnetic array.

**Wigglers** are typically considered to be devices with  $K \gg 1$ . In this regime, a band of light over a broad range of energies is emitted by each period of the magnetic structure that makes up the wiggler, which adds together to result in a much more intense source (Figure 2.7). Wigglers have a critical energy much the same as a bending magnet, but unlike a bending magnet the field strength can be adjusted by the beamline designer (and sometimes during operation) to optimize the  $E_c$  for a particular experimental technique. The dependence of  $E_c$  on  $B$  means that high magnetic field strengths can be very desirable for hard X-ray beamlines. To that end, super-conducting wigglers are common at third generation facilities.

**Undulators** are typically operated at  $K$  values of  $\sim 1$ , although undulator-like behavior can sometimes be seen<sup>7</sup> as high as  $K \sim 5$ . While the  $K$  value can be a good rule of thumb, what distinguishes an undulator is the fact that the small deflection within these devices and the inherent collimation discussed in Section 2.1.1 causes the light emitted to interfere constructively. This effect produces a strongly enhanced and narrow spectral peak at one fundamental energy and higher modes thereof (Figure 2.7).

By considering the trajectory and acceleration of an electron passing through a periodic magnetic structure, along with the necessary conditions for constructive interference, the so-called undulator equation can be derived<sup>7</sup>:

$$\lambda_n = \frac{\lambda_u}{2n\gamma^2} \left( 1 + \frac{K^2}{2} + \theta^2\gamma^2 \right) \quad (2.8)$$

which relates the ring energy (through  $\gamma$ ) and undulator parameters ( $K$ ,  $\lambda_u$ ) to the peak wavelength ( $\lambda_n$ ) for a given harmonic ( $n$ ).

Due to the narrow spectral width of the resulting energy peaks for a given undulator configuration, the range of usable energies is very small. This means that for an undulator to be useful for a reasonable range of energies,  $\lambda_n$  must be adjustable. This is typically accomplished through adjustment of the effective magnetic field strength by changing the gap between the upper and lower girders that the magnets are mounted on. Because the

higher order peaks can be quite intense, several different orders can be used to increase the usable energy range within the practical design limits of gap size and magnet strength. Traditional insertion device designs usually involve a specially designed flat vacuum chamber with the magnet arrays positioned above and below which limits the minimum size of the gap and the achievable field strengths. To produce high energy photons from a lower energy third generation storage ring, very small gap undulators with specially designed NEG pumped beam pipes or even undulators with the magnets placed inside the vacuum system are used to allow for the smaller gaps needed to produce higher field strengths. These In-Vacuum and Small Gap Undulators (IVUs and SGUs) are much more complicated and expensive to design, build and maintain, but they can provide excellent performance for hard X-ray beamlines.

Since the electron oscillations are confined to the plane of the storage ring, the light produced by bending magnets, wigglers and undulators is linearly polarized in that plane as long as it is viewed from within that plane. Above and below that plane the light appears elliptically polarized. There are a number of approaches to varying the magnetic structure to change the orientation of the electron acceleration, and hence the polarization of the resulting light. One increasingly common such design will be discussed here as it is in use on the beamline REIXS beamline.

**Elliptically Polarized Undulators** (EPU) add additional degrees of freedom to the motion of the girders that gives control over the polarization of resulting light (Figure 2.8). A 1.6 m long, 75 mm period second generation Advanced Plane Polarized Light Emitter (APPLE-II) EPU is installed at the CLS as the source for the REIXS beamline.

The APPLE-II undulator design<sup>18</sup> is a proven and increasingly popular design that consists of two girder pairs, one above and one below the electron beam path. By moving the one girder in each pair in the same or differing direction, either helical or sinusoid motions in varying orientations can be induced in the electron beam (see Figure 2.9) to generate linear or elliptically polarized light with adjustable orientation<sup>19</sup>.

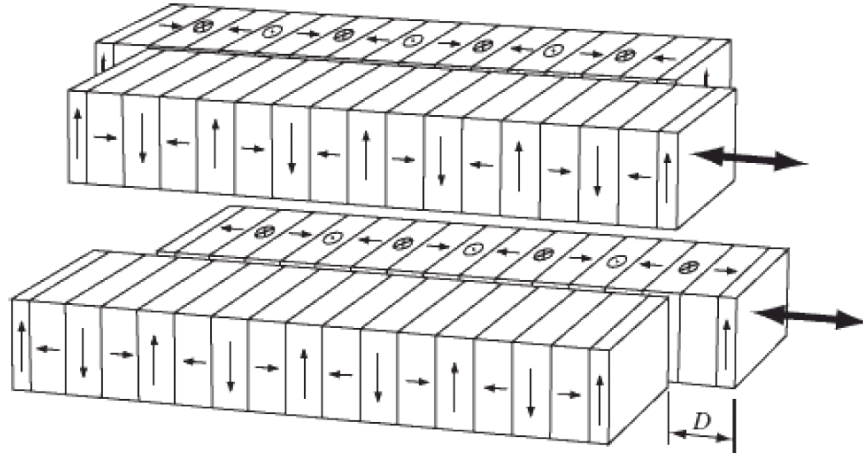


**Figure 2.8:** Schematic view of an APPLE-II type elliptically polarized undulator<sup>7</sup>.

## 2.2 The REIXS Beamline

Once the light has been generated by a source in the storage ring it is further refined and delivered to the experimenter by the carefully designed optics of the beamline. The endstation that is the focus of this document is one of two installed on the Resonant Elastic and Inelastic Soft X-ray Scattering (REIXS) beamline at the Canadian Light Source. This section will give a brief walk-through of the REIXS beamline and its key components.

The function of a beamline is to collect, condition (focus and monochromatize) and transmit the light generated by the source in the storage ring to the experimental endstations at the end of the beamline. How a beamline accomplishes this will depend greatly on the type of source, the design energy range and the requirements of a particular type of experiment. A carefully designed beamline will maximize the transmission of photons from the source within the established bandwidth requirements while conserving the inherent brightness of the source as much as possible. Like most engineering tasks, it comes down to establishing a careful balance between competing factors; flux versus energy resolution, cost versus performance, complexity versus flexibility.

The REIXS beamline is optimized for high-flux (high intensity and a small spot size) to facilitate the low yield photon-in photon-out experiments that the two endstations on the beamline are primarily designed for. It can efficiently operate though an energy range of 80-2000 eV.

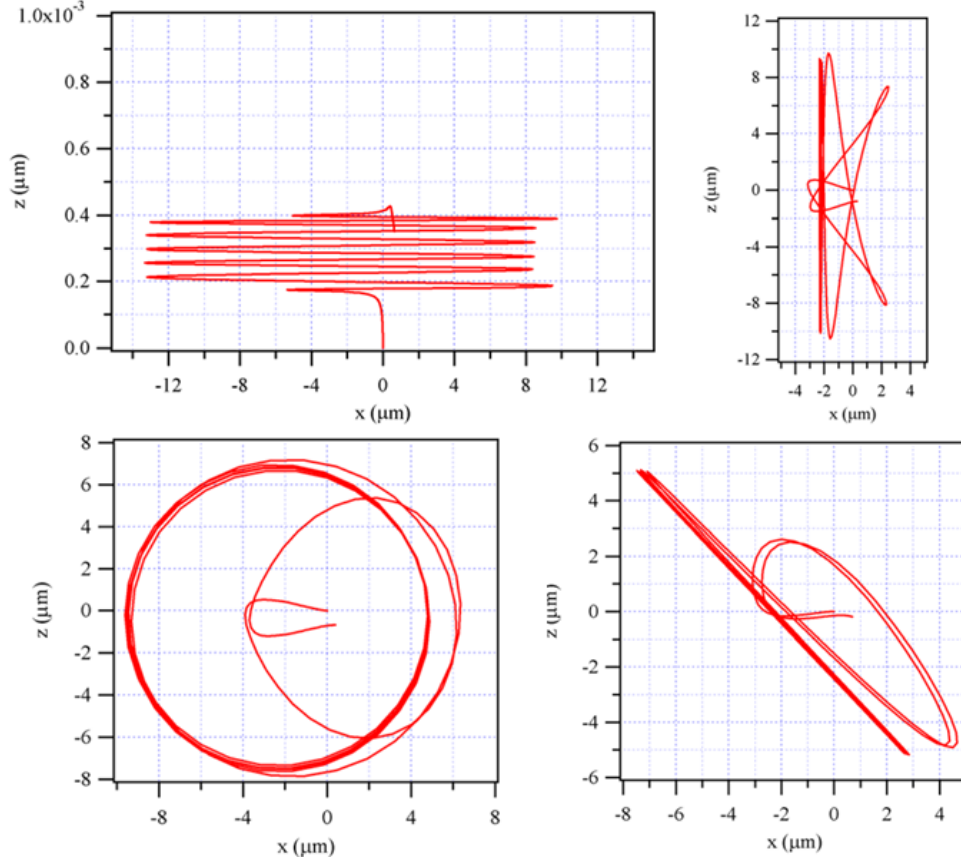


**Figure 2.9:** The calculated electron paths through the REIXS APPLE-II EPU for various grider alignments (polarization settings)<sup>20</sup>.

The REIXS beamline was constructed on port 10ID-2, sharing straight 10 in a chicaned configuration with the Spectromicroscopy (SM) beamline on port 10ID-1. Both beamlines use identical 1.6 m long, 75 mm period APPLE-II elliptically polarized undulators as sources. In addition to maximizing the scientific output from a single storage ring straight section, this arrangement has made possible unique 2-in-1 operating modes. By reconfiguring the chicane magnets in the storage ring, both sources can be used by one beamline, facilitating otherwise impossible techniques such as rapid switching of polarization (RSP), a technique of particular interest to the RSXS endstation on REIXS.

One of the biggest challenges faced by the designers of the REIXS beamline was the severe space constraints imposed by the fact that the beamline is located on a shared straight section and the beamline is itself shared by two endstations (see Figure 2.10).

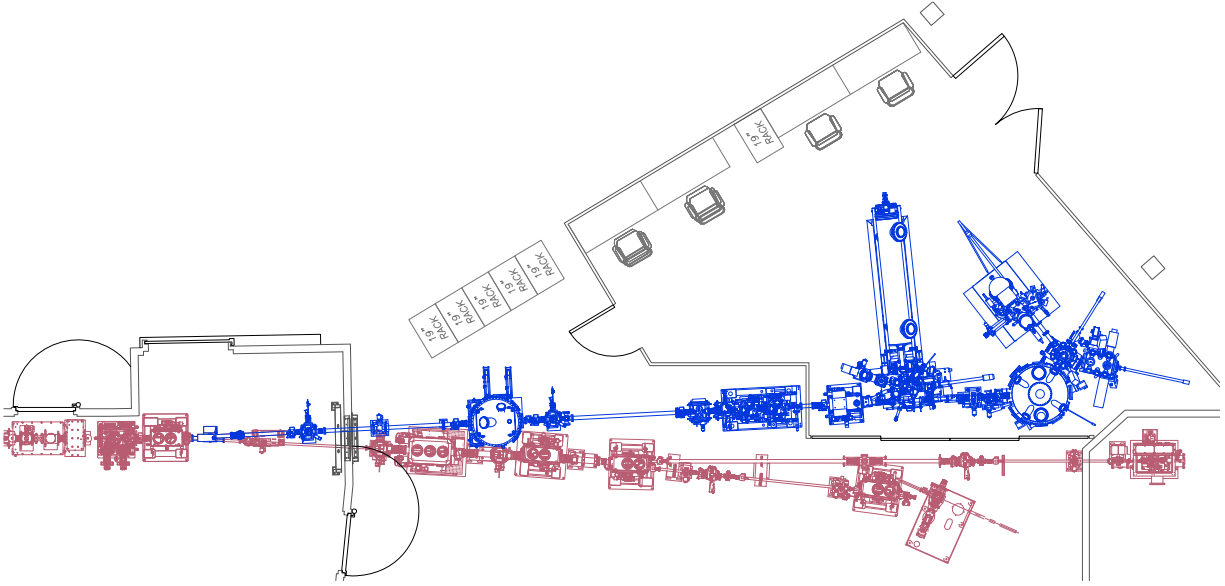


**Figure 2.10:** A CAD drawing of the REIXS beamline component layout (blue) demonstrating the extremely close proximity to the neighbouring SM beamline components (red)<sup>21</sup>.

### 2.2.1 Primary Optics

The first active beamline component is a shared variable aperture that can provide an arbitrarily adjustable horizontal and vertical opening to both the SM and REIXS beamlines simultaneously. Since this is the first component in the beamline, it needs to be able to handle the full power load from both EPUs simultaneously which can exceed 4000 W with a power density of nearly 60 W/mm<sup>2</sup> with overlapped beams in 2-1 operating mode<sup>22</sup>. This is achieved by using a shallow incidence design to distribute the heat load over large water cooled copper blades.

After the variable aperture is the first mirror tank which contains the prefocusing optics for both SM and REIXS. SM uses a single mirror and REIXS uses two separate mirrors (M1A and M1B), one to handle the beam from each EPU. These gold coated sagittal cylindrical mirrors collect and vertically collimate the light from the EPUs, conditioning it for the monochromator. Both mirrors are operated at grazing incidence and deflect the beam by approximately 3 degrees<sup>21</sup>. The beam can deposited up to 440 W of power with a density of 0.68 W/mm<sup>2</sup> on each mirror requiring both prefocusing mirrors to have integrated water cooling.

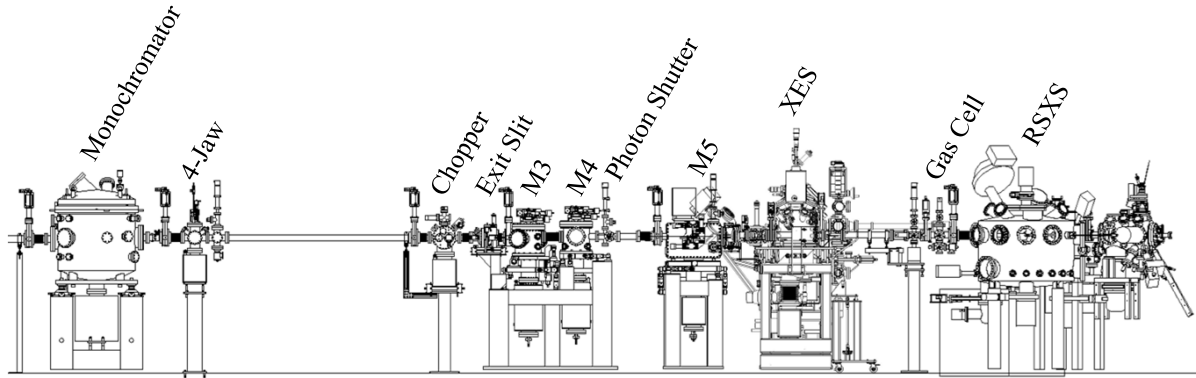


**Figure 2.11:** Elevation drawing of the REIXS beamline components outside of the primary optical enclosure.

Between M1A/B and the monochromator is an adjustable water cooled 4-jaw aperture. The electrically isolated blades facilitate measurement of the relative beam current and the 4-jaw can be used to characterize the beam and aid in the alignment of M1A/B as well as to refine the source size for the monochromator to reduce aberration for sensitive measurements.

## 2.2.2 Monochromator

The monochromator is the heart of nearly any beamline. The design implemented on the REIXS beamline is a Variable Line Spaced Plane Grating Monochromator (VLS-PGM) based on an existing design developed for use at the Photon Factory<sup>23</sup>. The design uses a plane mirror (M2) to accept the collimated beam from M1A/B and direct it onto a VLS Plane Grating at the correct angle to allow it to both disperse and focus the light onto the exit slit 4 meters further down the beamline (see Section 2.3.1 for more details on VLS gratings).

Four selectable mirror coatings (nickel, silicon, carbon and gold) and three selectable gratings with slightly different line density variations (nickel LEG, gold LEG and gold HEG) are installed to optimally cover the designed energy range. The selection of available coatings can also be used to minimize the transmission of higher order light when necessary. The monochromator optics all require water cooling, M2 has internal water cooling channels and the gratings have external water cooled heat sinks.

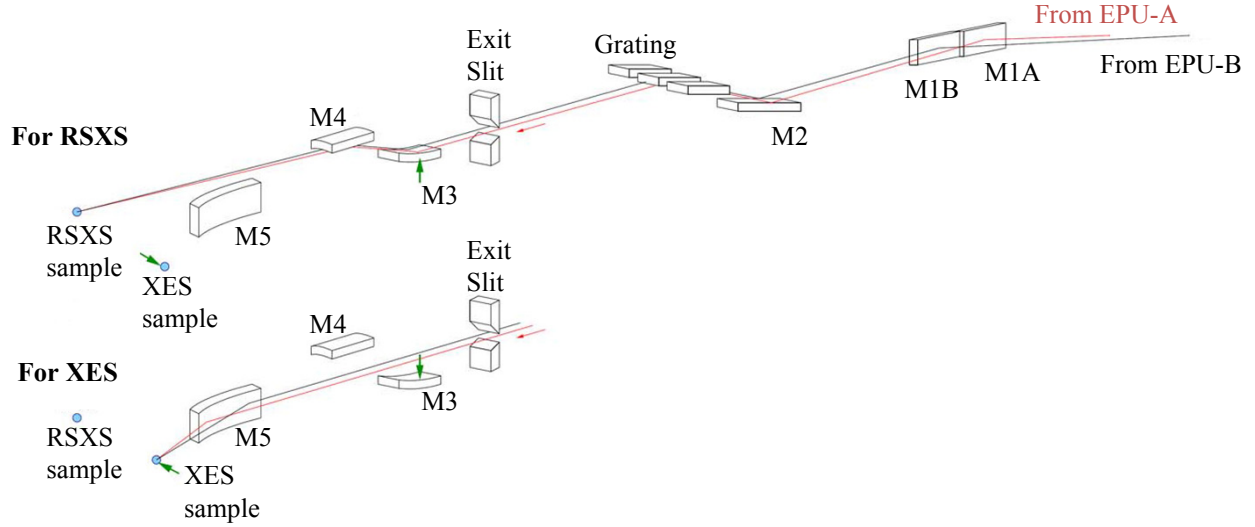


**Figure 2.12:** The optical layout for the REIXS beamline showing the configurations to deliver light to each endstation as well as the dual beam paths for 2-in-1 mode<sup>22</sup>.

### 2.2.3 Secondary Optics & Endstation Switching

After the monochromator is a second 4-jaw for characterization and further conditioning of the beam before the light passes through a beam chopper. In 2-in-1 mode, the light from the two EPU's is still physically separated at this point in the beamline and the chopper uses a rotating drum to select which beam continues down the beamline. By setting each EPU to a different polarization, the chopper allows the polarization incident on the sample to be alternated rapidly.

After the chopper is the exit slit that the monochromator focuses onto. The exit slit can be adjusted from fully closed to over  $500 \mu\text{m}$  wide. The exit slit performs the dual duty of determining the bandwidth of the monochromator and the source size for the final re-focusing optics. Because of the differing requirements and positions of the two endstations on REIXS, separate sets of re-focusing optics are used for each endstation.

The RSXS endstation uses two mirrors, an elliptical vertical focusing mirror (M3) and a cylindrical horizontal focusing mirror (M4). In addition to focusing the beam onto the RSXS endstation sample position, these two mirrors result in a parallel vertical beam shift that carries the resulting beam over the final mirror (M5).

M3 is designed to be lowered by several millimeters, which results in the beam bypassing

M3 and M4 where M5, an ellipsoidal toroid mirror focuses the beam vertically and horizontally onto the XES endstation sample position.

After the M5 mirror tank, the beamline branches with separate beam pipes supplying each endstation (see Figure 2.13). The beam pipe for the RSXS endstation passes behind the XES sample chamber and an arrangement of bellows allows the XES endstation to translate by approximately 300 mm to align the bypass beam pipe with the beamline when the RSXS endstation is in use.

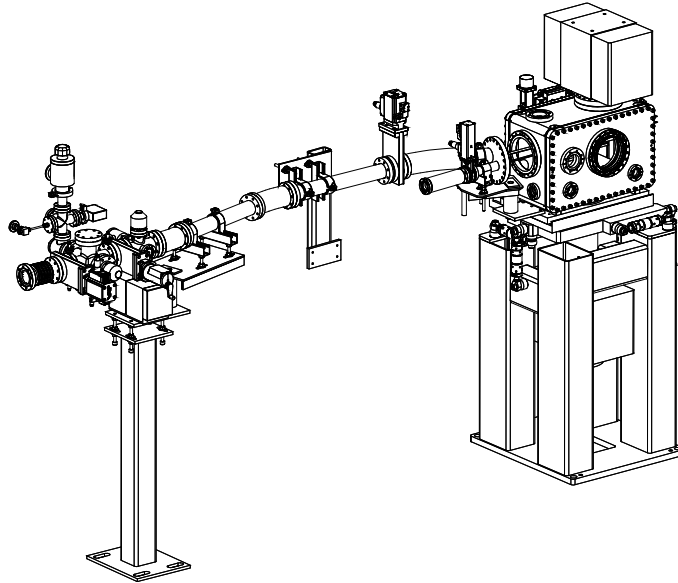


**Figure 2.13:** The REIXS bellows branch, M5 mirror tank and gas cell.

Between the two endstations, on the RSXS branch, is a gas cell that allows for gas phase soft X-ray absorption measurements. This is primarily used for calibration and verification of the beamline performance (see next section), but could potentially be used for scientific measurements.

## 2.2.4 Performance

There are three main characteristics of the light supplied by the beamline that are of concern to the experimenter for the majority of the measurements performed on this endstation. They are the total number of photons per second incident on the sample (flux), energy bandwidth of those photons (resolution,  $\Delta E$  or resolving power,  $E/\Delta E$ ), and the spot size. The beamline performs very well in all these regards.

The expected beamline performance at the XES endstation taken from the REIXS preliminary design report<sup>21</sup> is shown in Table 2.1. These numbers are based on the CLS reference specifications for operation from 2008 onward, all of which have been met except for 500 mA operation.

**Table 2.1:** REIXS beamline ultimate design goals for performance at XES endstation

Parameter	goal for 2008+
Flux at 100 eV	$\geq 7.5 \times 10^{11}$
Resolving Power at 100 eV	15000
Flux at 1000 eV	$\geq 3.0 \times 10^{11}$
Resolving Power at 1000 eV	6000
Spot size (for $25 \mu\text{m}$ exit slit)	$\leq 50 \times 10 \mu\text{m}$

The beamline flux was measured using two different photodiodes, a Hamamatsu G1127-02 photodiode<sup>24–26</sup> and an IRD AXUV100G photodiode<sup>27,28</sup>. One is located after M5 and one is on the endstation sample arm. Using their respective quantum efficiency curves to calibrate the measurements, the results were very nearly identical (see Figure 2.14).

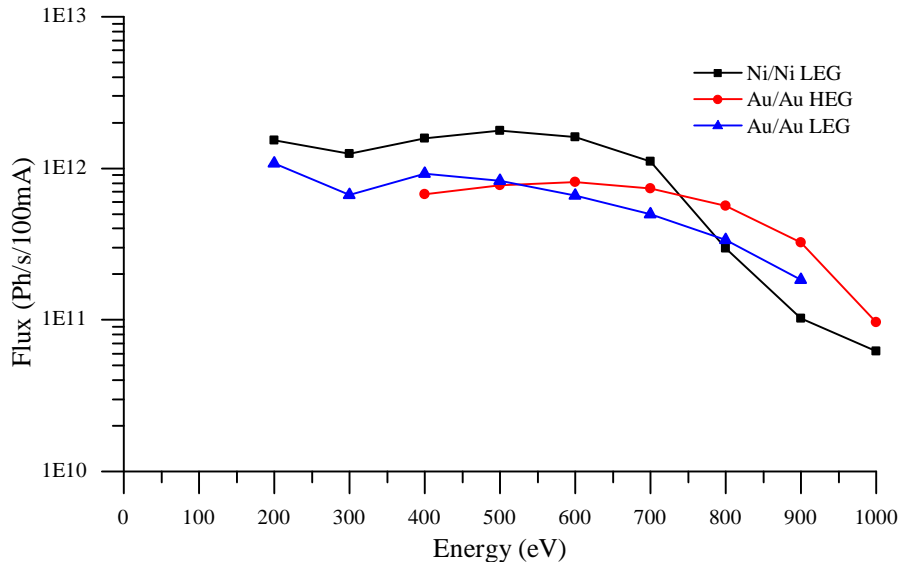


**Figure 2.14:** The flux at the XES sample position as measured by calibrated photodiodes with a  $25 \mu\text{m}$  monochromator exit slit.

The design goal for a flux of  $\geq 7.5 \times 10^{11}$  at 100 eV, while not measured directly, appears

likely achieved and the design goal for a flux of  $\geq 3.0 \times 10^{11}$  at 1000 eV is very nearly so. Performance much above 1000 eV is of less interest to users of the XES endstation, as it is beyond the designed operating range of the spectrometer. The noticeable drop in flux between 300 eV and 400 eV is C K-edge absorption by small amounts of carbon contamination on the beamline optics, which is unavoidable.

For optimum spectrometer emission performance, particularly when operating slitless (see Section 5.2), a small vertical beam height is critical. The optical layout of the beamline results in a beam spot at the sample position that is a 2-to-1 demagnified image of the monochromator exit slit. For best overall performance, the beamline is typically operated with a 10  $\mu\text{m}$  or 25  $\mu\text{m}$  exit slit but for non-resonant emission spectroscopy higher flux and lower resolution is ideal. Since the incident flux is roughly proportional the slit size, a wide range of exit slit sizes were studied. The vertical beam profile has been carefully measured for a variety of exit slit sizes by using a knife edge mounted to the endstation sample motion stage. Both vertical and horizontal scans were completed and while the beam spot size is very near the limits of the motion stage's precision, reasonable results were obtained. The less critical horizontal beam profile FWHM was found to be 64.7  $\mu\text{m}$  with the beamline horizontal 4-jaws wide open, and the vertical beam profile FWHM (see Figure 2.15) is less than 12.5  $\mu\text{m}$  for exit slit sizes as high as 50  $\mu\text{m}$ .

Experimental measurement of resolution can be very difficult, particularly for a very high resolution system that significantly exceeds the natural line widths of the systems that can be measured. Deconvoluting the various contributions can be more of an art than science. One useful empirical technique<sup>29</sup> involves the measurement of a  $\text{N}_2$  gas phase absorption spectra (see Figure 2.16) and the comparison of the ratios of the first valley height to the third peak height.

From that ratio, the approximate incident energy resolution can be determined. This was completed for the three common grating/mirror combinations for the REIXS monochromator. For all three combinations the resolving power for a 10  $\mu\text{m}$  monochromator exit slit is approximately 15,000 and for a 25  $\mu\text{m}$  slit it is 8,000-9,000. Voigt peak fitting to decouple the natural line width from the resolution was also performed on this data and agreed well. Similar measurements were completed at the 867 eV neon absorption edge and for the Au-

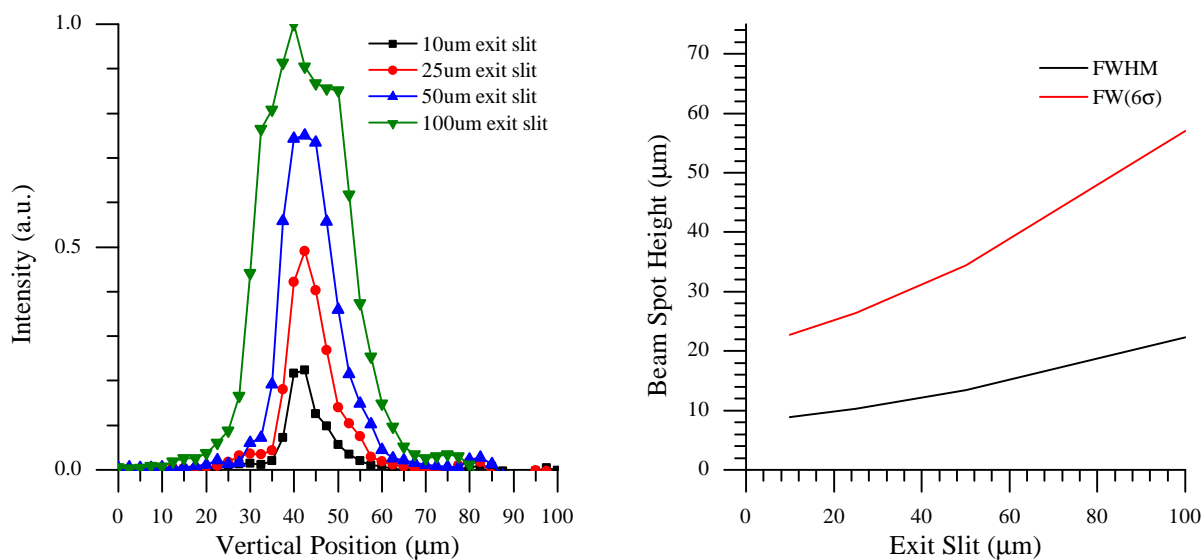


**Figure 2.15:** The vertical beam profile at the XES endstation as measured by knife-end scans.

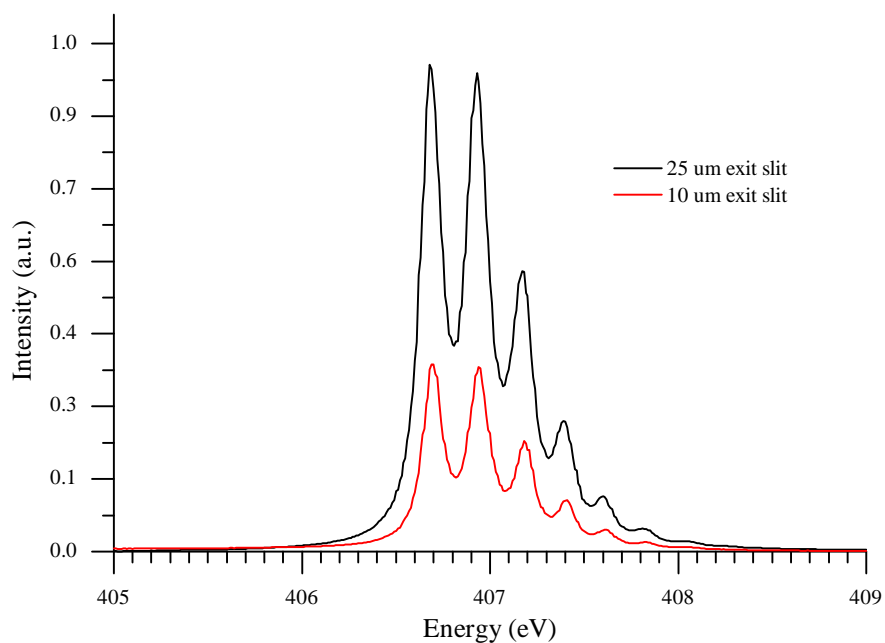


**Figure 2.16:** The  $N_2$  gas phase absorption measurements for the Nickel LEG monochromator grating using the REIXS gas cell to verify the beamline resolving power. The two different measurements show the effect of the exit slit size on the relative intensity and peak height ratio (resolution).

HEG grating intended for this energy the resolution was approximately 9,000 at 10  $\mu\text{m}$  slit and 5,000 at 25  $\mu\text{m}$  slit. All measured resolutions exceed the design goals for the beamline.

## 2.3 Diffraction Gratings

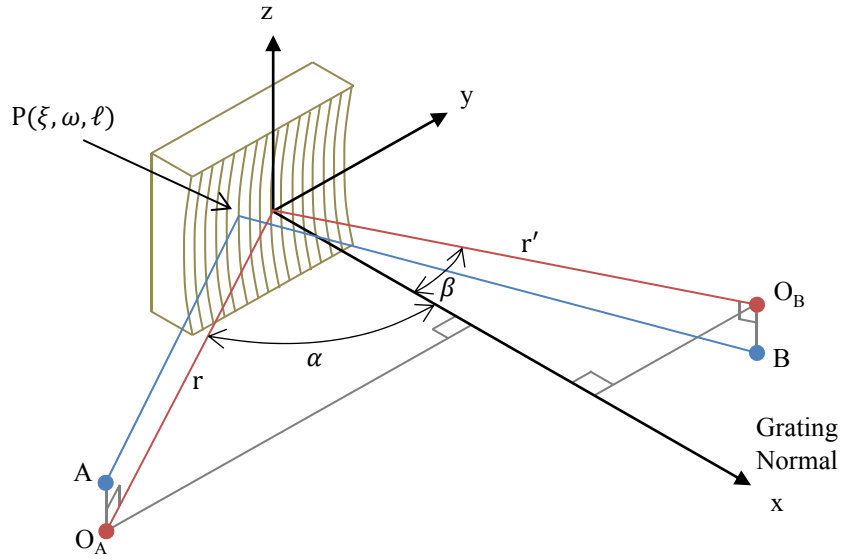


**Figure 2.17:** For an optical element to create an image at point  $B$  of a source at  $A$  all possible optical paths from  $A$  to  $B$  via the optical element must be of the same length.

To design an optical system such as the spectrometer discussed herein, relatively simple geometric optics can be applied to arrive at the complicated set of equations that describes behavior and optical characteristics of the system. Fermat's principle sets out the requirements for the formation of an image in an optical system, stating that for an image to be formed the optical path must be an extremum. What this means for reflective optics is that for an optical element to create an image at point  $B$  of a source at  $A$ , all the optical paths from  $A$  to  $B$  via the optical element must be of the same length (see Figure 2.17)<sup>8</sup>. If we describe the surface of the optical element as  $P(\xi, \omega, \ell)$  (where  $\xi, \omega, \ell$  define the location on the surface of element), then an arbitrary path can be described by an optical path function:

$$F = \overline{AP} + \overline{PB} \quad (2.9)$$

then satisfying the relations:

$$\frac{\partial F}{\partial \omega} = 0 \quad \text{and} \quad \frac{\partial F}{\partial \ell} = 0 \quad (2.10)$$

will lead to an aberration free image. If the optical element is a grating, then the phase advance resulting from diffraction must be taken into account by adjusting the optical path function as:

$$F = \overline{AP} + \overline{PB} + Nk\lambda\omega \quad (2.11)$$

where  $k$  is the diffraction order,  $\lambda$  is the incident wavelength and  $N$  is the grating line density.

This leaves only to define the optical path function, which can be done in terms of a power series expansion in the coordinate system shown in Figure 2.17 as:

$$F = F_{00} + \omega F_{10} + \ell F_{01} + \omega \ell F_{11} + \frac{1}{2} \omega^2 F_{20} + \frac{1}{2} \ell^2 F_{02} + \frac{1}{2} \omega^3 F_{30} + \frac{1}{2} \omega \ell^2 F_{12} + \dots \quad (2.12)$$

which leads to:

$$\begin{aligned} F_{00} &= r + r' \\ F_{10} &= Nk\lambda - (\sin \alpha + \sin \beta) && \text{grating equation} \\ F_{01} &= \frac{-z}{r} + \frac{-z'}{r'} \\ F_{11} &= -\frac{z \sin \alpha}{r^2} - \frac{z' \sin \beta}{r'^2} \\ F_{02} &= \frac{1}{r} + \frac{1}{r'} - \frac{1}{R} (\cos \alpha + \cos \beta) && \text{sagittal focus} \\ F_{20} &= \left( \frac{\cos^2 \alpha}{r} - \frac{\cos \alpha}{R} \right) + \left( \frac{\cos^2 \beta}{r'} - \frac{\cos \beta}{R} \right) && \text{meridional focus} \\ F_{30} &= \left( \frac{\cos^2 \alpha}{r} - \frac{\cos \alpha}{R} \right) \frac{\sin \alpha}{r} + \left( \frac{\cos^2 \beta}{r'} - \frac{\cos \beta}{R} \right) \frac{\sin \beta}{r'} && \text{primary coma} \\ F_{12} &= \left( \frac{1}{r} - \frac{\cos \alpha}{R} \right) \frac{\sin \alpha}{r} + \left( \frac{1}{r'} - \frac{\cos \beta}{R} \right) \frac{\sin \beta}{r'} && \text{astigmatic coma} \end{aligned} \quad (2.13)$$

According to Fermat's principle, and Equation 2.10, all of these terms with the exception of  $F_{00}$  must be identically zero for a perfectly focused and aberration free image to be formed.

Unfortunately, this is only possible for a normal incidence optical arrangement and due to the extremely low reflection/diffraction efficiency of all materials in the soft X-ray region, grazing incidence optics are necessary. With that in mind, the goal then becomes to minimize the aberrations as much as possible over the range of energies (i.e. diffraction angles) that the grating is intended for.

A clever way of achieving this, that is particularly useful for spectrometers, was devised over 130 years ago by H.A. Rowland<sup>30</sup>, and Rowland circle optical arrangements are still commonly used today. By simply recognizing that the factors:

$$\left( \frac{\cos^2 \alpha}{r} - \frac{\cos \alpha}{R} \right) \quad \text{and} \quad \left( \frac{\cos^2 \beta}{r'} - \frac{\cos \beta}{R} \right)$$

appear in  $F_{20}$  and  $F_{30}$  of Eqn. 2.13, two of the most dominant aberration terms can be made identically zero by setting both these factors to zero. Solving the resulting equations yields the widely used Rowland circle condition:

$$r = R \cos(\alpha) \quad \text{and} \quad r' = R \cos(\beta) \tag{2.14}$$

These two equations define a geometric layout of the optical elements that will guarantee that  $F_{20}$  and  $F_{30}$  are zero. The form of these equations defines a circle in space (Figure 2.18), with a diameter equal to the radius of the grating, commonly referred to as the Rowland circle.

By placing the source (as defined by  $r$  and  $\alpha$ ), the grating and the detector (as defined by  $r'$  and  $\beta$ ) on this circle, the meridional focus and primary coma aberration terms will be eliminated. For a spectrometer, the sagittal focus, which is perpendicular to the dispersion direction, is not critical and setting  $F_{10}$  to zero results in the familiar grating equation for an arbitrary incidence angle:

$$Nk\lambda = \sin \alpha + \sin \beta \tag{2.15}$$

If the entrance angle ( $\alpha$ ) and entrance arm ( $r$ ) are established and fixed, as is most common and practical from a mechanical standpoint, then the Rowland circle conditions (Equation 2.14) determine the require grating radius:

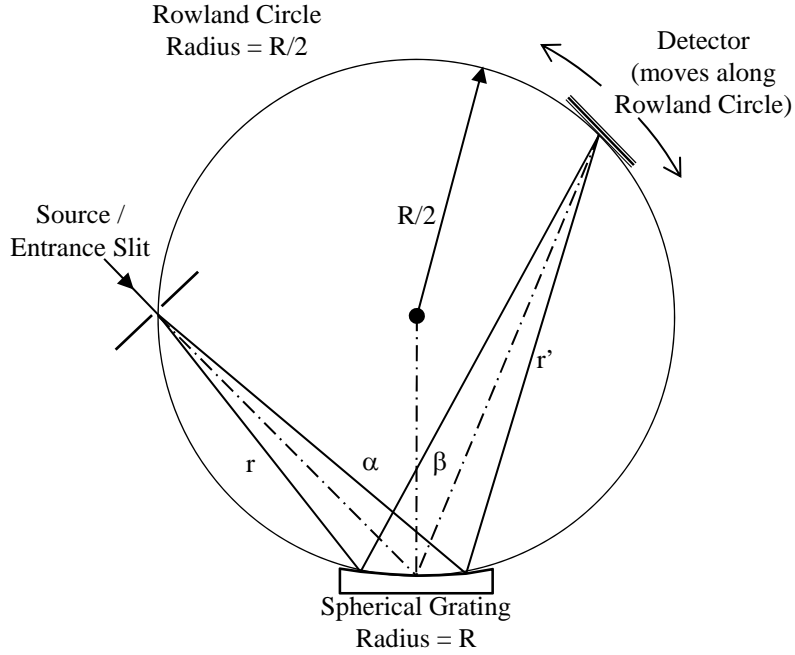


**Figure 2.18:** A graphical representation of the Rowland circle condition.

$$R = \frac{r}{\cos \alpha} \quad (2.16)$$

and the distance at which the image will be formed:

$$r' = R \cos \beta \quad (2.17)$$

if  $\beta$  is known, and  $\beta$  can be easily determined for the desired wavelength and order from Equation 2.15 once  $\alpha$  and  $N$  are established. So, from a purely geometric optics point of view, a Rowland circle spectrometer is defined by 3 parameters ( $\alpha$ ,  $r$  and  $N$ ), and the detector position ( $r'$  and  $\beta$ ) for a given wavelength ( $\lambda$ ) and order ( $N$ ) is then determined by equations 2.15 and 2.17:

$$\beta = \sin^{-1}\left(\frac{Nk\lambda}{\sin \alpha}\right) \quad \text{and} \quad r' = R \cos \beta$$

Rowland Spectrometer Alignment Formulae  
(2.18)

### 2.3.1 Variable Line Spacing

Additional control over the focal properties of a grating can be achieved at the cost of added complexity, in both design and fabrication, and reduced flexibility by varying the line density across the face of the grating. This can be applied in a number of different ways, from correcting for the remaining aberrations at a particular wavelength, to compressing the focal field to allow for simplified and more compact mechanics. Each requires the added parameters, along with those already discussed, to be optimized differently, but the mathematical formalism describing those parameters is the same.

As before, we have the optical path function:

$$F = \overline{AP} + \overline{PB} + N(\omega)k\lambda\omega \quad (2.19)$$

where  $k$  is the diffraction order,  $\lambda$  is the incident wavelength and  $N(\omega)$  is the grating line density which now depends on  $\omega$  and can be expressed as a polynomial<sup>31</sup>:

$$N(\omega) = N_0\left(\omega + \frac{b_2}{R}\omega^2 + \frac{b_3}{R^2}\omega^3 + \frac{b_4}{R^3}\omega^4 + \dots\right) \quad (2.20)$$

where  $R$  is the radius of the grating,  $N_0$  is the nominal line density and  $b_n$  are the polynomial coefficients used to describe the variation in line density. This is a general case and it is suitable for designing mechanically ruled gratings that can be fabricated with arbitrary line density variations. If other techniques, such as holographic ruling, are to be used then a different expression tailored to the parameters actually used to fabricate the grating is preferred<sup>32</sup>. These techniques are outside the scope of this document.

The same conditions for focus (Equation 2.10) can now be applied. This leaves only to define the optical path function which can be done in terms of a power series expansion in the coordinate system shown in Figure 2.17 as:

$$F = F_{00} + \omega F_{10} + \ell F_{01} + \omega\ell F_{11} + \frac{1}{2}\omega^2 F_{20} + \frac{1}{2}\ell^2 F_{02} + \frac{1}{2}\omega^3 F_{30} + \frac{1}{2}\omega\ell^2 F_{12} + \dots \quad (2.21)$$

which leads to:

$$\begin{aligned}
F_{00} &= r + r' && (*) \\
F_{10} &= Nk\lambda - (\sin \alpha + \sin \beta) && \text{grating equation} \\
F_{01} &= \frac{-z}{r} + \frac{-z'}{r'} && (*) \\
F_{11} &= -\frac{z \sin \alpha}{r^2} - \frac{z' \sin \beta}{r'^2} \\
F_{02} &= \frac{1}{r} + \frac{1}{r'} - \frac{1}{R}(\cos \alpha + \cos \beta) - \boxed{\frac{N_0 k \lambda}{R}} && \text{sagittal focus} \\
F_{20} &= \left( \frac{\cos^2 \alpha}{r} - \frac{\cos \alpha}{R} \right) + \left( \frac{\cos^2 \beta}{r'} - \frac{\cos \beta}{R} \right) - \boxed{\frac{2N_0 k \lambda}{R} b_2} && \text{meridional focus} \\
F_{30} &= \left( \frac{\cos^2 \alpha}{r} - \frac{\cos \alpha}{R} \right) \frac{\sin \alpha}{r} + \left( \frac{\cos^2 \beta}{r'} - \frac{\cos \beta}{R} \right) \frac{\sin \beta}{r'} - \boxed{\frac{2N_0 k \lambda}{R^2} b_3} && \text{primary coma} \\
F_{12} &= \left( \frac{1}{r} - \frac{\cos \alpha}{R} \right) \frac{\sin \alpha}{r} + \left( \frac{1}{r'} - \frac{\cos \beta}{R} \right) \frac{\sin \beta}{r'} && \text{astigmatic coma}
\end{aligned} \tag{2.22}$$

The boxed terms arise from varying the line density and are of special interest to this discussion. In order to have sufficient control over the optical system, the line space variation must usually be a fourth degree polynomial, which results in terms as high as  $F_{40}$  being required. Terms above  $F_{30}$  have been excluded since they involve at least a dozen terms each and do not directly reveal anything of interest upon examination.

By examining Equation 2.22 it can be seen that, due to the wavelength dependency, this can only be optimized for a single energy (or in some cases 2-3 specific energies). This is where the restrictions inherent in VLS designs become apparent. However, with careful design the added flexibility of the additional parameters that are introduced can allow for the creation of unique and high performance gratings for certain special applications, such as the one discussed in Section 4.1.3.

### 2.3.2 Grating Efficiency

A key aspect of the design of this spectrometer was obtaining an understanding of how diffraction efficiency (the fraction of incident photons of a given energy that are diffracted into the desired order) relates to the design variables of the grating. This was the subject of a Ph.D.

thesis by Mark Boots, a member of our research group. Beginning with the Neviere code (a commercial diffraction efficiency algorithm) he developed code to effectively optimize grating geometry to maximize diffraction efficiency within established constraints. Limitations with this code eventually lead to work on the development of completely new, more efficient and flexible software package which he has released under an open-source license<sup>3</sup>. This allowed our design to boast a careful balance of diffraction efficiency and resolving power. None of the existing spectrometer designs that could be found in the literature have included such efficiency calculations. Some calculations have been made of existing system's diffraction efficiency for comparison, however effective comparison is not possible as sufficient details of the gratings used are rarely published, or in some cases, even known. For a thorough discussion on the topic of grating efficiency the reader is directed to Mark Boots' Ph.D. thesis<sup>2</sup>. A brief overview of the subject will follow.

The Wood anomaly provides a useful tool to conceptualize what is happening at the grating surface from a wave theory perspective. Since the diffraction angle varies with incidence angle and energy (see Equation 2.18), for a given energy there will be an incident angle that results in the first outside order (Figure 2.19) reaching 90 degrees. At this point the wave becomes evanescent and the energy that was propagating into that order is redistributed, enhancing the efficiency of inside orders. This is true for a square grating, but more complicated for a blazed grating. Rigorous calculations are required to accurately predict the effect of blaze angle on diffraction efficiency.

In general terms, to accurately predict the diffraction efficiency of an arbitrary groove profile using electromagnetic wave theory, Maxwell's equations must be applied to solve for the fields in the vicinity of the grating surface. By setting up a periodic boundary value problem involving the incident, transmitted and reflected waves, the ratio of the intensity of the reflected wave to that of the incident wave can be used to determine the diffraction efficiency. The problem is not generally solvable analytically, however a variety of advanced numerical methods can be applied. Since these rigorous calculations are outside the scope of this document, it will suffice to mention that the following grating design variables determine the diffraction efficiency of a grating:

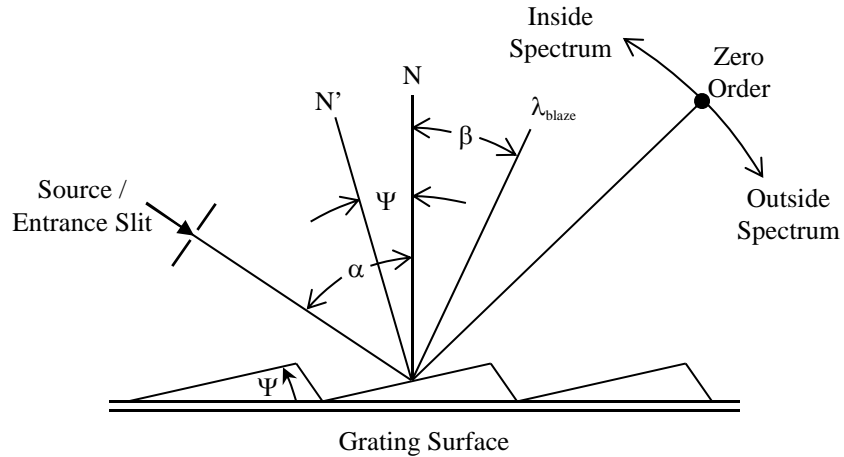


**Figure 2.19:** A blazed grating profile. Conceptually, the blaze angle shifts the effective surface normal and can be used to “aim” the specular reflection into the energy range of interest, increasing the efficiency of those energies. Rigorous wave-theory calculations produce answers that vary somewhat from this simple picture but it is still conceptually useful.

1. Groove Density ( $N$ )
2. Incidence Angle ( $\alpha$ )
3. Energy/wavelength ( $E / \lambda$ )
4. Groove Profile (see Figure 2.19)
5. Grating material (coating)

Variables 1-3 are also critical to the resolving power of the system. A careful balance is required for optimum overall performance since any gain made in either efficiency or resolving power by adjusting one of these parameters results in a loss in the other.

The groove profile (or blaze angle  $\Psi$  for the typical saw tooth profile) is used to optimize the diffraction efficiency of a grating for a given energy and diffraction order. It is tied strongly to the incidence angle. A helpful but not entirely accurate picture to explain this relationship is that the blaze angle is used to align the specular reflection to the diffraction angle of the energy of interest.

The grating material determines its index of refraction and reflectivity characteristics. Typical grating materials or coatings include carbon, gold, nickel, platinum and iridium.

The coating must be carefully chosen for the design energy range of the grating to maximize reflectivity, while carefully avoiding materials with an absorption edge within the desired performance range of the grating.

Some of the results of the calculations performed, and further insight into their usefulness to the design and commissioning process, can be found in Section 5.1.1.

## 2.4 Detectors

The relatively low overall efficiency of an emission spectrometer makes it impractical to collect data in a scanning mode with a single point detector. To accumulate an entire emission spectrum at once, a spatially resolved area detector is required. There are only two detector technologies that provide effective spatially resolved soft X-ray imaging, Charge-Coupled Device (CCD) and Micro-Channel Plate (MCP) detectors. While CCDs can provide much higher spatial resolution, for a number of practical reasons, an MCP detector was chosen during the design process<sup>1</sup> of this spectrometer.

An MCP detector system is comprised of a detector head, a preamplifier, a high voltage supply network and position analyzer electronics (see Figure 2.20).

Because the geometry of a Rowland circle spectrometer requires the detector to be tangent to the focal curve, the detector must be in a grazing incidence orientation. To accommodate this requirement without blocking the line of sight to the detector surface, a custom bias/support ring modification of a standard 40 mm diameter 5-plate MCP detector was created by Quantar Technology Inc. specifically to meet our needs (see Figure 2.21).

Due to the significant noise concerns discussed below, long cables between the detector head and preamplifier are not acceptable. To accommodate the required detector travel without unacceptable signal/resolution loss, a custom in-vacuum preamplifier was also required for this system (see Section 5.2.4)

### 2.4.1 MCP Operating Principle

Photon detection by an MCP begins as an incident photon strikes the top surface of the channel plate stack. If sufficiently energetic (UV or higher), the photon will generate a small

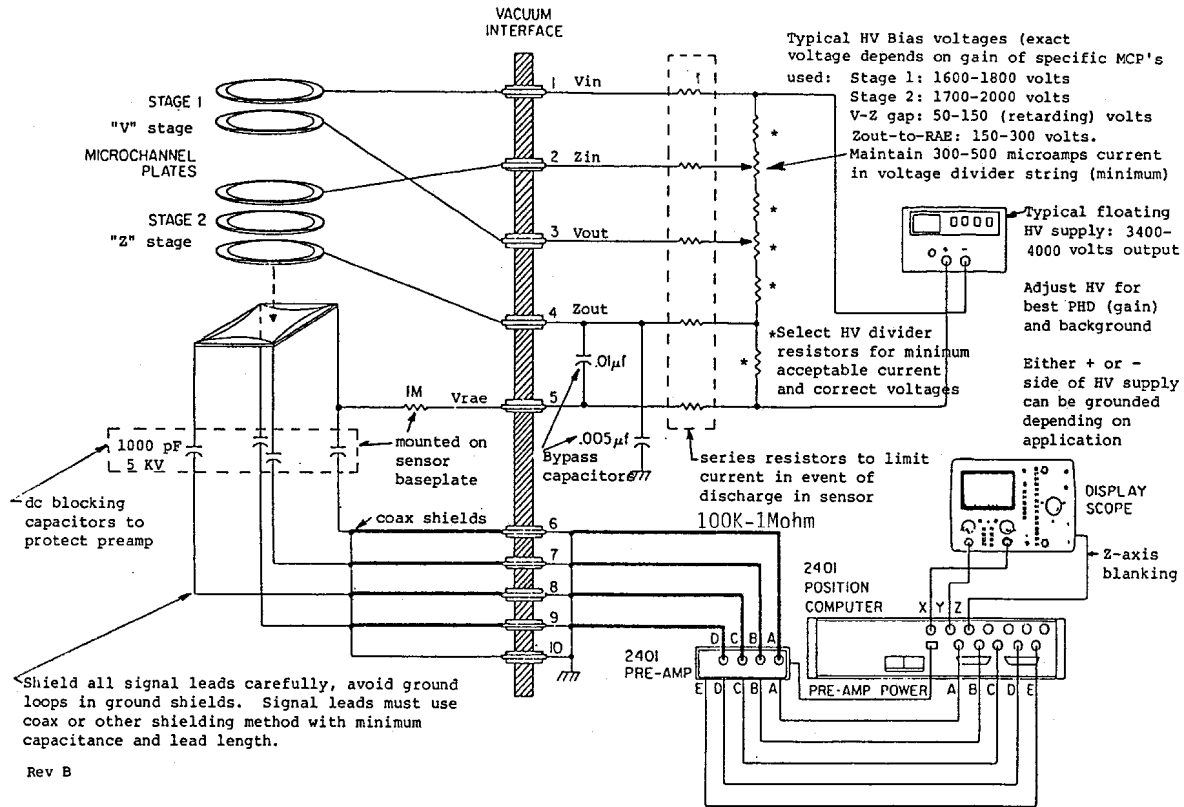


**Figure 2.20:** A system schematic for the 5-plate Quantar MCP used in this system, with the standard air-side preamplifier shown<sup>33</sup>.

cloud of secondary electrons. A coating, such as CsI, can be used to increase the conversion efficiency for soft X-rays. Typically, a bias between the top of the MCP stack and a bias plate or mesh above it will help collect and localize these electrons. The MCPs have a high voltage bias across them to accelerate the electrons into the microscopic ceramic channels passing through the plates. This results in high energy electrons undergoing multiple collisions with the channel walls leading to the emission of additional secondary electrons in a cascade (see Figure 2.22). A stack of five such channel plates with progressively higher voltage biases generates a gain on the order of  $5 \times 10^7$ .

The resulting picocoulomb charge pulse is deposited on a resistive anode encoder (RAE), a sheet of resistive material each corner of which is capacitively coupled to a separate charge sensitive shaping amplifier. The RAE is essentially four RC transmission lines that split the charge between the 4 corners/amplifiers proportional to the distance of the charge pulse from each corner<sup>35</sup>.

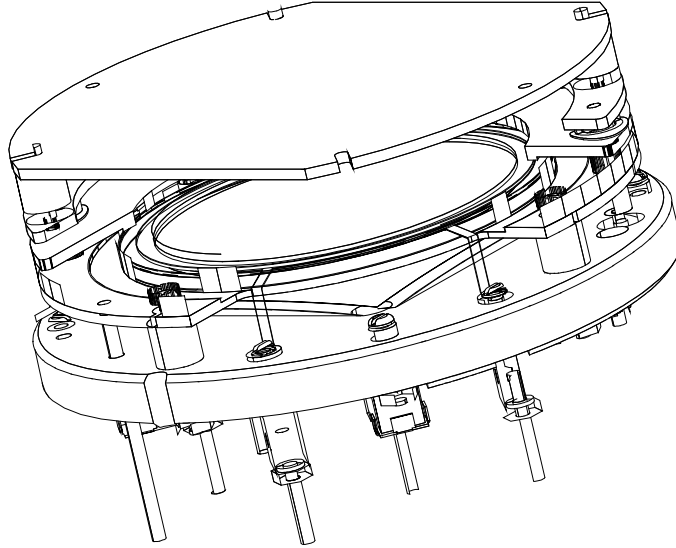


**Figure 2.21:** The CAD model of the custom 5-plate, 40 mm MCP detector head supplied by Quantar Technology Inc. and used in this endstation.

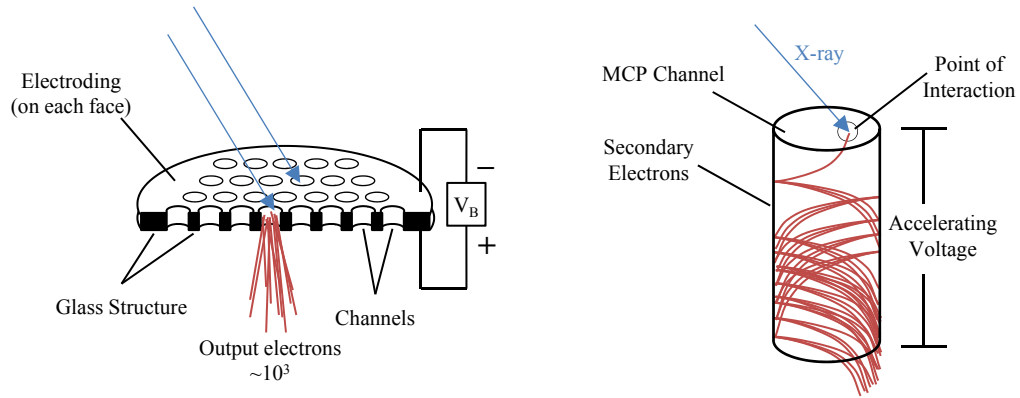


**Figure 2.22:** Principle of operation of a microchannel plate (MCP)<sup>34</sup>.

The four amplified signals, along with a fifth fast-sum channel, are sent to a position analyzer. A discriminator assesses the fast-sum pulse for threshold, peak and pileup, and triggers the position analyzer electronics for accepted pulses. The position analyzer performs a ratio comparison of the 4 signals and determines an analog position based on these formulae<sup>36</sup>:

$$X = \frac{B + C}{A + B + C + D} \quad \text{and} \quad Y = \frac{A + B}{A + B + C + D} \quad (2.23)$$

The resolution of the detector is limited by noise superimposed on the signal to about  $62.5 \mu\text{m}$ <sup>36</sup>. This is due to the noise causing a certain amount of randomization of the output

position values for like events. For an ideal system, the main noise contributions are from the sensitive preamplifier circuitry and the inherent thermal noise in the RAE. Any noise that can couple in to the system, particularly before the preamplifier, will rapidly degrade the resolution and all efforts must be made to reduce and eliminate all such noise sources. The cables between the detector and the preamplifier must also be as short as possible to minimize capacitance that can soak up the charge and reduce the signal to noise ratio.

The analog position signal from the position analyzer is then digitized by a 10-bit ADC, which provides 1024 channels along each axis. For a 40 mm square detector, this sufficiently over-samples the analog signal to ensure that the digitization process is not a resolution limiting step. The resulting digital events are then accumulated as a 2D array for the duration of a measurement to form an image. To reduce data file sizes, the image is binned at full 10-bit resolution only in the dispersion direction and is binned at 6-bit resolution along the other axis (see Figure 2.23).

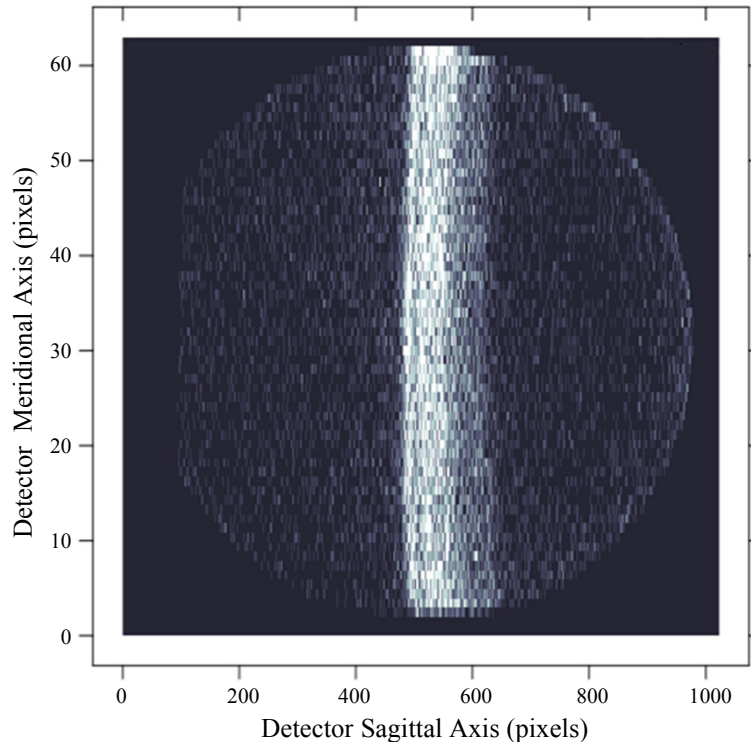


**Figure 2.23:** An image of a nitrogen emission line collected with an MCP detector. The curvature is an unavoidable aberration resulting from grazing incidence spherical optics that must be removed in post processing.

## 2.5 Vacuum Systems

Much of the complexity of the endstation arises from the need to operate the instrument in ultrahigh vacuum conditions. There are several factors that contribute to this need, the most pressing of which is the fact that soft X-rays are readily absorbed by air with a mean free path measurable in microns. In addition, many sample systems are sensitive to contamination by atmospheric gases such as oxygen and water. Finally, much of the instrumentation used in these systems is sensitive to either oxygen or water if not both, although the fact that an ultrahigh vacuum environment is already required is a key factor in the decision to use such technologies.

### 2.5.1 Levels of Vacuum

Vacuum systems can be broken, roughly, into three categories or levels. Rough vacuum ranges from atmospheric pressures (760 torr) down to  $10^{-3}$  torr, high vacuum (HV) ranges from  $10^{-3}$  torr down to  $10^{-8}$  torr and ultrahigh vacuum (UHV) ranges from  $10^{-8}$  torr down to  $10^{-12}$  torr. These levels are distinguished by the composition and behavior of the gases that remain in the system.

	ATM	Rough	HV	UHV
Pressure:	760 torr		$10^{-3}$ torr	$10^{-8}$ torr
Flow:	viscous (fluid)		molecular(random)	
Gases:	N <sub>2</sub> , O <sub>2</sub> , H <sub>2</sub> O		H <sub>2</sub> O, CO, H <sub>2</sub>	CO, H <sub>2</sub>
Gas Load:	volume		desorption	diffusion      permeation
Mean Free Path :	microns	centimeters		kilometers
Molecular Density :	$10^{19}/\text{cm}^3$	$10^{13}/\text{cm}^3$		$10^7/\text{cm}^3$
Monolayer Formation :	nanoseconds	milliseconds	seconds	minutes      hours

**Figure 2.24:** The typical characteristics of the different levels of vacuum.

Rough vacuum is simply the removal of the original atmospheric gases in the system. At these pressure levels, gases continue to behave as a fluid subject to viscous flow and the

time required to pump out a sealed system is purely a function of the volume of the system and the pumping speed. The composition of gases remaining in the system after roughing it out is the same as the original atmosphere it contained (usually air, 76% N<sub>2</sub>, 20% O<sub>2</sub>, 2% H<sub>2</sub>O). However, as roughing continues, desorption of water from the surface of the chamber plays an increasing role in the composition of the remaining gases. Over time, the fraction of residual molecules that are H<sub>2</sub>O in a rough vacuum system frequently exceeds 75%. As a result, even at rough vacuum level, sample/instrument contamination is a serious concern. It takes on the order of 10<sup>-2</sup>s for a monolayer of residual gas molecules to form on a clean surface exposed to a pressure of 10<sup>-3</sup> torr.

The transition from rough vacuum to HV levels is demarcated by the transition from viscous flow behavior of the residual gases to molecular flow. An intermediate transitional flow regime is often defined, but for systems destined to operate at HV or UHV levels the transitional regime is passed through so quickly that it is largely irrelevant to this discussion. At roughly 10<sup>-3</sup> torr the mean free path of the remaining gas molecules begins to exceed the dimensions of typical vacuum chambers and collisions with the chamber walls become more likely than collisions with other gas molecules. As such, gas flow in the system is by random motion and it is no longer possible for flow to result from a pressure gradient. This has significant consequences for pumping since the pressure of residual gas can no longer be relied upon to push the remaining molecules towards the pumping port and out of the system. As pumping continues though the HV range desorption of molecules from surfaces becomes the leading source of gas in the system<sup>37</sup> which will now, typically, be composed of 80% H<sub>2</sub>O and 20% N<sub>2</sub>, CO, H<sub>2</sub>, CO<sub>2</sub>. While it may seem intuitive that the chamber is largely empty by the time a pressure of 10<sup>-6</sup> torr is reached there are, in fact, still 3x10<sup>10</sup> molecules/cm<sup>3</sup> in the system and a molecular monolayer can form on a clean surface in a matter of seconds. At mid HV levels, the mean free path of soft X-rays is on the order of kilometers, allowing for efficient delivery of photons to the sample and from the sample to the spectrometer and other instruments.

In a HV system, H<sub>2</sub>O desorbing from the surface of the vacuum system is the leading contributor to the residual gas. This continues until the majority of the adsorbed water is removed from the system, at which point the system crosses into the UHV range. As with

the HV range, molecular flow dominates. To reach UHV levels, pumping speed alone is not sufficient. Careful attention must be paid to material selection, component design, and surface finishes. The vast majority of common construction materials have outgassing rates that become significant even in the HV range. Even with careful design, pumping alone can take weeks or months to reach UHV levels since the rate of desorption of water from the surfaces in the system becomes the limiting factor. It is common practice to heat or “bake out” vacuum systems, sometimes as high as  $200^{\circ}\text{C}$  -  $300^{\circ}\text{C}$  to speed desorption and pump down to UHV levels. This imposes additional significant design constraints as the vacuum system needs to be able to tolerate the stresses induced by such temperature changes. Even at  $10^{-9}$  torr it is surprising to realize that there are still  $3 \times 10^7$  molecules/cm<sup>3</sup> present in the system, however now it will take on the order of an hour for a molecular monolayer to form on a clean system and the virtual absence of water and oxygen means that the molecules that do accumulate will typically not adversely affect sample materials or instruments. At these levels  $\text{CO}$  and  $\text{H}_2$  are the dominant molecules present,  $\text{H}_2$  being particularly difficult to deal with because not only is it difficult to pump, but it is able to permeate most materials to some extent and find its way into even the best of sealed systems.

## 2.5.2 Vacuum System Design

There are a plethora of issues and complications that must be considered when designing an instrument that requires a UHV environment. These range from the relatively mundane concerns of restricted size, space and accessibility to more esoteric concerns such as materials affinity for  $\text{H}_2\text{O}$  and  $\text{H}_2$  permeation rates. Not only is the choice of material critical but fabrication, preparation and handling techniques become critical as well. In addition, there is a significant amount of equipment required to achieve, monitor and maintain a UHV environment. These issue will be addressed in this section.

### Mechanical Design Considerations

The mechanical design of UHV systems is far from trivial, and those meant for the close quarters of a typical synchrotron facility experimental floor face even greater limitations. The entire process becomes a painstaking balancing act as cost and size are weighed against

capability and convenience. Careful consideration must be given to the size and shape of vacuum chambers to ensure that the desired instrumentation has the space it requires while avoiding overcrowding or wasted expense. Easy access to vacuum chambers for installation and maintenance is always desirable, but an excessive number of access ports, in addition to increasing cost, increases the chance of minor leaks and makes tracking down such issues more difficult.

While each chamber must be carefully designed, the entire system must also be considered as well. How the chambers will be positioned with respect to each other and how they will be connected, mounted and aligned will affect the design of the individual chambers. Particularly when chambers are required to move with respect to each other, the weights and vacuum forces involved can be considerable. Ion pumps can weigh in excess of 150 kg and the rotational inertia of high speed turbo pumps may be an issue. While the atmospheric force exerted on vacuum chamber is easily withstood by stainless steel or even aluminum chambers, flexible bellows connections between chambers can result in significant force imbalances that must be considered. A standard 6" welded bellows can experience an effective load of over 850 N from vacuum forces, more than sufficient to shift chambers, bend frames and destroy motion stages if not properly accounted for.

Careful thought must be given to the design of every component to be placed within a vacuum chamber. Material selection is critical and will be addressed in the following section. Beyond that, the design must take into account the requirements of a UHV environment from the very beginning. Form is not only linked to function but must also take into account the space constraints of a vacuum chamber and the limited access to the inside of the chamber for installation and maintenance. This may seem obvious, but it is all too easy to overlook. The design must include a careful step-by-step plan for the installation of the components into the vacuum chambers and how that process will integrate into the system design and assembly as a whole. Several examples of small engineering oversights that created significant difficulties at assembly time can be found in Section 5.2.

One final consideration unique to vacuum environments is the so called virtual leak. Precision machined metal surface can be very effective at sealing against one another, but rarely are such seals perfect without being designed to seal. What can easily happen, however,

is that a volume between two in-vacuum components can be sufficiently well sealed that gas can be trapped within it during initial pump down. Since the seal is likely imperfect, the trapped gas will eventually bleed away - fast enough that it keeps the chamber pressure from dropping as quickly as desired but slow enough that it can take days or weeks to cease. One of the most common sources of such virtual leak is bolt holes. The significant forces applied to thread surfaces are perfect for creating metal-metal seals, so much so that care must be taken to avoid bolts of like material lest vacuum (or “cold”) welding may permanently fuse such connections. To eliminate these potential trapped volumes, bolt holes can be drilled all the way through, side vented with a second hole, or specialized vented fasteners can be used (see Figure 2.25). Through holes can also be a concern for which vent channels in the surfaces or vented washers are an effective solution. Finally, mating large flat surfaces should be avoided. Since no surface is ever truly flat, a slight concavity can result in a significant trapped volume.

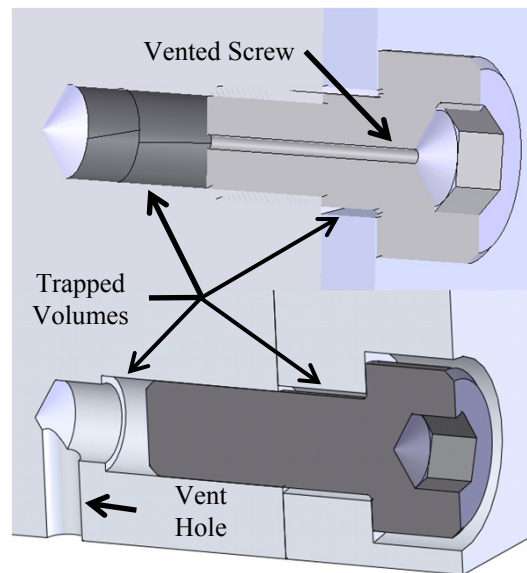


**Figure 2.25:** Two solutions to the potential virtual leaks from trapped gases under screws. The trapped volume in through holes can be dealt with by placing vent channels at the base of the screw head, on the plate surface, or by using a vented washer.

## Vacuum Compatible Materials

The selection of materials suitable for use in UHV is limited. Even some metals (zinc, cadmium) can outgas significantly, causing serious problems in vacuum systems and eventually coating and “poisoning” filaments and detectors in the system<sup>38</sup>. Zinc is often used to plate steel bolts for corrosion resistance so care must be taken when choosing fasteners. While most stainless steel alloys would perform acceptably in vacuum, the 300 series of austenitic stainless steels are typically preferred, 304L and 316L low carbon alloys being ideal. Austenitic steel has a face centered cubic primary crystal phase and shows increased resistance to H<sub>2</sub> permeation, reduced initial diffuse H<sub>2</sub> and a lower affinity for H<sub>2</sub>O. With proper material preparation and pretreatment, H<sub>2</sub> diffusion and H<sub>2</sub>O desorption can be all but eliminated<sup>39</sup>.

Aluminum is also a commonly used structural material, even for chamber walls. It has a slightly higher affinity for H<sub>2</sub>O leading to greater desorption during pump down and it is less resistant to H<sub>2</sub> permeation than stainless steel. Despite these drawbacks, the light weight and ease with which aluminum is machined and finished make it an appealing option. In addition, aluminum alloys contain significantly fewer atoms with K- and L- edges in the soft X-ray energy range which can drastically reduce ion background levels due to secondary electron emission. The specific alloy chosen is very important, since some aluminum alloys have a substantial amount of zinc. Aluminum alloy 6061-T6 is ideal, being in excess of 95% aluminum, containing no more than 0.25% Zinc, and having excellent machinability and mechanical characteristics.

Other metals can be used but are less common. Copper, particularly Oxygen-Free High-Conductivity (OFHC) copper is a common choice when good electrical and thermal conductivity is a concern. Gold and silver can also be used, the former often being used to plate heat shielding. Nickel plating can be used to improve the surface characteristics of necessary but less ideal materials, such as rare-earth magnets. It is important to note, however, that a thin plating layer is not adequate to prevent diffusion from the bulk - it serves only to reduce affinity for H<sub>2</sub>O and reduce adsorption by surfaces that are difficult to finish. Brass is a common material used in vacuum systems but it must be avoided in UHV systems due to a high zinc content. Tables 2.2-2.4 provide a more exhaustive list of materials that have

been tested in vacuum, although it dates to 1975.

**Table 2.2:** Measured outgassing rates of metals after vacuum baking<sup>40</sup>.

Material	Finish	$\text{torrL}/(\text{cm}^2\text{sec})$
6061 Aluminum	baked 15 h at 250°C	$4.0 \times 10^{-13}$
	baked 20 h at 100°C	$4.0 \times 10^{-14}$
Copper	baked 20 h at 100°C	$1.1 \times 10^{-12}$
Copper (OFHC)	baked 24 h at 100°C	$2.2 \times 10^{-14}$
	baked 24 h at 250°C	$1.4 \times 10^{-15}$
Cr (0.5%)-Cu (99.5%) alloy	baked 24 h at 100°C	$2.8 \times 10^{-15}$
	baked 24 h at 250°C	$2.7 \times 10^{-15}$
304 Stainless steel	baked 30 h at 250°C	$3.0 \times 10^{-12}$
316L Stainless steel	baked 2 h at 850°C	$3.5 \times 10^{-13}$

**Table 2.3:** Measured outgassing rates of metals without vacuum baking<sup>40</sup>.

Material	Finish	$\text{torrL}/(\text{cm}^2\text{sec})$
Aluminum	fresh	$6.0 \times 10^{-10}$
Aluminum	degassed 24 h	$3.1 \times 10^{-10}$
Aluminum	3 h in air	$4.7 \times 10^{-10}$
Aluminum	anodized 2-um pores	$3.2 \times 10^{-08}$
Brass	wave guide	$1.0 \times 10^{-08}$
Copper	fresh	$4.1 \times 10^{-09}$
Copper	mechanically polished	$1.3 \times 10^{-09}$
Copper, OHFC	fresh	$3.6 \times 10^{-10}$
Copper, OHFC	mechanically polished	$1.6 \times 10^{-10}$
Cr (0.5%)-Cu (99.5%) alloy		$7.7 \times 10^{-12}$
Gold (wire)	fresh	$5.1 \times 10^{-10}$
Mild steel		$5.0 \times 10^{-08}$
Mild steel	chromium-plated, polished	$9.0 \times 10^{-10}$
Steel	chromium-plated, fresh	$5.8 \times 10^{-10}$
Steel	nickel-plated	$2.3 \times 10^{-10}$
Steel	descaled	$2.9 \times 10^{-07}$
Stainless steel		$1.4 \times 10^{-09}$
Molybdenum		$3.7 \times 10^{-10}$
Zinc		$3.2 \times 10^{-08}$
Titanium		$1.8 \times 10^{-09}$

Even ideal material choices can result in poor UHV performance if the materials are not properly finished. Machined surfaces tend to be microscopically uneven, and can contain

**Table 2.4:** Measured outgassing rates of various non-metals<sup>40,41</sup>.

Material	Finish	$\text{torrL}/(\text{cm}^2\text{sec})$
Stea		$9.5 \times 10^{-09}$
Pyrophyllite		$2.0 \times 10^{-08}$
Pyrex	fresh	$5.5 \times 10^{-10}$
Pyrex	1 month in air	$1.6 \times 10^{-10}$
Butyl DR41		$4.0 \times 10^{-07}$
Neopreneb		$1.8 \times 10^{-05}$
Perbunan		$2.2 \times 10^{-06}$
Silicone		$2.0 \times 10^{-06}$
Viton A	bake 12 h at 200°C	$2.0 \times 10^{-10}$
Polyimide	bake 12 h at 300°C	$3.8 \times 10^{-11}$
Araldite	molded	$3.5 \times 10^{-07}$
Araldite D		$1.3 \times 10^{-06}$
Araldite F		$7.3 \times 10^{-07}$
Kapton (polyimide) Cable	fresh	$1.0 \times 10^{-05}$
polyimide	baked @ 300°C	$4.0 \times 10^{-08}$
Kapton (polyimide) Cable	168 h in vacuum	$2.4 \times 10^{-08}$
Kel-F		$1.7 \times 10^{-08}$
Methyl Methacrylate		$1.4 \times 10^{-06}$
Mylar	24-h at 95% RH	$4.0 \times 10^{-07}$
Nylon		$6.0 \times 10^{-06}$
Plexiglas		$1.8 \times 10^{-06}$
Polyester-glass Laminated		$8.0 \times 10^{-07}$
Polystyrened		$2.0 \times 10^{-06}$
PTFE		$2.0 \times 10^{-07}$
PVC	24-h at 95% RHY	$2.0 \times 10^{-08}$
Teflon	10 h in vacuum	$2.5 \times 10^{-08}$

cracks and fissures that drastically increase the effective surface area and even create trapped gas pockets. This will increase outgassing and result in significantly longer pump down times. Polishing can make a significant improvement but being a mechanical process it can have similar issues, just on a smaller scale. Electropolishing is ideal, resulting in a microscopically smooth surface (see Figure 2.26). Anodized aluminum should be avoided since, while it improves wear and corrosion resistance, it dramatically increases the microscopic surface area and H<sub>2</sub>O affinity of the surface.

In addition to the above metals, there are a few other materials that are suitable for UHV

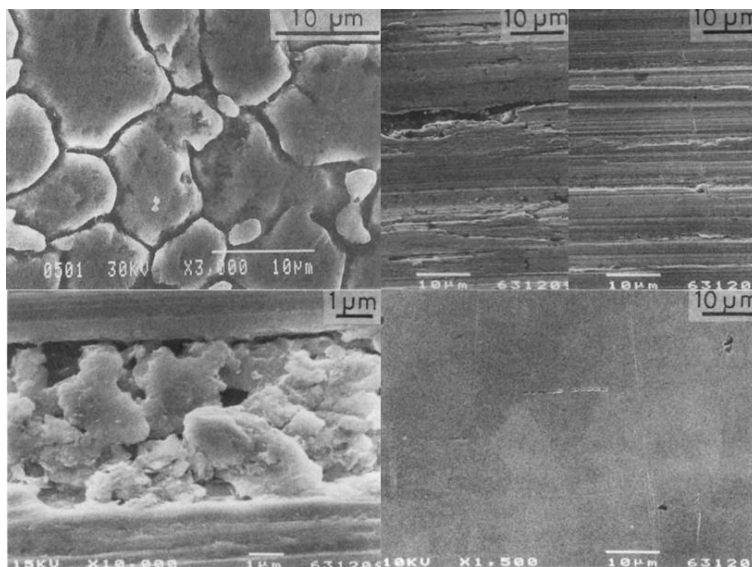


**Figure 2.26:** SEM images of different surface preparation techniques<sup>42</sup> including a typical unfinished surface (top left), belt-polished and buff-polished surfaces (top right), a typical dust-containing fissure in buff polished surface (bottom left) and an electropolished surface (bottom right).

environments. Many glasses and ceramics are acceptable and are invaluable for viewports and insulators. Borosilicate glass and fused silica (quartz) are most common for viewports, but other materials such as calcium fluoride and zinc selenide can be used for enhanced infrared transmission. Macor, Alumina and Steatite are common ceramics that make excellent insulators and perform well in vacuum. Plastics and polymers are generally not acceptable due to their high outgassing rates and H<sub>2</sub>O affinity but PEEK, PTFE and Kapton can be used in limited quantities to good effect. Certain rubbers can also be used, Viton being the most common, particularly for O-rings and seals in HV systems. While they outgas far less than one would expect, their H<sub>2</sub>O and H<sub>2</sub> permeability<sup>43</sup> makes them not suitable for UHV systems for long-term use. Certain epoxies, if prepared correctly, can have excellent UHV performance and there is an increasing range of greases and lubricants coming on the market that are specifically engineered for HV and even UHV use. They can be difficult to work with, often requiring exotic and highly toxic solvents, and in most cases they can be avoided in favour of dry-film or powder lubricates such as WS<sub>2</sub> and MoS<sub>2</sub>.

Following machining and polishing, all materials destined for HV or UHV environments must be carefully cleaned. There are different approaches to this but a typical basic approach

is to roughly wash with a detergent to remove oil and grease residue from machining/cutting fluids and then emersion in a heated ultrasonic bath of solvent or cleaner before thoroughly rinsing and hot air drying. Other techniques include bead blasting, acid etching, power washing and vapour degreasing but they are less commonly used. Electropolishing is an effective surface finishing and cleaning technique and it is possible to only rinse and dry parts before installation following such treatment.

Heat treatment beyond simple hot air drying, ranging from pre-installation vacuum baking to vacuum remelting, can be used not only to prepare the surface but also to speed the diffusion of hydrogen from the bulk. These techniques are typically only used for extremely high vacuum systems or for those systems where an in-situ bake out will not be possible due to temperature limitations imposed by other components.

Once cleaned, parts must be handled with extreme care. Gloves must always be worn as oils in fingerprints can easily contaminate a vacuum system. Clean rooms/tents are often used for UHV assembly to prevent dust particles from accumulating on parts, particularly optics. It is common practices to wipe parts down with a volatile solvent such as methanol or isopropanol immediately prior to installation to remove dust and to reduce accumulated moisture, although care must be used as excessive quantities of residual solvent can take a long time to remove from a system by pumping.

With a carefully designed UHV system fabricated, cleaned and assembled, the next step is to pump down the system. A large variety of high-tech equipment is available for this purpose and it will be discussed in the next section.

### **2.5.3 Vacuum Hardware & Instrumentation**

A vacuum system can be thought of as two distinct components. The vacuum chamber designed to “hold” the vacuum and the equipment required to evacuate and monitor it. Now that the design and preparation of the chamber and included systems has been discussed, attention must be given to the pumps and gauges that will be required to achieve and monitor the desired system pressure. During the design process this should clearly not be two discrete steps since this equipment is integral to the overall system design, but it is a suitable dividing point for the sake of this discussion.

There are numerous pumping and gauging technologies readily available, each with different strengths and weaknesses and each suited to different applications. To achieve UHV no one technology is adequate and the endstation that is the topic of this document uses no less than five distinctly different pumping technologies to pump down to and maintain a UHV environment. These systems will be discussed in this section, but a complete survey of pumping technologies is outside to scope of this document. Technologies such as diffusion pumps and cryopumps are in common use in research and industry and anyone taking on the design of a UHV system should familiarize themselves with their strengths and weaknesses before deciding on those best for a particular application.

## **Vacuum Pumping**

While modern vacuum pumps are sufficiently powerful and economical that choosing equipment clearly and dramatically exceeding the minimum required specifications is not only possible but reasonably cost effective. However, a basic understanding of pumping speeds, vacuum conductance, and throughput makes intelligent selection and system integration a relatively simple process.

Rough pumping is relatively trivial, as it is simply a matter of displacement of gas from the system. Pumping speeds are typically quoted in litres per minute and, calculating pump down times is a simple matter. Effective pumping speeds do fall off as the molecular flow regime is approached, but it is at this point that high vacuum pumps such as turbomolecular pumps are brought online. Since it usually takes only minutes to reach this point, even for relative large chambers, the base operating pressure of the pump becomes a more important factor.

Once in the molecular flow regime, pumps cannot remove molecules from the system that they are not able to directly interact with. Thanks to the high velocities and long mean free paths in the molecular regime, it is just a matter of time before molecules in the chamber make their way to a pump. How quickly a kinetic molecule is able to make its way to a HV pump to be removed from the system is largely dependent on the geometry of the system. As such, chamber design and pump positioning often play a larger role in effective pumping speed than does the base speed of the pumps.

An analogy to Ohm's law works very well in predicting the effective pumping speed of a system with throughput ( $Q$ ) taking the place of current and pressure ( $P$ ) taking the place of voltage. Conductance ( $C$ ), in this analogy, is a measure of the net speed that molecules can move through a region and is determined primarily by geometry, although temperature and the specific gases present can influence it. This gives<sup>44</sup>:

$$Q = C \times (P_1 - P_2) \quad (2.24)$$

Throughput is the mass flow rate through the system which can also be expressed as:

$$Q = P \times \dot{V} = P \times S \quad (2.25)$$

where  $S$ , in units of volume/time, is a pumping speed (typically litres/min).

The Ohm's law analogy holds when considering series conductances:

$$\frac{1}{C_T} = \frac{1}{C_1} + \frac{1}{C_2} \quad (2.26)$$

which is equally valid for determining the effective pumping speed of a pump connected to a system via a path of limited conductance  $C$ :

$$\frac{1}{S_{eff}} = \frac{1}{S} + \frac{1}{C} \quad (2.27)$$

which highlights the importance of careful design of system geometry in optimizing pumping speeds.

Acceptably accurate conductance values can be calculated for common geometries with simple, generally accepted, empirical formulae<sup>45</sup>. Two of the most useful are:

$$C = 78 \frac{D^3}{L} \quad (2.28)$$

which gives the conductance in litres/sec for a tube diameter  $D$  and length  $L$  (in inches) and:

$$C = 75A \quad (2.29)$$

which gives the conductance in litres/sec for an orifice of area  $A$  (in inches).

More accurate values for conductance can be calculated using Monte Carlo based simulations of molecular flow for the exact geometries in question, but with the typical levels of uncertainty in determining the gas load in a system, the empirical formulae are more than adequate.

If the required throughput  $Q$  is known, then by Equation 2.25 the necessary pumping speed to achieve a given base pressure can be determined:

$$S = \frac{Q}{P} \quad (2.30)$$

The trick then is to determine the total gas load,  $Q_{total}$ , which is where the trouble starts. In an ideally designed, prepared and assembled system there are a limited number of sources contributing to  $Q_{total}$ . The initial volume,  $Q_{volume}$ , is quickly removed by roughing pumps leaving only surface outgassing,  $Q_{outgas}$ ,  $H_2$  permeation through the chamber walls,  $Q_{permeation}$ , and any process gases that may be introduced into the chamber  $Q_{Process}$ . In the real world leaks both real and virtual,  $Q_{leak}$ , can be present, even if undetectable. Outgassing rates will be hard to determine since surface finishing and preparation is never perfect and the diffusion of gases present in the chamber walls,  $Q_{diffusion}$ , can only be avoided by the most rigorous pre-treatment. This gives a rather lengthy:

$$Q_{total} = Q_{volume} + Q_{outgas} + Q_{permeation} + Q_{Process} + Q_{leak} + Q_{diffusion} \quad (2.31)$$

Despite the complexity, reasonable estimates for the most important steady state contributions, such as  $Q_{permeation}$ ,  $Q_{diffusion}$  and  $Q_{outgas}$  can be made based on published values for commonly used materials and surface conditioning<sup>39,42,46</sup>, which allows an estimate of the achievable system base pressure. More often, however, such calculations become more useful when known significant process gas loads are introduced and the pumping required to achieve the desired pressures and transition times can be determined with relative ease.

## Roughing Pumps

Rough vacuum pumps are relatively simple devices with more in common with a household vacuum cleaner than a high-tech instrument. None the less, rough pumping technology has

advanced over the last couple of decades. The majority of modern roughing pumps are dry (oil-free) pumps that eliminate inevitable backstreaming of pump oil into vacuum system. Oil sealed rotary vane pumps and diaphragm pumps are still in use, but are typical only used for special applications.

In addition to being oil-free, scroll pumps are generally quiet, compact, have good pumping speeds and low (millitorr) base pressures. While blower/booster pumps and screw pumps can have dramatically higher pumping speeds, that is typically not required for UHV systems since they are generally small in volume and rarely cycled up to rough vacuum levels. Other than occasional pump down after venting a chamber, roughing pumps are usually used only to back high vacuum pumps that require low foreline pressure to maintain optimal compression ratios. With these applications in mind, scroll pumps are ideal and other currently available roughing technologies are not worth discussing.

Scroll pumps operate by moving two eccentrically mounted Archimedean spirals with respect to each other such that a volume is trapped and moved from the outside of the spiral where the intake is located to the center of the spiral where it is exhausted (see Figure 2.27). The inherent geometry of the spiral results in the volume continual decreasing as it is moved towards the exhaust creating a substantial compression ratio. The nature of the relative motion means that the surfaces of the two spirals tend to roll against each other with little relative motion. This is what allows these pumps to be operated without lubricant. Only the inner tips of the spirals experience any significant friction and this is minimized by the use of PTFE seals that need to be replaced during routine maintenance roughly every 18 months.



**Figure 2.27:** A compact Varian/Agilent scroll pump and diagram illustrating how the spirals trap and transport gas<sup>47</sup>.

Scroll pumps are capable of pumping down to the edge of the molecular flow regime, at which point the lack of a pressure gradient at the inlet to move gas into the pump reduces their effective pumping speed to zero. At this point, different technologies are required to continue evacuating the chamber.

### **High & Ultrahigh Vacuum Pumps**

High and ultrahigh vacuum pumps cannot simply evacuate gas to create an effective pressure gradient to pump out a chamber. Several approaches are used to continue pumping in these regimes. Local pressure gradients can still be created within pumps, but to do so momentum must be imparted to the remaining molecules directly. This can be achieved mechanically or electrostatically. Molecules can then be further compressed and expelled from the system through rough pumping stages or trapped within the system either mechanically or chemically. Pumps using various combinations of these approaches will be discussed below.

**Turbomolecular & Molecular Drag Pumps** rely on mechanically transmitting momentum to molecules that enter them. Turbomolecular pumps (or turbo pumps) use a stack of alternating stationary (stators) and high speed rotating (rotors) angled blades which become gradually steeper towards the output side of the pump. Molecules that enter the pump have a high probability of being struck by the rotators and being accelerated into stators which work together to impart a net momentum towards the output. This effectively creates a pressure differential moving molecules towards the output. The now compressed gas that reaches the output is of sufficiently high pressure to be removed by a rough vacuum pump. To operate most efficiently, however, a backing pump capable of maintaining near molecular regime pressures is required to maximize the compression ratio within the turbo pump.

Molecular drag pumps operate in a similar fashion, but instead of rotors they use rotating solid disks, stators and circumferential pumping channels. When molecules collide with the disks, momentum in the tangential direction is transferred to them moving them towards the stators which deflect them into pumping channels that work their way down through the stages of the pump. Many turbo pumps on the market today actually use a combination of these two technologies in more robust designs to maximize compression ratios and durability

(see Figure 2.28).

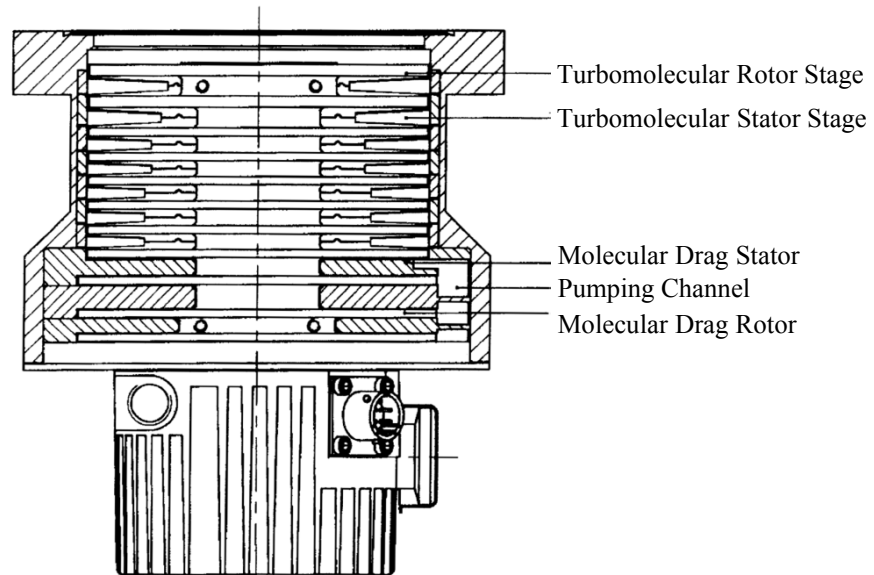


**Figure 2.28:** Cross section of a typical turbo pump design employing a combination of turbomolecular and molecular drag stages<sup>48</sup>.

Turbo pumps are able to operate effectively over a wide range of pressures and pump all gases with high efficiency. Since they exhaust the pumped gases, there are no issues with saturation. Because they are open to the air through a roughing pump, isolation valves must be used to guard against chamber venting in the case of power or mechanical failure. Being a mechanical pump, noise and vibration can be an issue, and they do require periodic maintenance to mitigate the risk of failure. They can also be rather delicate and improper used or handling can easily destroy them. The need for a backing pump increases cost, size and noise/vibrations. With dry roughing pumps, pump oil backstreaming is not a concern but a small amount of ambient air does make its way into the vacuum system. Turbo pumps are used almost universally to transition through the HV regime and are frequently use to supplement other pumps at UHV levels.

**Ion Pumps** use electrostatic forces to interact with molecules that enter them in place of the mechanical forces used by turbo pumps. A high voltage is applied to an anode to create a Penning cell that generates free electrons. These free electrons ionize molecules that enter the pump which are in turn trapped by a magnetic field and the high voltage potential accelerates

them towards titanium cathodes (see Figure 2.29). This ion bombardment results in sputtered titanium coating the anode. Further interactions depends strongly on the specific molecule. All molecules have a chance of being buried in the cathode on impact, but only  $H_2$  diffuses through titanium readily enough to stay trapped in the bulk. All other gases are likely to be re-emitted as the titanium cathode continues to sputter. Usually within hours or days of initial startup, this burial and re-emission process will reach equilibrium and the pump is said to be saturated. Since this is the main way for an ion pump to remove noble gases, the pumping speed for these gases falls off dramatically upon reaching saturation. Molecules can also be effectively removed from the system by interaction with the anode. Noble gases must strike the cathode with sufficient energy to be buried, or physisorbed. Since this only happens when an accelerated molecule is naturalized as it is reflected off the cathode, it is not an effective way to pump nobel gases. Active gases that come into contact with the anode have a high probably of being trapped through chemical interaction with freshly sputtered titanium and being permanently chemisorbed.

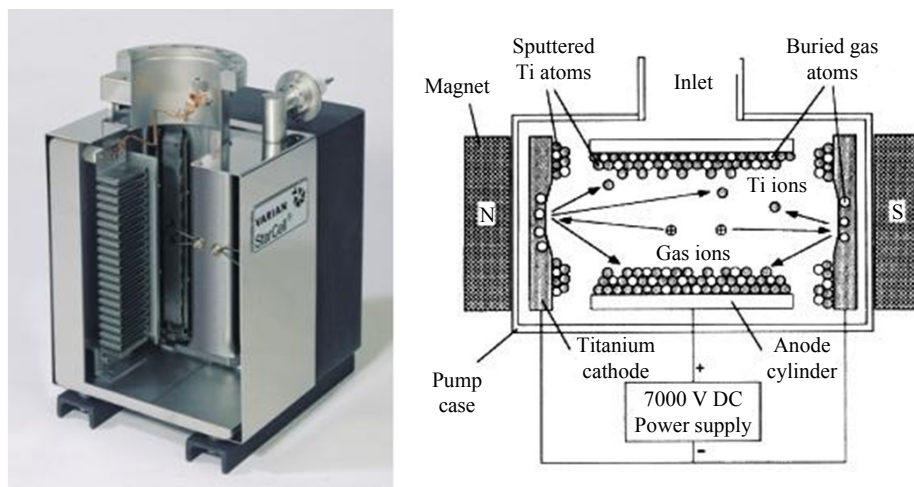


**Figure 2.29:** A Varian Starcell ion pump<sup>49</sup> (left) and a diagram of the key elements of a diode ion pump and illustration of its operating principle<sup>50</sup> (right).

There are several variations on the basic ion pump design aimed at improving certain aspects of the pumps performance. Noble diode pumps use one titanium and one tantalum cathode to increase the odds of neutralizing and reflecting noble gases to be trapped in the anode. This increases the noble gas pumping performance at the cost of reduced  $H_2$  and active gas pumping speeds. Triode pumps use grounded anodes and separate cathode

fins between the anodes and the grounded pump walls to create the ionizing field. The combination of the walls and anodes provides a large surface area for sputtered titanium to settle on thereby improving the active gas pumping speed. The orientation of the cathode fins also increases the probability of a glancing strike neutralizing a noble gas molecule allowing it to be permanently implanted. Because the walls are grounded and have no current flowing through them, initial outgassing on startup is reduced. The pumps most commonly used at the Canadian Light Source are Varian Starcell pumps, which are a proprietary variation on the triode pump principle.

With no moving parts and steady state voltages, ion pumps are silent and are not a significant source of electrical/RF noise. With no moving parts, ion pumps tend to be very reliable and since they are not open to the atmosphere, there is no risk of backstreaming or venting on failure. The high voltage present in the pump results in much higher concentrations of free ions in the whole vacuum system which can be a problem for certain sensors and detectors. The sputtering of titanium and high energy re-emission of other gas molecules can be of concern when ion pumps are used in close proximity to optical elements, and care must be taken to avoid a direct line of sight between them to prevent slowly coating the optics with unwanted materials. Ion pumps can be brought online to assist pump down through the middle of the HV regime, but they are best used at UHV pressures. They are the most common UHV pumps in use today.

**Getter Pumps** remove gas from the system by chemisorption and/or physisorption of molecules incident upon them. They fall into two categories. Titanium Sublimation Pumps (TSP) are active getter pumps that require power to evaporate and deposit fresh layers of titanium that readily chemisorbs active gases, much like the anode in an ion pump as described in the previous section. TSPs are very effective supplemental pumps that can speed pumping through the HV range (although at the cost of reduced pump lifetime), and help maintain superior UHV pressures. TSPs are relatively inexpensive and are available intergraded directly into ion pumps or as a separate pumping system. TSPs have zero pumping speed for noble gases. If installed independently, care must be taken to ensure that the evaporated titanium does not migrate and contaminate sensitive optics and instruments.

Non-Evaporative Getter (NEG) pumps are typically made from specialized, highly porous and reactive ceramic materials. While they do not require power to operate, they do need to be initially activated by direct heating or baking to remove inactive oxide layers. Periodic reactivation may also be required when pumping speed falls off to help speed diffusion of absorbed molecules into the bulk of the material, to desorb and pump off physisorbed molecule and to create a fresh active getter layer. NEG pumps are otherwise completely passive during normal use. NEG pumps are most effective when installed directly in the chamber they are to pump, but this can present difficulties if equipment in the chamber is too sensitive to handle the high temperature activation. They can be installed in adjoining mini-chambers with isolation and rough pumping valves to facilitate activation without risking the contents of the main chamber, but the reduced conductance through the isolation valve can dramatically reduce the effective pumping speed.

### **Vacuum Gauges & Monitoring Technologies**

To achieve and maintain a UHV environment, the level and quality of the vacuum must be monitored. There are almost as many technologies for gauging and analyzing a vacuum system as there are for pumping, and this section will look at those commonly used in UHV systems. As with pumping, no one gauging technology is able to operate from atmospheric pressures all the way down to UHV.

**Thermocouple Gauges** (TCG) are the most commonly used class of gauges for measuring pressure from atmosphere down to the edge of the HV regime. There are a number of variations on this technology including Pirani gauges and convection gauges but all such gauges rely on the fact that the thermal conductivity of a gas is dependent on the density (and therefore pressure) of that gas. Different arrangements of thermocouples and heated filaments with fixed or varying currents offer sensitivities over different pressure ranges, but typical TCGs can read between 1,000 torr and  $10^{-3}$  torr. Since different gases have different thermal conductivities, these gauges must be properly calibrated if precision pressure readings are required. In most applications on UHV systems this is not the case. TCGs are used to monitor initial rough pumping and to trigger the activation of HV and UHV gauges when

the pressure is low enough for them to operate. They are also commonly used to monitor the foreline pressure behind turbo pumps to ensure that backing pumps are operating properly. These applications generally demand only order-of-magnitude accuracy.

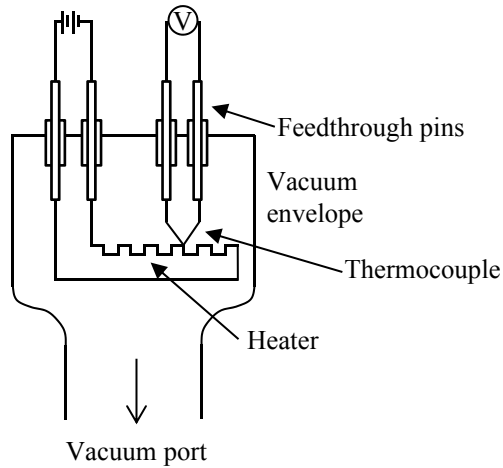


**Figure 2.30:** Schematic diagram of the essential parts of a 2-wire-type thermocouple gauge<sup>49</sup>.

**Ionization gauges** are the only practical means of measuring pressure in the HV and UHV regimes and come in two distinct types<sup>51</sup>. Both types of gauges operate by generating ions from the gases present in the system and measuring the resulting current at a cathode. Both gauges generate ions which, depending on the installation geometry, can create issues for other instruments.

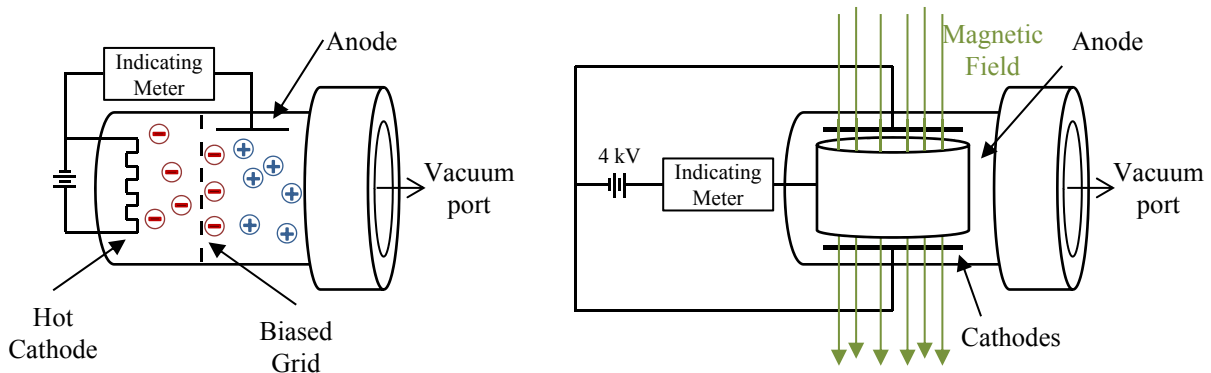


**Figure 2.31:** Schematic diagrams explaining the operation of hot (left) and cold (right) cathode gauges.

Hot Cathode Gauges (HCG) work by using a biased, heated cathode filament to emit

electrons that ionize the gases present. The electrons are trapped by a grid and the current generated by the ions collected at the anode is used to determine the pressure. The Bayard-Alpert type cathode/grid/collector arrangement is the most commonly used. It can be installed in a glass tube connected to the vacuum system, but for UHV applications a “nude” installation with the electrodes inserted directly into the vacuum chamber is more common. Modern HCGs can accurately measure into the  $10^{-10}$  torr range. The visible light given off by the hot cathode filaments can cause problems for some detectors, and the filaments will eventually burn out. The hot filaments can cause substantial outgassing as well, and they need to be conditioned regularly when used in a UHV environment to maintain accuracy. The type of gases present at the gauge can affect the measurement as well, by as much as a factor of 4, so their sensitivity must be properly adjusted if better than order of magnitude pressure accuracy is required.

Cold Cathode Gauges (CCG), also known as inverted magnetron gauges, operate by using a high voltage (2-6 kV) to create a circulating electron plasma trapped by a magnetic field. The pressure is determined by monitoring current flowing between the anode and cathode and is exponentially related to it. CCGs are simpler and more robust gauges due to the absence of delicate filaments. Depending on the specific design they can be accurate to much lower pressures than HCG, but typically operate accurately down to the  $10^{-9}$ - $10^{-10}$  torr range. The magnets are often not stable at high temperatures and they may need to be removed when baking a chamber. The high voltage needed to generate the plasma can result in high energy ions in the chamber that may interfere with some detectors. Establishing a plasma in a chamber that is already at a low pressure can take a significant amount of time so they can not be counted on to provide stable readings if they must be cycled on and off regularly. Ion pumps operate on a principle very similar to CCGs and the anode/cathode current can be used to determine the pressure in the pump. Most ion pump controllers will report this pressure, but it does not always accurately reflect the pressure in the system as a whole.

**Residual Gas Analyzers** (RGA) are specialized vacuum monitoring devices that are often included in UHV vacuum systems and can be extremely useful for diagnosing and maintaining them. An RGA is basically a hot cathode gauge with a quadrupole mass filter between

the cathode and the collector that separates the ionized molecule by charge-mass ratio and determines the partial pressure of each species. As with a HCG, a resistively heated and biased filament acts as a source for kinetic electrons that ionize gas molecules presents in the system. From there, the generated ions enter the filter where two pairs of steel rods are DC biased to create a quadrupole field and RF voltages, 180 degrees apart, are superimposed on the two pairs. Qualitatively, one pair of rods acts as a high-pass mass filter by causing light ions to oscillate off axis until they collide with a rod and the other pair acts as a low-pass mass filter by using the RF voltage to stabilize heavy ions that would otherwise be removed by the DC voltage. By adjusting the RF and DC voltages together, only ions with a given mass-charge ratio are able to pass through the quadrupole filter to reach the detector. For the SRS RGA200 installed on this endstation, the ions are collected by one of two detectors. A simple Faraday cup provides sensitivity down to partial pressures of  $5 \times 10^{-11}$  Torr, and an electron multiplier can be used at higher vacuum levels for sensitivity down to  $5 \times 10^{-14}$  Torr.

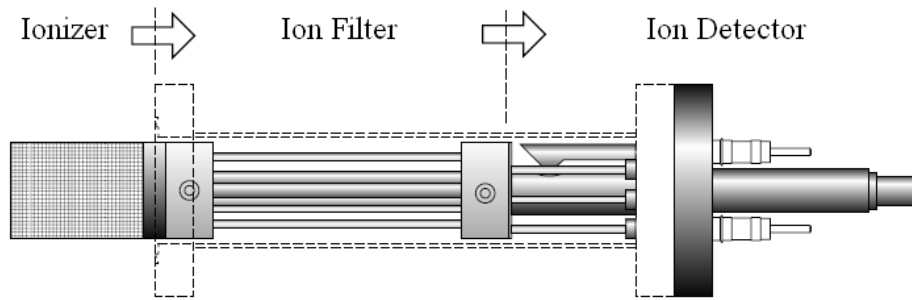


**Figure 2.32:** The basic components of a residual gas analyzer (RGA)<sup>52</sup>.

Careful analysis of the provided mass spectra can provide very detailed information on the composition of the gas in the system, but such effort is not generally required for basic vacuum system maintenance. For vacuum diagnostic purposes, a qualitative interpretation based on a thorough understanding of the fragmentation patterns (charge-mass ratio peak distributions) that result from all the molecules commonly present in vacuum systems in different pressure ranges is usually adequate to assess the health of a vacuum system and to assist in tracking down problems. Unexpectedly high levels of atmospheric gases can indicate leaks, high levels of water can indicate the need to bake a system, high levels of assorted heavy mass peaks can indicate oil contamination, high levels of noble gases could indicate saturated

ion pumps and indicate the need for changes to the pumping systems. RGAs can also be used to detect and isolate leaks in the system by continuously monitoring the mass-charge ratio of a test gas, typically helium, as small amounts are sprayed around the flanges and joints in the system. If a leak is present, the helium level in the system will rise suddenly when helium enters the chamber. This not only allows the presence of a leak to be verified, but by careful administration of very small amount of helium the exact location of the leak can often be identified.

# CHAPTER 3

## SPECTROSCOPIC TECHNIQUES

The vast majority of this endeavor over the past 3 years has been project management, assembly and related activities (i.e. troubleshooting). It is important, however, not to forget that the purpose of this endeavour is science. With the completion of the construction and commissioning close at hand, there will soon be the opportunity to use this excellent system for the purpose for which it was designed. This section will provide a very brief survey of the techniques that are available on this endstation.

This endstation has two different excitation sources available. In addition to the synchrotron light that inspired the creation of this spectrometer, there is also an electron gun to increase the range of possible experiments that can be conducted and facilitate simple studies when synchrotron light is unavailable. There are a total of four detection systems to analyze the excited sample: the spectrometer, a Channel Electron Multiplier (CEM), a Cylindrical Mirror Analyser (CMA), and a current preamplifier/scaler. The following section will describe the most common techniques and measurements that can be performed with various combinations of these sources and detectors.

### 3.1 Soft X-ray Spectroscopy

X-ray spectroscopy is a powerful tool that can be used to study the electronic structure of matter. Soft X-rays are particularly well suited for the study of some of the most abundant and important elements in nature such as carbon, nitrogen and oxygen. The electronic structure of matter accounts for nearly all of the properties of materials, from colour to conductivity to hardness. As such, a tool that can effectively probe electronic structure is indispensable in the quest to understand the nature of matter and materials. Drawing

connections between the electronic structure of matter and its material properties is the key that will unlock new materials that can be custom engineered to solve problems in every field of modern technology including electronics and devices, environmental science and medicine.

The primary purpose of this endstation is to perform soft X-ray spectroscopy. This involves photoexcitation of a sample with highly monochromatic synchrotron radiation and then monitoring the sample with a variety of sensors to evaluate the induced processes. The first process, common to all soft X-ray spectroscopic techniques, is the excitation of the sample through absorption of an incident photon. This is shown schematically in Figure 3.1. An atom in the sample, initially in a ground state (Figure 3.1a), interacts with an incident photon which results in the excitation of one of its core level electrons. Depending on the energy of the photon and the electronic structure of the atom or molecule in question, this can be either a resonant excitation, where the core electron is excited to an unoccupied bound state within the atom, known as photoexcitation (Figure 3.1b), or a non-resonant excitation where the electron is completely removed from the sample, known as photoionization (Figure 3.1c).

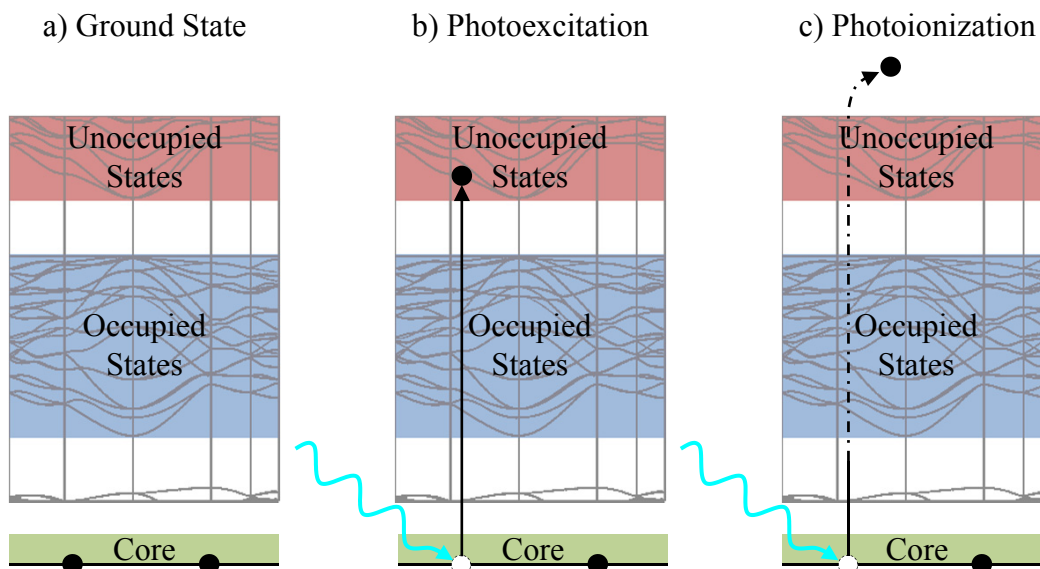


**Figure 3.1:** Schematic of the X-ray absorption processes. An incident photon excites a core level electron into a bound state, or removes it completely.

The study of this process is known as X-ray Absorption Spectroscopy (XAS), and there are a variety of experimental techniques that can be used to collect data on this process.

Those available on this endstation will be described in the next section.

Once a system is in an excited state, it will naturally try to find its way back to a ground state as quickly as possible. There are two common processes that can lead to this de-excitation. The one most studied by the techniques this endstation was designed for is decay via fluorescence. In this process, an electron from an occupied orbital drops to fill the core hole created by the incident photon and it sheds the excess energy of its previous state by emitting a photon (Figure 3.2).

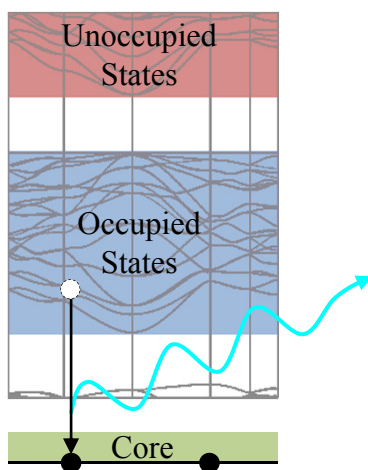


**Figure 3.2:** Schematic of the fluorescence de-excitation process. An electron from an outer shell drops to fill the core hole, shedding excess energy by emitting a photon.

Unfortunately, for atoms with low atomic numbers, less than 1% of the core holes created are filled by this radiative, or fluorescent, process (see Figure 3.3) and this includes many of the most interesting elements such as C, N and O. This low fluorescence yield is one of the reasons why soft X-ray fluorescence studies are limited to synchrotron facilities where the incredible intensity of synchrotron light means there is still a significant and measurable signal due to fluorescence decay.

More than 99% of the excited states created will decay through non-radiative processes, such as Auger decay. Here, as with fluorescence decay, an electron from an occupied orbital drops to fill the core hole, but instead of emitting a photon, the electron sheds its excess energy by transferring it to a second electron as kinetic energy. This electron may then

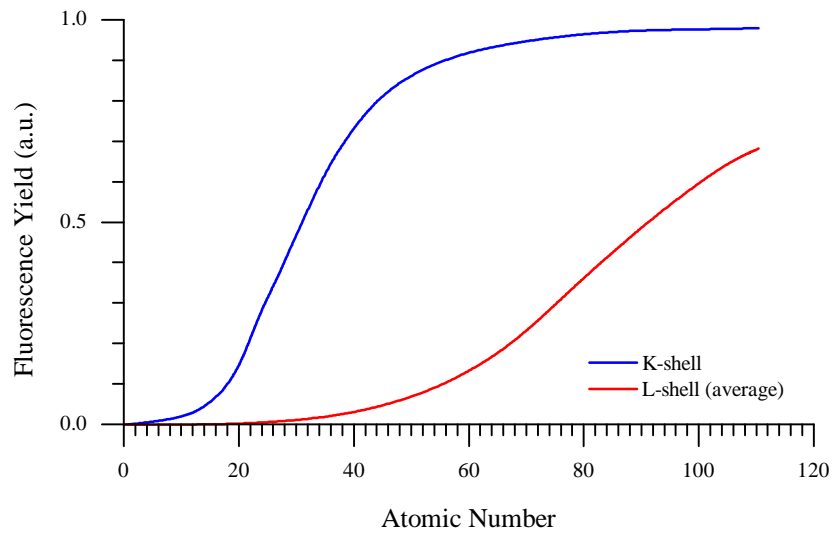


**Figure 3.3:** Fluorescence yields, or the fraction of core holes filled by radiative processes, for K and L shells for a range of elements<sup>4</sup>.

escape to vacuum as an Auger electron (see Figure 3.4).

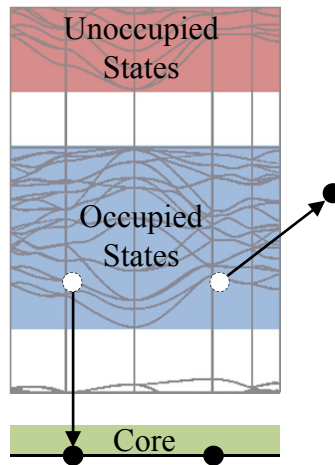


**Figure 3.4:** Schematic of the Auger de-excitation process. An electron from an outer shell drops to fill the core hole by transferring the excess energy to a second outer shell electron which escapes to vacuum.

## 3.2 X-ray Absorption Spectroscopy

X-ray Absorption Spectroscopy is the measurement and interpretation of the probability of absorption of a photon by a material as a function of photon energy. A photon will be more strongly absorbed when it is tuned to an energy corresponding to the energy required to resonantly excite an electron from a core level to a particular unoccupied state, resulting in specific features appearing in the absorption spectra at these energies. The light will be strongly absorbed as the energy passes the photoionization threshold for the element being excited, known as its absorption edge. Absorption will continue at energies above this edge resulting in an increased background above that energy.

The pre-edge region, well below the photoionization energy, may contain a few low intensity features relating to excitations of the less tightly bound valence electrons. Just below the photoionization energy, a number of sharp, intense, near-edge features are common and result from the resonant excitation of core level electrons into bound states. The detailed study of these near-edge absorption features is referred to as NEXAFS (Near Edge X-ray Absorption Fine Structure), or XANES (X-ray Absorption Near Edge Structure). The intensity of these near edge features is related to the probability of absorbing a photon and depends on the availability of unoccupied states for the core electrons to be excited into. Since a greater number of available states results in stronger absorption, this gives a direct probe of the density of these unoccupied states (DOS) within the studied system. Quantum mechanical selection rules and momentum conservation restrict the states into which transitions are possible, so these techniques only truly probe a portion of the existent unoccupied states in the system, and this portion is thus commonly termed the partial density of states (pDOS). Additional structural information is present in the post-edge features, and the study of certain characteristics of these features is called EXAFS (Extended X-ray Absorption Fine Structure), but this technique is not well suited to the soft X-ray regime since the elemental absorption edges are often too close together to allow a sufficiently large extended spectra to be collected for analysis.

The electronic transitions that absorption spectroscopies are probing are characteristic of the particular element. XAS can be used to identify particular elements within a sample

but, more importantly, it can also provide information about the electronic and structural properties and bonding environment of that element within a molecule or solid, and can even distinguish between different sites or bonding environments of the same element within the system. Not all XAS studies involve core-level excitations of inner (K-shell) electrons; heavier elements with K-shells outside the soft X-ray range can also be studied by using soft X-rays to excite their outer electrons (L-,M-,N-shells). The interpretation of these spectra can vary significantly from K-edge spectra since a different set of selection rules apply. The erbium 4d-4f absorption spectra in Figure 3.5 is an example. The dotted line just past 168 eV indicates the approximate location of the ionization threshold. The sharp features to the left are the NEXAFS spectra and a few pre-edge features are present below 163 eV.

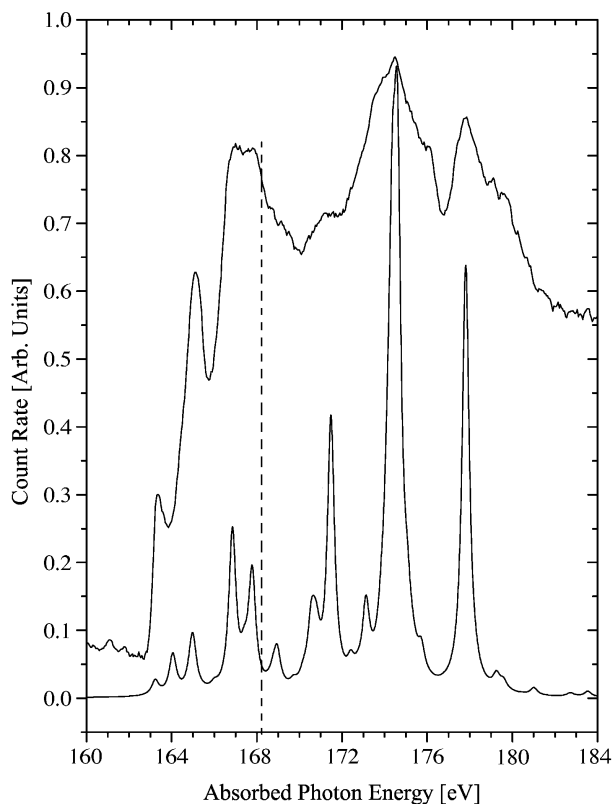


**Figure 3.5:** Absorption data for Er 4d-4f transitions along with a calculated spectrum labeling the involved transitions<sup>53</sup>.

The majority of the sensors on the sample chamber are used to collect X-ray absorption data in one form or another; each provides slightly different information and has its own strengths and weaknesses.

### 3.2.1 Total Electron Yield

The simplest practical method for measuring XAS spectra is to measure the Total Electron Yield (TEY). There are a couple of experimental approaches to achieving this, but they all rely on measuring the minute flow of electrons to the sample required to keep it electrically neutral as the incident light excites electrons out of the sample. TEY can measure absorption by both resonant and non-resonant transitions because the non-ionizing excitations lead to the emission of an Auger electrons more often than not and it therefore still results in the loss of an electron to vacuum generating a measurable current.

To measure this sample current, the sample holders must be carefully designed to keep the samples electrically insulated so that they can be grounded through a meter. There are numerous different ways to approach this metering, but two that have been used on this system will be discussed. The first is to ground the sample through a high sensitivity current amplifier such as a Stanford Research SR570, which outputs a voltage proportional to the measured current. This voltage is converted to a frequency proportional to its magnitude and transmitted to a scaler card where it is interpreted by the control system as a count rate which can be integrated over the exposure time. The second way is to directly measure the sample current using a picoammeter such as a Keithley 6485. The control systems can interface with the 6485 directly over a serial line and instruct it to perform the required integration over the exposure time. A Keithley 6485 picoammeter is available on the endstation for special applications such as calibrated current measurements, but to integrate into the beamline systems and provided the best possible synchronization with normalization mesh currents and concurrent TFY/PFY measurements, the SR570/Scaler interface is set up for TEY measurements by default.

TEY is the least bulk sensitive of the techniques that are available because it relies on electrons escaping the sample so their replacements can be measured and electrons have escape depths several orders on magnitude smaller than photons<sup>54</sup>. This can be advantageous if one is interested in studying surface effects or identifying surface contaminants. TEY measurements can be complicated when dealing with insulating samples, as the samples can build up a charge which will affect the measurement.

### 3.2.2 Total and Partial Fluorescence Yield

The other commonly used approach for measuring X-ray absorption is to detect the photons that are emitted through fluorescence decay. This can be done in one of two ways with this endstation. The first method is to use a Channel Electron Multiplier (CEM) to collect the photons escaping from the sample. The opening of the CEM is coated with a material with a low ionization threshold so that incident photons are likely to result in the emission of one or more electrons. The CEM has a large negative bias ( $\sim 3000\text{V}$ ) which then accelerates these electrons along a curved path where they will frequently collide with the surface generating a secondary electron cascade that can be detected as a current pulse at an anode at the back of the multiplier. This pulse output is then amplified and either integrated and converted to a voltage by a ratemeter or, as is the case on this endstation, fed directly to a scaler.

A CEM will detect all incident photons above the ionization threshold of the coating and therefore measurements of this type are termed Total Fluorescence Yield (TFY) spectra. An alternate approach to fluorescence yield measurements is to use the spectrometer as a detector. By doing so, only a small energy range of the emitted photons will reach the detector and these measurements are called Partial Fluorescence Yield (PFY) spectra. This can provide additional information of interest by tuning the spectrometer to collect only photons originating from certain transitions. There is a drawback to this technique however, as the CEM has a significantly higher efficiency and accepts a solid angle two orders of magnitude greater than the spectrometer so TFY measurements collect significantly more photons than PFY measurements. This means that extremely long count times are required to achieve acceptable statistics with PFY.

Fluorescence yield measurements are more bulk sensitive than electron yield measurements due to the greater escape depth of photons; however the measured absorption profile does not always give an accurate picture of the relative absorption probabilities because the emitted photons can be reabsorbed by the sample. The rate of this re-absorption is not constant, varying with energy. This effect is referred to as self-absorption, and must be considered when analyzing fluorescence yield data in most cases. For TFY measurements, the high voltage required to operate the channeltron can result in the presence of a significant

electric field in the chamber. In some cases, this field can effect the electronic structure of the sample and distort the results of the measurement.

Fluorescence decay is not a preferred decay pathway, Auger decay is far more likely<sup>4</sup>. For most lighter elements, the fluorescence yield is generally below 1% (see Figure 3.3), as discussed above. In addition, the photons are generally emitted isotropically and the detector spans a limited solid angle. As a result, TFY and especially PFY measurements can take significantly longer to achieve acceptable statistics.

### **3.3 X-ray Emission Spectroscopy**

X-ray Emission Spectroscopy (XES) is the technique at the heart of this endstation. XES involves measuring the energy and rate of photons emitted by fluorescence decay from an excited sample. This is what the soft X-ray spectrometer was designed for. Basically, the spectrometer consists of three optical elements: A source, a grating and a detector. The source is the synchrotron beam spot on the sample (or possibly an entrance slit), which illuminates one of several interchangeable diffraction gratings that disperses the light into different energies and focuses it onto an area detector. This detector collects a 2-dimensional image of a region of the spectrum that can be chosen by moving the detector to the focal point of the grating for the desired energy range. This 2-dimension image is then processed into a spectrum.

Because the measured fluorescence is due to transitions from occupied states to the vacated core level states (core holes), XES provides information about the density of various occupied states within the sample, which compliments XAS nicely. As with TFY and PFY, XES relies on the relatively infrequent radiative decay process and when combined with the even smaller small solid angle that the spectrometer is able to collect it necessitates the use of a high intensity synchrotron excitation source. XES is typically measured by exciting the sample with photons having energies well above the ionization threshold of the of the element of interest. Exciting the sample in this non-resonant manner does not favour any particular excitation pathway and the collected spectrum reflects the natural transition probabilities that arises from the occupied pDOS of the sample.

### 3.3.1 Resonant Inelastic X-Ray Scattering

Thanks to the high resolution of modern synchrotron beamlines, emission spectra can also be collected while excited with photons tuned to preferentially excite one particular transition. This results in an increased absorption cross section and a strong, resonant excitation of that one particular transition from a core level to a particular previously unoccupied state. This technique is called Resonant Inelastic X-ray Scattering (RIXS), and it provides additional insight into the electronic structure and bonding environment of a sample.

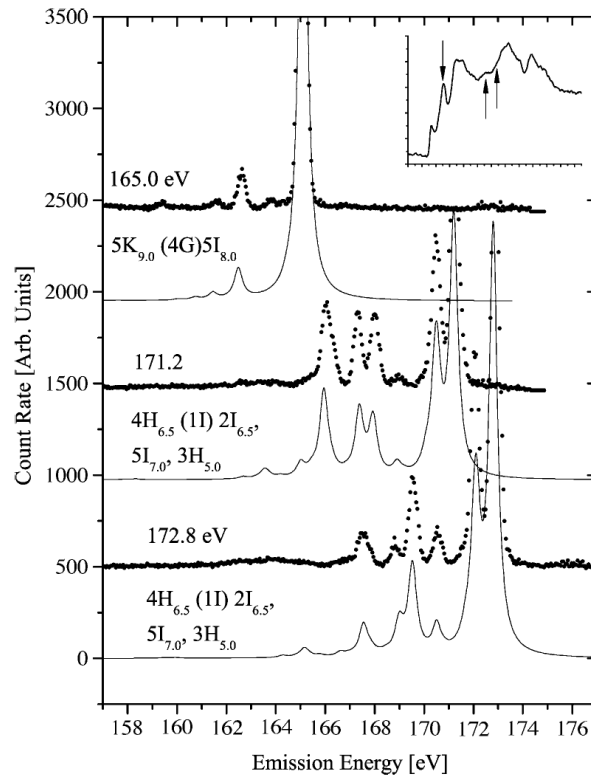


**Figure 3.6:** A series of RIXS measurements of Er 4d-4f transitions along with a calculated Raman spectra. The inset absorption spectrum indicates the features that were excited to obtain each RIXS spectrum<sup>53</sup>.

It turns out that the physical processes involved are quite different when exciting a system in this manner. With non-resonant XES, the emission process is a function of the excited state and the state that it decays into. The excited state is stable enough that how it became excited has no effect on the emission process. That is why the exact excitation energy, bandwidth and source do not affect the emission process. Resonant emission is a one

step process that can be thought of as absorption into a virtual state followed by immediate re-emission. It is, however, more correctly understood as an inelastic scattering process that results in the fixed emission peaks expected from non-resonant excitation, although with modified selection rules and expectation values, as well as energy loss features that differ from the excitation energy by the difference between the initial and final states involved.

### 3.4 Theoretical Interpretation

Application of quantum mechanics theoretically allows the density of states for any given system to be calculated, which would allow for a relatively simple interpretation of any given absorption spectra by the application of Fermi's golden rule to determine the probability ( $W$ ) for any given transition<sup>55</sup>:

$$W \propto \frac{2\pi}{\hbar} |\langle \Psi_f | \Delta | \Psi_i \rangle|^2 \delta(E_f - E_i - \hbar\omega) \quad (3.1)$$

The strength of a given spectral feature is directly related to the transition probability ( $W$ ) of that feature which is the direct result of the density of initial and final states ( $\Psi_i, \Psi_f$ ), the coupling between those states ( $\Delta$ ) and the energy of the involved photon ( $\hbar\omega$ ). Depending on the choice of initial and final states, and the form of the operator in the matrix element, this formalism can be applied to both absorption and non-resonant emission processes.

The Kramers-Heisenberg formula describes the intensity of inelastically scattered (RIXS) photons<sup>56</sup>:

$$I(h\nu_{in}, h\nu_{out}) \propto \sum_f \left| \sum_m \frac{\langle f | \mathbf{p} \cdot \mathbf{A} | m \rangle \langle m | \mathbf{p} \cdot \mathbf{A} | i \rangle}{E_m - E_i - h\nu_{in} - i\frac{\Gamma}{2}} \right|^2 \delta(E_f + h\nu_{out} - E_i - h\nu_{in}) \quad (3.2)$$

where  $E_i, E_m, E_f$  refer to the initial, intermediate, and final states for the system respectively, during an interaction with an incident ( $h\nu_{in}$ ) and a scattered ( $h\nu_{out}$ ) photon. Central to the expression,  $\mathbf{p} \cdot \mathbf{A}$  accounts for the interact between the electron momentum vector ( $\mathbf{p}$ ) and the electromagnetic vector potential ( $\mathbf{A}$ ) of the incident radiation.  $\Gamma$  accounts for the lifetime broadening, specific to the given element.

While theoretically simple, calculating the matrix elements for most of these equations, for all but the simplest systems, is analytically impossible. A variety of theoretical techniques exist to approximate and numerically perform these calculations including a number of density functional theories, molecular orbital theories and crystal field theories. The strengths, weaknesses and applications of these approaches is well outside the scope of this document.

Knowing the relative intensities of the expected spectral features, and accounting for broadening within the sample (life-time broadening) and the experimental (instrumental broadening), theoretically expected spectra can be produced. Comparison of these calculated spectra with experimentally measured spectra allows the validity of the structures, models and assumptions used to calculate the spectra to be tested and refined which allows the fundamental nature of the system to be probed and understood.

## **3.5 Other Techniques**

The inclusion of an electron gun and cylindrical mirror analyzer grants access to a number of other measurement techniques. They are not the focus of the endstation or this document and will only be briefly discussed in the follow sections.

### **3.5.1 Kinetic Electron Excitation**

Since it only requires that the sample be placed in an excited state and allowed to decay, non-resonant XES can be performed with any excitation source. The endstation includes an EFG-7 electron gun from Kimball Physics that can be used for this purpose. It has an energy range of 50 eV to 1500 eV, similar to that of the photons supplied by the beamline, with an energy spread of about 0.4 eV. The beam current can be adjusted between 1 nA and 100  $\mu$ A and the spot size can be adjust between 1 mm and 100 mm. This excitation source will allow for different experiments that can reveal additional information about more complex systems as well as provide a basic excitation source when synchrotron light is unavailable.

### 3.5.2 Cylindrical Mirror Analyzer

Cylindrical Mirror Analyzers (CMA) are simple and compact electron energy spectrometers. This endstation includes a retractable MINICMA made by LK Technologies mounted on a 2.75 flange opposite to the X-ray spectrometer on the sample chamber. It employs double pass optics with an energy resolution of better than 1.5% over an energy range of 0 - 3000 keV. The sample is excited by either of the sources and the emitted electrons are collected by the CMA where an electric field between the inner and outer cylinders forces them through a curved path. By careful placement of apertures and the detector along this path, only electrons within a given energy range are passed through to the detector. By varying this potential between the inner and outer cylinders, different energies can be swept across the detector to measure the relative emission intensities across the energy spectrum. Electrons of different energies that enter the analyzer with different trajectories are able to pass through at a given cylinder potential. This is the most significant factor limiting the resolution of CMAs, and it is minimized by use of the double pass design.

#### Auger Electron Spectroscopy

When an electron gun is used as the excitation source for a CMA, the technique is typically referred to as Auger Electron Spectroscopy (AES), although this technique can also use X-rays as the excitation source (XAES). The process of interest for this technique is the non-radiative decay by the release of an Auger electron described above (see Figure 3.4). This Auger electron will have a kinetic energy which is the difference between the energy of the core hole and that of the electron that is decaying to fill it, minus the binding energy of the ejected electron ( $E \approx E_{corehole} - E_{decaying} - E_{binding}$ ). The energy of these Auger electrons is characteristic of the energy levels of the atoms that emitted them, allowing for analysis of materials and chemical states through AES. Due to the extremely short mean free path of electrons in a solid, this is considered to be a surface analysis technique.

## X-ray Photoelectron Spectroscopy

X-ray Photoelectron Spectroscopy (XPS) is also known as Electron Spectroscopy for Chemical Analysis (ESCA). This technique is very similar to XAES in that it uses incident photons at energies above the ionization threshold to eject core level electrons into vacuum, however it then measures the kinetic energy of these ejected electrons (given roughly by  $E_k \approx E_{incident} - E_{binding}$ ) instead of the Auger electrons. Because the incident energy is known and the kinetic energy is being measured, the binding energy can be determined. This can provide valuable information about the composition and binding environment of the studied material.

## **Part II**

# **The Project**

# CHAPTER 4

## THE DESIGN

### 4.1 Optical Design

For a detailed discussion of the optical design process, the reader is directed to the author's M.Sc. thesis<sup>1</sup>. A summary of that work is given here.

After analyzing the theoretical performance of existing systems, our calculations suggested that it would be possible to design a spectrometer that exceeded existing designs at that time in resolving power and efficiency by focusing our efforts on optimizing for specific energies of interest and not sacrificing performance to create a compact design. After seeing the performances achieved by existing designs, the goal was set to aim for a minimum resolving power of 2500 through a 90-1000 eV range and strive for excellent efficiency in a reasonably sized and flexible design.

In addition, in the course of this analysis enhanced efficiency in the third diffraction order (as compare to the second order) was observed and a novel grating system was devised to exploit it. These designs are outlined below.

#### 4.1.1 A Rowland Circle Spectrometer

A Rowland circle design was settled on for maximum reliability and resolution. As discussed in Section 2.3.1, VLS design's strengths lay in creating compact designs with controlled focal curves allowing mechanically simpler flat-field systems, and reduced aberrations at specific energies. Since mechanical simplicity and compactness are not important factors in this design it was decided that the increased dispersion, reliability and flexibility of a Rowland design with a 2-D detector motion table was favorable.

The gratings were designed without constraint on the focal curves (other than total length) to allow maximum optimization of resolving power and efficiency. The incidence angle, line density and blaze angle were carefully balanced for each designed grating and the grating radius of curvature was calculated to satisfy the Rowland circle condition (Equation 2.14). This was done with the goal of maintaining resolving powers above 2500 and good efficiency at each of the points of interest (Si: 92 eV, C: 285 eV, N: 410 eV, Fe: 710 eV). This was accomplished using 3 gratings, a low energy grating (LEG) optimized 90 eV - 250 eV, a medium energy grating (MEG) optimized 250 eV - 500 eV and a high energy grating optimized for 500 eV - 1000 eV. A fourth impurity grating was added to provide superior efficiency and reasonable resolving power over a wide energy range for measuring low intensity sample (see Table 4.1, Figure 4.1).

**Table 4.1:** The design specifications for the standard resolution gratings<sup>1</sup>.

Grating	LEG	Impurity	MEG	HEG
Groove Density (lines/cm)	6000	9000	12000	20000
Grazing Incidence Angle (deg)	4	3	2	2
Sample Grating Distance (cm)	35	35	35	35
Radius (cm)	501.7	668.7	1002.9	1002.9
Blaze Angle (deg)	1.85	1.11	1.48	1.52
Coating	Au	Ni	Ni	Pt
Energy Range (eV)	30-300	75-750	250-2500	400-4000

The overall size of the system was more-or-less arbitrarily chosen to be reasonable as exact space constraints were not known at the time. A total maximum length of around 1.5 m was taken as a starting point. An entrance slit to grating distance of 35 cm was chosen to result in good illumination of a 4x4 cm grating at the lower 86° incidence angle with a 50  $\mu$ m entrance slit. This results in almost full illumination of the higher incidence angle gratings with as low as a 10  $\mu$ m slit. 4x4 cm gratings were found to be the largest size possible before spherical aberration significantly impacted the image at the detector resulting in a marked decrease in resolving power. A focal range of 50 cm - 115 cm was settled on so that the total

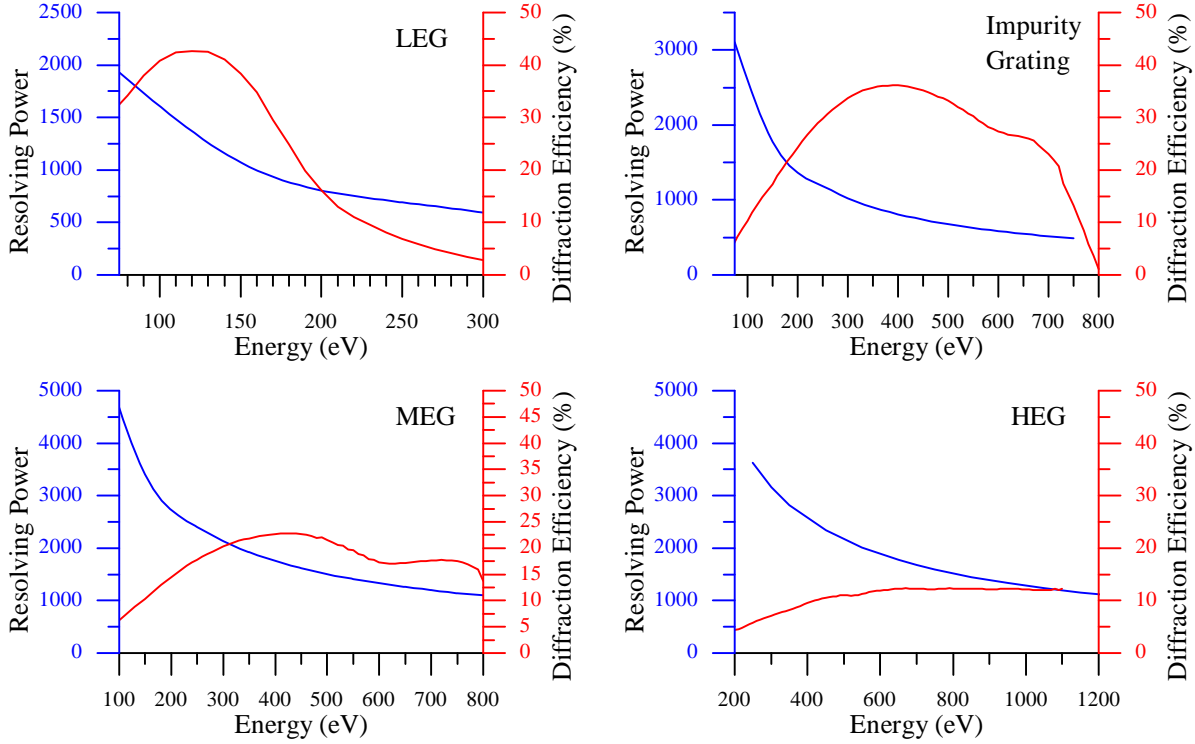


**Figure 4.1:** Calculated resolving power and diffraction efficiency curves for the designed standard gratings.<sup>1</sup>

optical path ( $\sim 35$  cm + 115 cm) was near the targeted 1.5 m.

### 4.1.2 High Resolution Third Order Gratings

As mentioned, in exploring the behavior of the diffraction efficiency it was noted that the third order provides superior performance over the second order if the gratings are properly blazed to take advantage of it, a discovery made possible by the careful analysis of diffraction efficiency undertaken during this design. It was proposed that this may be exploited as a novel method of achieving extremely high resolving powers. This was attempted with the goal of achieving a resolving power of over 10,000 throughout the high end of the spectrum. This resulted in the design of two high resolution gratings covering the medium and high energy ranges (HRMEG and HRHEG). These gratings have very large focal curves (grating-detector distances as high as 220 cm) with relatively low efficiency but stunning resolving power (see Table 4.2, Figure 4.2). When the available space turned out to be sufficient to accommodate an instrument of this size, the decision was made to include these two gratings in the design.

**Table 4.2:** The design specifications for the high resolution gratings<sup>1</sup>.

Grating	HRMEG	HRHEG
Groove Density (lines/cm)	18,000	26,000
Grazing Incidence Angle (deg)	2	1.75
Sample Grating Distance (cm)	35	35
Radius (cm)	1002.9	1146.1
Blaze Angle (deg)	4.85	4.05
Coating	Ni	Pt
Energy Range (eV)	285+	400+

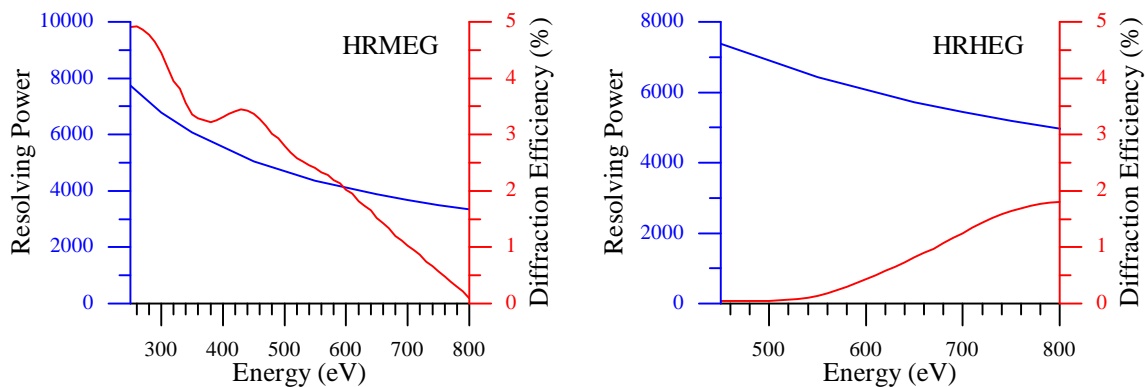


**Figure 4.2:** Calculated resolving power and diffraction efficiency curves for the designed high resolution gratings.<sup>1</sup>

### 4.1.3 VLS Spectrometer

Our research group had the opportunity to work with a spectrometer designed by Oliver Fuchs<sup>57</sup> that employs a single planar VLS grating and a pre-focusing spherical mirror to capture moderate resolution spectra containing the C (285 eV), N (400 eV) and O (525, eV) edges in one exposure. This allows for a rapid survey of spectral emission from multiple elements within a sample at the same time, saving time and reducing the time that a sensitive sample is exposed to potentially destructive radiation.

The unique capabilities of this instrument are achieved by using the dispersion control afforded by VLS gratings to compress the focal field and focus multiple diffraction orders onto the detector at the same time. The desire for a similar spectrometer for our endstation

led to the expertise gained in designing the first spectrometer to be applied in an attempt to produce an instrument superior to this design. The pre-focusing mirror was abandoned to improve efficiency and a single spherical VLS grating was designed to focus and disperse with one reflection.

A complex spreadsheet was designed to allow these equations to be managed and optimized. For a grating to create a perfectly focused image, all the focal terms shown in Equation 2.22 must be exactly zero. While it is not possible to achieve this at multiple energies simultaneously, by optimizing the focal properties of a grating at multiple energies of interest (in multiple diffraction orders) at one time, acceptable foci can be found for each by minimizing the  $F$  terms as much as possible. For this design, a least-squares-fit was used to find the best possible focus at 5 energies between 90 eV and 710 eV, and the geometry of the system was adjusted to allow all 5 energies to fall onto the active area of a high resolution, stationary, CCD camera so that it can capture all 5 emission edges in a single exposure with one fixed geometry.

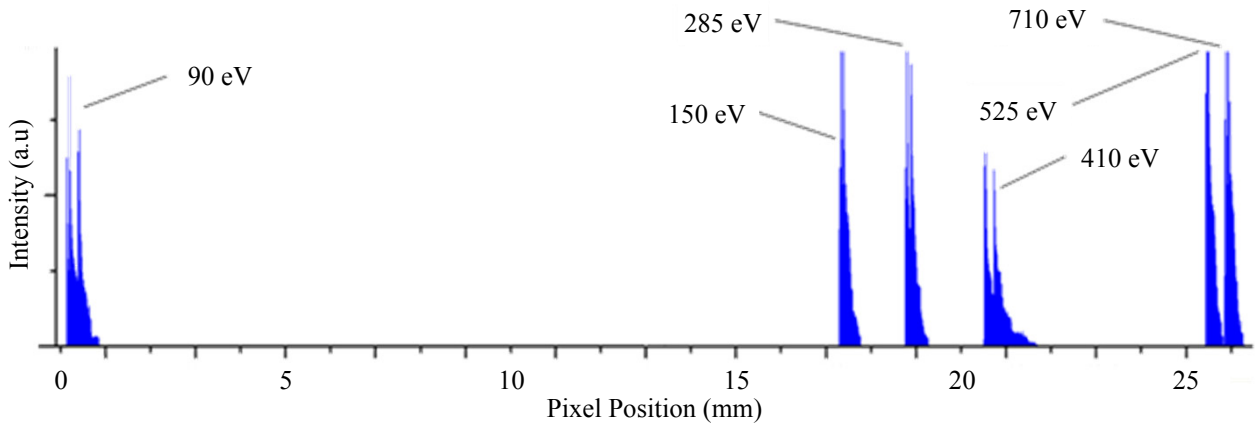


**Figure 4.3:** Cross section of a predicted CCD image, perpendicular to the dispersion direction, with several resolvable spectral line pairs shown.

The CCD camera that this spectrometer was designed to use is a back-illuminated Princeton Instruments PI-SX with 4.2 million 13.5  $\mu\text{m}$  pixels. Figure 4.3 shows a cross section of the detector area, perpendicular to the dispersion direction, from a ray-traced simulation of the spectrometer's performance. The rays that reached the detector surface were sorted into pixel sized bins and displayed as a plot of counts versus detector position along the dispersion direction. Two discrete peaks with slightly different energies are shown in each region of

interest from 90 eV to 710 eV. This demonstrates how the resolving power was determined: if there is one full pixel space between the FWHM of the two peaks, then they are considered resolvable.

A large, 80 mm long grating will maximize the acceptance angle of the spectrometer and, in addition to having only one optical element, it is designed to operate without an entrance slit. These design choices will maximize the diffraction efficiency of the spectrometer allowing dilute samples and samples susceptible to radiation damage to be quickly and effectively measured. A ray trace study of the spectrometer's resolving performance shows that it should achieve a resolving power of approximately 1000 across the entire range of operation from 90 eV to 710 eV.

The mechanical design for this spectrometer has already been completed, and the sample chamber is equipped to accept it. The vacuum chambers for it have been purchased and are on hand. Completion of this second spectrometer is dependent on additional funding for the purchase of the CCD detector and a precision ruled spherical VLS grating. A drawing and cut-away view of the final design is shown below in Figure 4.4.

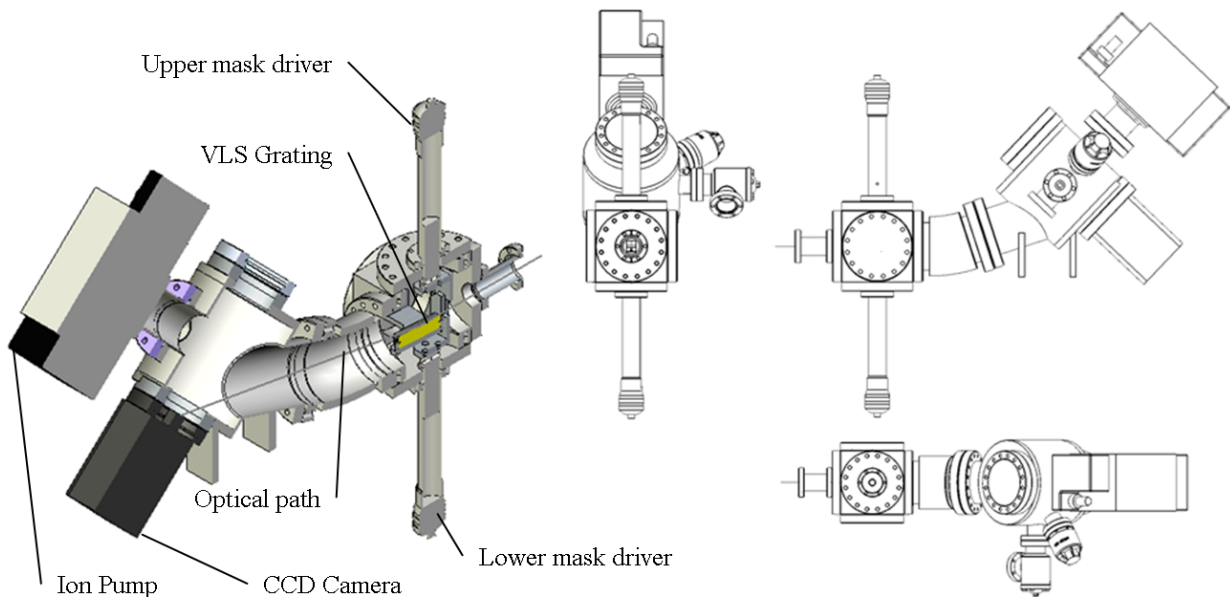


**Figure 4.4:** A rendering of the 3D CAD model of the VLS Spectrometer design with key components called out.

## 4.2 Mechanical Design

Following the completion of the optical design, Loken Engineering engineering was retained to assist with the mechanical design. Working closely with them and numerous vendors a mechanical design for a complete endstation was created that would allow the optical design for this spectrometer to be realized. The completed mechanical design required in excess of 500 drawings. A rendering of the final endstation design is shown in Figure 4.5.

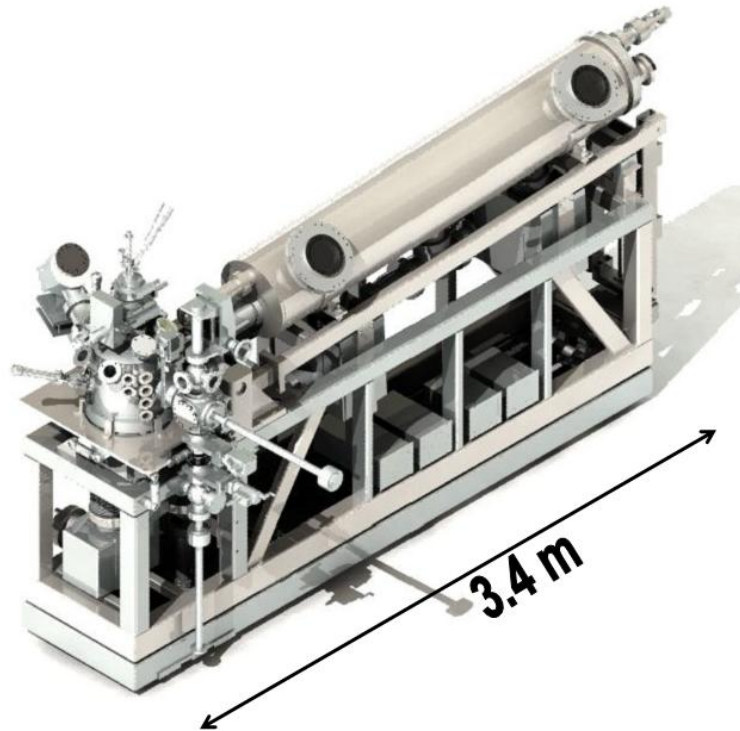


**Figure 4.5:** A rendering of the 3D CAD model of the completed endstation design.

There were numerous challenges faced in designing this endstation. As with all soft X-ray systems, the sample and entire spectrometer had to be within an Ultra-High Vacuum (UHV) environment, since soft X-rays would be completely absorbed by only a few centimetres of air. This means working within confined vacuum chambers, with a limited selection of materials and no lubrication for moving parts. Additionally, as is always the case on the floor of a synchrotron, space is at a premium. The spectrometer had to be designed to fit within a relatively small experimental hutch which it shares with a second endstation and this endstation has to be able to move out of the light path to allow the other endstation

to use the synchrotron light. Large size and long motion range were required to place the detector at the long focal lengths for the high resolution third diffraction order gratings while still reaching the relatively short focal lengths of the standard gratings (a total range of 35 cm - 220 cm). These size and space constraints created a significant challenge. A novel translation design for the in-vacuum detector was required and it has been the source of many of the interesting and challenging problems that were encountered. The remainder of this section will serve as a walk-through of the endstation. It is divided into sections based on the physical arrangement of equipment and follows the light path through the system. Figure 4.6 is a cutaway view of the original endstation design CAD model with the most significant parts called out and it can be used to follow along through the following sections.

### 4.2.1 Sample Chamber

The first chamber in the spectrometer system is the sample chamber. The main sample positioning arm is located here at the intersection of the optical axis of the spectrometer and the synchrotron beam path. The sample is mounted on an X-Y-Z- $\theta$  motion platform to allow for sample alignment and transfer. The sample holder (Figure 4.8) will be able to heat the sample plate with a tungsten filament inset behind the sample plate. Features to allow for the possibility of future use of electron beam heating to achieve higher temperatures have been included in the design. The sample arm incorporates a cryostat capable of using liquid nitrogen and liquid helium for sample cooling to allow temperature dependent studies or to reduce beam damage to sensitive samples. The sample plate is electrically isolated and connected to a electrical feedthrough to allow for sample current measurements. Four separate electrical contacts are provided for custom sample plates with built in sensors or probes. In addition to the X-Y-Z- $\theta$  motions required to align the beam, a tilt (“ $\phi$ ”) motion which pivots the sample by a few degrees around the beam axis was incorporated because a similar motion has been found to be critical to the optimal alignment of the spectrometer on BL 8.0.1 at the ALS.

Our research group has designed a 0.7 T sample plate mounted permanent magnet array (see Figure 4.8) that will be available to conduct experiments with the sample exposed to in-plane and perpendicular magnet fields to study magnetic dichroism effects. The sample



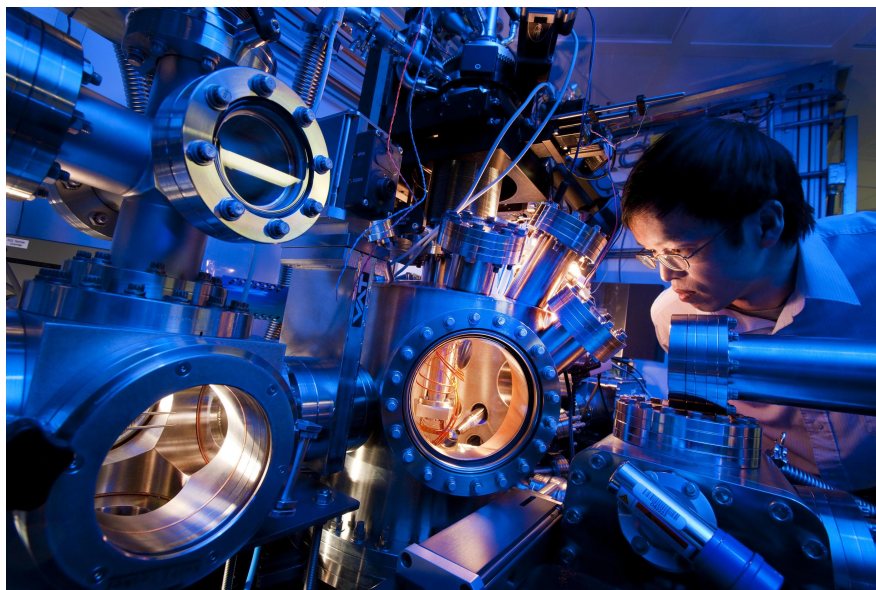


**Figure 4.7:** REIXS beamline scientist Feizhou He inspecting the XES sample chamber. The sample load lock access port is visible in the lower left. Photo courtesy of Canadian Light Source Inc.

arm also mounts a second fixed sample plate for standard reference samples and a calibrated photodiode for beam current measurements. This, in addition to the requirements for sample tilt positioning and sample exchange, resulted in an extremely complex sample arm that was quite interesting to design and construct.

Attached to the sample chamber is a load-lock system with a sample carousel that can store 4 sample plates under vacuum (Figure 4.9). From there, samples can be inserted into the system and transferred into the sample chamber without breaking the main chamber vacuum. A vacuum “suitcase” has also been designed and built that will allow samples to be moved from the separate sample preparation chamber to the load lock and into the sample chamber without leaving vacuum. This mobile vacuum cart docks at the base of the load lock to transfer samples into the system. A direct connection between the prep chamber and the endstation was not possible due to floor space limitations.

While holding samples in vacuum and aligning them relative to the spectrometer and photon beam during measurements with the spectrometer is the main purpose of this chamber, it was designed to support a wide range of secondary capabilities to make this a full featured endstation capable of a variety of experimental techniques. In addition to the soft X-ray

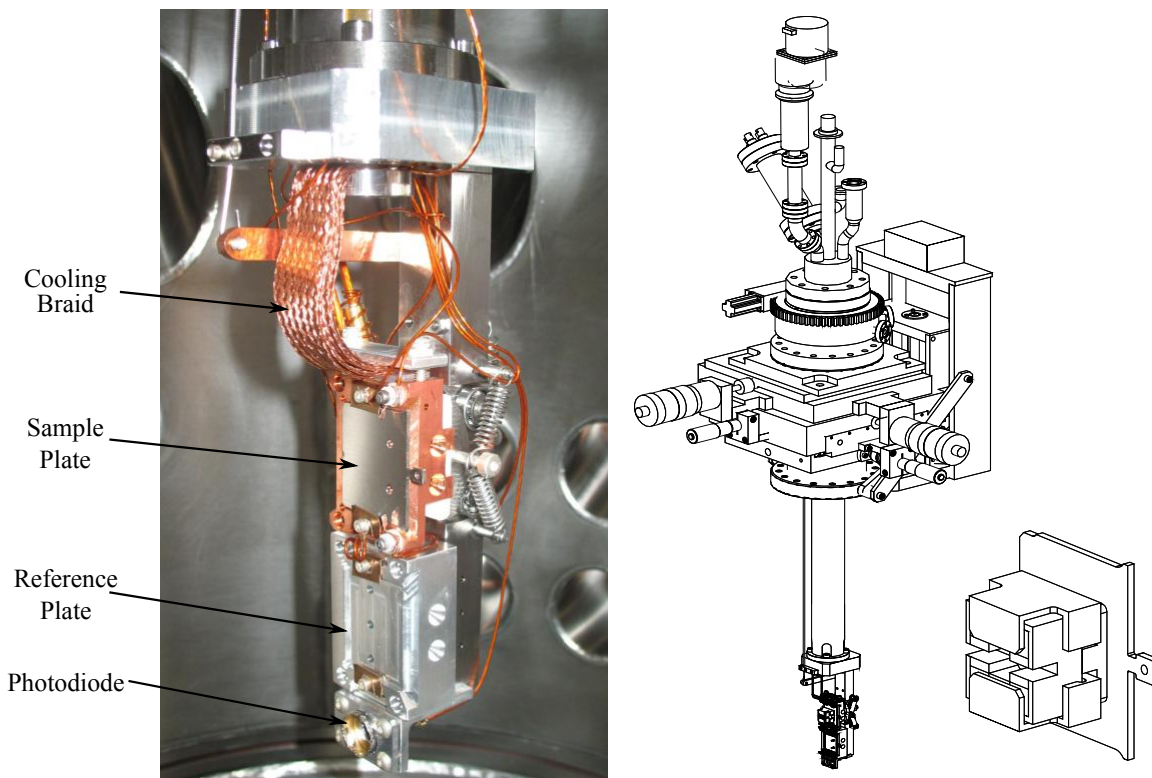


**Figure 4.8:** The main sample holder head (left), the sample holder on the cryo-arm and X-Y-Z- $\theta$  motion stage (center), and the permanent magnet array sample plate (right).

emission spectroscopic techniques that the endstation was primarily designed for, instrumentation has been included to allow for Total and Partial Fluorescence Yield (TFY/PFY) and Total Electron Yield (TEY) X-ray Absorption Spectroscopy (XAS) and X-ray Photoelectron and Auger Electron Spectroscopy (XPS and AES). There is also an integrated electron source to expand the range of possible experiments. The design includes the ability for further expansion including the addition of a liquid sample cell, a high efficiency VLS spectrometer, an optical spectrometer and a silicon drift detector.

Achieving UHV in the sample chamber is more critical than in any other chamber since it is required not only to minimize soft X-ray attenuation, but also to protect sensitive samples from contamination and oxidation. Vacuum is achieved by an attached 300 L/s turbo pump that is backed by a molecular drag and scroll rough pumping system to increase the compression ratio to the turbo pump and supply differential pumping to rotation stage of the main sample arm. This pump is supported by a 300 L/s ion pump with integrated

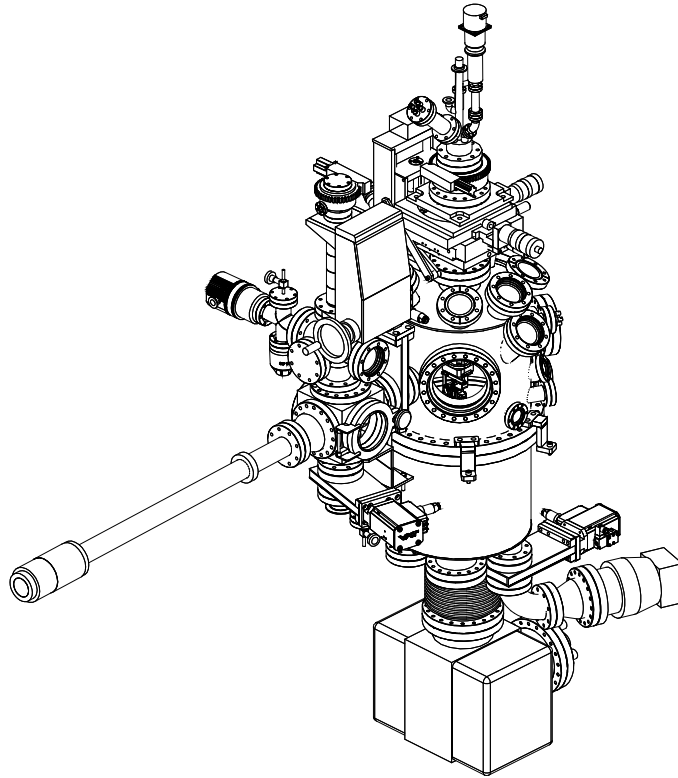


**Figure 4.9:** The sample chamber (right) and load lock (left).

TSP.

The sample chamber is made out of a 14" diameter tube bisected by a 16.5" CF flange. This flange was needed primarily to facilitate fabrication, but the large lower hemisphere was initially designed to allow a large retractable permanent magnet, or possibly an electromagnetic, for X-ray Magnetic Circular Dichroism (XMCD) measurements. The surprising success of the sample plate mounted permanent magnet array has resulted in this early plan being abandoned. The lower hemisphere has four CF flanges for mounting pumping systems. The upper hemisphere has 29 CF flanges ranging from 2.75" to 8" for mechanical and electrical feedthroughs, secondary instrumentation, vacuum monitoring, and viewports.

The final device initially intended for the sample chamber was a variable horizontal entrance slit (Figure 4.10) to act as the optical source for the spectrometer. It is comprised of two precision mounted Piezo actuators positioned 10 mm from the sample to provide a well defined source for the spectrometer that can be adjusted between 10  $\mu\text{m}$  and 250  $\mu\text{m}$ . Light passing through the entrance slit will enter the grating chamber and illuminate the diffraction grating centered within it.

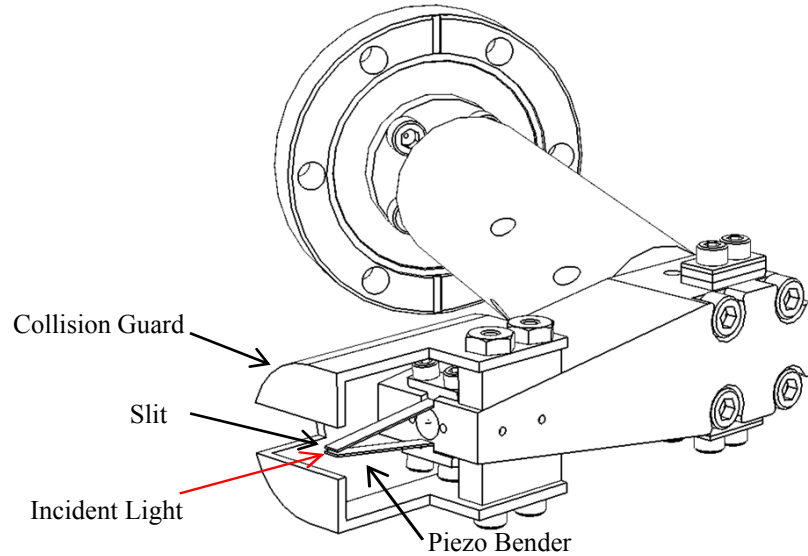


**Figure 4.10:** The entrance slit and holder. Two precision piezo benders form the adjustable slit. They are mounted to a support arm and protected from sample collisions by a hood.

## 4.2.2 Grating Chamber

Once light emitted from a sample passes through the slit or mask (see Section 5.3.5) located in the sample chamber it enters the grating chamber. Here the six diffraction gratings are housed on a two-story mount with four on the top level and two on the bottom. This mount is connected by a support tube and bellows to a high precision hexapod 6-axis positioning system from Physik Instrumente (Figure 4.12). This hexapod is one of the truly excellent features of this design. Not only does it allow for automated, precise and repeatable grating changes ( $\pm 2 \mu\text{m}$ ,  $\pm 20 \mu\text{rad}$ ), it gives unprecedented freedom to align the gratings and compensate for unavoidable dimensional stack up errors in the fabrication and assembly. As powerful as it is, it is not without limitations.

The biggest design challenge with this approach was the limited load carrying ability of the hexapod. While the weight of the aluminum mount and silica gratings is well within the load limit of the hexapod, the gratings are mounted inside vacuum and coupled to the hexapod by a bellows and CF100 conflat flange. The vacuum force acting on that flange must be considered. Since the pressure inside the chamber will be essentially zero, the full force of atmospheric pressure will be applied to the outer surface of any vacuum chamber. When a

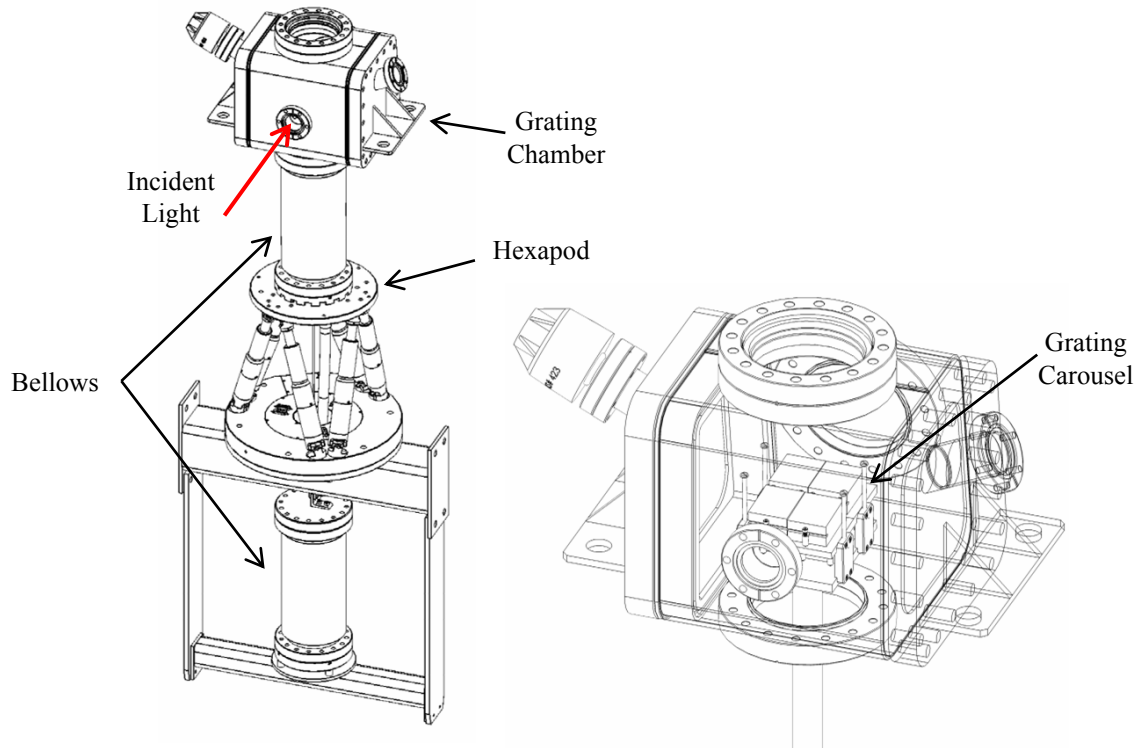


**Figure 4.11:** The grating chamber and surrounding structure. The chamber is shown transparent revealing the gratings and mount within. The hexapod and counter-force bellows can be seen below.

bellows is involved, this results in a rather extreme force working to compress the bellows. In this case, the 100 mm ID of the bellows results in an upward force in excess of 800 N, well in excess of the hexapod's rated 15 N holding force. To compensate, a second bellows is installed below the hexapod with its base mounted to the frame and a cable connection is made to the flange mounted to the hexapod (see Figure 4.11). The two bellows are also connected with a Swagelok tube fitting so that they pump down at the same time and maintain a neutral force on the hexapod at all times. The conductance of the small Swagelok will be quite poor, but it is more than adequate to ensure that both chambers pump down to rough vacuum levels at the same time, at which point any pressure differential that may exist will result in a very small force acting on the hexapod.

The second design limitation imposed by such a motion system is a complicated and restricted range of motion that couples together all 6 degrees of freedom. With the platform level, the motion envelope in any plane is basically trapezoidal - any change in  $Z$  from



**Figure 4.12:** The Physik Instrumente M-840 HexaLight 6-Axes micropositioning system used to align and change the gratings<sup>58</sup> (left). Upper “hemisphere” of a typical translational motion envelope, or “workspace”, of a hexapod positioning system (right)<sup>59</sup>.

the home position will reduce the available travel in  $X$  and  $Y$  (Figure 4.12). Any tilt or rotation quickly reduces that available travel as well. To manage this, the grating mount was designed with precision machined flats for each grating to pre-tilt them to the appropriate incident angle. This freed sufficient translational range of motion for the hexapod to be able to reach the optical center of all 6 gratings while reserving a small amount of motion for final alignment. Even so, the hexapod had to be surveyed into place to within a few tenths of a millimeter using the technique described in Section 5.3.1 to ensure that all 6 gratings were reachable. The initial mechanical design did not allow for positioning of the hexapod with this level of accuracy, so this was accomplished with a custom machined shim plate based on precision survey data. The final challenge for this chamber, one shared by most equipment on the floor of a synchrotron, is making it fit in the available space. The requirements imposed by the optical design required that the center of the grating in use be 35 cm from the source point in the sample chamber, and that the detector be able to move as close as 50 cm on the other side. Unfortunately, the source point is at the center of a 14” diameter chamber and there needs to be a valve separating the sample chamber from the grating chamber/spectrometer. In addition, a bellows long enough to handle the rotation of the detector chamber is required on the other side of the chamber. Finally, a spool piece

for the detector bellows extends from the detector chamber above the grating chamber and the pivot points of the detector chamber are located on either side of the grating chamber, collinear with the optical origin. Taking all this into account, there is barely enough room for the required motion of the grating mount. This meant that a custom chamber shape was needed and standard vacuum flanges could not be used. Instead, a wire seal side flange was used, which is a flexible sealing technique that generally requires much skill and effort to seal properly. The back wall of the grating chamber is canted slightly to minimize the deflection required from the detector chamber bellows. There was not sufficient space for a valve between the grating chamber and the detector chamber which means that the entire spectrometer is one vacuum section. Due to the extreme space limitations, it would not have been feasible for the grating chamber to have dedicated pumping and gauging. SO while not ideal, this arrangement is practical. Since it is optimal to maintain ultra high vacuum in the grating chamber at all times to keep the gratings clean and minimize soft X-ray attenuation, the vacuum requirements for this chamber match those of the detector chamber.

### **4.2.3 Detector Chamber**

The detector chamber is the final chamber in the system which houses the detector and the motion system required to position the detector at the desired focal point. The entire chamber is mounted on a frame that pivots about the optical axis of the gratings, allowing the detector to be rotated into the position corresponding to the diffraction angle of the energy of interest. Figure 4.13 shows a cut-away of the initial design that we set about to construct. This section will cover the details of this part of the design. Some of the problems encountered during assembly and the solutions that were found are discussed in Section 5.2.4.

Inside the nearly 2.5 m long cylindrical vacuum chamber, the detector, along with its preamplifier enclosed in an air-filled box, is mounted to a carriage that hangs by a rail and bearing system mounted to the wall of the chamber. The preamplifier is inside the vacuum chamber mounted immediately behind the detector to minimize the noise and position jitter that would result from a long cable. The necessity of this design feature was verified with the help of Quantar Technology Inc who performed tests with their controlled setup using extended length detector-preamplifier cables which indicated a resolution loss of as much as

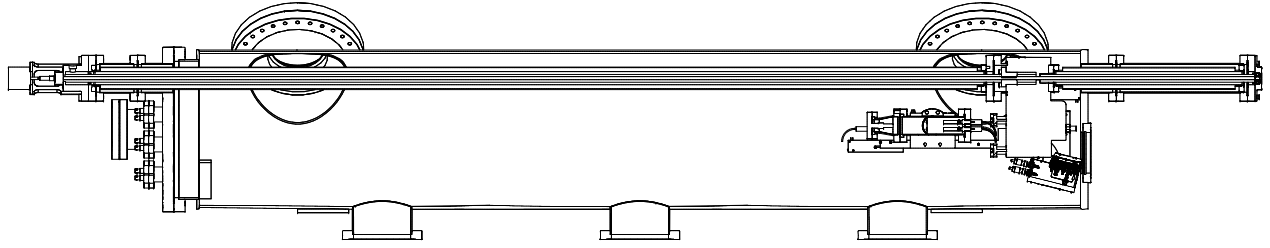


**Figure 4.13:** A cutaway of the detector chamber. The detector carriage can be seen on the right hand side at its minimum travel position. The grating chamber connects to the right.

a 30%. The carriage is driven by a standard oiled ballscrew that is isolated from the vacuum by two 3 m long custom made vacuum bellows. Two 4.625" spools extend from either end of the main chamber to give the bellows enough space to compress into. The original design also used these bellows to circulate a small amount of cooling air through the inner chamber that houses the preamplifier electronics.

In addition to translating to the proper focal position, the detector needs to tip about an axis perpendicular to the optical axis to maintain the surface of the detector tangent to the Rowland circle, thus minimizing the deviation of the flat detector from the circular focal curve. Finally, since the detector was designed to have high and low resolution operating modes accessed by rotating it 90 degrees, a rotation about the detector normal was also required. These two motions were accomplished using UHV rated motorized linear motion stages from Micos, a well-respected manufacturer of vacuum motion systems.

Access to the chamber for installation of the in-vacuum components is facilitated by a 16.5" Conflat flange (Figure 4.14) making up the back face of the chamber and two 13.25" conflat flanges on the side of the chamber rotated 45 degrees from the top near the front and back.

Good HV or UHV is required in the chamber to protect the hydrophilic channel plates of the detector and to minimize attenuation of the low intensity soft X-rays travelling up to 2.2 meters from the grating to the detector. The design called for initial roughing and pump down via a 2.75" all metal angle valve at the base of the chamber and maintenance of UHV with two 500 L/s ion pumps, one with an integrated TSP, mounted to 8" conflat flanges on the bottom of the chamber and supported by the frame. While a turbo pump

can be a flexible, compact and effective means of reaching and maintaining UHV, especially in combination with an ion pump, the high rotational velocities of the pump blades results in significance rotational inertia and rotation required by the detector chamber would apply sufficient force through torque-induced gyroscopic precession to destroy such a pump, making it impractical to mount a turbo pump to the chamber for use during normal operation. A third 8" CF flange is centered on the base of the chamber and uses a multiport reducer to mount the roughing angle valve and vacuum gauges for the chamber.

Power and signal connections to the preamplifier, in-vacuum motors and high voltage bias connections to the detector channel plates are facilitated though 8 2.75" conflat flanges on the 16.5" rear flange (Figure 4.14), using metal-ceramic seal UHV electrical feedthroughs. The in-vacuum cable bundle is 10' and contains several custom, kapton insulated coaxial and multi conductor cable sets.

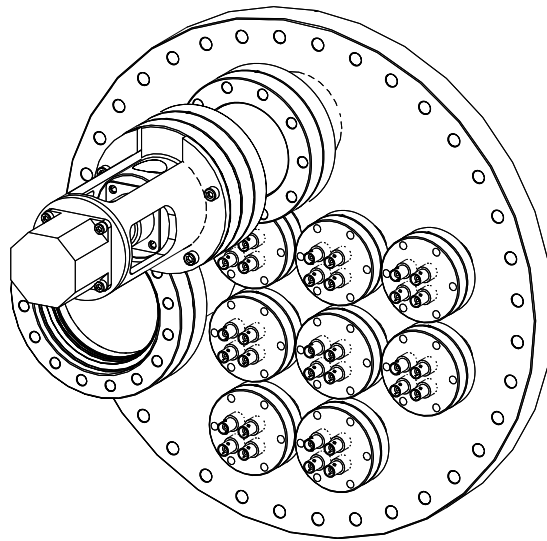


**Figure 4.14:** The 35 kg rear flange of the detector chamber. There are 8 2.75" CF flanges for electrical feedthroughs, one 4.625" CF flange for the bellows spool and motor mount and one 6" flange for a viewport.

### 4.3 Sample Preparation System

As mentioned, there are numerous plans for the endstation that include more capabilities than just X-ray emission spectroscopy. To facilitate all of the desired experimental capabilities without over crowding the sample chamber or risking contaminating, it was decided

that a separate sample preparation chamber was required with a vacuum transfer cart that will allow samples to be prepared and characterized independent of the beamline and transferred in vacuum to the XES sample chamber. This chamber will provide a range of in-situ material preparation and analysis techniques that includes heating/annealing, ion bombardment/sputtering, e-beam evaporator deposition, cleaving, LEED, and RHEED. This system has been designed and built and the included instruments are currently being commissioned. Details of the capabilities and operation of this system are outside the scope of this document.

# CHAPTER 5

## CONSTRUCTION & COMMISSIONING

### 5.1 Procurement

Working closely with University of Saskatchewan Research Services and Purchasing Services, over 150 significant transactions totalling over 1.4 million dollars were completed. Many of these purchases required involved multiple vendor quotations (RFQ) or lengthy formal Request For Procurement (RFP) processes (resulting in over 3000 archived emails and a filing cabinet *full* of documentation). The process began in August 2006 with the RFP for the long lead time diffraction gratings and the bulk of the remaining component purchases were completed during the second and third quarters of 2007. Most of the required instruments, parts and custom machined components were on hand by mid 2008 which, at the time, seemed to be significantly behind schedule. Much of the pressure to procure the required components at the time was due to the fact that the engineering firm that produced the mechanical design was in the process of going out of business at the end of 2007 and limited support from their staff would only be available for a few months into 2008.

The most significant areas of spending included the diffraction gratings (\$140,000), the vacuum chambers (\$83,000), motion and manipulation systems (\$170,000), in vacuum parts and hardware (\$73,000), the MCP X-ray detector (\$55,000), vacuum pumps, gauges and valves (\$161,000), secondary instrumentation (\$226,000), and support frames and airside hardware (\$75,000).

Considering the complexity of the components involved, the majority of the purchasing went relatively smoothly. There were a number of issues with the custom fabricated components, mostly stemming from the fact that the engineering company that generated the drawings was rushing to complete them before they went out of business and they were never

properly reviewed or signed. That being said, there were problems in other areas as well. For example, the vacuum chambers that were ordered in May 2007 and expected 8 weeks later arrived in December. Also, the long custom ballscrew to move the detector stage was fabricated wrong when the vendor misread the drawing and made it 20 cm too short. Due to its unusual length, a replacement took 18 weeks to deliver. Again, because of the rushed conclusion to the mechanical design, there were numerous errors in the Bill of Materials (BOM), upon which the part ordering was based. It may seem minor, but a 3 week delay to wait for a dozen absolutely crucial silver-plated vented vacuum fasteners is extremely frustrating. The most significant issues that were encountered during procurement were with the diffraction gratings. Those issues were (are) sufficiently complex to justify discussion in their own section.

### 5.1.1 Diffraction Gratings

The very first items ordered were the six diffraction gratings that make up the primary optical elements of the spectrometer. Being notoriously long lead time items, the procurement package for the gratings was put together as the mechanical design for the spectrometer was just beginning. Bach Research was chosen as the vendor and the gratings were ordered in September 2006 with delivery expected within 9-10 months. All 6 gratings were finally on hand by November 2007, right around the time that most of the other major components began to show up. Upon arrival, the CLS optical metrology lab analyzed the gratings using a Long Trace Profilometer (LTP) and an interferometer to verify that the roughness, line spacing, radius of curvature and slope error of the gratings were all within an acceptable range (Table 5.1).

In February 2008 AFM measurements of the gratings were performed here at the University's Saskatchewan Structural Sciences Center. While the equipment at the SSSC was not optimized for optical metrology, very useful information was obtained (Figure 5.1), particularly concerning was the roughness of the groove profiles for the two highest line density gratings, the HEG and HRHEG. Accurate blaze angles were difficult to extract from the measurements since the staff at SSSC did not have much experience in calibrating the Z axis of the AFM that was used, but there was sufficient cause for concern that further investigation

Grating	Surface Roughness ( $\text{\AA}$ )	Line Spacing [spec] (1/mm)	Radius [spec $\pm 0.1\%$ ] (cm)	RMS Slope Error ( $\mu\text{rad}$ )
LEG	-	593.02 [600]	502.56 [501.7]	1.735
IMP	-	892.86 [900]	669.98 [668.7]	1.535
MEG	7.4849	1187.8 [1200]	1001.8 [1002.9]	-
HEG	4.066	1985 [2000]	1001.4 [1002.9]	0.976245
HRMEG	4.492	1780 [1800]	1001.6 [1002.9]	-
HRHEG	4.261	2551 [2600]	1144.9 [1146.1]	0.976245

**Table 5.1:** Grating measurements from CLS optical metrology lab.

was warranted.

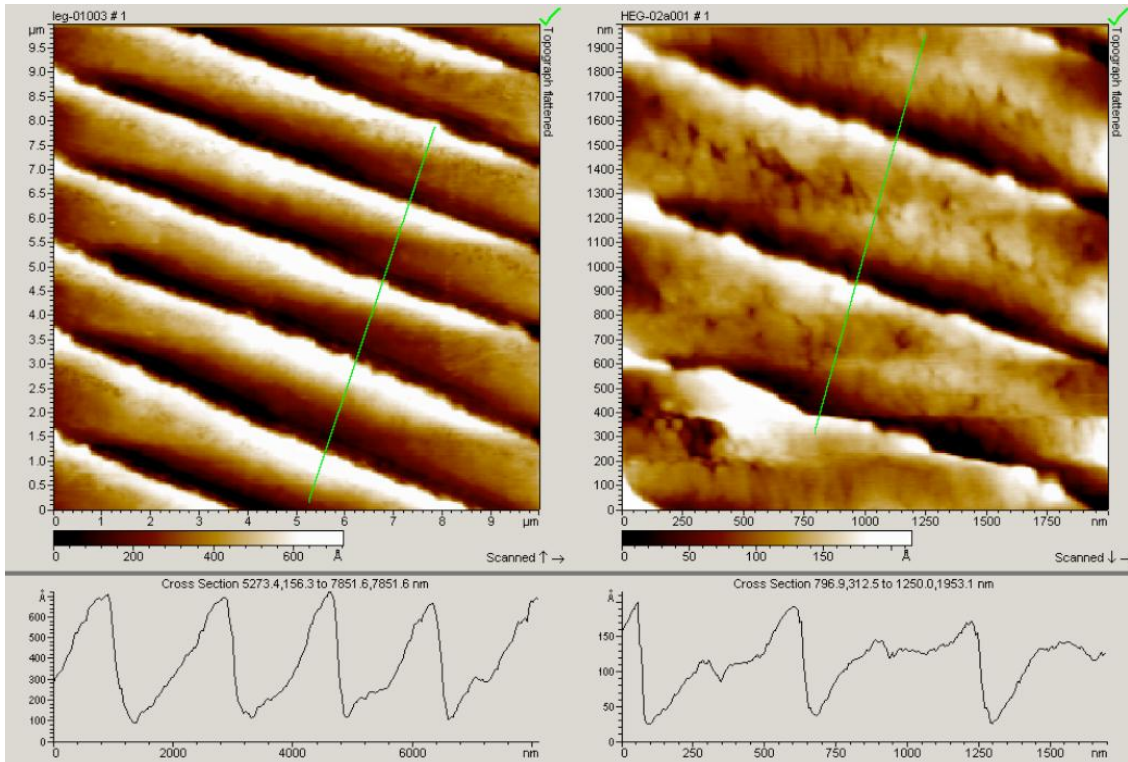


**Figure 5.1:** Two of the grating AFM measurements taken at the SSSC. False colour images (top) and cross section profiles (bottom) taken along the green lines are shown. The LEG (left) appears to be quite good with a reasonably consistent and flat blaze profile. The HEG (right) appears to be very rough with non-uniform, irregular profiles.

Based on our findings at the SSSC, we made arrangement to have the gratings measured by the Center for X-Ray Optics (CXRO) at the Advanced Light Source in Berkeley, CA. Not

only do they have experience with applying AFM measurements to gratings and extracting accurate calibrated blaze profiles and angles, they also have a beamline (the calibration and standards beamline 6.3.2<sup>60</sup>) designed for diffraction efficiency measurements of X-ray optics. The resulting data was excellent and confirmed our fears regarding the quality of two of the gratings.

	LEG	IMP	HEG	HRMEG	HRHEG
Specified blaze (deg)	1.85	1.11	1.52	4.85	4.05
Measured blaze (deg)	2.45	1.60	non-triangular	4.43	6.35

**Table 5.2:** Actual blaze angles extracted from CXRO AFM measurements compared to specified angles (specification  $\pm 10\%$ )

While none of the blaze angles are perfect, calculations showed that errors on the order of 0.5 degrees would not significantly impact the diffraction efficiency. More revealing were the diffractometer measurements. In addition to directly measuring the the actual diffraction efficiency - regardless of what the blaze angle appears to be, it is the resulting diffraction efficiency into the desired diffraction order that is of interest - the blaze angles could be back-calculated using the same methods used to predict the gating efficiency in the first place. Examples of the measurements taken and comparative calculations are shown in Figures 5.2-5.5. Mark Boots, a fellow research group member, was responsible for the diffraction efficiency calculations and measurements, a much more in depth look into these measurements and their analysis, including the results from the third order gratings (HRMEG, HRHEG), can be found in his Ph.D. thesis<sup>2</sup>.

The net result of all the measurements performed was to show that, while not perfect, the LEG, IMP, HRMEG should perform acceptably. The remaining three gratings (MEG, HEG and HRHEG), however, were not acceptable and would not produce acceptable results if used as is. Without such unusually careful analysis of the delivered gratings the performance of the system would have been severely compromised. Due to a lack of foresight, the purchasing arrangements did not include any provisions for acceptance testing, and the gratings had already been paid for by the time this was discovered. The concerns were presented to the manufacturer and they graciously consented to re-rule the gratings free of charge since

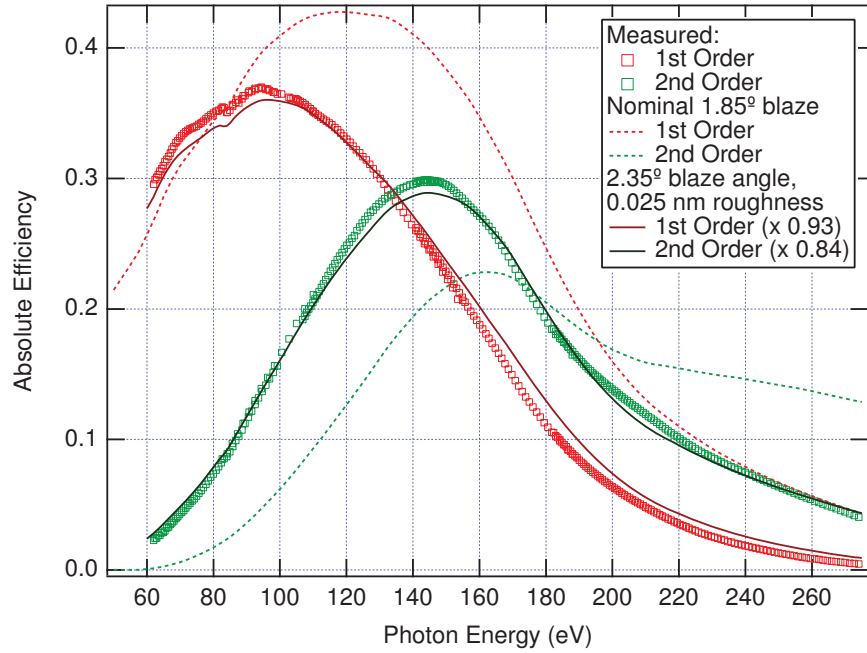


**Figure 5.2:** The predicted diffraction efficiency for an ideally ruled LEG as compared to the measurements conducted at ALS BL 6.3.2 including calculations to determine the actual blaze angle based on the measured performance<sup>3</sup>.

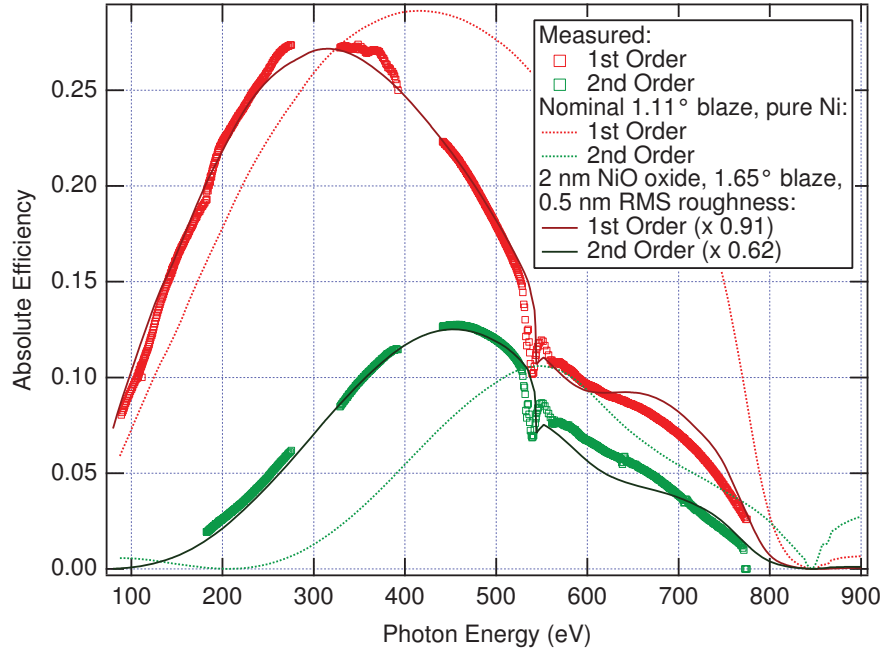


**Figure 5.3:** The predicted diffraction efficiency for an ideally ruled Impurity Grating as compared to the measurements conducted at ALS BL 6.3.2 including calculations to determine the actual blaze angle based on the measured performance<sup>3</sup>.

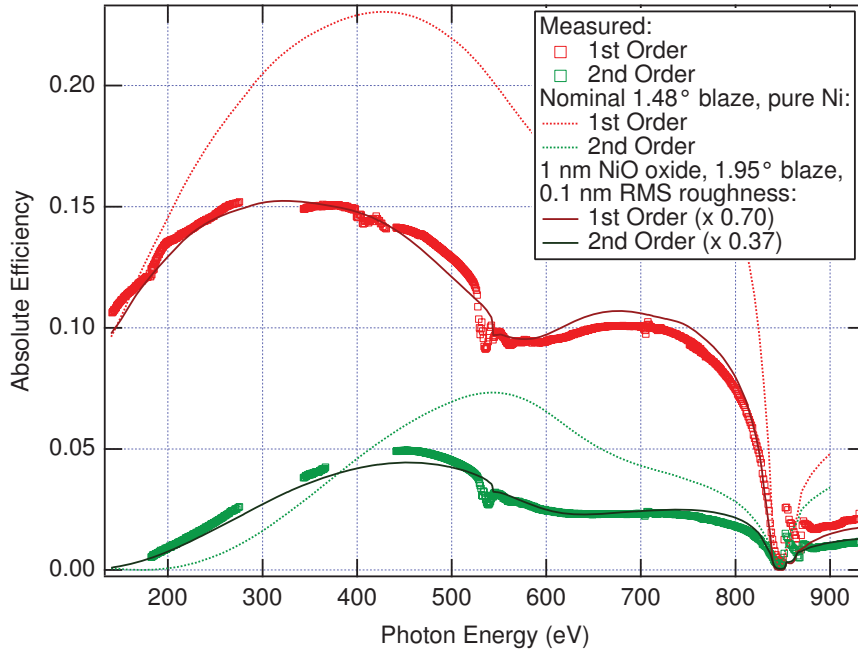


**Figure 5.4:** The predicted diffraction efficiency for an ideally ruled MEG as compared to the measurements conducted at ALS BL 6.3.2 including calculations to determine the actual blaze angle based on the measured performance<sup>3</sup>.

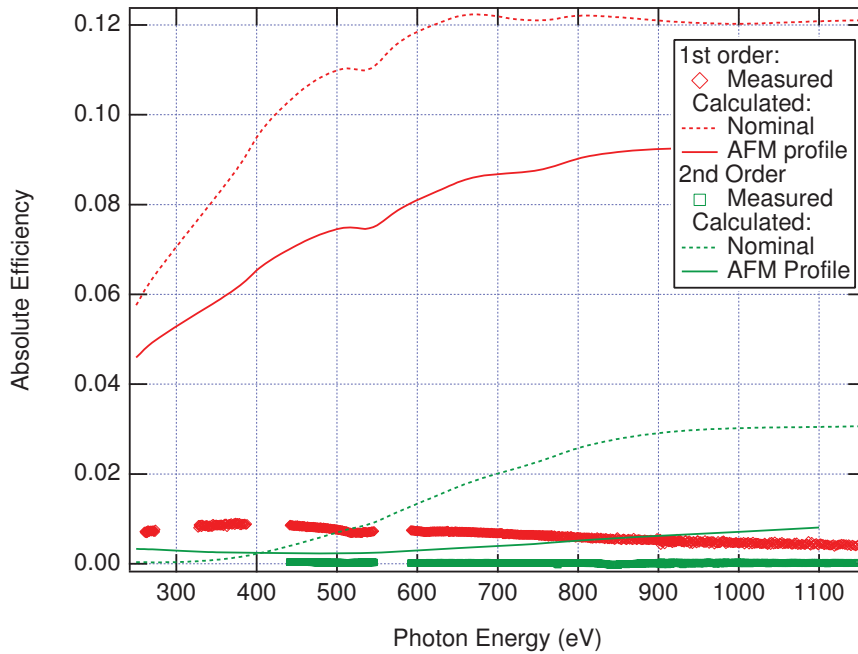


**Figure 5.5:** The predicted diffraction efficiency for an ideally ruled HEG as compared to the measurements conducted at ALS BL 6.3.2<sup>3</sup>. The abysmal performance is not surprising after examining the AFM measurements of this grating (Figure 5.1 (right)).

they were obviously outside the specifications in the purchase agreement. The gratings were returned to Bach Research for re-ruling in August of 2008. Unfortunately, by this time Bach Research had taken on several high priority US government contracts and our *pro bono* project was placed on hold.

The re-ruled gratings were received in June of 2010 and immediately taken to CXRO for measurement. The MEG passed testing and appeared to be a solid grating. While slightly improved, the other two gratings were still not going to perform acceptably, if at all. The HRHEG profile was relatively clean but the blaze angle was out by nearly 1.5 degrees. This would lead to a 75% relative loss in diffraction efficiency in the order of interest. The HEG was again very rough (Figure 5.6) and it appeared that in the process of stripping and re-ruling the grating, not enough of the previous ruling attempt was removed, leading to a clear double-peak structure. Bach Research agreed to try re-ruling these two gratings again. The HEG was returned in September 2010. Bach agreed to re-rule the HRHEG on the spare grating blank and let us keep the current grating. The dramatic error in the blaze angle of the HRHEG which made it all but useless in the third order happened to result in reasonable performance in the first order. It was installed as a temporary stand-in for the HEG since the decision had been made to proceed with final assembly of the endstation with the gratings that were on hand.

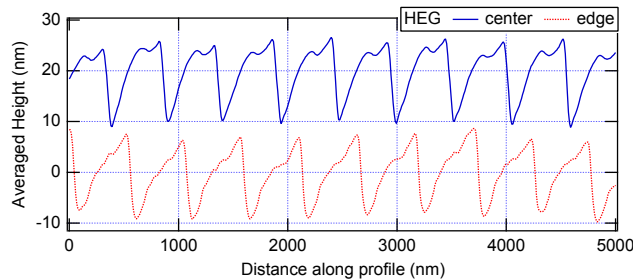


**Figure 5.6:** AFM measurements from CXRO of the re-ruled HEG from two different locations on the grating. The double peak structure may indicate that the previous ruling was not adequately stripped resulting in a blaze profile made up of the superposition of two rulings.

The decision to proceed at that time turned out to be a good one as numerous delays including further US government contracts, break downs of their ruling engine, problems with the gold undercoatings requiring them to be completely stripped and redeposited, and

evacuations due to wild fires resulted in final delivery of the re-re-ruled gratings being scheduled for April 2013. Fortunately, among the delays was a substantial investment by one US government agency to upgrade their ruling engine for their project, which should result in a better final product. In that time Bach has also acquired their own AFM allowing them to more thoroughly analyze their ruled test patches and do a much better job of dialing in the ruling parameters. The AFM measurements of the ruled test patches that Bach Research has recently provided look very promising, exhibiting very clean sharp profiles and accurate blaze angles (Figure 5.7). All indications are that this third attempt at ruling these gratings will turn out substantially better than the previous two. Even still, arrangements have been made to have their performance verified at CXRO upon delivery.

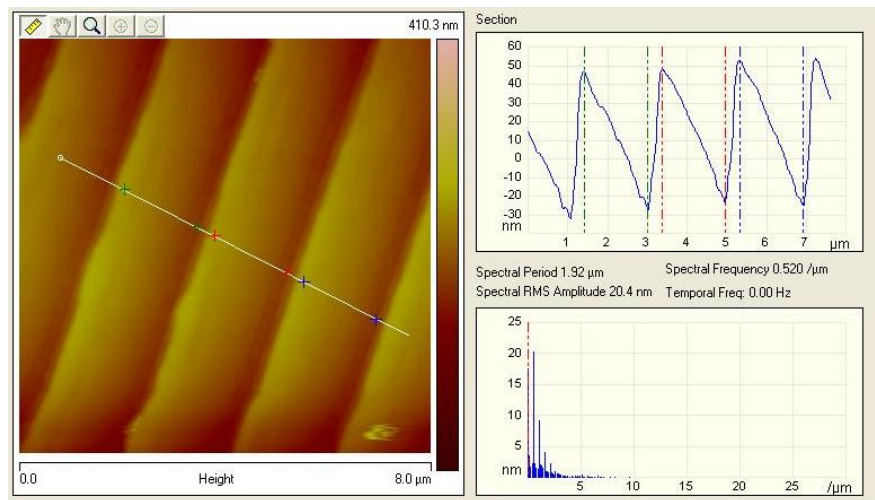


**Figure 5.7:** AFM measurements of a ruled test patch taken while Bach Research dialed in their ruling engine for a third attempt at ruling the HEG.

Clearly, the gratings have proven more difficult to manufacture than the vendor anticipated. This is partly due to the fact that our careful efficiency calculations led to narrow tolerances, but mostly due to the fact that we have gone to greater lengths than any previous client to verify that the final product was within those tolerances. Progress on the endstation halted while awaiting the re-ruling of the last three optical elements which did not meet our specifications when they were first delivered. After the second attempt to rule them only resulted in one more grating meeting our specification, the decision was made to proceed with only four gratings. Unfortunately, two missing gratings were the two designed to cover the high energy range which left a large gap in the performance of the spectrometer.

## 5.2 Assembly

### 5.2.1 Main Frame

One main support frame is the base upon which the entire spectrometer is assembled. This frame marks the exchange point between CLS and University of Saskatchewan responsibility for design and construction according to the agreement between the two organizations. Everything from the frame up was the responsibility of our research group. Initially, the engineering of the frame mount and translation system was completed by the same company that designed the frame. After reviewing the proposed translation stage design which used air bearings and conic positioning feet, it was designed by the CLS engineering department to mount on linear rails (Figure 5.8). The rail system was very well designed and has functioned flawlessly so far. The redesign turned out to be a fortuitous decision, as it has made the transition to slitless operation quite simple (see Section 5.3.4).

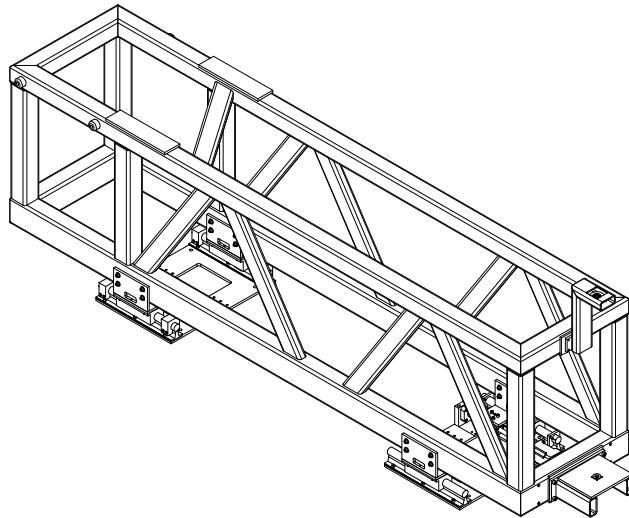


**Figure 5.8:** The endstation frame design, with the rail translation system as redesigned by CLS engineering.

The frame itself was fabricated by a local machine shop and delivered in November 2007. There were a few fabrication errors, mostly minor drawing errors or mis-read drawings. One part was welded together backwards. All of these were remedied quite easily.

With the translation stage redesign, the installation of the frame was delayed until September 2008. Prior to that, the sample chamber and associated pumps as well as some

of the rack mount electronics were installed on it.

When the rail system arrived, it was mounted to a jig that held the four rails in precision parallel alignment, to ensure the system would travel smoothly on the rails. The CLS mechanical technicians surveyed the frame into place and secured it to the floor with Hilti anchors and grout. The frame was then lifted onto the rail system and secured in place (Figure 5.9).



**Figure 5.9:** The endstation frame right after installation with the sample chamber and pumps, detector chamber frame sub-assembly and several rack mount controllers already in place.

The extra expense and care taken to ensure that the rails were as close to perfectly parallel as possible paid off since the 3500 kg endstation moved so smoothly on the rails that it could be positioned by hand prior to the motor drive system being installed with the rest of the endstation motor controls in February 2011.

## 5.2.2 Sample Chamber

The sample chamber was the first part of the vacuum system to be installed on the main frame. This was completed in early 2008 before the frame had been permanently installed, and afforded the opportunity to connect the vacuum pumps and gauges as designed for testing. The initial pump down revealed that the large 16.5" circumferential flange was leaking. Tightening the flange bolts did not resolve the problem, as the flange faces had already met. Due to the design of the chamber mountings, this flange could not be opened

without removing the chamber from the stand. A retrofit chamber mounting system was devised that would allow the top half of the chamber to be lifted off. This allowed the gasket to be replaced. Doing so resulted in a good seal, although this would not be the last time that a 16.5" flange seal would complicate matters.

Once the chamber was mounted and the basic vacuum systems verified, the chamber was baked to achieve UHV vacuum levels. Further installations of more delicate components were held until the frame had been moved to its final location. Assembly and pre-installation testing of the sample arm was completed during this time, with a typical number of complications. The sample arm had two significant design flaws. The sample  $\phi$ -tilt mechanism relied on a push-pull control cable to transfer the motion from a linear actuator vacuum feedthrough mounted on a 1.33" flange in the top of the cryostat to the sample holder. However, the design did not provide sufficient mounting points or support to allow the cable to push without buckling. A simple and effective solution was found by connecting a spring to existing bolts between the actuator lever arm and the back plate (see Figure 5.10 (right)) to preload the tilt mechanism allowing the push-pull cable to remain under tension.

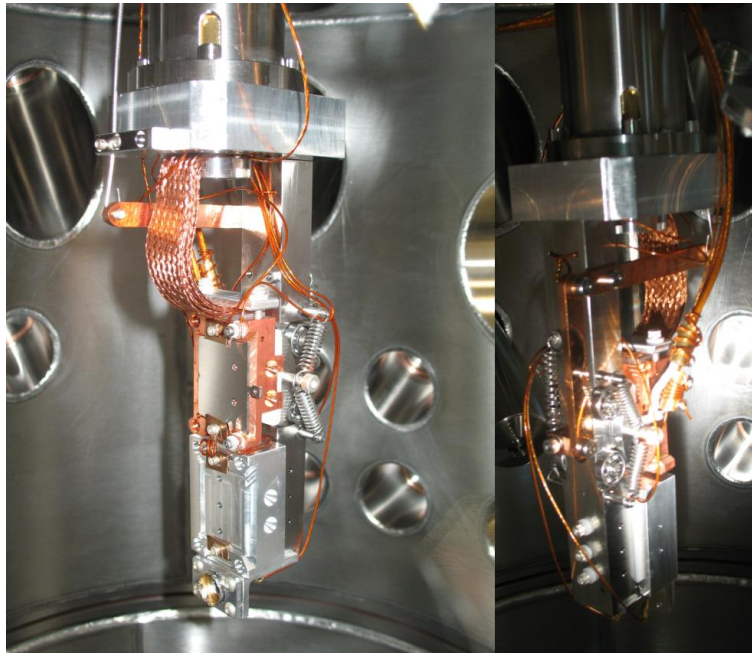


**Figure 5.10:** The assembled sample arm installed in the chamber from the front (left) and back (right).

The second design flaw found illustrates why mechanical engineers should not be tasked

with electrical component design. However, this still should not have been overlooked. The copper block that the sample clips to has a purchased tungsten heater coil embedded in it. According to the CAD model the electrical connection to the heating coil is made within the small channel between the copper block and a ceramic insulator plate by touching the wire to tungsten lead, with no provision made for securing it (see Figure 5.11 (center)). Considering that the tungsten must run through ceramic beads to insulate it from the copper block, there was not even space for a solder connection if that was an option. With the tungsten reaching nearly 2000°C however, even high temperature UHV rated gold solder is not an option. TIG welding was investigated, but bonding different materials can be extremely difficult, tungsten in particular, especially with the space constraints involved. The solution was to start with tungsten wire and coil an element by hand with leads of sufficient length to clear the back channel completely so that screw terminal butt connectors could be used to make the connection (see Figure 5.11 (right)). While still not ideal due to the significant length of hot tungsten that will be inside the ceramic beads, it is workable in the short term for limited sample heating.

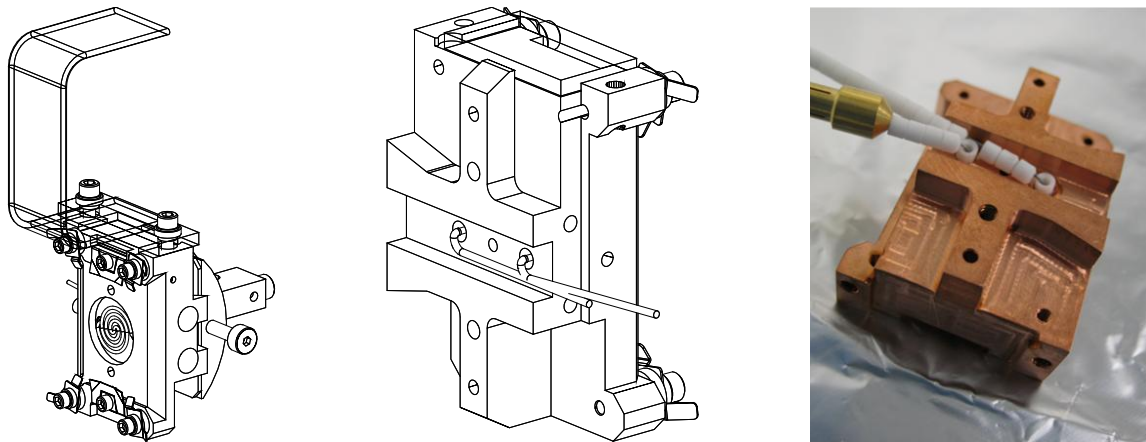


**Figure 5.11:** The sample mount block showing heater coil, copper braid “heat-pipe” leading to the cryostat head and the  $\phi$  tilt pivot mechanism (left). The designed tungsten coil electrical connection (center). The assembled sample block and heater coil (right).

Experience with this system has shown that the tilt stage is not, in fact, required for proper sample alignment and was only of use at the ALS spectrometer due to a quirk of the particular beam geometry found there. A similar sample holder is used in the sample

preparation chamber and problems achieving desired temperatures and maintaining ground isolation of the sample have recently prompted a redesign of that holder. The lessons learned there may be applied to this sample arm eventually as well. Alternately, since this design was implemented, both the RSXS endstation on REIXS and the SGM beamline have moved to a similar sample transfer system with a more robust sample holder that may eventually be adopted to allow users to easily move samples between the different endstations and sample preparation systems (Figure 5.12).

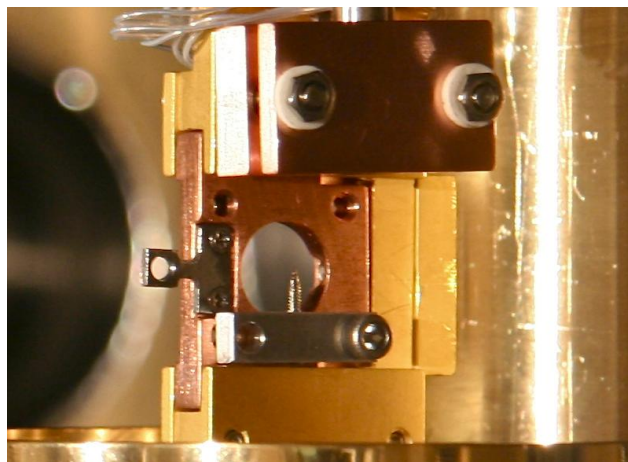


**Figure 5.12:** An RSXS/SGM style plate sample with a goniometer alignment pin, in the RSXS chamber.

Towards the end of 2008, after the frame was in place, the sample arm, load lock and sample transfer arm were installed with only minor issues found. Two are of note, as important lessons learned. First, the load lock mounts to a 4.5" flange and weights over 100 kg, so additional support beyond the flange bolts is required. The support bracket that was designed would secure the load lock chamber to the the same frame that the sample chamber mounts to. While this would be very effective, the bracket that was designed was rigid with no adjustability. If all dimensions of the fabricated items had been ideal, it may have worked very well, but it turned out to be roughly 1 mm too tall. The net result of using this bracket would have been to reverse the orientation of the excess force applied to the 4.5" flange tube and increase it by applying a portion of the weight of the entire sample chamber. A simple steel plate was fabricated to fit the base of the load lock and secure to the sample chamber frame with threaded rods so that the applied force could be adjusted (see Figure 5.13).

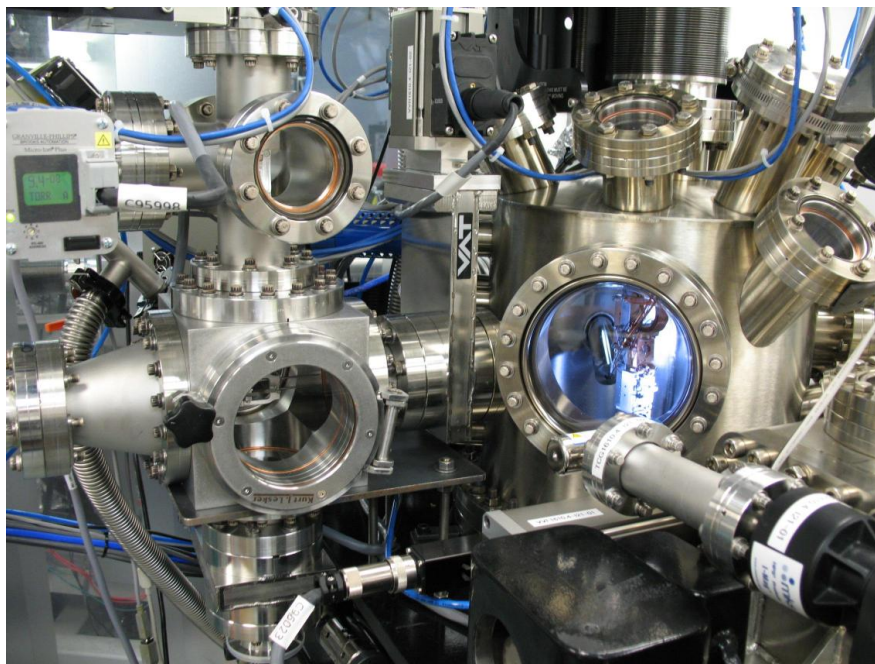


**Figure 5.13:** The sample chamber with load lock and sample arm installed. The modified load lock support can be seen at the base of the 6" CF cube.

The second lesson learned was to use caution when incorporating CAD models from other sources - even directly from vendors. The X-Y-Z stage provided by McAllister Technical Services was a later revision than the CAD model that they supplied. The support bracket for the Z-stage had been changed from a simple rigid linkage to a larger L-bracket and this resulted in a clearance issue with a flange on top of the chamber (see Figure 5.14). This required the removal and disassembly of the X-Y-Z stage so that the L-bracket could be machined to create adequate clearance. In addition, the supplied CAD model was for the manual drive version of the stage and did not have the drive motors in place. The Z-stage drive motor extended upwards significantly further than the manual drive which created a risk of collision between the cryostat and the Z motor when the theta stage is rotated with the Z stage below a certain position. This risk was eliminated by designing a chain and sprocket drive stage that allowed the motor to be flipped upside down and mounted parallel to and behind the Z stage, clear of any chance of collision. While these particular issues were solvable, it could have been significantly worse.

With the sample chamber vacuum systems operational and the sample handling system in place, the secondary instruments (Cylindrical Mirror Analyzer, Channel Electron Analyzer

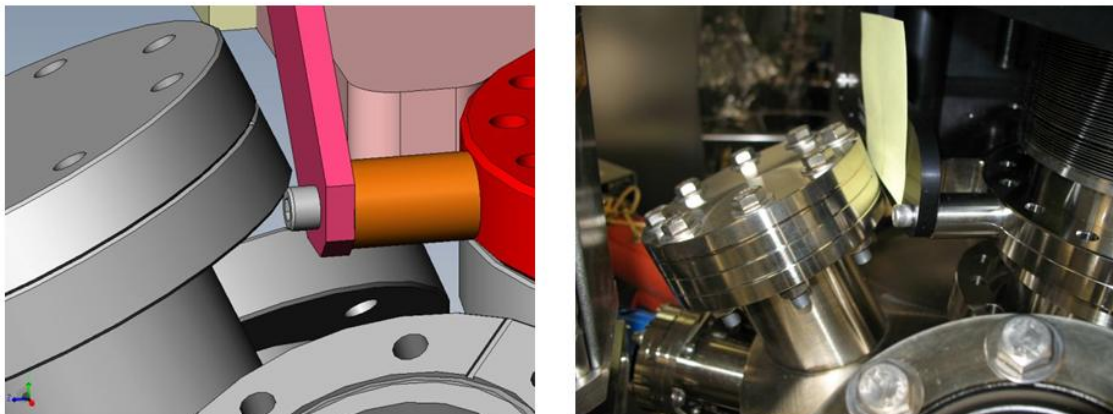


**Figure 5.14:** The CAD model of the X-Y-Z stage on the chamber (left) and the actual stage not quite in place due to interference between a flange and a bracket that differed from the CAD model supplied by the vendor.

and the Electron gun) could be installed and tested. This was completed in early 2009, and in March of that year the very first measurement from this endstation was recorded - elastically scattered electrons from the electron gun were observed using the CMA (Figure 5.15).

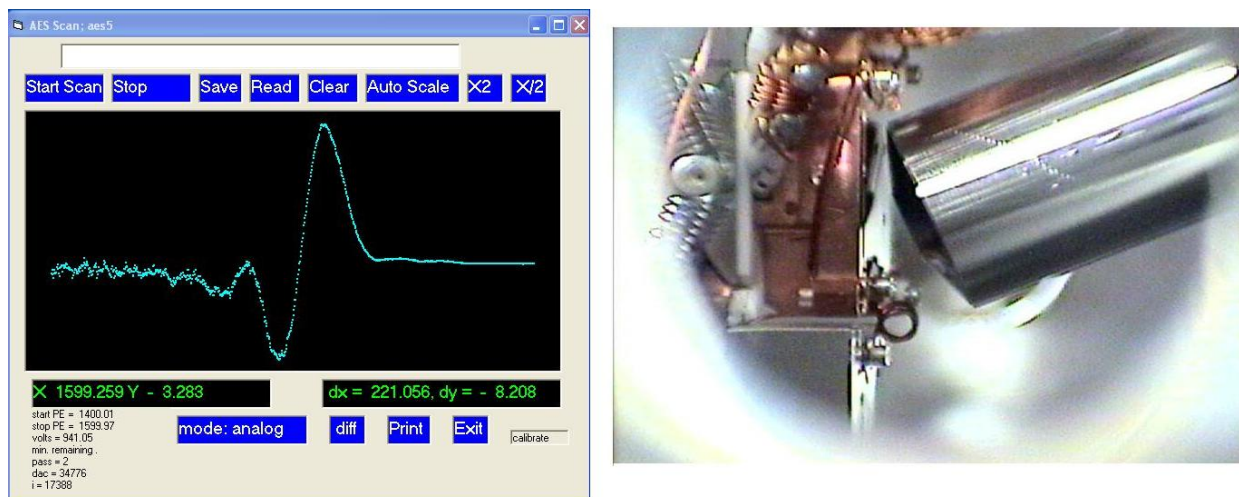


**Figure 5.15:** The first measurement from the endstation (left), An elastic peak from the electron gun observed with the CMA (right).

The final piece of hardware required in the sample chamber was the entrance slit for the spectrometer. The entrance slit piezo actuators were assembled and tested and then calibrated using an optical microscope with a micron accurate alignment stage prior to installing it in the chamber. It was installed shortly before the gratings were installed in September 2010. This was the first time it became evident that sufficient steps had not been taken dur-

ing the design process to allow for adequate alignment of key optical elements. Best efforts were made to align the rotatable flange that the entrance slit is mounted to by eye (see Figure 5.16), and work began on developing the alignment methods described in Section 5.3.1.

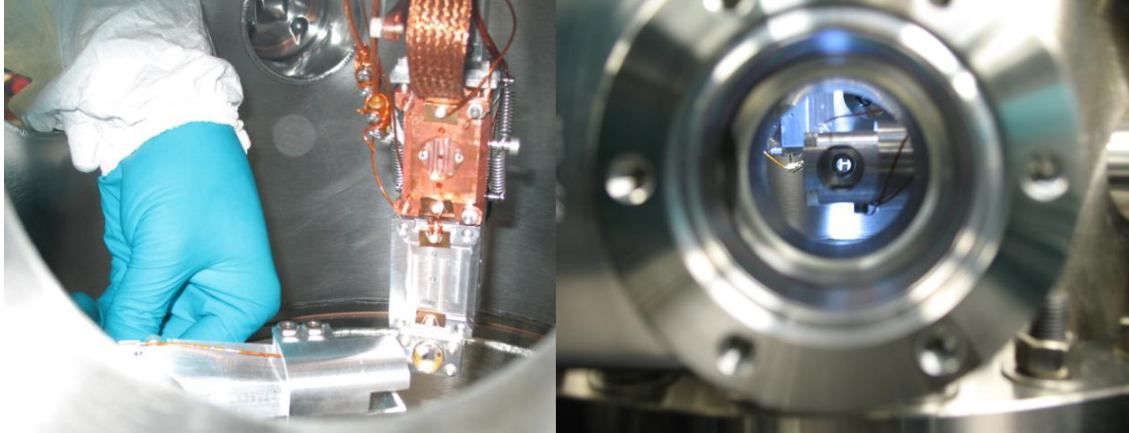


**Figure 5.16:** Installation of the entrance slit in the sample chamber (left). A view of the entrance slit from the perspective of the spectrometer (right).

With the entrance slit in place, the sample chamber assembly was complete. Before the spectrometer commissioning began, additional work was done using the systems in place including aligning the beamline post-focusing optics and test XAS measurements using the CEM for TFY and a picoammeter for TEY, some of which are discussed in Section 6.1.

### 5.2.3 Grating Chamber & Optics

The grating chamber was installed in September 2010, encountering only a few minor complications that were easily overcome. Since it had already become clear that alignment was going to be critical and challenging, and that the plan of the mechanical engineer to work from dimensional stack-ups was not adequate, work had begun on investigating options for surveying and aligning the gratings and the rest of the spectrometer as discussed in Section 5.3.1.

The gratings mount to two stacked platforms, four on the top level and two on the bottom. The gratings are secured using spring clips and a kinematic positioning system that provides accurate positioning while ensuring that no strain is placed on the delicate optical elements. Each grating has three detents on the back and two grooves along the front and back faces.

The platform has three holes with precision fabricated inserts (Figure 5.17). For each grating, one insert has a hole, one has a v-groove and one is a flat. A ball bearing sits in each detent on the grating and aligns to the insert. The hole provides a fixed alignment point, leaving three rotational degrees of freedom. The groove constrains two of the remaining degrees of freedom by creating a single axis of rotation about the line connecting the first two balls. The third ball rests on the flat which constrains the remaining degree of freedom, rigidly defining a single position and orientation relative to the grating platform. Spring clips are used to apply an even downward force to keep the gratings in contact with the kinematic mount.

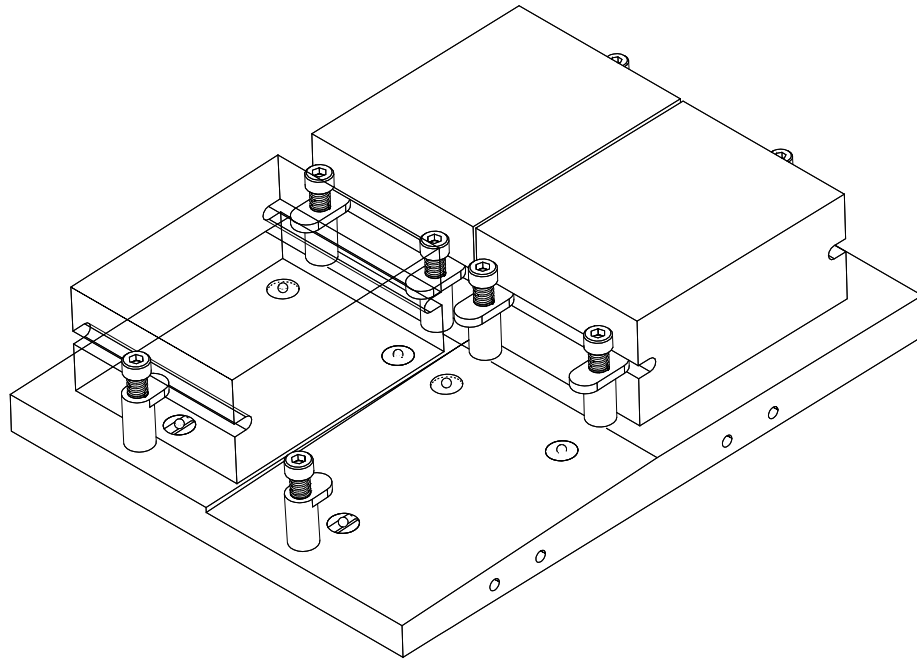


**Figure 5.17:** The top grating platform, the hidden/transparent gratings reveal the zero-stress kinematic mounting system used to secure the gratings.

Only one minor change was made to the grating mount design. After assessing the expected awkward and delicate procedure that would be required to install the gratings, a simple grating guard consisting of four long bolts was added to the top of the platform spacers (Figure 5.18). Careful use of Solidworks' dynamic collision detection was used to ensure that, with those guards in place, there was no possible position or angle that would

result the gratings coming into contact with the chamber wall while the platform was being installed on the hexapod. With this small change completed, the gratings were installed and the the platform was assembled. Considering the delicate nature of the gratings and the how challenging it can be to align the balls to the detents, the grating installation went remarkably smoothly (Figure 5.18).

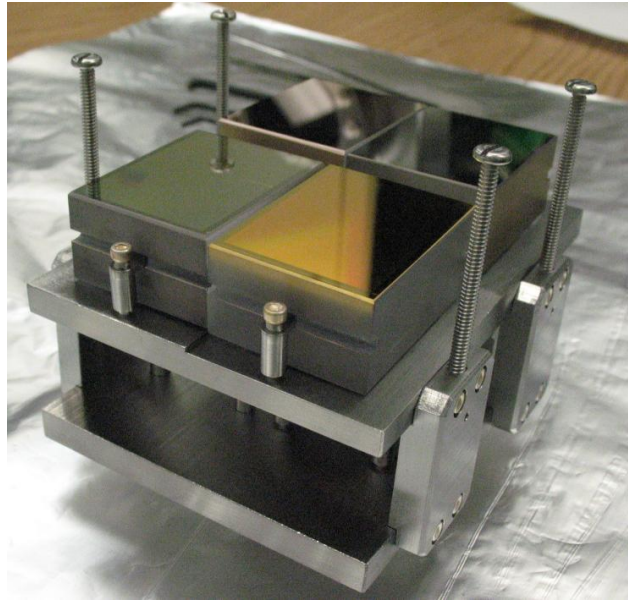


**Figure 5.18:** The five available gratings mounted and ready to be moved into the chamber. The four bolts retrofit as grating guards can be seen.

The proximity of the detector chamber axles on either side of the grating chamber meant that these side flanges could not be removed with the chamber in place to install the gratings. The grating mount had to be placed in the chamber with the chamber on a bench and then sealed and leak tested. The wire seal used on these odd-shaped side flanges was a bit tricky to achieve since no provision was made for securing or pre-tensioning the wire, but once a suitable technique was developed, it was completed successfully without too much trouble. With the chamber sealed and verified, it must then be carefully lifted into place on the endstation stand, with \$140,000 of custom precision optics sitting on the bottom of the chamber. This all must be complete before the detector chamber is in place due to the spool that extends from the detector chamber above the grating chamber. The delay in the delivery of the last two gratings resulted in a rather difficult decision because of this fact. As the delivery date slipped for a third time, the decision was made to proceed with the final

assembly of the endstation with the 4 accepted gratings that were on hand.

At this point, another design flaw was noticed. The custom flange that mounts to the hexapod and makes the seal to the grating bellows should have been specified with tapped bolt holes, since it was required to sit flush to the hexapod leaving no clearance for fasteners beneath it (Figure 5.19). The root of this issue was the fact that the fasteners were not included in the CAD model - doing so would have revealed the problem during the design stage. This problem was solved by having channels carefully machined in the bottom of the flange over each bolt hole with the width matched to that of 5/16" hex nut. The bolt could then be trapped in the recess, essentially creating tapped holes and studs to bolt the flanges together.

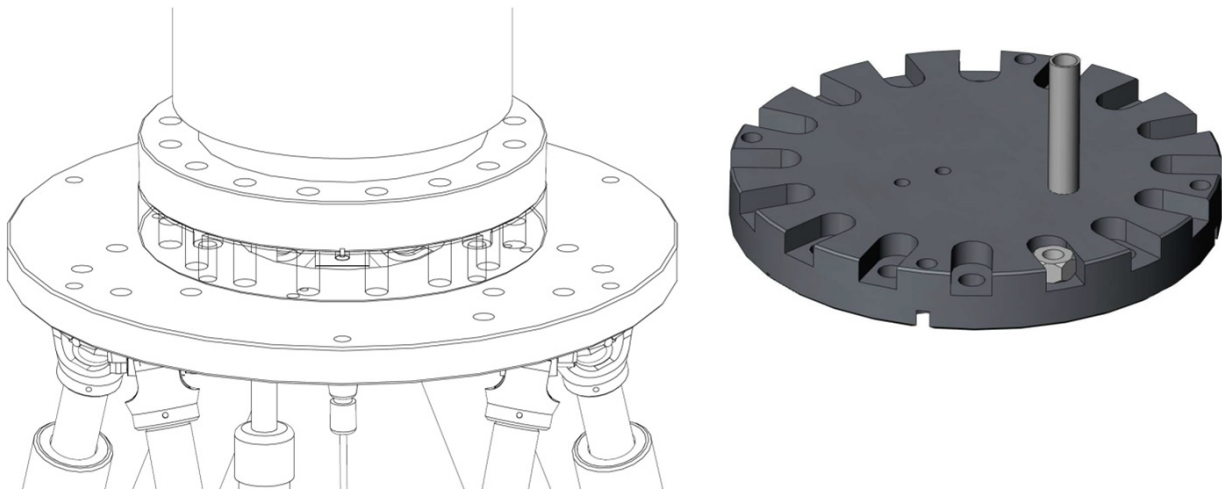


**Figure 5.19:** The original design for the gratings mounting flange shown in place (left). The flange should have been specified with tapped holes. A 3D model of the modification to the grating mounting flange required for it to mount as designed (right).

Once the grating chamber was in place, it was connected to the sample chamber fast valve and the lower 6" CF flange was removed to reveal the bottom of the grating mount sitting on the floor of the chamber. The grating mounting post was secured to the base of the grating mount and the bellows was then sealed to the flange. Next was the single most delicate step, and the reason for the grating guard mentioned above. With the base flange already mounted to the hexapod and the hexapod in its lowest position, the gratings and bellows were carefully lifted by hand while the hexapod was slid into place beneath it. The base of the grating mounting post was then secured to the base flange and the bellows was

sealed to the base flange.

Finally, the hexapod was bolted into place with an initial best-effort rough alignment. The cross brace for the counter-force bellows was installed and that bellows, once sealed and leak tested, was installed in place with a temporary support since it is unstable without internal vacuum. The counter force bellows could then be connected to the upper bellows by a Swagelok hose and aircraft cable.

With the grating chamber assembly complete, albeit with only four of six gratings installed (as well as the HRHEG which was hoped to be of use as a temporary HEG), the chamber was then pumped down and leak tested without issue. The only remaining connection was to the detector chamber bellows, once that chamber was installed.

#### **5.2.4 Detector Chamber**

More difficulties were encountered during the assembly and commissioning of the detector chamber and its integral components than in the rest of the project combined. As mentioned earlier, the troubles began during procurement with the delays in acquiring the required ballscrew and with the delivery of the chamber itself. It only became worse from there.

When the chamber did arrive, initial attempts to pump it down and verify its ability to hold vacuum were not successful. Helium leak tests revealed that the large 16.5" conflat flange at the back of the chamber was not air tight, exhibiting a leak rate greater than  $1 \times 10^{-6}$  Torr·L/s. Three attempts were made to seal the flange by replacing the copper gasket, and while the leak rate improved, it was still unacceptably high. The root of the problem appeared to be that the two flange faces were meeting before the knife edges bit into the copper gasket sufficiently to create a positive seal. After researching the issue, it was found that commercially available copper conflat gaskets are very uniform in thickness, with manufacturers quoting between 0.078" and 0.083". The gaskets that were being used had a thickness of 0.08", which made it unlikely that purchasing gaskets from another source would solve the problem. The obvious solution was to have thicker gaskets custom fabricated. The gasket manufacturers approached were not interested in producing a small custom run of gaskets, or were willing to do so for remarkably high price. One manufacturer did warn that the specific material properties of the OFHC copper used in Conflat gaskets is critical to

ensure a good seal and to avoid damage to the stainless steel knife edges. They claimed that they must be annealed after fabrication to ensure that they are soft enough.

Since there were no other options available, 1/8" (0.125") OFHC copper sheeting was ordered to be sent to a local fabricator for water-jet cutting to the required size. To ensure that the end result was going to work and not damage the knife edge and cause further problems, samples of a commercial gasket and the material used for the custom gasket were tested to compare their hardness by the UofS engineering labs. The results are tabulated in Table 5.3. Surprisingly, the surface of the commercial gasket was so badly oxidized that the hardness test could not be performed without first polishing it. The custom gasket material was in better shape. The results of the testing showed that the copper sheeting was actually softer than the commercial gasket. Using the custom made thicker gasket created a positive seal with leak rate below the detectable limit, solving the problem.

When the detector arrived in January 2008 and was inspected, it was found that even though the vendor had been consulted on our plan to use the detector in two orientations, and had even commended the idea of an asymmetric RAE, they did not point out that the support structure for the MCPs and top bias plate allowed for a clear line of sight to the detector surface at grazing incidence from only one direction (Figure 5.20 (left)). After much discussion and work with the vendor, a carefully designed and thoroughly reviewed mechanical modification to the detector was agreed upon. The detector was returned to the vendor for modification and the rebuilt detector was received in July that same year (Figure 5.20 (right)).

The detector translation mechanism was plagued with difficulties. The first issue encountered involved the rail and bearing system that the detector carriage moves on. The rails were sent to a specialized vendor to be coated with MoS<sub>2</sub>, a vacuum compatible dry film lubricant. Unfortunately, the thin-film that they ended up applying was rather thick and even had hardened drips in places. This thick film, in addition to the tighter than expected tolerances on the pillow block bearings, meant that the bearings would not move freely (or at all, in places) on the rails. After much time spent trying to reduce the thickness of the coating, and exploring the possibility of replacing the coated rails and using Teflon infused ceramic bearings, this design was abandoned. After some research, a vacuum compatible

Item	Polish	Load	d1	d2	HV
2 mm Gasket	As received	100 gf	n/a		
2 mm Gasket	1 um	100 gf	47.15	47.46	82.9
2 mm Gasket	1 um	100 gf	45.92	44.9	89.9
2 mm Gasket	1 um	100 gf	45.69	44.77	90.6
2 mm Gasket	1 um	200 gf	64.98	65.87	86.7
2 mm Gasket	1 um	200 gf	65.03	63.08	90.4
Average					88.1
1/8 inch sheet	As received	100 gf	45.18	46.7	87.9
1/8 inch sheet	As received	100 gf	44.48	44.47	93.7
1/8 inch sheet	As received	100 gf	45.4	47.13	86.7
1/8 inch sheet	As received	100 gf	46.49	46.01	86.6
1/8 inch sheet	As received	100 gf	47.19	44.59	88.1
Average					88.6
1/8 inch sheet	1 um	100 gf	45.81	45.9	88.2
1/8 inch sheet	1 um	100 gf	46.84	45.79	86.5
1/8 inch sheet	1 um	100 gf	45.8	46.57	86.9
1/8 inch sheet	1 um	200 gf	65.78	67.2	83.9
1/8 inch sheet	1 um	200 gf	66.81	65.19	85.1
Average					86.1
Reference(700 HV)	1 um	500 gf	36.13	36.54	702.3

**Table 5.3:** Vickers Hardness for commercial copper vacuum gaskets and the 1/8" OFHC copper plate purchased for custom made gaskets. The commercial gasket was too badly oxidized to obtain a measurement without polishing. Tests conducted on Mitutoyo MVK-H1 by the UofS engineering lab.

v-rail and roller bearing system was found and it was possible, with relatively little effort, to modify the chamber and carriage to accept it. Due to the length of the v-rail, this was also a custom order and custom adapters had to be fabricated to facilitate its installation, which led to a couple months additional delay.

With the new v-rail on hand, the detector carriage was finally assembled and installed in the vacuum chamber. Upon first pump down of the chamber, the next significant setback was discovered. The bellows that surround the ballscrew were ordered with an internal guidance system to support them and prevent them from riding on the ballscrew. Unfortunately the vendor allowed too much clearance for the ballscrew (the ID of the guidance rings was  $\sim 5$  mm

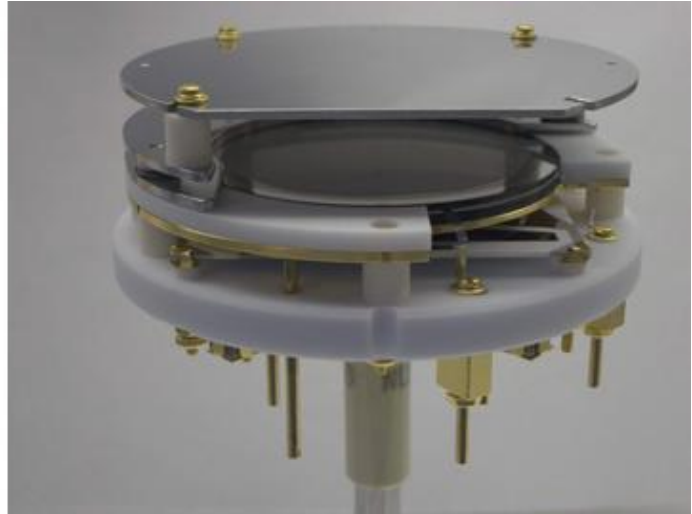
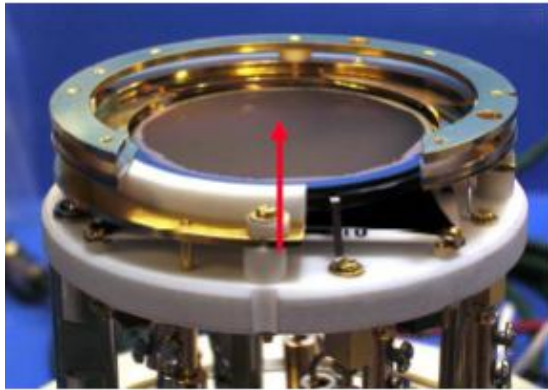


**Figure 5.20:** The Quantar MCP detector as received (left) and after returning it for modification to allow grazing incidence from two directions (right).

larger than the ballscrew) so that when the chamber was pumped down, the bellows snaked in an attempt to maximize their volume and clamped onto the ballscrew (Figure 5.21). Since these bellows were extremely expensive and took many months to deliver, replacing them was not a feasible option. The solution that was settled on was to modify the design of the end flanges that the bellows mount to in order to allow the inside of the bellows to be pumped down to rough vacuum levels which would eliminate the forces acting to distort them.

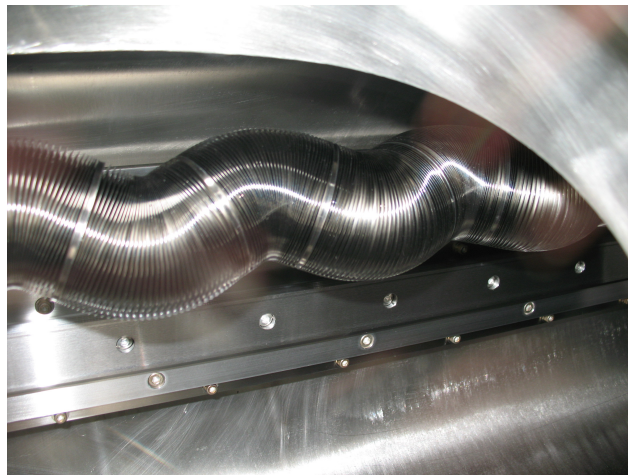


**Figure 5.21:** The long ballscrew isolation bellows in the detector chamber when the chamber is pumped down and full atmospheric pressure is present within the bellows. Constrained by the ballscrew within, the bellows seeks to maximize its internal volume by assuming the observed S shape.

This, again, required custom designed and fabricated parts that were created with the assistance of CLS engineering and they were fabricated by the CLS machine shop. The resulting parts worked better than hoped and good vacuum within the bellows was easily maintained. Because the bellows are no longer air filled, the preamplifier would no longer have cooling air circulated to it. The hope was that there would be sufficient conductive cooling to prevent overheating, since the preamplifier only consumes approximately 2 W of power. The support brace for the preamplifier box was redesigned to allow it to be sealed with air inside to allow some convection cooling and to maximize thermal contact between the box and the carriage. The wiring was modified to allow for the installation of a thermal diode to monitor the preamplifier temperature while in use.

Once the chamber could be safely pumped down without risking damage to the bellows, it was found that reaching UHV levels within the chamber was not possible. Using a residual gas analyzer it was determined that there were significant levels of heavy organic molecules within the chamber (Figure 5.22), contaminating the vacuum. After disassembling the chamber and investigating, it was found that the vacuum-ready v-rail bearings were the source of the problem. They are closed bearings that are lubricated with a unique vacuum compatible lubricant called Fromblin that should have been acceptable, yet further tests showed that they did appear to be the source of the heavy organics. Disassembling and opening one of the bearings revealed pockets of “gunk” within the axles (Figure 5.23).

After much discussion with the vendor, it was finally determined that they rinsed the bearings with kerosene and let them air dry as part of their cleaning process, and the gunk is likely residue from this rinse that worked its way into the axel through the vented screw. Since kerosene is comprised of a number of different high mass organic molecules, this explains the residual gas observations and why it was not possible to narrow down a culprit compound based on the RGA measurements. Because of the Fromblin, which is insoluble in nearly anything except Freon, it was not practical to safely clean the bearings and arrangements were made with the vendor to replace them with unlubricated open bearings that can be properly prepared for UHV use once here.

With the new bearings on the way, the chamber was opened and scrubbed down by hand using acetone, methanol and isopropanol to remove as much of the contamination as possible

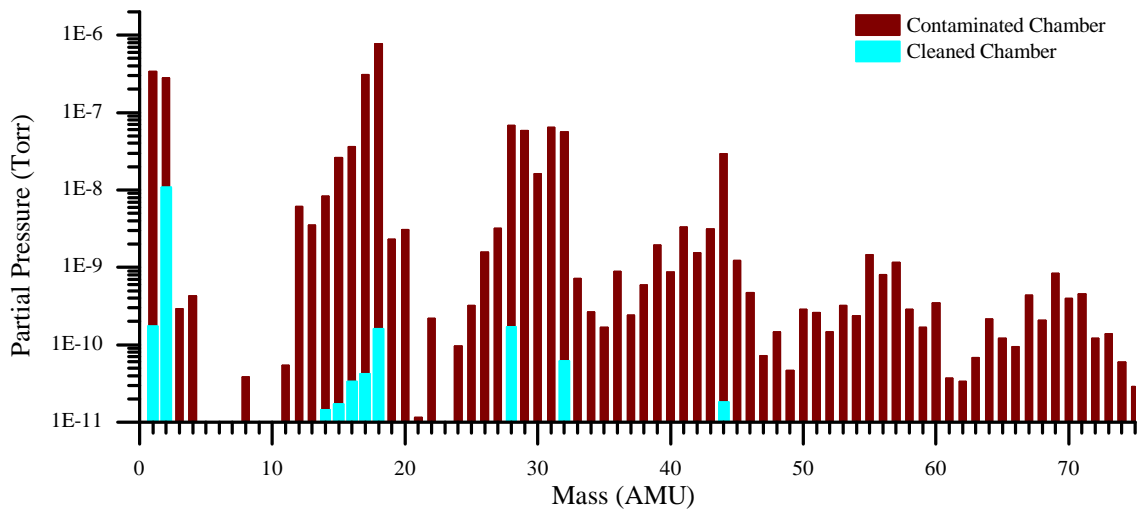


**Figure 5.22:** The RGA measurements of the detector chamber after pumping down with the kerosene contaminated bearings inside, and following hand cleaning and an extended high temperature bakeout.

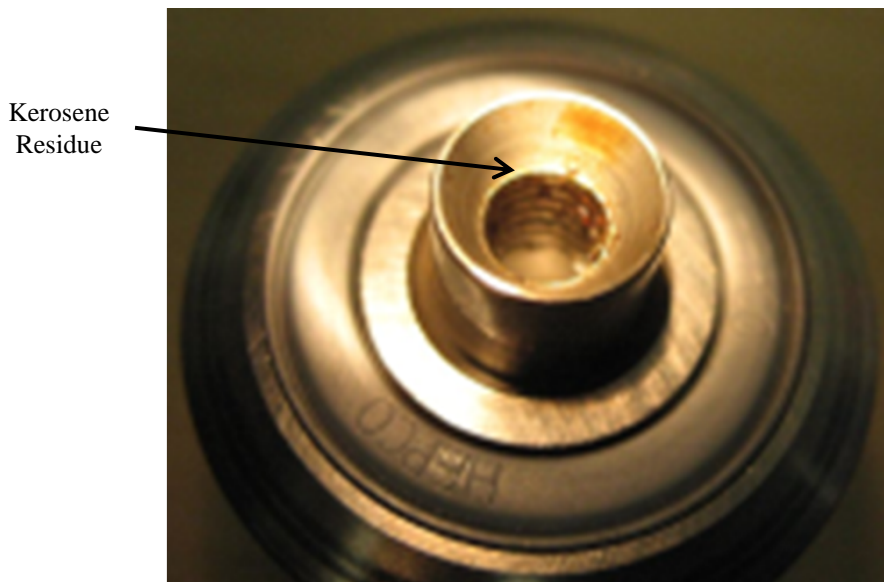


**Figure 5.23:** An image showing what was found in the axle bolt hole upon disassembling a V-rail bearing that had been supplied as “vacuum-ready”.

since facilities to properly UHV clean a chamber of that size were not available. The chamber was then sealed, pumped down, and baked at high temperatures while empty for 3 weeks. This resulted in a nearly perfect UHV ready chamber to proceed with the installation (Figure 5.22).

As discussed earlier, the preamplifier that needs to be as close to the detector as possible to maintain resolution was to be wire sealed into an air-box within the detector chamber and mounted right behind the detector. In June 2009, it was found that this box was poorly designed in that the number and size of the flange bolts were insufficient to properly compress the wire and create a seal. Fellow group member Mark Boots ambitiously suggested that the discrete 1980s electronics of the preamplifier could be miniaturized into a smaller form factor using surface mount devices, based on the complete schematics included with the detector documentation. This would allow it to be mounted inside a standard 3.38" CF flange tee, eliminating the problematic wire seal. With the help of another group member, Robert Green, the required circuit boards were successfully fabricated (Figure 5.24) while work on the required mechanical modifications to mount it into the new tee, mount the tee in the detector chamber and integrate it into the system was completed. This was complete and ready to install by November 2009. The detector carriage modified to accept the new preamplifier can be seen in Figure 5.25.

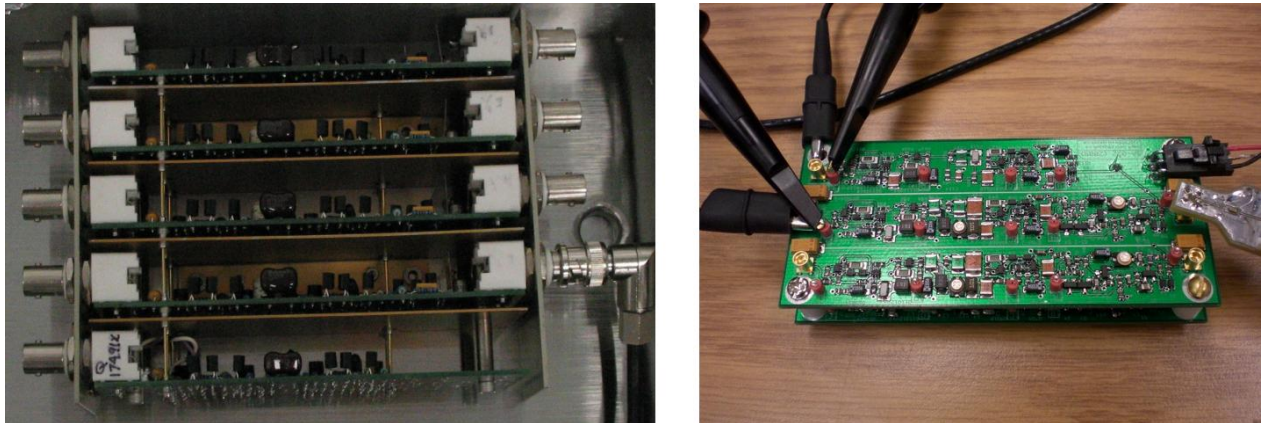


**Figure 5.24:** The original preamplifier (left) and miniaturized SMD based preamplifier (right) laid out and fabricated by Mark Boots and Robert Green.

Unfortunately, this was not the only change to the detector carriage that would be needed. As the installation continued, several major flaws were discovered with the detector mount

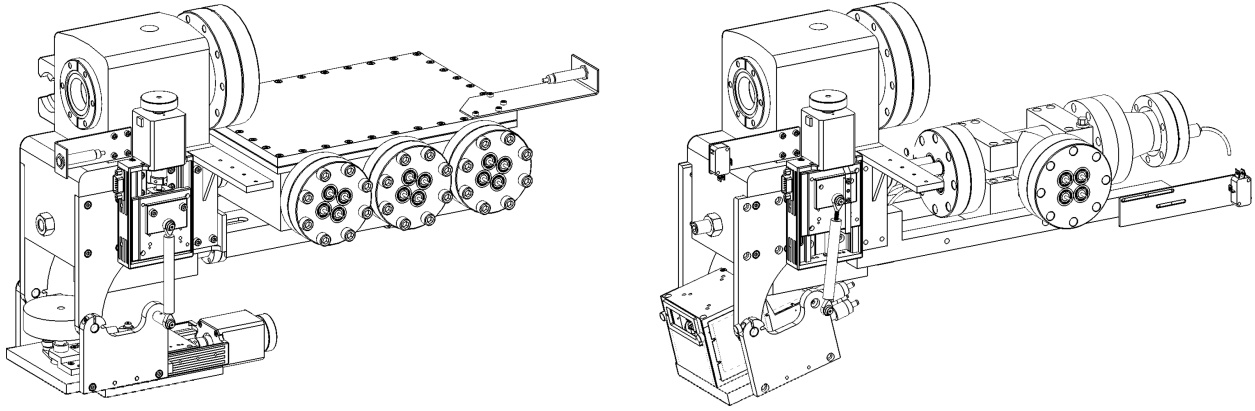


**Figure 5.25:** The original detector and preamplifier carriage design(left) and the final as-built assembly(right). This assembly underwent more dramatic changes during assembly and commissioning than any other part of the of the spectrometer.

itself. These resulted from a combination of poor engineering and incomplete modelling. The detector was mounted on a shaft and bushing, to allow for the desired 90 degree rotation, which did not have tight enough tolerances to prevent wobbling and the shaft did not mount securely to the detector. The cam that rotated the detector left no space for the electrical connections to the detector, because they were not included in the CAD model. The cam was also able to reach top-dead-center, creating the possibility of a stall. These issues were resolved by redesigning the carriage to more securely mount the detector to a shaft that was press fit into a pair of bearings instead of a bushing, and by flipping the motion stage to move the cam below the mounting plate leaving room for the electrical connections (Figure 5.26).

Completing this design, procuring and fabricating the required parts took until February 2010. Following this, and a further minor delay awaiting new in-vacuum cabling and connectors that were not specified properly on the bill of materials, the detector chamber was completely assembled, wired, sealed and vacuum tested, and ready to install on the beam-line by June 2010. As mentioned before, once the detector chamber is installed the grating chamber is nearly inaccessible so the installation of the detector chamber was held until the last two gratings were available. By August 2010 it was clear that the vendor would not be able to deliver the last two gratings before the first quarter of 2011 at the earliest. Being sure there were more problems yet to be encounter, the decision was made to proceed with the assembly with the gratings on hand, even though this would create difficulties with the

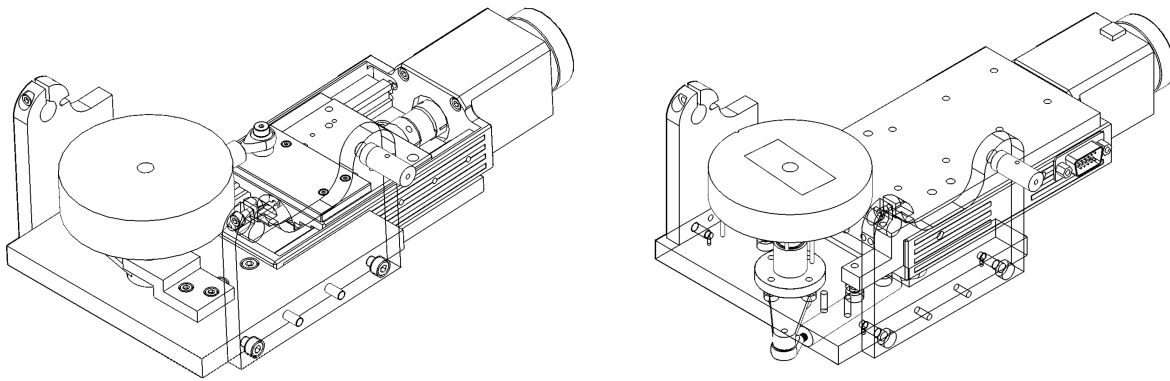


**Figure 5.26:** The original detector mount design had several issue with stability and wiring (left). Significant changes were required to resolve these issues (right).

installation of the remaining gratings in the future.



**Figure 5.27:** The detector chamber was installed onto the main frame in October of 2010 with the extremely skilled assistance of CLS mechanical technicians Noel Craddock(left) and Ed Unrau(right).

The detector chamber was installed in October 2010, which went remarkably smoothly. Once this was in place, it provided the needed leverage with CLS controls and management

to have resources allocated to completion of the motor and control systems. Even still, it took until February 2011 to get the key motor controls in place that were needed to begin commissioning. The delay did provide time to revamp the motion systems to include encoders and limit switches on all axes which resulted in a much smoother initial alignment and will provide much more reliable and repeatable operation.

## 5.3 Commissioning

With the detector chamber installed and key control systems in place, the spectrometer assembly was essentially complete and the commissioning process could begin. This involved initial alignment and calibration, initial testing, optical calibration refinement, and benchmark measurements. However, since this phase of the project did not go any more smoothly than the previous work, there were numerous setbacks and design refinements along the way.

### 5.3.1 Initial Alignment

The initial plan for aligning the system was to rely on the mechanical alignment and dimensions from the CAD model to determine the initial position of the optical components, and to refine the alignment from that point optically once the system was operational. During the course of assembly it became clear that none of the components were designed or fabricated with the alignment features that would be needed for the theoretical CAD model to provide a sufficiently accurate starting point. Mechanical alignment systems are often used to ensure accurate assembly of such systems, but very careful consideration must be given to tolerances, fabrication error, clearances, and alignment guides<sup>61</sup>, and this had not been done. Furthermore, because mechanical alignment was thought to be sufficient, it was deemed unnecessary to consider surveying during the design process. As a result, most key optical elements were not accessible by traditional survey techniques and fiducial marks to reference them to were not built into the system.

With the assistance of the CLS technical staff, ways were found to align the rotation plane of the detector chamber with the optical axis of the system using traditional survey techniques and a laser tracker. The height of the optical axis of the endstation was adjusted relative to

the beam height using similar techniques by using the extensive survey monument system maintained by the CLS. This, theoretically, placed the source point for the spectrometer at the desired location and would allow the detector to move properly relative to it. However, aligning the gratings within this system and knowing the initial position of the detector relative to them required a less traditional approach.

Fortunately, the CLS owns a FaroArm, a micron accurate encoder driven inverse kinematic arm (Figure 5.28), and when its potential was realized it was used as a means to extract the required information for alignment. This turned out to be a painstaking task requiring much ingenuity, but in the end it provided exactly what was needed. Reference points for all three optical elements in the system - the entrance slit, the gratings and the detector - were located by opening all three chambers for the briefest possible time and using the FaroArm probe to measure their true locations within its own coordinate frame. More importantly, the position and orientation of the hexapod was accurately measured so that its native coordinate system could be referenced to the survey coordinate frame. Without access to a well fiducialized absolute coordinate system, much care was taken to find a placement for the FaroArm such that all required measurements could be made within one reference frame. Obtaining precise measurements of delicate components that were not easily accessible through small vacuum chamber flanges was challenging, but it turned out to be possible.

The data collected using the FaroArm (Figure 5.28) was imported into the mechanical CAD package used to design the spectrometer along with models of the key optical components of the system. A new as-built model was created using the FaroArm data to align those key components to within a few microns of their real world positions. From this model, the parameters required to calibrated the motion system were extracted.

### **5.3.2 Motion Modeling and Control Calibration**

The most basic goal of the spectrometer motion control system is the ability to choose a grating and energy and have the control system position the spectrometer components correctly to collect an image centered on that energy and properly in focused. The relationships required to accomplish this are the diffraction equations derived in Section 2.3, specifically:

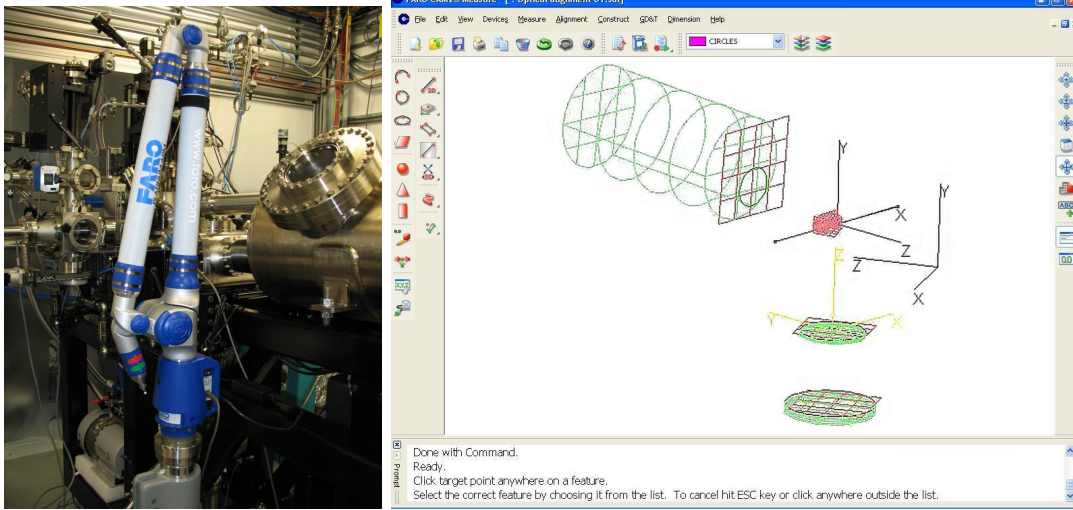


**Figure 5.28:** The FaroArm (left) and the precision survey data gathered with it to align the optical components and calibrate the spectrometer positioning model (right).

$$\beta = \sin^{-1}\left(\frac{Nk\lambda}{\sin \alpha}\right) \quad \text{and} \quad r' = R \cos \beta \quad (2.18)$$

These equations allow the calculation of the angle that the detector should be at relative to the grating normal ( $\beta$ ) and the focal length ( $r'$ ), knowing the incidence angle ( $\alpha$ ), grating radius and line density ( $R, N$ ) and the desired diffraction order ( $k$ ), which are related by:

$$R = \frac{r}{\cos \alpha} \quad (2.16)$$

and while critical to the spectrometer, this relation does not play a role in the operational positioning of the system. Ideally, this relationship was used to determine the fixed incidence angle ( $\alpha$ ) and entrance arm ( $r$ ) for the specified grating radius, and these parameters become constants in operation. These are simple relationships, but the trick comes in relating these values to the real world motor positions needed to position the physical system.

## The Model

In developing the spectrometer control software (discussed in Section 5.4), Mark Boots incorporated an extensive 3D mechanical model of the spectrometer that could be used to

determine the required motor positions for any desired spectrometer configuration, taking the real world kinematics of the system into account. Included within this model was the ability to compensate for known misalignments in the system by, for example, analytically determining the ideal grating position relative to the sample to compensate for the deviation from ideal grating radius, as per Equation 2.16. While an excellent idea, in theory, the problem with this approach turned out to be the large number of degrees of freedom in the model. More information on the initial positions and alignment of the key components would have been required for it to work properly than the ad-hoc survey method that was developed could provide. Initial measurements were completed using this model, but it was found that absolute calibration of the system required too many fudge-factors, and the complexity became more of a liability than the flexibility and power of the approach could justify.

This calibration system was replaced with a much simpler empirical model that was developed by carefully considering the degrees of freedom in the system, and the potential mis-alignments that would matter most. Being able to align the gratings with six degrees of freedom in-situ is a remarkable advantage, but adds dramatic complexity to any model that attempts to incorporate it. Instead, some of the key optical parameters, such as the entrance arm length ( $r$ ), incidence angle ( $\alpha$ ) and grating spacial alignment were taken as correct and ideal within this new model, and best efforts were made to optimize them using survey data and beam-based optical alignment before calibration.

## **Optical Alignment**

The grating alignment was determined and optimized with a series of scans across each degree of freedom. These included several 2D matrix scans since it was found that different orientation changes can have similar affects on the image, and image degradation from one motion can sometimes be compensated for my another. For example, a 2 degree yaw (rotation about the grating normal) will dramatically reduce the resolution of the image. However, when combined with at 0.2 degree roll (rotation about the incident direction), the image obtained is almost indistinguishable from the original position (Figure 5.29).

After many hours of exploring the effects on the image and resolution of every combination of motions, the end result was that, with the exception of the incidence angle, the system was

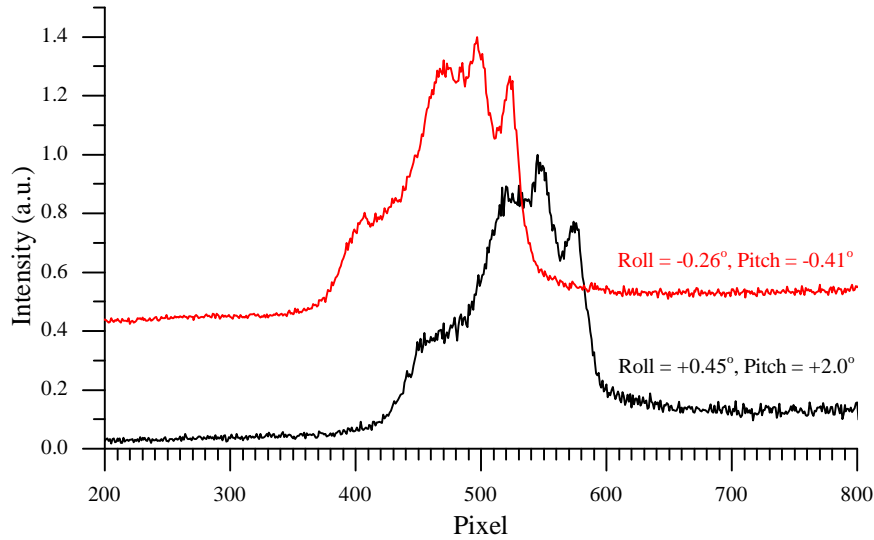


**Figure 5.29:** Two *h*-BN N emission spectra extracted from a 2D matrix of grating angle alignment scans. The edges of the scan matrix, with extreme yaw or roll values, show significant loss of resolution. There are, however, extreme combinations, such as these two, with large yaw and roll values that are essentially the same.

less sensitive to grating alignment than was expected. Calculations were performed during the optical design to explore the effects of misalignment and fabrication errors, but they were not exhaustive. The incidence angle was considered, but grating yaw and roll were not. Grating position along the beam path was considered, but not along the other two axes<sup>1</sup>. The calculations performed at that time suggested that a significant loss in resolving power would be expected for incidence angle ( $\alpha$ ) misalignments as small as 0.025 degrees and entrance arm ( $r'$ ) misalignments as small as 3 mm.

Experience with aligning this system tends to support those calculations. The actual angle of the installed gratings could not be directly measured with the FaroArm due to the limited access to the grating chamber, and the angles that were measured were not terribly accurate due to the short moment arm between the measurement points that could be reached. This made the incidence angle alignment the key to achieving well resolved spectra. The values eventually settled on for the other two rotational directions were very close to the surveyed values. They are less sensitive to small changes and larger moment arms were available for those survey measurements. The predicted 3 mm sensitivity for the entrance arm is actually quite large as compared to the micron level accuracy of the survey values. The grating

translational alignments used were taken directly from the survey data, and attempts to further refine them proved fruitless.

The incidence angles were refined by completing a series of scans synchronizing the grating tilt to the detector chamber rotation, so that a well known emission edge could be repeatedly measured with different grating incidence angles. If the focal length is taken to be correct, then the best focused of these scans should be the one with the correct incidence angle on the grating.

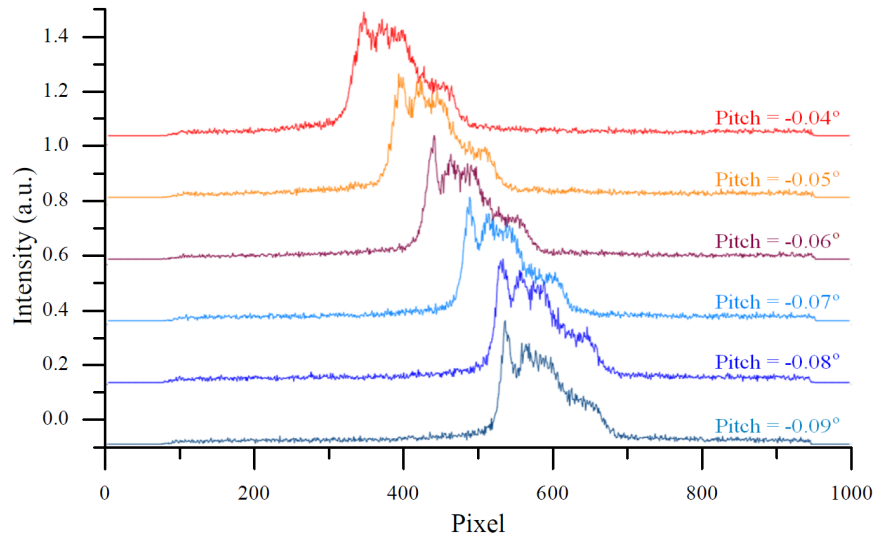


**Figure 5.30:** A series of scans with different grating incidence angles. The grating pitch was changed by 0.01 degrees between each scan. The drastic reduction in the peak/valley ratio shows how a change of only 0.05 degrees can dramatically impact the resolution.

## Calibration

In the simplified motion control model, the hexapod move required to properly place each grating at the optical origin is taken from the survey data, and can be fine tuned later. The initial position of the detector relative to the grating was among the more accurately surveyed values, and the drive and encoder system used for that motion is direct-drive and extremely accurate. Calibrating the home position of the detector translation motor's encoder relative to the optical origin by using the survey data allows the encoder feedback to be taken as the

true optical focal length. This leaves only the angular position of the detector chamber to be calibrated.

The relationship between the detector chamber lift stage and the diffraction angle ( $\beta$ ) is far from trivial. First, while the incidence angle onto the grating has been taken as correct after optically aligning it, the true positional relation between the source (slit/beam spot) and the grating is difficult to measure and not known accurately. Thus, the actual angle of the grating and height of the beam are not known, just the fact that the beam is striking the grating at the correct angle. What this amounts to is that the  $\beta$  angle that corresponds to the lift stage home position is unknown. Steps have since been taken to use a specially designed sample plate that has been aligned to the beam to determine the true beam position relative to the gratings and this method will be used when the system is resurveyed after the last two gratings are installed. This should make the optical alignment much smoother by giving better initial values for  $\alpha$  and  $\beta$ .

The second issue is that the double-hinge kinematics of the lift stage produce a rather complicated geometric relationship between the lift height and the frame angle. However, since the angular range of motion is rather small, and the lift arm and frame remain near perpendicular during the whole range of travel, the small-angle approximation would suggest a roughly linear relationship between the two. Being slightly more rigorous, the CAD model was used to plot a series of height/angle points (Figure 5.31) and while the relationship is very nearly linear, a quadratic gives a near perfect fit for very little additional computational overhead. The same approach was used to arrive at an equation for the detector tilt angle in relation to the in-vacuum motor stage linear position.

Finally, there was no practical way to determine the angular relationship between the frame/chamber axis and the line of motion of the detector. If the line of motion of the detector does not pass through the center of rotation of the frame, then detector translation will change the effective detector angle. To account for this, and deal with the unknown initial frame angle relative to the grating, an equation with two fit parameters was devised. An attempt was made to geometrically relate the two fit parameters to the two unknowns in the hopes that physically meaningful values would emerge during the fitting process. The frame angle  $\theta$  was fit as:

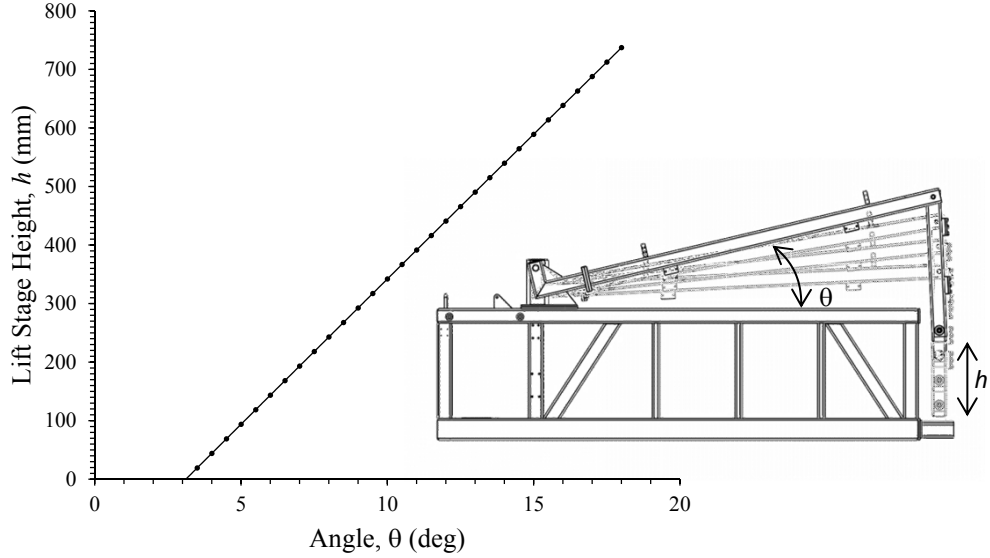


**Figure 5.31:** The relationship between the motor position and the frame angle is very nearly linear, as the small-angle approximation would suggest.

$$\theta = (90 - \beta) + \theta_f + \arctan\left(\frac{y_f}{r'}\right) \quad (5.1)$$

where  $\beta$  is the desired diffraction angle,  $r'$  is the detector translation position,  $\theta_f$  is the home angle fit parameter and  $y_f$  is the detector height offset. Once fit, this will give the frame angle needed to achieve the desired diffraction angle alignment. Combined with the quadratic function fit to relate the frame angle to the lift height, everything needed to command the motion control system to the correct position is available.

After aligning the sensitive parameters optical (see Section 5.3.4), if a known emission line is centered on the detector then the effective  $\beta$  for that position is known. By repeating this process for two to three emission lines within the energy range of each grating, a least squares fit can be used to determine values for  $\theta_f$  and  $y_f$ . Interestingly, as hoped, there was a grouping of fit  $y_f$  values around 0.7 mm, *suggesting* that there is physical merit to the assignment of fit parameters and that the alignment of the system is surprisingly close to ideal.

### 5.3.3 Initial Testing

Once the motors and controllers were in place, the survey plan described in detail in Section 5.3.1 was implemented. Before those measurements could be taken, however, it became clear that the lift system for the detector chamber was horribly flawed. There were several combinations of actions that could lead to the lift ballscrew back driving and the 1,100 kg chamber falling. Such design oversights are not uncommon and are typically referred to as ‘vertical load mistakes’<sup>62</sup>. Luckily these flaws were discovered with the chamber lifted only a few millimeters for testing and not at its full height of nearly a meter. By mid-February 2011, a number of drive and controls system changes had been implemented to insure that no combination of inputs or system failures could result in the chamber dropping. These included a failsafe break, changes to the motor timing, independent wiring of the drive break to ensure near-instantaneous activation and finally a closed circuit passive hydraulic cylinder designed to limit the velocity of the chamber and bring it down safely, even in the event of a catastrophic drive failure. Due to the magnitude to the potential consequences of such a failure, the CLS health and safety department reviewed the system after these changes were made and determined that operation of the system could not be approved until personnel protection shielding was in place. This resulted in a further delay that prevented the use of most of the beamtime available in the first quarter of 2011.

By implementing temporary shielding and rigorous administrative controls, measurements were attempted during a few remaining days of beamtime towards the end of February. It was at this point that numerous problems with noise swamping the detector signal were discovered. The major culprits were identified within a couple of days - the ion pumps were generating enough stray ions to create very high background count rates, and having any of the motors on or in the detector chamber even powered on (or in some cases just being plugged in) generated enough electrical noise in the chamber to create false counts. By painstakingly securing and powering off all motors after every movement, and carefully maintaining the vacuum in the chamber by working with the detector in short shifts while the pumps were shut down, a first image from the spectrometer was collected on March 1, 2011 (Figure 5.32).

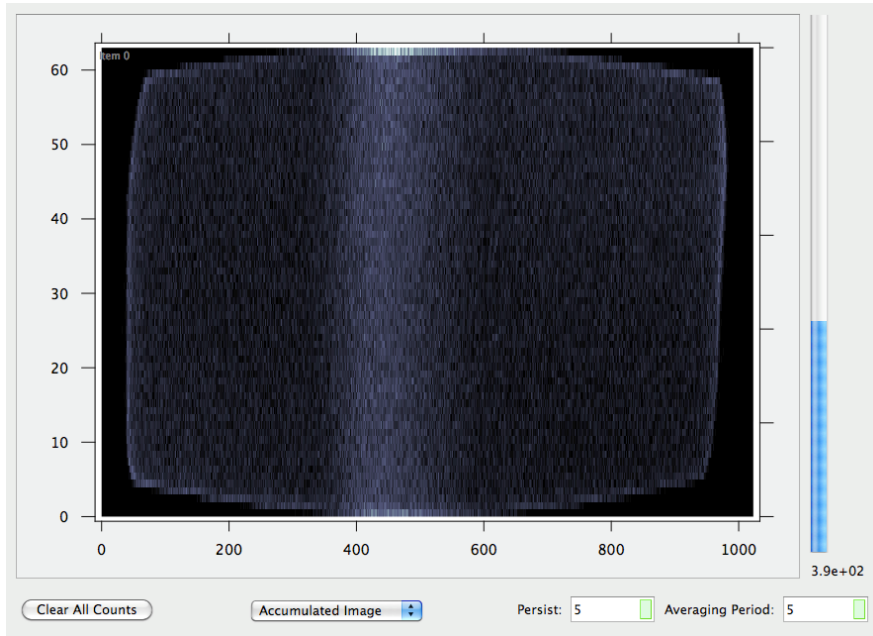


**Figure 5.32:** First image from the spectrometer - March 1, 2011. Experience now suggests that this was in fact a second order emission line being observed from the first order focal position, explaining the absence of any features.

While it was believed at the time that the lack of spectral features was due to the large entrance slit size needed to ensure a bright signal to look for at first, and that it was likely slightly out of focus, it was later discovered that there was a small mathematical error in the spectrometer positioning model and, by chance, the machine had aligned to a second order diffraction peak but at the correct focal length for first order emission. Regardless, it was definitely an emission line! Unfortunately, the next day it was found that the noise levels generated by a moving motor attached to the system (Figure 5.33) were sufficient to burn out a channel of the in-vacuum pre-amplifier, bring commissioning to an end for a period.

It took another several months to diagnose the damage to the preamplifier circuitry, find ways to guard against it in the future, and acquire the parts required for the repair. At the same time, efforts began to track down and eliminate enough of the noise sources that commissioning could proceed safely. A passive Non-Evaporative Getter (NEG) pump was ordered to maintain the vacuum without ion pumps.

It would be impossible to cover, in any detail, the entire process of identifying, understanding and eliminating all of the noise sources that were affecting the detector. The discriminator can tolerate a background noise of, at most, 15 mV from the preamplifier. The noise ob-

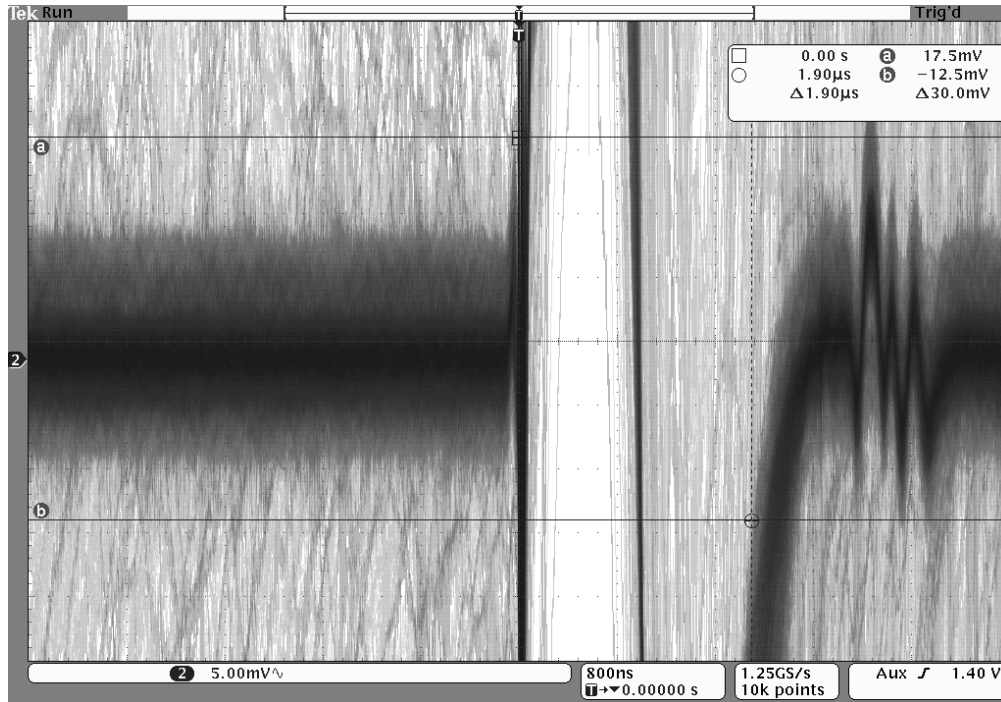


**Figure 5.33:** Output from the preamplifier when the translation motor attached to the chamber was moved. The relatively high background noise level to the left is followed by a massive pulse that extends well beyond the display and decays as a damped sine wave to the right.

served was often several times that level and under certain circumstances the output from the preamplifier was as high as 30 V peak-to-peak, the full range of the preamplifiers supply voltage. It took many weeks of measurement and discussion to find most of the sources and to try to understand how and why they were impacting the system the way they were.

Two main issues complicated the process. First, there were numerous sources of noise acting simultaneously, such that if one source was removed it may not even be noticed in the output signal until other sources were eliminated first. Second, beamlines and synchrotrons are complicated systems with *many* potential noise sources - most of which can not be powered down without careful planning and forethought, if at all. Despite this, numerous noise sources were identified including motors on and in the detector chamber (even when not moving - Figure 5.34), motors on the beamline, ground noise that appeared to be systemic throughout the CLS, RF noise from any one of a number of sources coupling into the chamber via open circuited in-vacuum limit switches (Figure 5.35), and ions generated by gauges in the vacuum system, just to name a few.

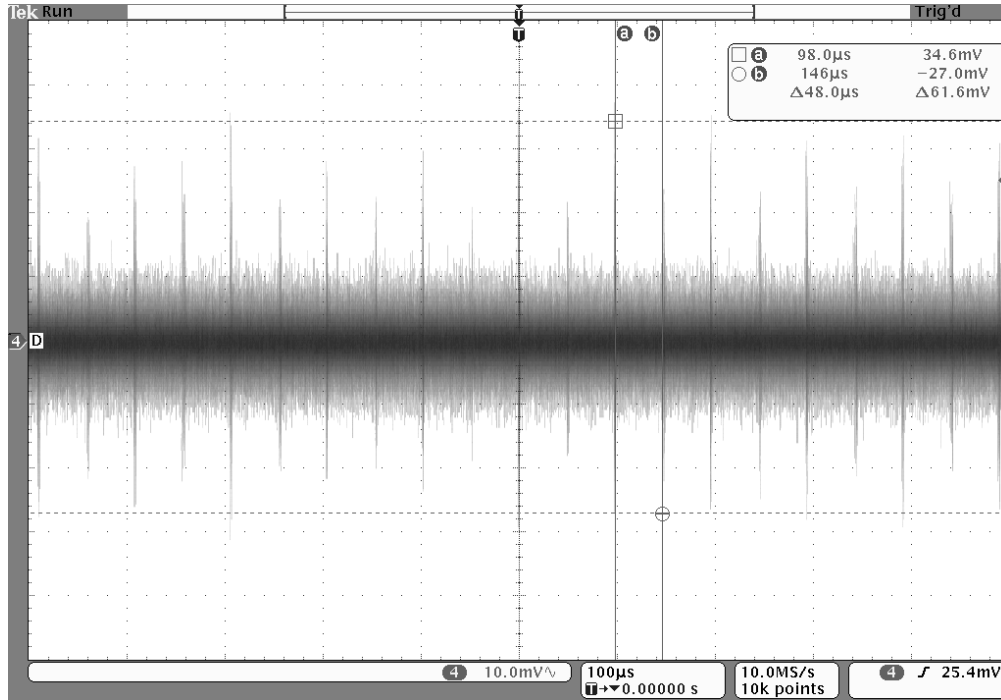


**Figure 5.34:** Noise spikes seen on the preamplifier output when the airside translation motor was connected to its driver. The tolerable noise level is 15 mV. Oscilloscope capture,  $\text{mV}/\mu\text{s}$ .

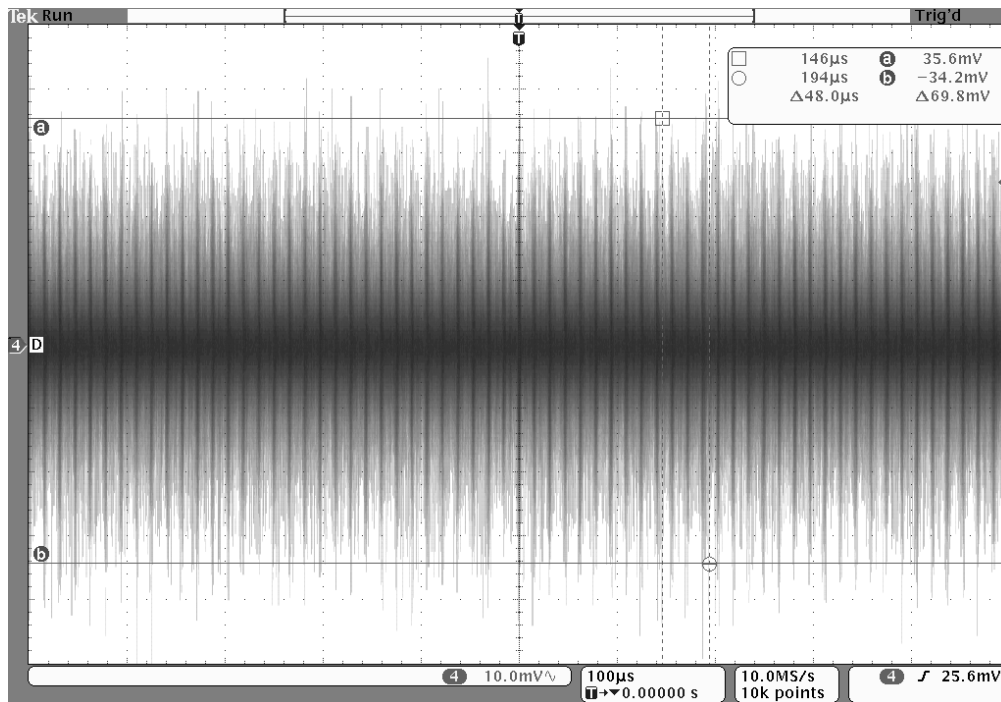


**Figure 5.35:** RF noise seen on the preamplifier output when the air-side cables for in-vacuum limit switches were connected to the chamber but open circuited, acting as antennae. Oscilloscope capture,  $\text{mV}/\mu\text{s}$ .

Many of these issues could be addressed with relatively minor changes to the system. The troublesome hot cathode vacuum gauge was replaced with a cold cathode gauge - which was better but still an issue until it was moved onto a flange connected to the grating chamber with no line of sight to the detector. The AC motor drivers were replaced with DC drivers and separate regulated power supplies that had true “off” modes instead of only low-current holding modes, and the cable paths were rerouted to reduce signal coupling. Attempts were also made to improve the system grounding to eliminate potential ground loops.

Despite these efforts, not all noise sources could be eliminated without a dramatic redesign and there was still too much noise present to operate safely or effectively. One working theory was that the noise was coupling into the high voltage bias lines, and the resulting voltage fluctuations were creating small current pulses in the detector that emulated real counts. This was supported by the fact that many of the noise sources were only visible when the detector high voltage was applied, and were not seen with only the preamplifier on and the detector unbiased. The solution that resulted was a rather impressive vacuum compatible filter circuit board, designed and hand-fabricated to filter the detector bias voltage right at the detector (Figure 5.36). A custom PCB board was designed to fit around the existing detector rotation stage, and was fabricated at the CLS out of a fiber-reinforced PTFE laminate designed for high frequency PCBs that happens to have good vacuum compatibility.

Sadly, this high voltage filter did not eliminate the noise problems and the situation went from bad to worse. Despite best efforts, the moisture sensitive detector may have seen too much time in air, with the numerous times the chamber had to be vented to diagnose and repair various problems, and while rewiring the chamber. In late July the system was brought back up, and about a month was spent struggling with the remaining noise sources and trying to understand some very erratic behavior of the detector. While some of these problems were solved, the erratic behavior continued to develop until it became clear that something was seriously wrong with the detector itself. Intermittent massive current pulse were observed from the detector, one of which damaged a preamplifier channel limiting our ability to further diagnose the problem (Figure 5.37).

The detector was returned to the vendor at the beginning of August, where several issues were found. The channel plates were damaged, likely by moisture, which can cause buckling

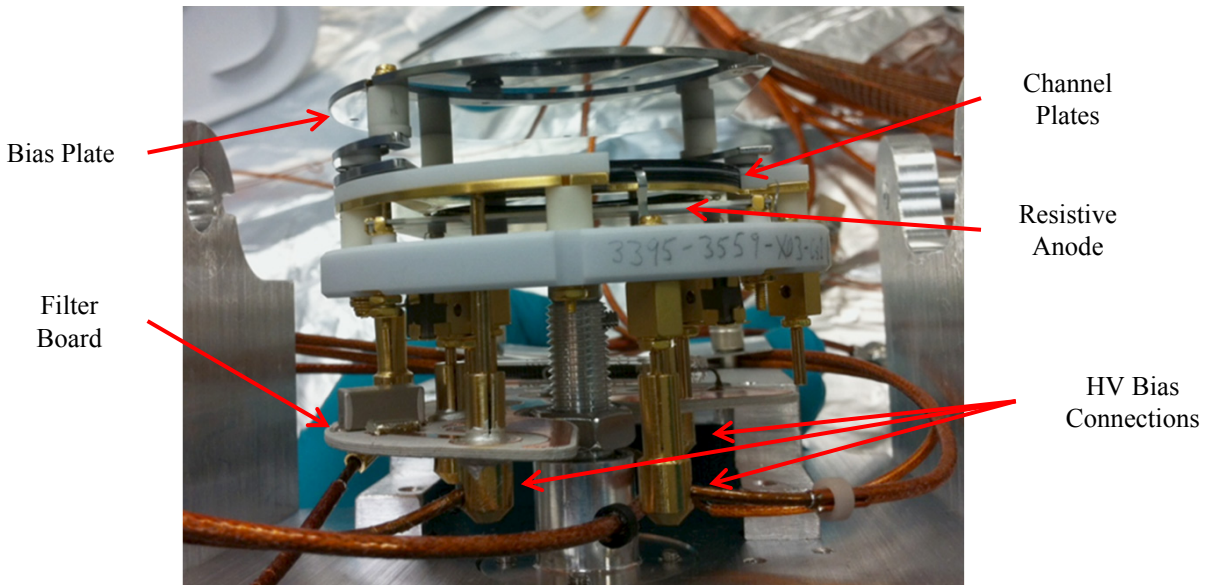


**Figure 5.36:** The detector mounted to the carriage with the rotation stage in place. The in-vacuum filter circuit board can be seen below the detector.

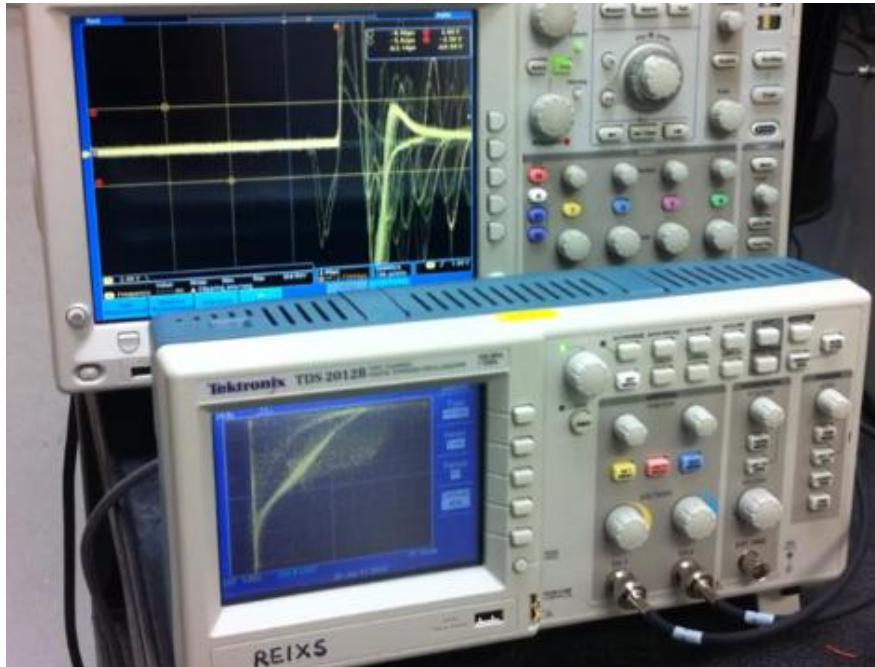


**Figure 5.37:** A frame from a video attempting to capture a transient noise spike that instead recorded a preamplifier channel failing. Oscilloscope capture,  $\text{mV}/\mu\text{s}$  (top). X-Y detector output (bottom).

that leads to high voltage discharges that burn the channel plates (Figure 5.38). A decoupling capacitor had also failed on one corner of the detector which masked the symptoms of the first problem resulting in the discharge burning a hole through the plates without obvious detectable signs. There was additional damage, that may have been the result of a high voltage short to ground, that had destroyed a capacitor on the filter board and a bias resistor on the detector. Due to the numerous issues, the erratic behavior of the detector, and the complex nature of the system, lengthy discussions with the vendor did not result in a definitive understanding of the failure. The numerous problems undoubtedly form a chain of cascading failures but there was no way to know for sure what the catalyst was. Moisture damage due to repeated air exposure is most likely, but if it was present it was not pronounced enough to observe directly.



**Figure 5.38:** The top surface of the detector, the small spot to the right side of the darker active area is damage due to high voltage discharge (left). One of the filter capacitors on the in-vacuum PCB that failed and cracked, possibly due to a high voltage short to ground or the discharge in the channel plates mentioned above (right).

After over a week of in depth analysis and discussion with the vendor, it was concluded that there were too many coincident/overlapping issues to ever learn, for sure, what instigated the failure. The best approach to ensuring that this does not happen again is to take a wide range of preventative measures and safe guards. Many of these modifications were already required to reduce noise on the signal lines to a manageable level, and allow operation of the detector without powering down all the motor on the endstation first.

The detector required rebuilding, so the decision was made to use a newer, less hydrophillic channel plate that the vendor had sourced from a different manufacturer. The plan to have a

rotatable detector for selectable resolution was abandoned and a 40 mm square resistive anode encoder replaced the 20 mm by 40 mm rectangular encoder. This allowed for the design of a more robust detector mount with a grounded enclosure and better cable grounding (Figure 5.39). This enclosure was used as the center of a carefully designed star-grounding arrangement to eliminate ground loops. The in-vacuum cable bundle was completely redesigned. A custom cable set was ordered that used shielded cable not only for the signal lines but also the high voltage supply lines. The in-vacuum cabling was split into two separate cable bundles each further shielded, separating the potential noise sources from the detector wiring, and the two bundles were run through the chamber in opposing spirals to minimize any remaining cross-talk. The air-side wiring was also completely re-run to permanently separate the cables that had been found to be noise sources from the signal lines. All of the motor cables were upgraded with better shielding as well. The specifications for the control system interface were changed to allow the detector high voltage power supply to be interlocked to potentially destructive systems like the ion pumps, preventing them from being turned on at the same time. Finally, careful thought was put in to the new detector enclosure design to simplify the installation process and procedures were developed to ensure that the detectors time-in-air was minimized.

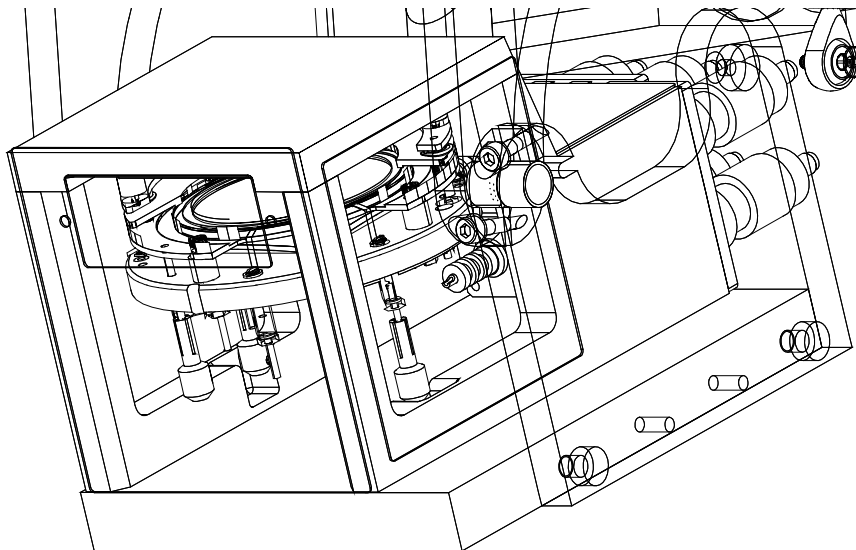


**Figure 5.39:** The new fixed mount grounded detector enclosure design. The ability to rotate the detector was lost, but the more robust mount, a grounded enclosure and the cabling redesign completely eliminated the noise issues.

The rebuilt detector was received in November 2011, and the parts for the new detector enclosure were completed shortly thereafter. Taking nothing for granted, the detector was installed in a test chamber that had been prepared while awaiting its arrival. This allowed for testing the detector in a more controlled environment and also for final testing of the rebuilt preamplifier and a side by side performance comparison between it and the factory preamplifier with identical, real inputs - something that had not been possible before. The detector and custom preamplifier performed perfectly in the test chamber.

The custom in-vacuum cable bundle was received and installed in December. The redesign allowed the installation of the cabling to be completely separate from the detector installation so that the cabling and preamplifier could be in place and tested before the detector was exposed to air for installation. In January 2012, the detector was removed from the test chamber and mounted in the new enclosure (Figure 5.40). The wiring inside the enclosure was already in place having been test assembled with a proxy detector that had been fabricated for this purpose. Once the connections were made and the cabling checked, the detector was installed and the chamber pump down began.

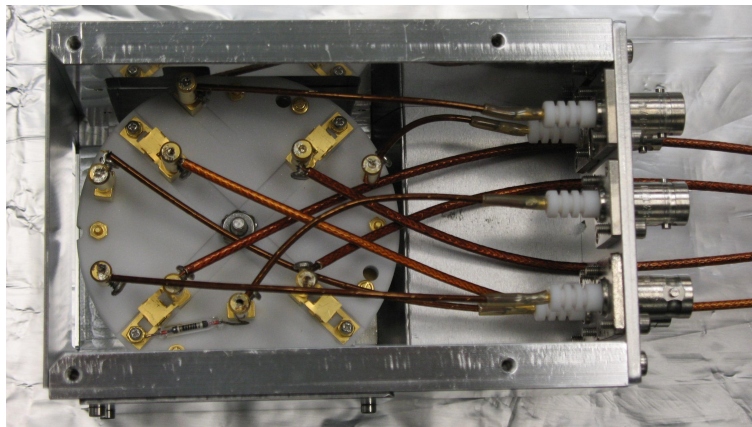


**Figure 5.40:** The detector installed in the new enclosure, wiring in place, moments before final installation in the chamber. The four copper clips holding the decoupling capacitors in place are clearly visible.

It was found that a drawback to the large amount of braided shielding used in the cable bundle was that it effectively added a massive surface area to the vacuum chamber that was not well vented. It took a week of pumping to get the chamber pressure low enough to safely apply high voltage to the detector for testing. At this point all seemed well, however the

grounded enclosure was not sufficient to allow the detector to be safely operated with the ion pump on, and better vacuum had to be achieved before the detector could be operated continuously. After a 2 week low temperature bake out, the chamber pressure was stable in the mid  $10^{-8}$  torr range without the ion pump and testing could begin in earnest.

No matter how carefully a plan is crafted and executed, there is always at least one problem too obscure to be avoided. In this case, once the vacuum was conditioned sufficiently to allow the detector to be operated normally, it was found that the signal from one of the four output channels was weak, with about half the average amplitude of the other three. It took over a day of testing and experimenting, and unfortunately the chamber was vented twice before the problem was found. The decoupling capacitor (Figure 5.40) on that channel was not securely clamped in place. This is something that should have been caught on the wiring bench test prior to installation, but the way the capacitor sat, it was in good electrical contact when the detector was up-side-down on the bench, and was in poor contact as soon as the detector was turned right side up and installed. Finding the source of such a problem at all is quite a feat, but thanks to the extremely thorough understanding of the detector gained while troubleshooting all the other issues encountered it was found quite quickly and was easily remedied.

Having vented with dry nitrogen, it did not take long to attain high enough vacuum to continue with testing, at which point it was found that with the ion pump off and all other systems operating normally, the noise on the preamplifier outputs was down to a few millivolts. When moving any of the motors, the output signal did not exceed 50 mV which is not a threat to the preamplifier and did not generate false counts. The background (“dark”) count rate was 3-5 counts per second, which is on the low side of the manufacturer’s specifications. By the end of January 2012, the detector was fully operational and performing better than expected. Alignment and calibration began during the next available beam time, in early February.

### **5.3.4 Flux and Beam Alignment**

Once the detector and noise issues were resolved, the very first measured spectra were less than spectacular. The flux at the detector, in particular, was very disappointing. The few

samples that any signal could be detected from were at least two or three orders of magnitude less intense than similar measurements taken at BL 8.0.1 at the Advanced Light Source, where other research group members often measure.

The first partial explanation came when the expectation that performance should be similar to that beamline was re-evaluated. During the optical design, the performance of the endstation was estimated based on the early conceptual design report<sup>63</sup> for the REIXS beamline, which set performance goals for the REIXS beamline which included flux on the order of  $10^{13}$  photons/s at high resolution - similar to or better than the high resolution flux on BL 8.0.1. Later documents<sup>21</sup> revised this goal, reducing it by more than a factor of 20. Even still, the expected beamline flux should have been adequate and the endstation performance was falling short.

One likely problem was the alignment of the spectrometer entrance slit. The REIXS beamline was designed to deliver a very small spot at the XES endstation sample position, on the order of  $20\ \mu\text{m} \times 60\ \mu\text{m}$ , which was confirmed by knife-edge scans during the commissioning of the beamline. The alignment of a 20-100  $\mu\text{m}$  entrance slit to a 20  $\mu\text{m}$  high spot must clearly be extremely accurate to get any flux through the slit at all. The mechanism for completing this alignment was cumbersome, relying on raising and lowering the entire endstation on threaded support bolts, but it should have had the requisite precision to accomplish the task. Precision centering of the slit with respect to the beam was expected to take time, but getting the full flux through the slit when wide open should not have been so difficult. Hours of careful adjustment did not yield any improvement, however. Moreover, issues with the slit in general became apparent. The piezo benders that form the slit were not stable, and tended to drift closed under constant voltage. Since there was no feedback on the slit size other than count rate, this lack of reliability was a serious problem. Attempts were made to recalibrate the slit piezos using an optical telescope and autocollimator, but these observation served only to confirm the lack of stability of the piezos.

To eliminate these slit issues as a variable and continue exploring the lack of flux while a solution was sought, the entrance slit was removed in May 2012 and the endstation was realigned to operate slitless, which was theoretically possible due to the small spot size. Doing so instantly improved the flux by an order of magnitude, but attempts to refocus

the spectrometer to regain resolution initially failed. Repeating the knife-edge scan used to confirm the beamline spot size performance revealed that the spot was over 40 times larger than it should have been, indicating that M5 was no longer properly aligned. Adjustment of the post-focusing mirror, M5, revealed that it was out of alignment by 0.7 degrees. Upon refocusing M5, the observed emission spectra immediately regained resolution (Figure 5.41).

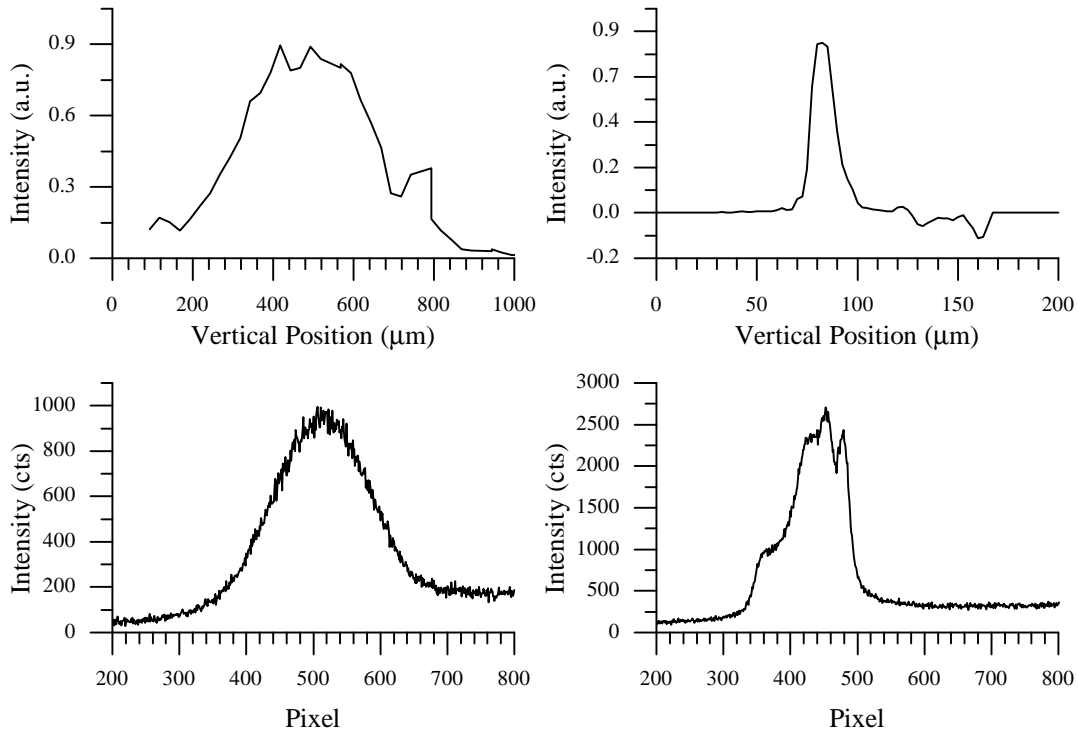


**Figure 5.41:** The vertical beam profile before and after M5 realignment (top) and an *h*-BN N K-edge emission spectra before and after realignment (bottom).

After working with the endstation without an entrance slit, it was decided to proceed with slitless operation due to the vastly improved flux. The lack of an entrance slit goes a long way towards compensating for the lower incident flux, and the small spot size delivered by the REIXS beamline provides an excellent, well-defined source point for the spectrometer. The fact that the spectrometer dispersion direction is vertical and nearly perpendicular to the beamline means that the critical alignment parameters, the entrance arm length and incidence angle, are defined by the beam and not the sample position, making sample alignment easier without an entrance slit, which is not the typical case. Finally, A precision entrance slit is one of the most delicate mechanisms in any optical system, and the need to get samples as

close as possible to the slit to maximize the collected solid angle means that sample collisions with the delicate slit are inevitable. A slitless spectrometer is much more robust, reliable and easier to operate.

Not wanting to risk missing any potential performance gain, tests were conducted using a temporary, fixed 25  $\mu\text{m}$  entrance slit mounted directly to a sample plate. This setup allowed for only one sample to be examined at a time and is by no means exhaustive, but it is an inexpensive approach to exploring any possible benefits of an entrance slit. *h*-BN and  $\text{SiO}_2$  were chosen as test samples due to the sharp features present in their emission spectra. With such a small spot size, grain orientation in *h*-BN powder samples can lead to significant variations in the emitted spectra which made fair comparison between two different sample spots difficult.  $\text{SiO}_2$  proved to be far more consistent (see Figure 5.42). The slit was approximately 10 mm from the beam spot, which is a typical configuration. Spectra were collected at a range of different monochromator exit slit sizes with and without the entrance slit for comparison. As expected, the entrance slit noticeably reduced the flux at the detector. For a monochromator exit below 100  $\mu\text{m}$  this loss was roughly 25% with increasing losses as the exit slit was opened beyond 100  $\mu\text{m}$ . This is consistent with the knife edge scan results that suggest the beam spot FWHM is below 25  $\mu\text{m}$  for exit slit sizes up to 100  $\mu\text{m}$  (see Section 6.3).

The presence of the entrance slit did allow for any size monochromator exit slit without degrading resolution of the recorded spectra, but a monochromator exit slit 30%-40% larger is required to achieve any gain in flux (see Figure 5.43). The resolving power does show an improvement of more than 20%, although improvements in the beam spot alignment and uniformity may improve the slitless performance, reducing this difference. Figure 5.44 shows a comparison of two emission measurements, with and without an entrance slit, with the exit slit adjusted to achieve similar flux at the detector. The two measurements show similar apparent resolution, demonstrating that similar results can be obtained either way for non-resonant emission measurements.

Since these measurements were completed, work has already begun on further optical fine tuning of the beamline and the fruits of these efforts are reflected in the results presented in Section 6. Slitless operation has proven to be a very desirable operating mode, and before

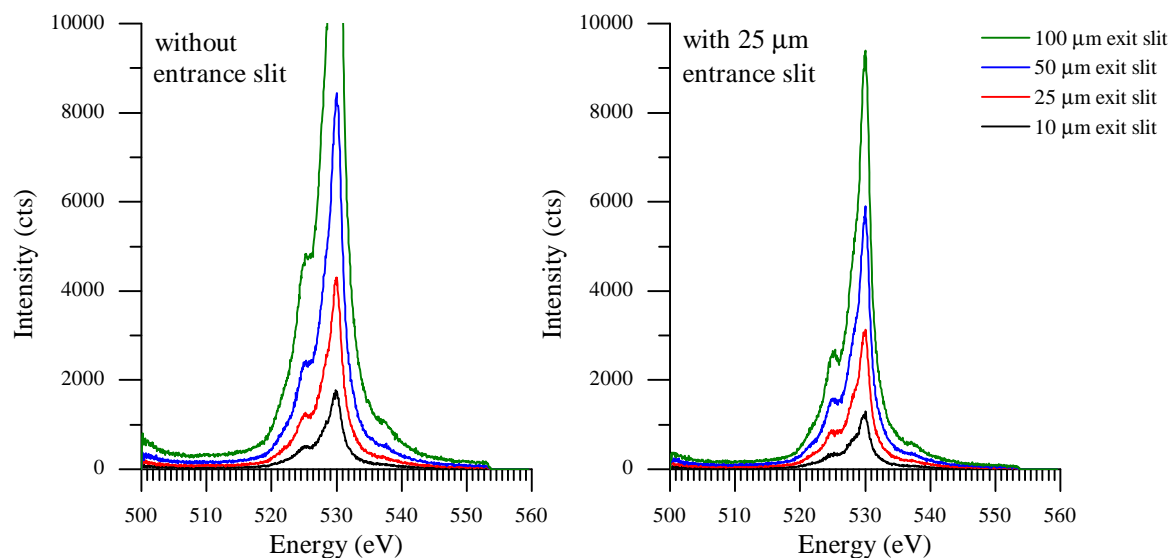


**Figure 5.42:** Qualitative comparison of  $\text{SiO}_2$  O K-edge emission spectra with and without a  $25 \mu\text{m}$  entrance slit for various monochromator exit slit sizes.

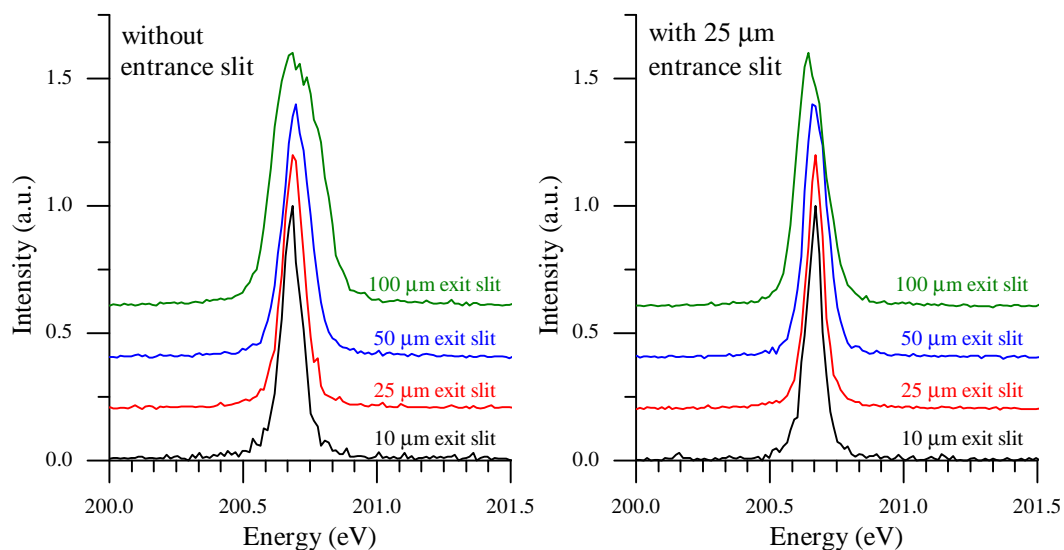


**Figure 5.43:** A comparison of elastic peaks with and without a  $25 \mu\text{m}$  entrance slit for various monochromator exit slit sizes.

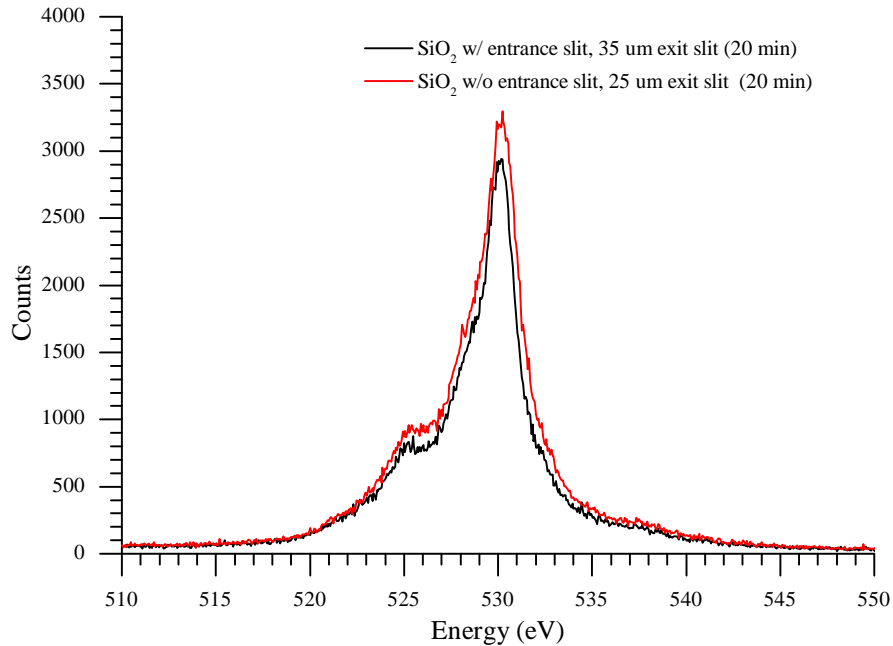


**Figure 5.44:** SiO<sub>2</sub> O K-edge emission spectra with and without an entrance slits collected in 20 minutes. The monochromator exit slit was adjusted to give similar count rates for comparison.

a redesigned entrance slit is considered, every effort will be made to maximize the slitless performance. For non-resonant emission measurements, the bandwidth of the incident light does not affect the recorded spectra, as long as the sample is being excited well above the elemental edge. This makes compensating for the flux lost at the entrance slit by opening the exit slit feasible. For RIXS measurements, which rely on a narrow incident bandwidth for their resolution, this is not an option.

### 5.3.5 Stray Light and Photoelectron Noise

Several unexpected optical noise sources were identified during the course of commissioning the spectrometer. Depending on the elements in a particular sample and the geometry of the system for a given grating and energy, stray light turned out to be a significant issue. The inclusion of baffles to help control stray light was discussed during the design process, but the engineer felt that there was not adequate physical space to include them. Some of the issues encountered may have been less significant if the entrance slit had been retained but, in the end, failing to include baffles was a design oversight.

With relatively clear lines of sight throughout the system, there were numerous positions where large noise features were observed. These features were not optical in nature and had no energy dependence. Careful sample positioning, or detector realignment could reduce the noise in some cases. There were two main causes identified. Stray soft X-ray photons that struck the stainless steel detector enclosure would create secondary electrons, some of which could be caught in the detectors bias field and generate a large number of counts. This was most often observed as a large, unevenly shaped blob at the front of the detector (Figure 5.45). Commonly this was due to the higher energy elastic peak striking below the detector, but a similar effect has been observed at the back of the detector in certain rare cases when the second order emission from a second element in the sample happens to line up in such a way that it could enter the detector enclosure at the right angle to pass over the detector and strike the back wall of the enclosure.

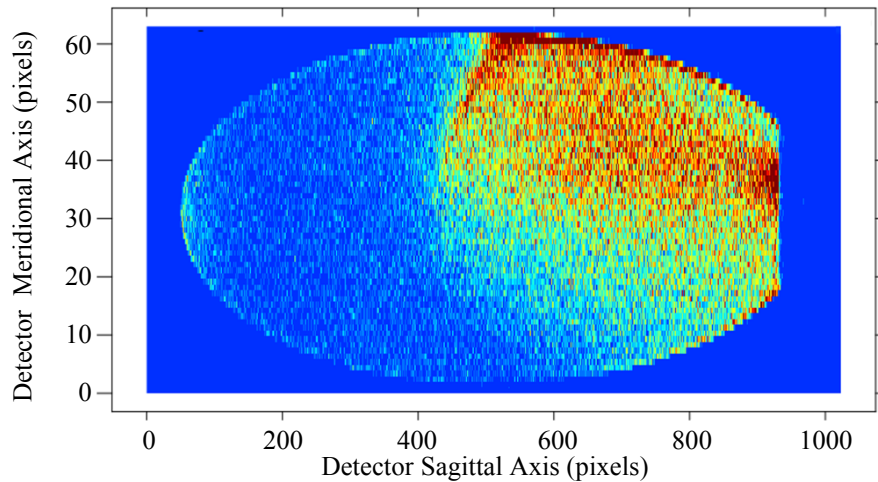


**Figure 5.45:** A secondary electron cloud swamping the signal, resulting from photons striking the detector enclosure.

Smaller secondary noise features are also commonly seen around the edge of the detector, and a careful comparison of these features with the physical shape of the detector reveals the cause (Figure 5.46). A mounting and bias ring partially encircles the channel plates and is elevated by a few mm. If the right energies are present and the detector is at the right angle relative to the grating, photons can strike this ring and create small secondary electron clouds. Due to the proximity to the MCP surface and the bias field, these electrons are localized to the outer edge of the detector.

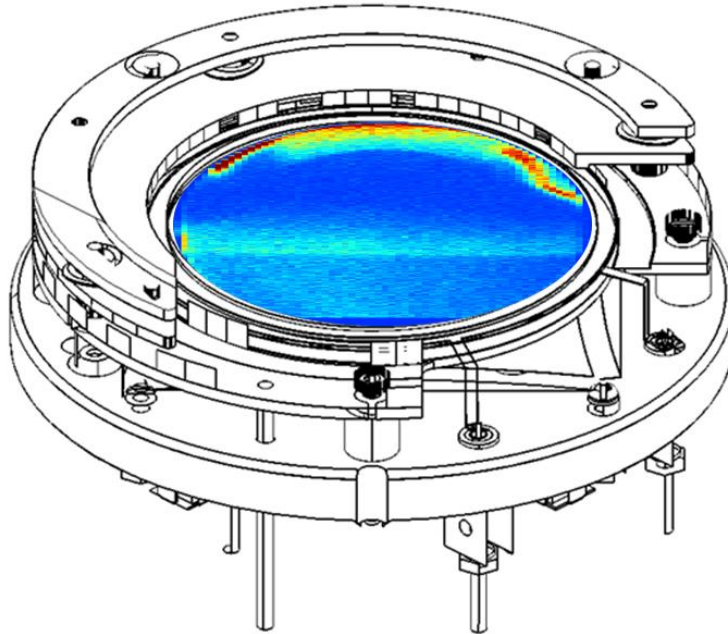


**Figure 5.46:** An image of a measured emission line overlaid onto the model of the detector. The location of the noise in relation to the channel plate mounting and bias ring reveals their cause.

In most cases, this noise was minor and isolated and the ability to mask off affected areas of the detector was added to help mitigate the problem. In certain cases, particularly towards the high end of the energy range of a particular grating when the detector is close to the front of the chamber, at a low angle and relatively flat, these noise sources can completely swamp the detector. Figure 5.46 shows one such case. The large noise feature present in that figure is due to secondary electrons generated by either zero order light sticking the detector enclosure, or possibly even a portion of the enclosure with a direct line of sight to the sample, by-passing the grating.

Another interesting issue was discovered when work started on commissioning the HRMEG. Initial attempts to locate the emission lines failed and relatively high background noise was observed. A complete scan across the whole diffraction space showed emission peaks that did not correspond to the location of any of the expected peak positions for any diffraction order from the HRMEG (Figure 5.47). Initially, the remarkable intensity of the peaks was exciting, as with the expected efficiency of the third order gratings this was unexpected. Further investigation revealed that these peaks were actually from the zero through third order

light diffracted by the impurity grating which sits in front of the HRMEG on the grating carousel. Without masks or baffles, the 1.5" diameter pipe from the sample chamber to the grating chamber is wide enough to allow both gratings to be illuminated at the same time. With the HRMEG in position, the impurity grating was at the wrong incident angle, but it still had sufficiently high diffraction efficiency, aided by the large solid angle it can collect by being 50 mm too close to the sample, to completely swamp the signal from the HRMEG with defocused emission lines. Even when the light from the impurity grating does not fall directly on the HRMEG in a measurement position, the increased number of secondary electrons in the chamber resulting from this stray light was enough to significantly degrade the already weak signal to noise ratio for the HRMEG.

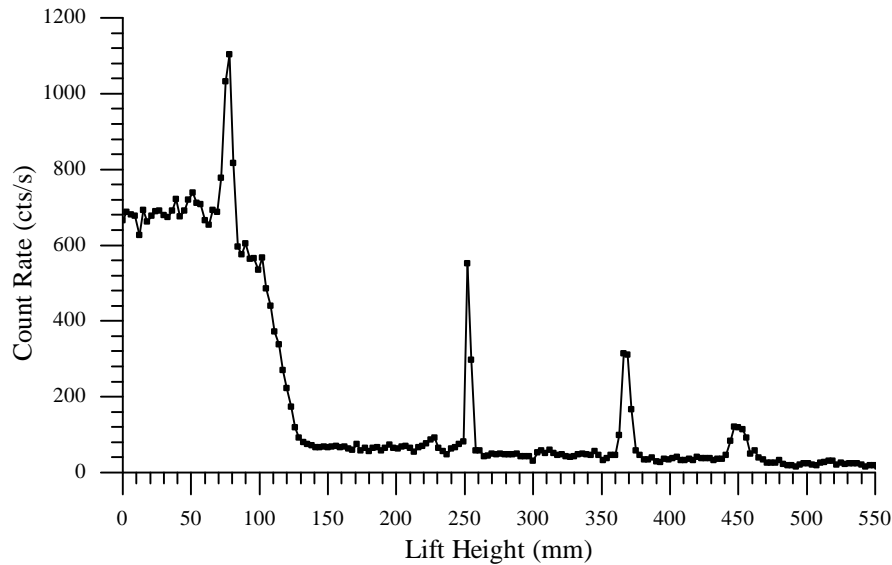


**Figure 5.47:** A scan across the diffraction space of the HRMEG grating for nitrogen emission. The sharp peaks are stray, defocused diffraction peaks from the impurity grating. The diffracted light from the HRMEG is lost in the background. The large step below 100 mm is a direct line of sight to the sample.

In addition to the software features added to help work around some of these noise issues, several upgrades were made to the spectrometer to help eliminate them. Two masks were designed, and added to the system. One was placed in the sample chamber between the sample and the gratings to prevent the over illumination that was noticed when working with the HRMEG and to block direct lines of sight light from the sample (Figure 5.48 (left)). This mask consists of a single slit large enough to allow complete illumination of any one

grating, mounted on a vertical linear stage so that it can be precisely aligned. Two additional features were incorporated into this mask, a pin hole that could be used to quickly and easily center the sample on the optical axis of the spectrometer and a second slit with an electrically isolated mesh that can be biased to keep electrons out of the spectrometer when the electron gun is used as an excitation source.

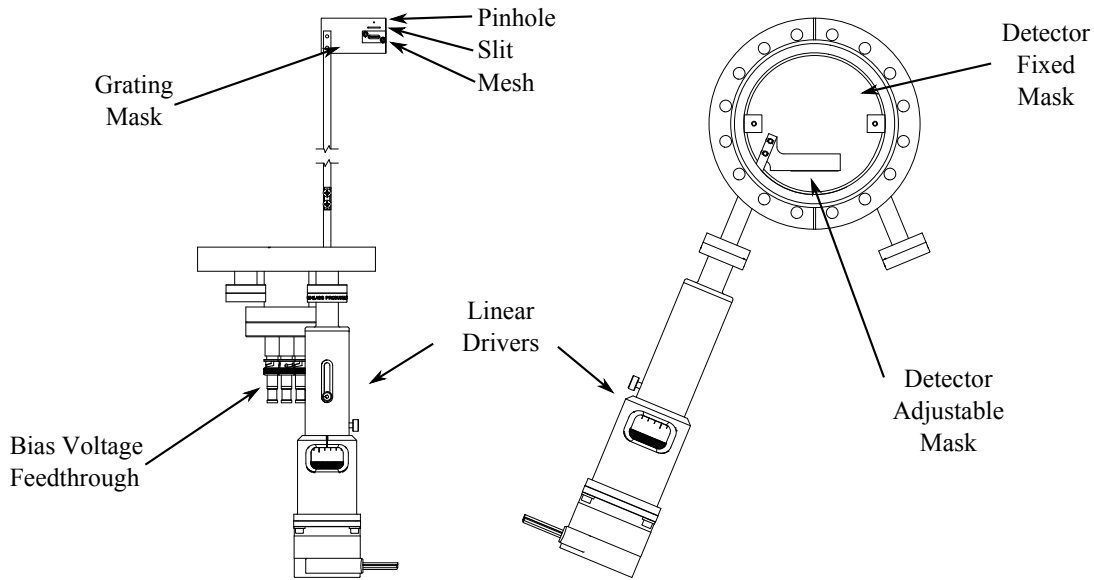


**Figure 5.48:** Drawings of the adjustable grating and detector masks designed to reduce stray light and improve signal to noise ratios.

Because the detector chamber rotates with the detector, the position of the optical axis relative to the chamber remains constant. For this reason, it was possible to work out a way to squeeze a second mask on a zero-length 6" CF flange between the detector chamber and the bellows. This flange mounts a fixed mask large enough to fully illuminate the detector at the minimum focal length. This mask will eliminate almost all of the off axis stray light from direct line of sight and unwanted orders. It also has a single adjustable blade that can be used to reduce the height of the top or bottom of the fixed mask, when the detector is further from the mask and a troublesome noise peak appears. This blade can not be used to completely block all unwanted light, such as elastic peaks or second order lines, because the grating is not a point source and the diffracted light is not fully separated until it reaches the focal plane, but it can be used to further reduce stray light entering the detector chamber.

Finally, the enclosure front and back panels that would occasionally be hit by stray light

were changed from stainless steel to aluminum. Because aluminum alloys contain significantly fewer elements with absorption lines in the energy range of interest this change dramatically reduces the secondary electron noise near the front and back of the detector.

Combined, these modifications virtually eliminated the noise problems initially observed, and greatly reduced the dark count rates and background levels for all energies. This change was particularly noticeable for the HRMEG, where having a dark count rate on the order of one to two counts per second is critical to successfully measuring weak, high resolution RIXS spectra.

### 5.3.6 Image Linearity

Among the residual aberrations present in a grazing incidence Rowland circle system is a sagittal curvature or warping in the resulting image. This is because the Rowland circle condition prioritizes the meridional focus critical to the resolution of spectral features and leaves strong aberration in the sagittal direction. In effect, at grazing incidence spherical gratings can not effectively focus in the meridional direction. The resulting curvature is in the form of a conic section, with the detector tangent to the Rowland circle it should ideally be parabolic.

Such a curvature is easily corrected for with image post processing, and can be automated with a relatively simple peak tracing algorithm. Such algorithms are not perfect and can not always handle the levels of statistical noise common in emission spectra but, with the known expected parabolic line shape, fitting a quadratic to the result should produce very good results.

During the course of the commissioning measurements, it was found that this approach did not perform as well as expected. A quadratic did a poor job of fitting the line shape across the full width of the detector and, worse yet, the line shape tended to vary from one end of the detector to the other. Careful examination of sharp spectral features revealed a subtle non-linearity or warping of the detector image (Figure 5.49).

The manufacturer's acceptance test data includes a linearity test, which does show some subtle non-linearities. Inherent non-linearities in the detector, most likely subtle variations in the resistive anode, are likely the cause of the observed image warping, but they did not

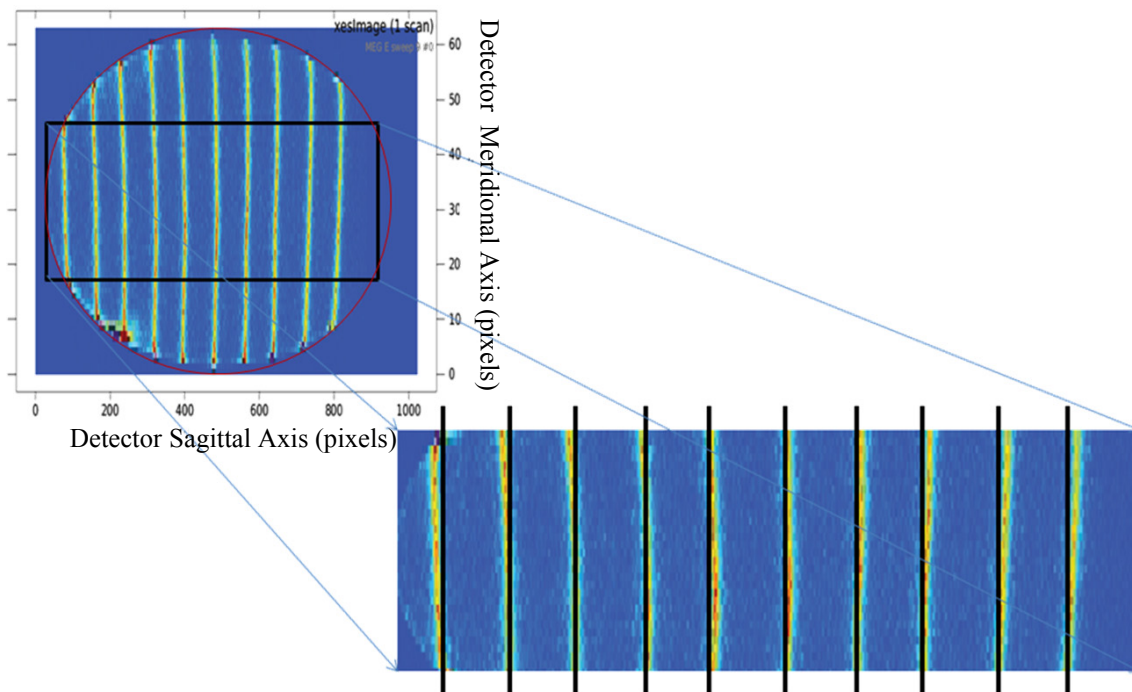


**Figure 5.49:** A detector image of a sharp elastic peak moved to several different energies. The call-out illustrates the change in the line curvature across the detector by overlaying straight reference lines. A perfect circle is overlaid on the detector image in red, revealing no substantial preamplifier imbalance.

correlate perfectly with the observed image warp. Several potential causes were explored to ensure that there were no other correctable issues present.

The most obvious explanation is an imbalance in the four preamplifiers resulting in a skewed image, but this possibility was quickly ruled out. The circular channel plates make an effectively perfect mask over top of the square resistive anode, so any preamplifier imbalance would result in a non-circular image area (see Figure 5.49). Careful examination of several detector images showed no detectable deviation from a perfect circle.

When a photon strikes the detector, a charge cloud is created. The detector relies on a small bias field above the top channel plate to contain and localize this charge cloud to maximize resolution and quantum efficiency. If this bias field was non-uniform, the charge clouds could be displaced by it. To rule this out, the high voltage power supply/divider was modified to allow the top bias field to be adjusted from the preset 350 V up to 820 V. Several tests were conducted with different biases (Figure 5.50), and the image shape showed no

change whatsoever, ruling out this cause.

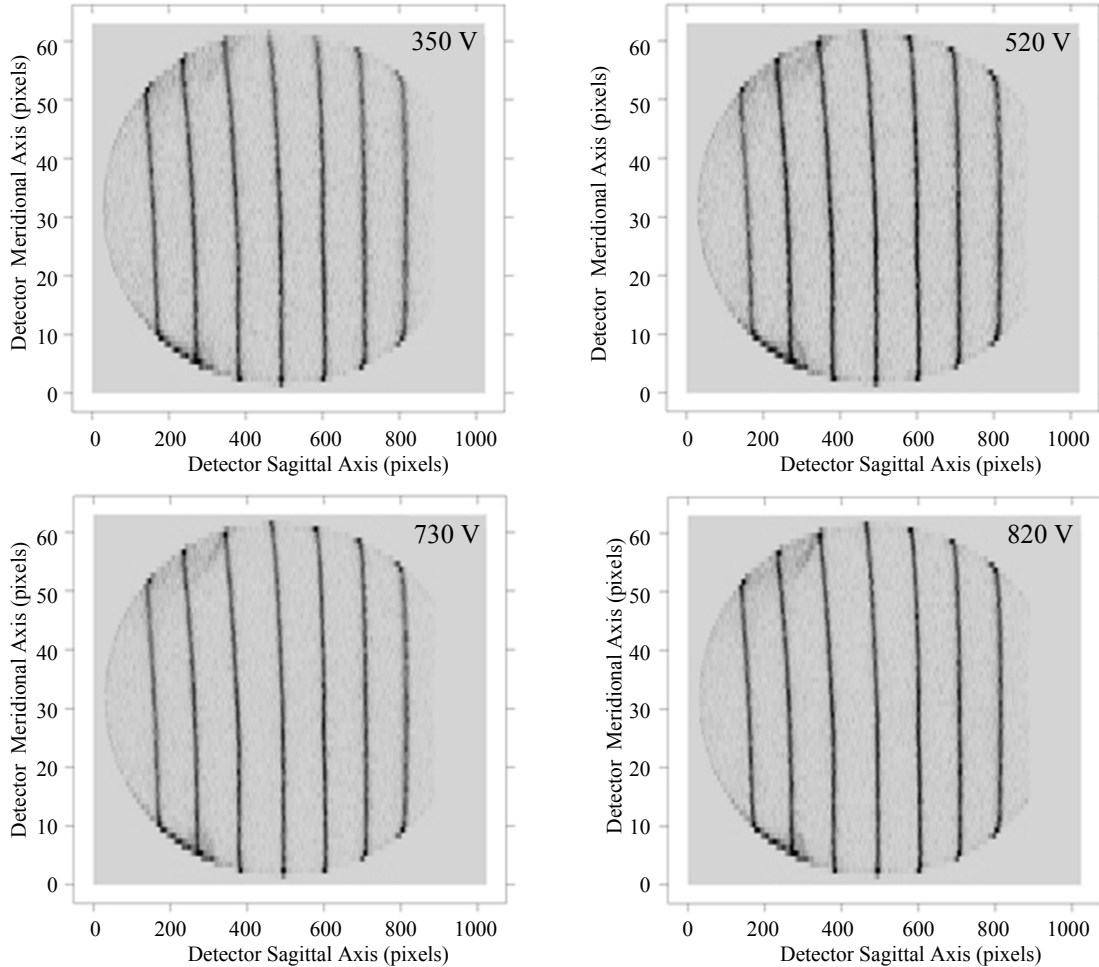


**Figure 5.50:** A series of linearity test images collected with different top bias voltages, ruling out a non-uniform bias field as a factor.

An optical misalignment was the final cause considered. If the detector was off axis, tilted with respect to the incidence direction, the apparent non-linearity could be caused by non-uniform defocus or an off-center image. The general mechanical design of the optical system was a great advantage in exploring this issue. With eleven motorized degrees of freedom relevant to the optical alignment, nearly every conceivable misalignment can be created and the effects observed. While some very interesting behaviors were observed, the nature of the image warp stayed constant, ruling out this cause.

Being left with no explanation, one last effort was made to verify that an inherent non-linearity in the detector was a likely cause. Images collected by members of our research group on a similar detector in the emission spectrometer on BL 8.0.1 at the ALS were examined.

Similar non-linearities were found and had even been noticed by those researchers, although they were assumed to be normal Rowland circle optical aberrations. With no way to eliminate this distortion, work is underway to enhance the image post processing to compensate for it. Early attempts to quickly modify the existing curvature correction routine to fit higher order curves works well for some cases, if the spectrum is confined to a small region of the detector. Since there is no physical rationale for using a higher order polynomial, it is not surprising that this does not work in all cases. Work is under way on several additional improvements. If the non-linearity can be well determined, a two step image correction algorithm will be implemented that will correct for the image warp before fitting the expected polynomial. If this does not prove to be reliable, the curve fitting will be removed and a smoothing algorithm such as a median filter will be applied to the raw peak tracing instead. Finally, a routine that interpolates between two different curvatures across the detector, developed by fellow group member Robert Green<sup>64</sup> to improve images taken at the ALS, is being implemented here.

### 5.3.7 Thermal Stability

During early commissioning measuring by members of the research group, a concerning problem was observed. While watching a single long emission scan accumulate counts, the main features were seen to split and broaden as the scan progressed over several tens of minutes (Figure 5.51).

Investigating further, a series of short scans on a relatively bright sample system were used to gain more insight into the problem (Figure 5.52). Similar measurements were completed on different sample systems, with different beamline and spectrometer configurations and at different times of day. Higher resolution measurements demonstrated a greater sensitivity to the observed effect. Repositioning the primary beamline components between scans did not affect the outcome.

The CLS maintains an archive of a substantial number of system and environmental parameters. Since the tests performed seemed to rule out mechanical instability in the beamline and endstation motion control systems, an attempt was made to correlate the observed drift to every recorded variable in the CLS data archive that had any relation to

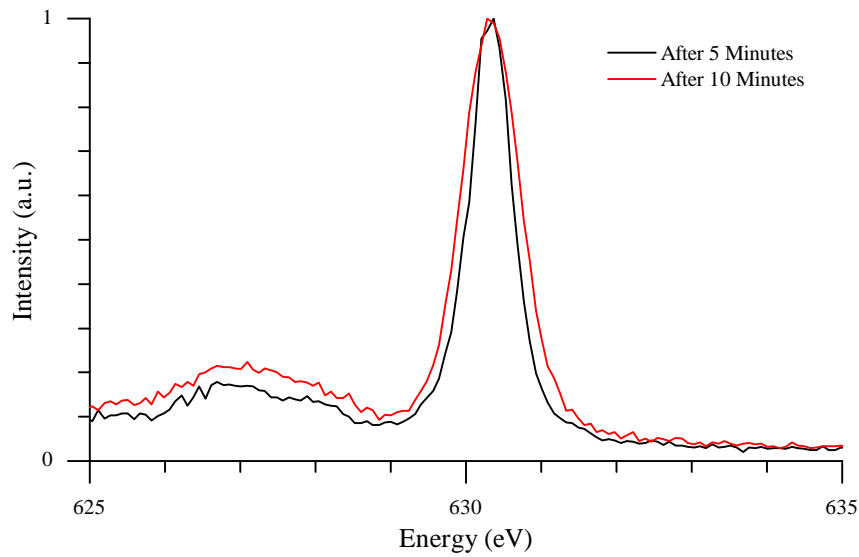


**Figure 5.51:** Two Mn emission scans data sets, one a continuation of the other. The broadening and shifting to lower energy is readily apparent.

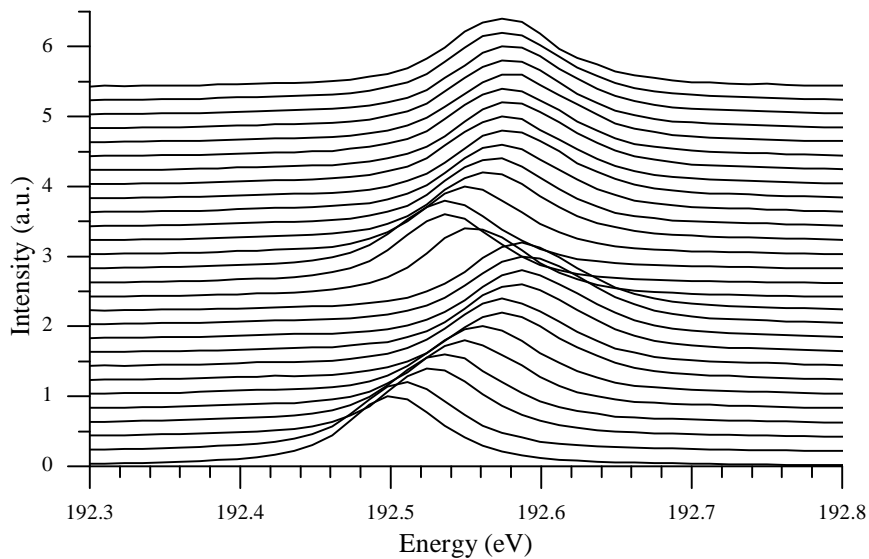


**Figure 5.52:** An elastic peak measured with the MEG, 28 sequential 10-minute emission scans. The energy drift is cyclic suggesting some form of mechanical drift as opposed to a loss of resolution or blurring from vibration or similar effects.

the REIXS beamline. Through a stroke of luck, a very strong correlation was found and suggested a very likely explanation, thermal instability (Figure 5.53).

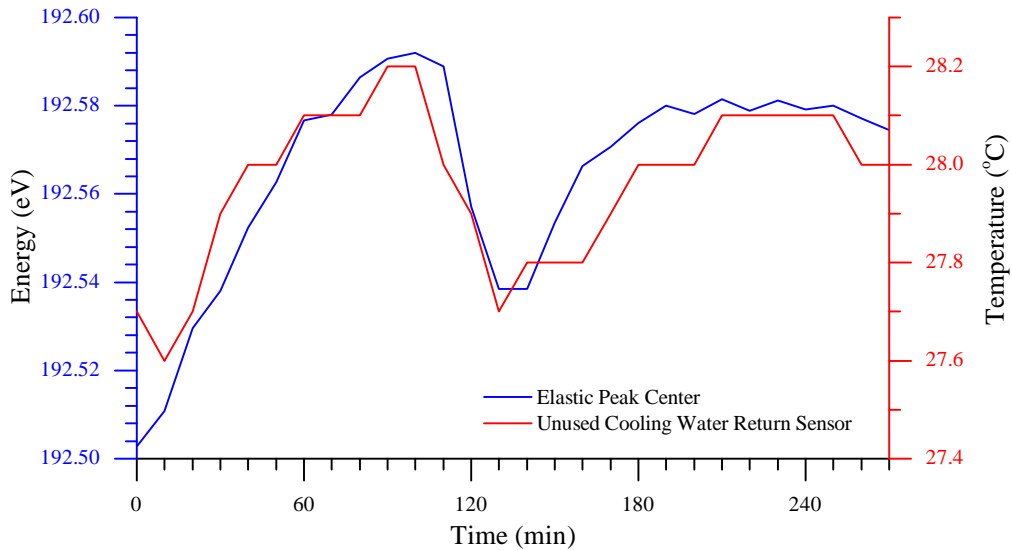


**Figure 5.53:** The temperature recorded by an unused water cooling line thermocouple inside the REIXS endstation hutch plotted against the peak position of sequential scans recorded throughout one night.

While the room temperature inside the REIXS endstation hutch was not being recorded by the data archiver, the temperature of an unused cooling water return was being recorded and, since there was no water flow across the sensor, it tracked closely with the temperature of the room. The fact that it was in thermal contact with the cooling loop meant that the warm return water did pull the recorded value up several degrees above the true room temperature, but later tests showed that it did follow it only slightly out of phase. This temperature was plotted against the recorded peak position as a function of time and the correlation was remarkably good (Figure 5.53). No adjustment in the time axis positions or scales was made in generating the plot. It was clear that changes in the experimental enclosure temperature were directly affecting the energy calibration of the spectrometer.

Investigations into the exact mechanism of this thermal drift were inconclusive. There are several potential explanations, the most obvious would seem to be that the lift stage for the detector rotation was expanding and contracting, effectively rotating the spectrometer with changes in temperature, but considering the coefficient of thermal expansion for steel, and the fact that the room temperature, once directly monitored, was shown to be drifting

over a range of only  $0.7^{\circ}\text{C}$ , the potential change in length would not be sufficient to explain the observed drift. Further, the entire endstation frame is steel, and if the temperature of the whole frame changes uniformly then it should behave as a series of similar triangles and the angles should not change. However, it is possible that the black powder coated frame responds to changes in air temperature differently than does the bare metal ballscrew holding the chamber up and the exact positions of ceiling air vents may result in a temperature differential when the Air Handling Unit (AHU) is running. The hexapod would also have a different thermal response than the frame and, finally, the changes in size of the entire endstation could result in a relative shift of the beam position (source) relative to the optical axis of the spectrometer. It is possible that some or all of these effects are taking place simultaneously and act to compound each other which could explain the larger than expected drift. Systematically analyzing the problem would be a very complicated task, and would not likely lead to a practical solution.

The most obvious solution was to stabilize the temperature of the endstation enclosure. Since the enclosure has its own dedicated AHU this is possible, but since it contains only a cooling coil and no re-heat loop this turned out to be a challenging task. Additionally, upgrades were required to the control system, since the existing system was only capable of measuring the room temperature to a precision of  $0.5^{\circ}\text{C}$  and upgrades to the cooling water control valve were required to have full scalable analog flow control. With these upgrades in place, and after much experimenting and tweaking and many lively discussions on the inner workings and proper tuning of PID control loops with the CLS controls engineers, the temperature stability inside the experimental hutch was improved to  $\pm 0.05^{\circ}\text{C}$  (Figure 5.54). This order of magnitude improvement in the temperature stability resulted in an apparent reduction of the oscillation on the time scale of the room temperature changes by roughly the same factor. However, once that source of drift was reduced, a second behavior was observable. Further investigation found a correlation between this drift and the temperature of the CLS experimental hall, as suggested by the data shown in Figure 5.54. Additional measurements will be needed to verify that this is the cause of the instability, but calculations show that a vertical beam spot drift at the sample of  $48\ \mu\text{m}$  would be sufficient to cause the observed drift. Considering the length of the beamline optical paths, this is a possibility.

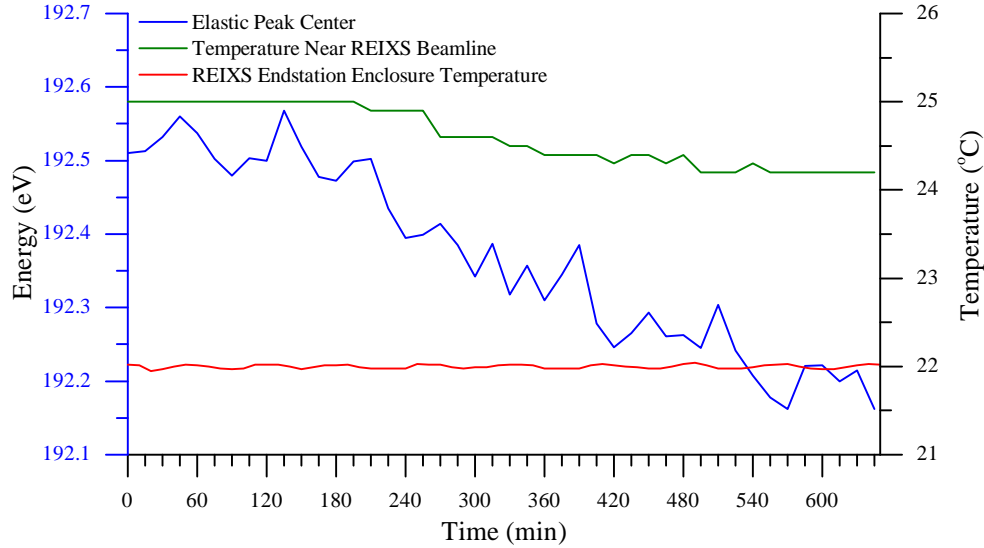


**Figure 5.54:** Improving the temperature stability of the experimental enclosure by an order of magnitude resulted in a reduction in the magnitude of the energy calibration drift *with room temperature* by roughly the same factor. This revealed a longer period drift that appears to correlate to the temperature of the main experimental hall.

The remaining calibration drift is an outstanding issue and it will be investigated further as beamtime and resources allow. For the time being it is not a critical issue due to the long time scale of the drift. Very few measurements are taken over periods long enough for the drift to noticeably impact the resolution. Those that must be taken over long periods can be collected as a series of shorter scans and then shifted to align the main spectral features. Other recently constructed very high resolution spectrometers have found it necessary to operate in a similar sum-of-short-scans mode<sup>65</sup>. Realistically, if it is proven that the temperature variations of the main experimental hall are the cause of the observed drift, there is very little that can feasibly be done to improve the situation.

## 5.4 System Integration and User Interface

Completion of the mechanical assembly is far from the end of the road. The endstation includes numerous systems that require control, monitoring and adjustment, not to mention the numerous beamline functions and facility wide variables that are critical to the endstation operation. Without a carefully planned and well executed controls integration plan, a device

as complex as this endstation would be all but unusable.

A synchrotron as a whole is clearly far more complex and as a result the CLS has the experience, expertise and systems to manage this integration process with relative ease. That being said, this process requires the coordinated effort of more individuals than any other step in the project. Research group members, beamline staff, controls engineers, CAD technicians, electrical and mechanical technicians, software developers and even health and safety technicians have all been involved in the process at one time or another. This can make it a lengthy and complicated project, especially when many of these resources are already in high demand throughout the facility.

The first step in this process is the creation of a Process and Instrumentation Diagram (P&ID) which provides a high level overview of the systems involved and their required inter-connectivity (Figure 5.55). This diagram starts with the endstation designer and their vision of how the systems should work, and is completed in cooperation with electrical engineers and CAD technicians.

From the P&ID, numerous Process Flow Diagrams (PFD) are generated for everything from plumbing and pneumatics to optics and vacuum systems. These drawings serve as a reference for low level mechanical and electrical drawings which detail the route and placement of every pipe and cable. The P&ID also serves as a reference for the development of detailed wiring diagrams, for all the equipment in the system, which detail every cable, connector and interface setting for every piece of equipment integrated into the system.

The integration, monitoring and control of almost all system at the CLS is done through open-source, distributed, real-time controls software developed by the Argonne National Laboratory called EPICS, the Experimental Physics and Industrial Controls System<sup>66</sup>. Basically, EPICS distils every control and variable in a system down to a series of software Process Variables (PVs) that can be monitored and adjusted through software ranging from Linux command line tools to elaborate custom GUI applications. Connection to EPICS is generally facilitated in one of two ways.

Lower level hardware systems are connected to network enabled Programmable Logic Controllers (PLCs) that have low level digital and analog inputs and outputs that can be configured to communicate with nearly any device with such interfaces available. Some of

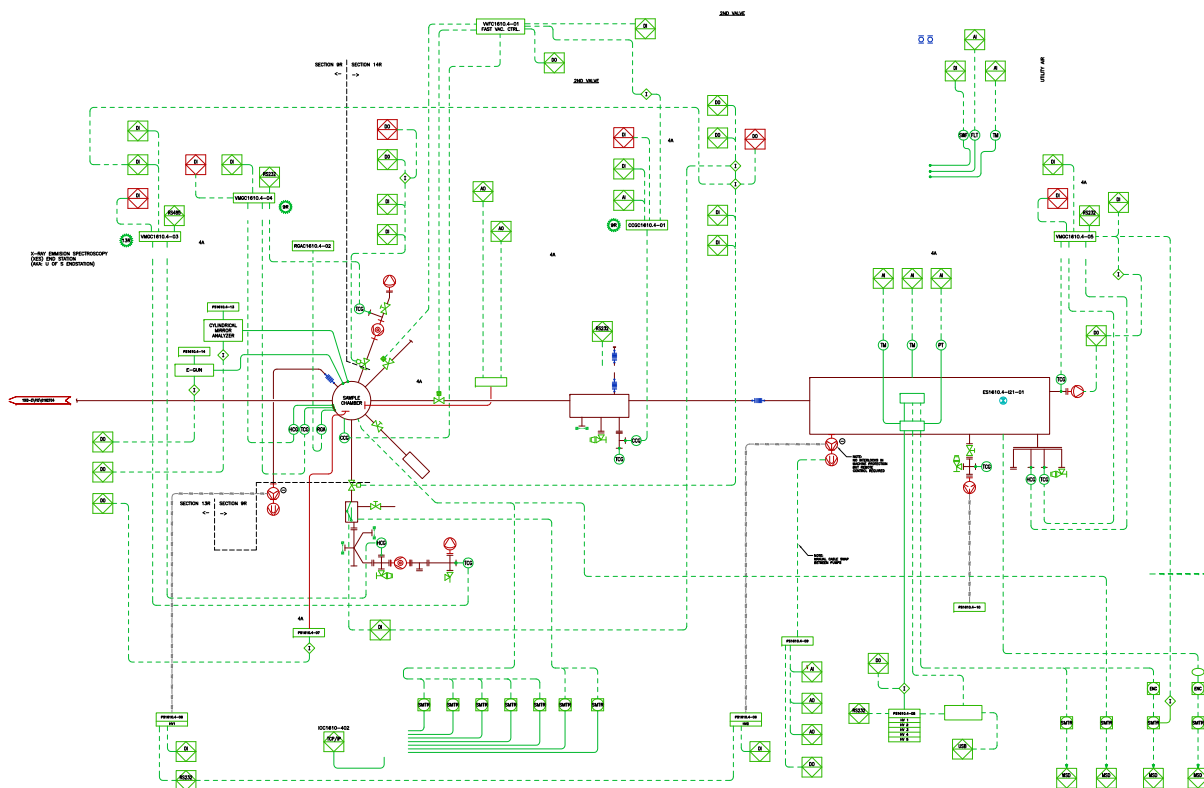


**Figure 5.55:** The process and instrumentation diagram for the XES endstation, all but impossible to effective display as anything smaller than poster size, gives just a glimpse of the complexity of such a system.

these inputs and outputs are translated to PVs and made available over the EPICS controls network, while others are monitored directly by the PLCs as part of a low level machine protection system which monitors safety critical operations such as vacuum systems, photon shutters and high voltage supplies to ensure protection of personnel and equipment, and to respond quickly to failures to mitigate potential damage. The XES endstation has its own dedicated PLC.

Devices that use higher level communication protocols, such as RS232/485 or USB serial interfaces can be integrated into EPICS by developing custom drivers (when EPICS interface drivers do not already exist), that run on Linux PCs or industrial serial device servers such as MOXA DA-662s set up as Input/Output Controllers (IOCs).

Once PVs exist for a device's parameters, they can be checked, monitored or changed with standard command line tools, but this is rarely an efficient way to interact with them.

Libraries exist for the integration of EPICS PVs access and control into custom software solutions in numerous programming languages. However, for quick, customizable GUI interface for PVs, the CLS often uses the Extensible Display Manager (EDM), developed by the Spallation Neutron Source<sup>67</sup>. EDM allows for the development of custom GUIs with a reasonable degree of flexibility and without the need for programming. This makes the continuous development of an EDM screen in parallel with the development of the controls systems feasible and extremely useful for testing and development. It also allows the endstation designer to create a control interface that matches the desired workflow, and even create custom interfaces for temporary control processes such as system commissioning. An EDM screen was developed for the XES endstation early in the controls integration process, and it continues to evolve as details of the controls system are finalized and the endstation operations expand (Figure 5.56).

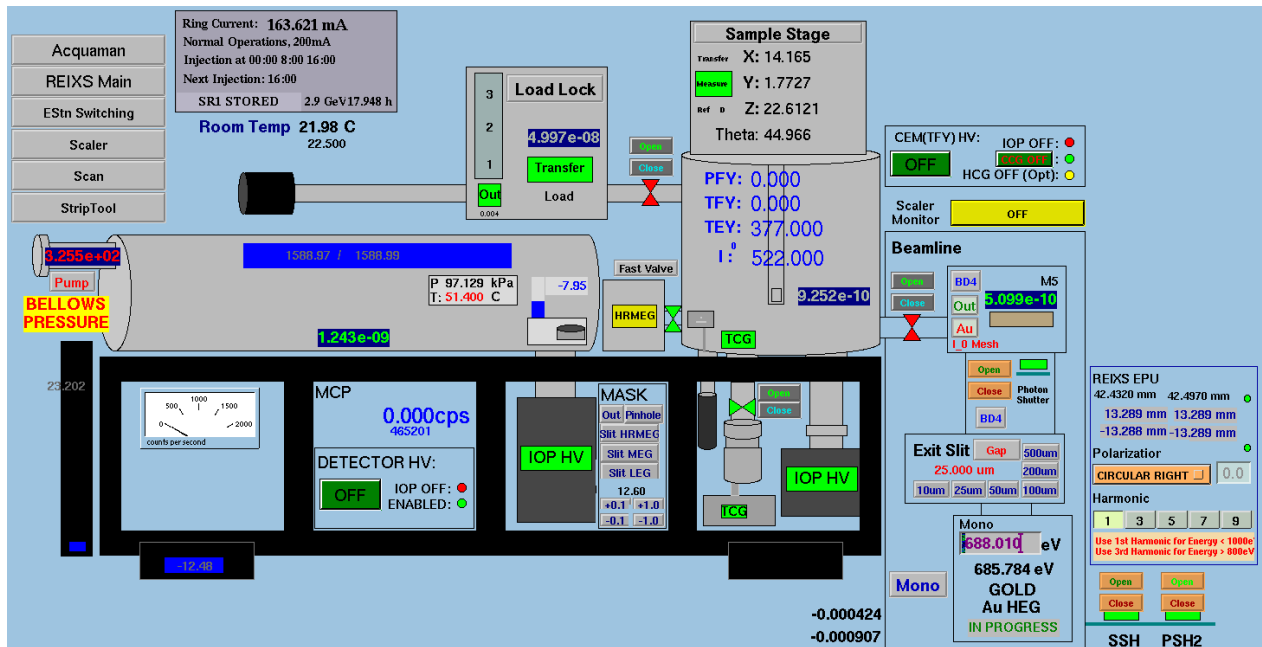


**Figure 5.56:** The Extensible Display Manager (EDM) interface for the EPICS PVs relevant to the XES endstation.

Having an easy way to monitor and adjust PVs is critical to the operation of the endstation, but it is not an ideal way for users to operate an extremely complicated instrument for typical experimental measurements. Mark Boots put an extreme amount of effort into developing a GUI for the operation of the endstation starting from the needs of the user and

the experimental process and working down to the low level control of motors and detectors. This software, called Acquaman (Acquisition Manager) has become an extensive and complicated software package that handles all the low level hardware control allowing users to focus on their science and not the equipment (Figure 5.57).

It also manages the collected data and provides a user friendly interface for monitoring, viewing, comparing, storing, organizing and exported all data collected by a user, along with all the relevant details of the experiment (see Figure 5.58).

A built in workflow system allows mundane and repetitive tasks in the experimental process to be largely automated, freeing the user to focus on the results.

Acquaman has been so successful that it has been adopted and extended by two other beamlines at the CLS as their primary experimental user interfaces, and two more and in the process of doing so. Acquaman is open source<sup>68</sup>, and under continuous development. Interest in adopting Acquaman has been expressed by other facilities.

A complete description of Acquaman's features and operation is outside the scope of this document. This quick overview is intended only to share knowledge of its existence and help stimulate interest in further development and adoption by other similar facilities.

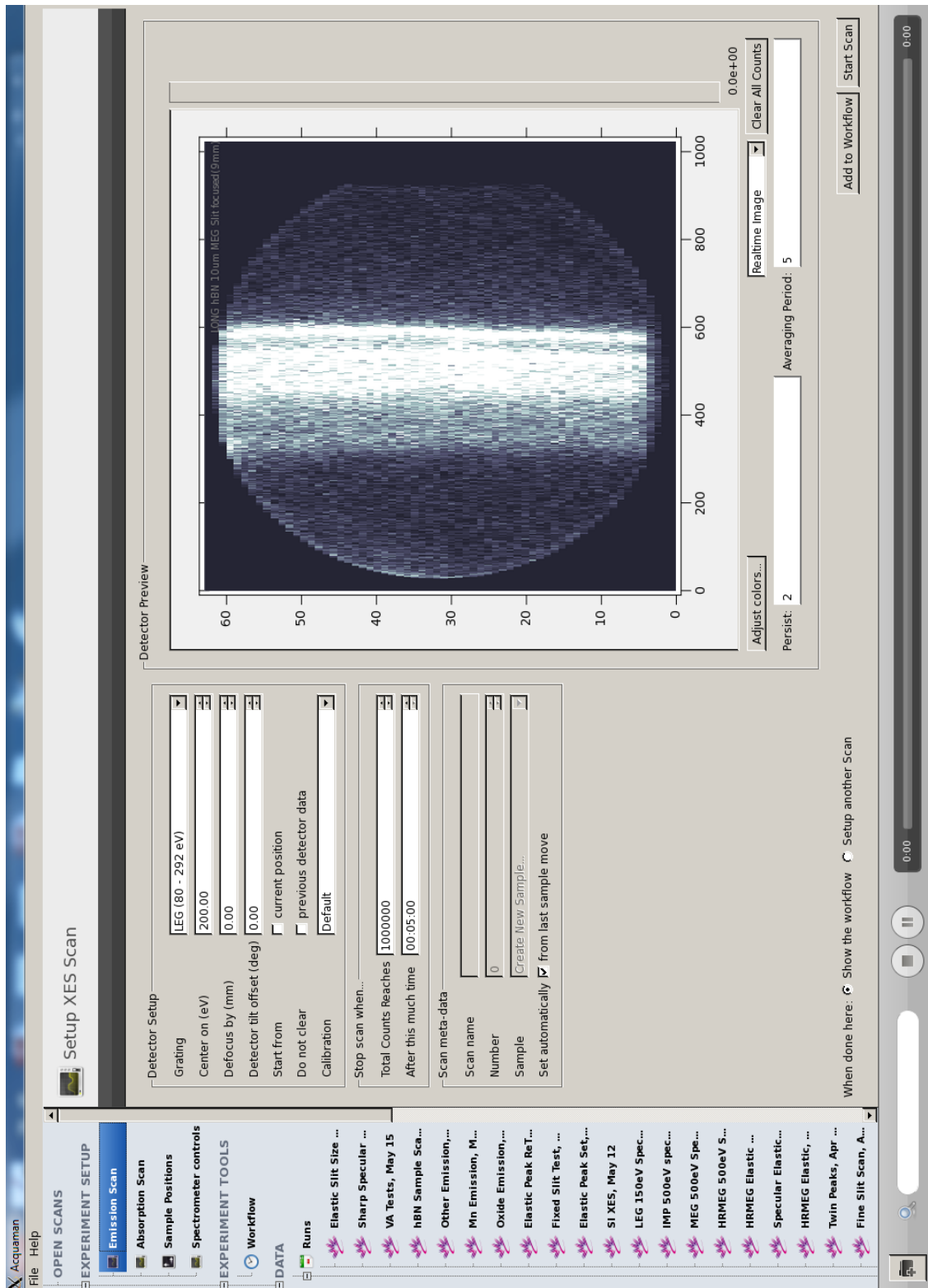


**Figure 5.57:** The Acquaman experiment setup screens allow the user to set up measurements using variables relevant to them instead of worrying about low level settings and motor positions.



**Figure 5.58:** Acquaman stores all user data in a searchable, visual library for easy sorting and browsing.



**Figure 5.59:** Acquaman allows the user to queue a series of measurements, automatically handling sample re-positioning, spectrometer and beamline configuration and data collection.

# CHAPTER 6

## RESULTS

After the epic journey that preceded this section, its contents maybe a bit anticlimactic, as there is nothing left but to demonstrate that it *works*, and quantify its performance. While considering the next several plots, it is hoped that the reader will keep the journey leading up to this point in mind and consider carefully the fact that, in the end, it *does* work.

With the endstation still under commissioning, two-thirds of the optics still being manufactured, and the technical problems that the Canadian Light Source has encountered over the last year, the results given below must still be considered as preliminary. As more beam time and higher currents become available, more and more will be possible with this instrument. Additional refinement of the beamline optics and continued development on the post-processing software will further enhance results. With the lessons learned during the first round of surveying and alignment, resurveying after the last two optics are installed will result in much finer optical alignment. That having been said, the initial results are impressive and suggest a productive future for this endstation.

### 6.1 X-ray Absorption Measurements

Absorption measurements are relatively straight forward from the point of view of the endstation. All that is required is a functioning transducer and the work of the scan is done by the beamline. Ensuring careful design in terms of geometry and electrical isolation, and minimizing noise is important to optimizing the collected signals, but in comparison to the challenges faced while commissioning the spectrometer these are simple tasks.

The results of initial commissioning measurements, as well as early absorption measurements by beamline team members, have been excellent. Signal to noise ratios are qualitatively

on par with other beamlines and the resolution is exceptional. TEY yield measurements are the simplest to execute from an instrumentation stand point and were among the first measurements ever collected by this endstation (Figure 6.1).

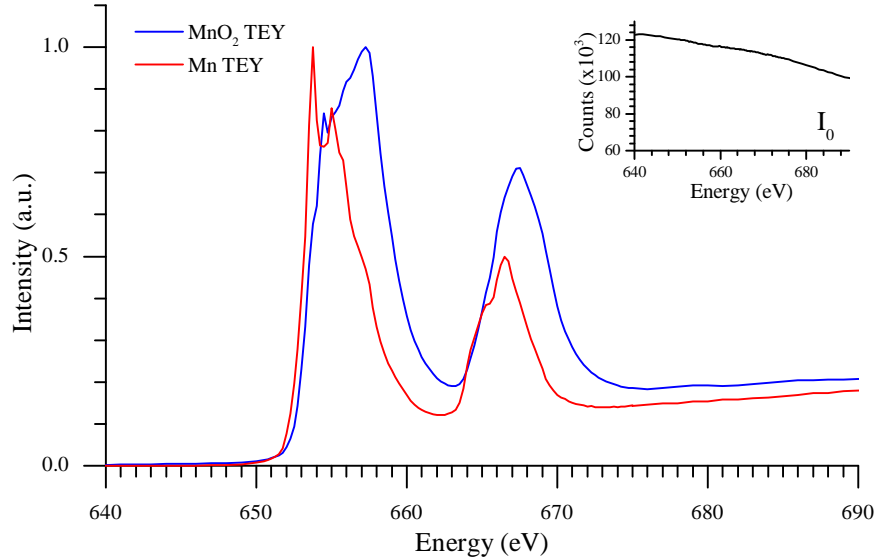


**Figure 6.1:** Example TEY XAS scans at the Mn K-edge for Mn and MnO<sub>2</sub>, collected with a 1 second dwell time at 0.25 eV steps. The mesh current,  $I_0$ , used to normalize these measurements is shown inset.

All signals, TEY, TFY, PFY and the normalization beamline current  $I_0$  are collected by one multichannel scaler to allow for easy synchronous measurement. All three measurements can be taken simultaneously, although the experimenter must consider the effects of the TFY detector's high voltage bias in proximity to the sample if it is turned on during a TEY measurement. This effect can vary from nonexistent to dramatic depending on the electrical properties of the sample and the specific geometry. The inherently lower count rates produced by using the spectrometer to measure PFY require that technique to employ significantly longer dwell times. Excellent TEY and TFY measurements can be gathered at 0.5 s - 1.0 s dwell times, PFY often requires 30 s or more per point in order to accumulate sufficient counts to have acceptable statistics (Figures 6.2 & 6.3).

Since no beamline can provide completely consistent flux across a range of energies, the incident flux is measured during absorption scans by measuring the current generated by passing the beam through a 90% transmission gold mesh located after the last beamline mirror. This normalization current,  $I_0$ , is divided out of the measured absorption spectra

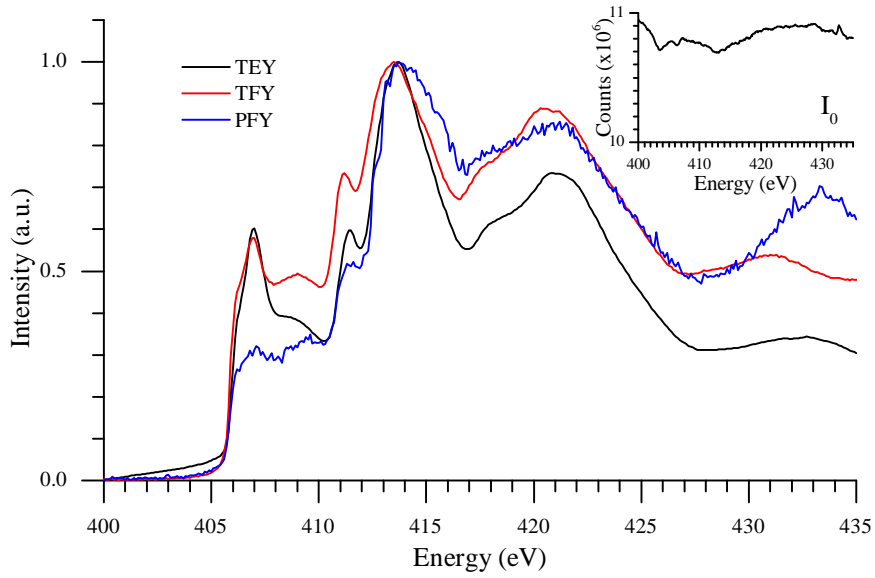


**Figure 6.2:** One XAS scan set of the N K-edge of a *h*-BN sample, collecting data by all three techniques, TEY, TFY and PFY simultaneously with a 20 second dwell time at 0.1 eV steps. The mesh current,  $I_0$ , used to normalize these measurements is shown inset.

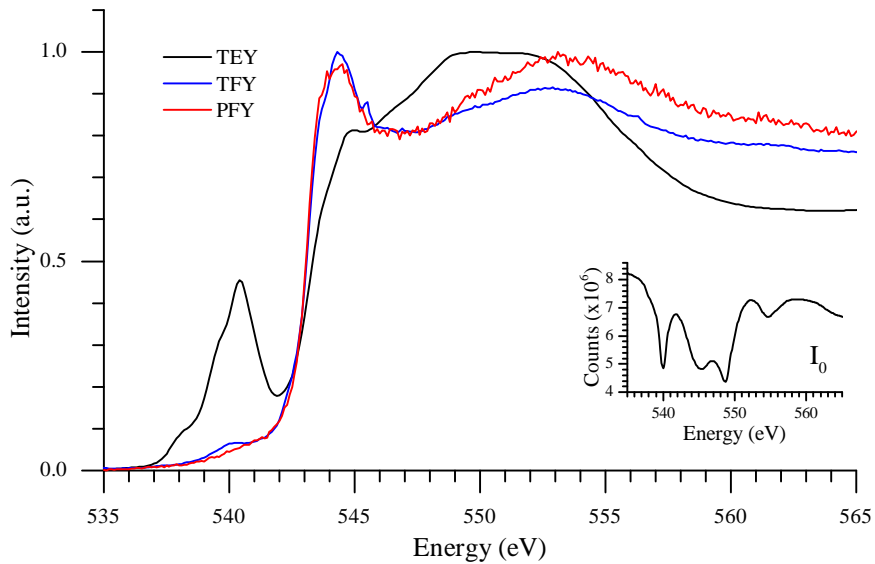


**Figure 6.3:** One XAS scan set of the O K-edge of a  $B_2O_3$  sample, collecting data by all three techniques, TEY, TFY and PFY simultaneously with a 10 second dwell time at 0.1 eV steps. The mesh current,  $I_0$ , used to normalize these measurements is shown inset, the significant loss of flux at the oxygen edge is due to oxidation of the beamline optics, a common problem for soft X-ray beamlines.

to correct for variations in the incident flux. A common cause of this variation in flux is absorption by the beamline optics. Inevitable oxidation and accumulation of small amounts of carbon on the beamline optics are the most significant causes. This contamination results in a substantial drop in flux passing over those edges. The significant variation in incident flux passing over the O K-edge, around 543 eV, can be seen in the inset plot in Figure 6.3.

## 6.2 Emission Reference Standards

One key metric to determine the performance of the spectrometer is to compare measurements of common reference materials taken with this endstation to measurements taken on other operational systems. Because this research group has done a significant amount of work with the spectrometer on beamline 8.0.1 at the Advanced Light Source in Berkeley (ALS BL 8.0.1), a large library of measurements were available for comparison. In addition, the results of the calculations completed during the optical design of this system rank it as one of the strongest competitors. For these reasons, comparisons of reference measurements were made to measurements from that spectrometer.

### 6.2.1 Relative Performance Considerations

A couple of factors must be taken into account when considering the following comparisons. The two spectrometers, at least as far as the first order gratings are concerned, are very similar, both being Rowland circle systems. The beamline and storage rings are quite different, however. The ALS is a much larger facility that operates a lower energy storage ring more well suited to soft X-ray production. The larger ring and greater space means that, not only does ALS BL 8.0.1 have an entire straight section to itself, but that straight section is significantly longer than the CLS straight section that REIXS shares with another beamline.

The end result of these differences is that the ALS BL 8.0.1 has a 4.5 meter insertion device with 89 periods while the REIXS beamline has a 1.6 meter undulator with 21 periods. This gives BL 8.0.1 more than a factor of 4 higher flux and nearly 18 times higher brightness. The ALS is currently operating at a constantly topped-up 500 mA, whereas the CLS is operating in decay mode, averaging 200 mA at this time. This yields roughly 12 times more

photons entering BL 8.0.1 than are entering REIXS, on average. The optical layout of the two beamlines differs significantly as well. That fact and the higher brightness are harder to factor in to the comparison.

The other key difference is that the REIXS XES spectrometer is operated in a slitless configuration at present, and the BL 8.0.1 spectrometer employs an entrance slit. This means that the process of sample alignment and the sensitivity of the experimental results to that alignment varies significantly. Variation in the samples themselves can play a role too, as no two samples are identical in surface geometry, mounting, oxidation state, contamination, etc. Since none of these measurements were taken by the same experimenters and of the exact same samples, there are numerous unknowns present.

In the end, the resolving power of non-resonant measurements is due purely to the optical characteristics of the respective spectrometers and can be reasonably compared in most cases, but the flux at the detector can vary dramatically.

### **6.2.2 Non-Resonant Emission**

The following spectra provide a good estimation of the relative resolving performance of the REIXS XES spectrometer in relation to the ALS BL 8.0.1 spectrometer. The relative exposure times and count rates are interesting but, keeping the notes from the previous section in mind, they are not particularly informative. However, due to the significant difference in incident flux, the fact that a count rate for a measurement on REIXS can come within an order of magnitude of a similar measurement on BL 8.0.1 speaks well of the relative efficiency of the REIXS beamline and spectrometer, and the ease of sample alignment afforded by the REIXS XES slitless configuration.

Several reference standards were measured at a variety of energies to give an idea of the relative performance throughout the operating energy range of the spectrometer. Due to the as yet undelivered HEG and HRMEG, the performance at the oxygen edge and above (525 eV+) is limited.

Non-resonant emission spectra from lighter elements toward the low end of the soft X-ray spectrum tend to have rather broad natural line widths and very little detail. The hexagonal boron nitride (*h*-BN) B K-edge emission spectra shown in Figure 6.4, an example of such a

system, are not a challenge for the resolving power of either of the spectrometers discussed here. The measurement from the LEG on the REIXS XES endstation was accumulated over 11 minutes at an average count rate of 175 counts per second as compared to 15 minutes at 227 counts per second for that from grating #2 on ALS BL 8.0.1. During the design of the LEG, the decision was made to reduce the resolution in favor of higher efficiency, since these typically broad features are easily resolved without the extremely high resolution that is achievable at lower energies. This higher efficiency combined with the improved statistics resulting from a similar number of counts being distributed over fewer pixels allows the REIXS LEG to compete extremely well with the ALS BL 8.0.1 grating #2.

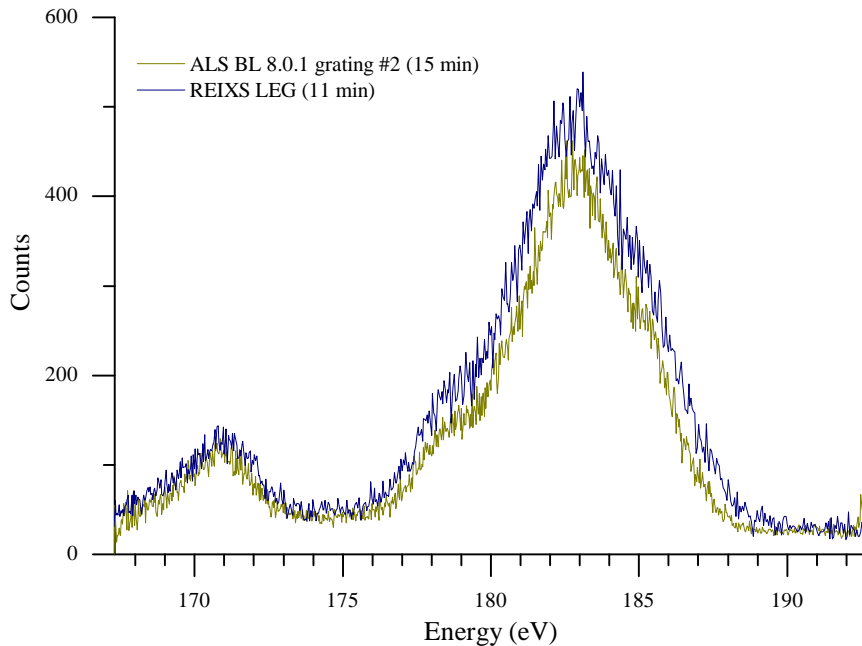


**Figure 6.4:** *h*-BN B K-edge emission spectra collected on REIXS with the LEG (11 min, 175 cts/s) versus ALS BL 8.0.1 with grating #2 (15 min, 227 cts/s).

Figure 6.5 shows the N K-edge emission from that same *h*-BN sample. The REIXS XES spectrum was collected with the MEG in 5 minutes at 962 counts per second versus 60 seconds with ALS BL 8.0.1 grating #4 at 2181 counts per second. *h*-BN was measured frequently during the commission process because it has a relatively high photon yield and it has a sharp feature in its emission spectrum. It was found to be one of the least reliable samples to measure, in that very small changes in sample alignment, or even moving the beam spot between different locations on the powder sample could change the emitted flux by a factor

of three or more and the relative height of that sharp feature would vary along with it. This may have to do with powder density, grain size and self absorption effects or variation in incident angle relative to the powder grains which are on the same scale as the beam spot, but a conclusive explanation has yet to be established. Regardless, all else being equal, *h*-BN can provide a very good qualitative indication of the resolving performance, if not by the sharp first peak, then by considering the second peak and its adjoining valleys. The fact that the REIXS XES flux is as comparable as it is, is likely due to sample alignment issues along with the fact that the measurement at BL 8.0.1 was taken with the lower efficiency, higher resolution grating four which would be roughly equivalent to the REIXS XES HEG, when it arrives.

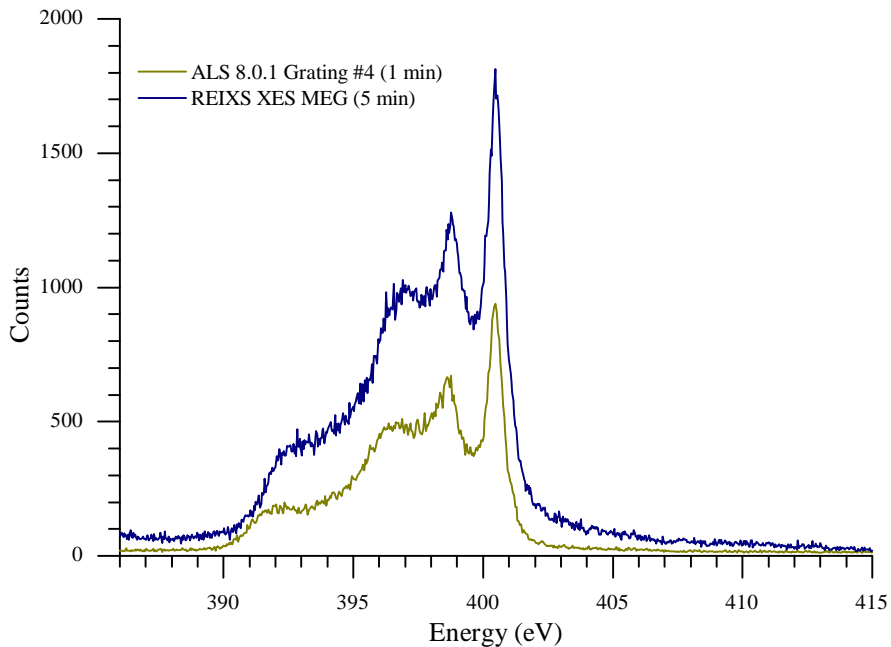


**Figure 6.5:** Comparison of an *h*-BN nitrogen emission spectra collected with the REIXS MEG (5 min, 962 cts/s) compared to a measurement with ALS BL 8.0.1. grating #4 (1 min, 2181 cts/s).

The final selection of non-resonant emission spectra (Figure 6.6) is a measurement of the O K-edge emission for a number of different oxide samples comparing the relative performance of the three different gratings currently available on the REIXS XES endstation. Once available, the HEG and HRHEG will provide even better resolution at this energy and likely higher efficiency due to their oxidation resistant platinum coatings as compared to the nickel

coatings of these three gratings which has been shown to be heavily oxidized (see Section 5.1.1). A wide selection of gratings provides the users of this instrument with many options to optimize the relative efficiency and resolution to their experiments, to acquire the required data in the least possible time.

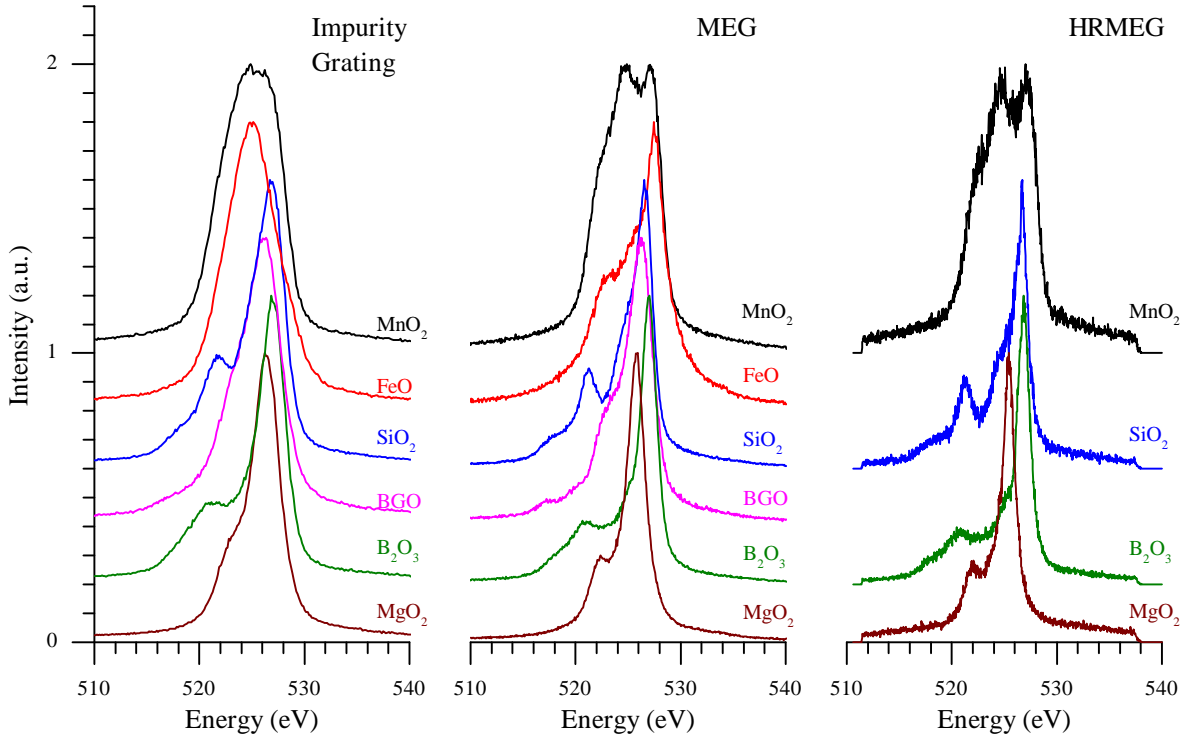


**Figure 6.6:** A series of oxide O K-edge emission spectra collected with each REIXS XES grating, demonstrating the different resolutions available. Due to the lower relative efficiency of the HRMEG, not all measurements were feasible with that grating.

Due to the low flux, not all samples could be reasonably measured with the high resolution 3<sup>rd</sup> order grating (HRHEG), and the measurements that were conducted with it required between one and four hours to be accumulated. The low background count rates and mechanical stability of the system make the results of such long scans quite impressive. Table 6.1 lists the average counts rates at the detector during the measurements shown in Figure 6.6, providing an indication of the relative efficiency of each grating at the O K-edge. The changing current in the storage ring was taken into account by normalizing to the maximum current (170 mA) at the time that these measurements were conducted.

**Table 6.1:** Average count rates at the detector for the emission measurements in Figure 6.6 (normalized to 170 mA ring current).

	IMP	MEG	HRMEG
	(cts/s)	(cts/s)	(cts/s)
MgO <sub>2</sub>	928	354	14
SiO <sub>2</sub>	2456	792	27
BGO	124	41	n/a
MnO <sub>2</sub>	1257	420	20
FeO	726	154	n/a
B <sub>2</sub> O <sub>3</sub>	2750	1036	41

### 6.2.3 Resonant Emission

RIXS is a more advanced and time consuming technique, and these measurements are typically only conducted on samples of particular interest, not on common reference samples, making comparison difficult. A series of RIXS measurements collected on ALS BL 8.0.1 for one readily available sample was found. This last set of comparative emission spectra presented is a series of RIXS measurements of FeO, comparing results from 2-5 minute measurements with the REIXS XES high efficiency low resolution Impurity grating to 5-10 minute measurements from the higher resolution BL 8.0.1 grating #4. An FeO TEY absorption scan is shown inset, with markers denoting the energies excited during the RIXS scans.

The relative energy between the two beamlines and spectrometers was not carefully calibrated, and as such some variation in the excitation energies and resulting spectra are expected. These results are presented only as a qualitative performance comparison.

The flux at the detector at the ALS was 2-3 time higher. The use of the high efficiency grating on the REIXS spectrometer is the likely cause of this very favorable comparison. Again, the yet to be delivered HEG would be the likely grating choice for this measurement, having significantly higher resolution at this energy.

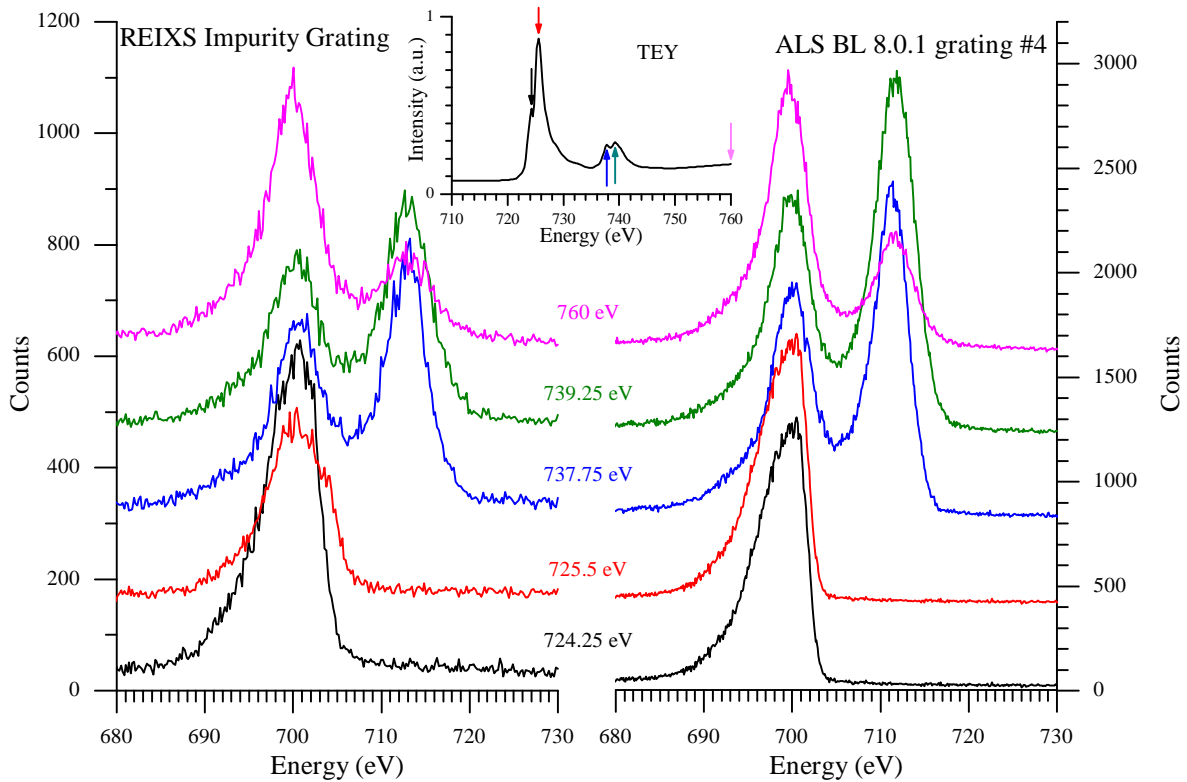


**Figure 6.7:** A series of RIXS measurements of the FeO Fe L-edge from the REIXS XES Impurity grating (left), with an XAS scan inset indicating the features excited. A similar FeO RIXS series collected on ALS BL 8.0.1 grating #4 (right).

### 6.3 Performance

Between the choice of spectrometer gratings and monochromator exit slit size, numerous combinations of resolving power, incident flux and spectrometer efficiency are possible. An excellent example of this is shown in Figure 6.8, which shows two nearly identical *h*-BN N K-edge emission spectra, one using the low resolution high flux Impurity grating with a small monochromator exit slit, and the other using a large monochromator exit slit and a higher resolution lower efficiency grating. Quantifying and understanding the spectrometer performance for different configurations will be critical to optimizing the experiments conducted on the endstation.

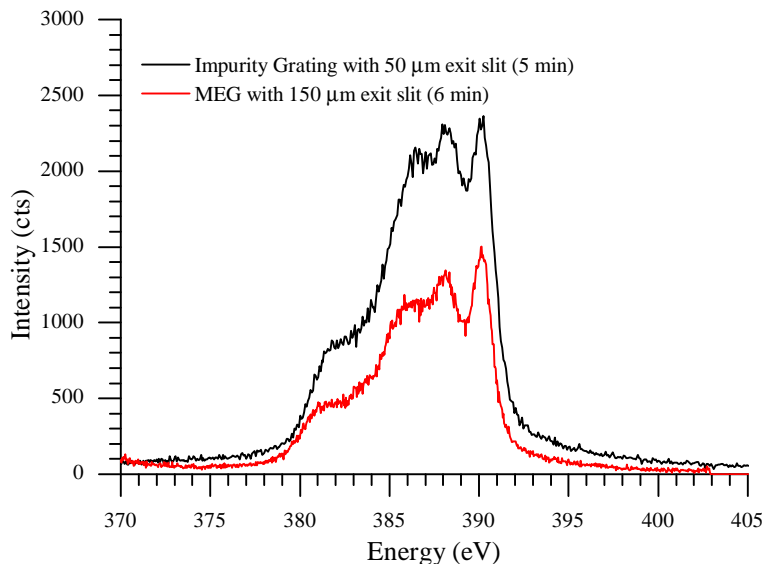


**Figure 6.8:** *h*-BN N K-edge emission spectra collected with nearly identical flux at the detector and similar resolution using two different spectrometer configurations: MEG with a 150  $\mu\text{m}$  monochromator exit slit for 6 minutes at 848 cts/s versus the Impurity grating with a 50  $\mu\text{m}$  monochromator exit slit for at 1016 cts/s.

### 6.3.1 Resolving Power

Because of the heavy demands placed on the limited available beamtime, it was not feasible to rigorously measure the performance of every useful combination of system parameters. An attempt was made to accurately gauge the ideal performance of the system, as well as collecting additional supplementary information to aid in the understanding of the impact of all relevant factors.

The starting point was to complete a survey of the resolving power of the spectrometer for an ideal 20-25  $\mu\text{m}$  source point. Figure 2.15 shows that a monochromator exit slit of 25  $\mu\text{m}$  will deliver a source spot full width of approximately that size. A polished Si substrate was used to create a sharp elastic peak, the bandwidth of which should be due to the monochromator resolution alone, and it should not be related to the electronic states in the sample. Such elastic peaks are roughly Gaussian (see Figure 6.9). By measuring the FWHM and deconvoluting the known monochromator bandwidth the resolution of the spectrometer can be determined (see Appendix A for details). Figure 6.10 show the results of these measurements for the currently installed gratings, plotted against the theoretical resolving power

based on the calculations performed during the optical design of the spectrometer<sup>1</sup>.

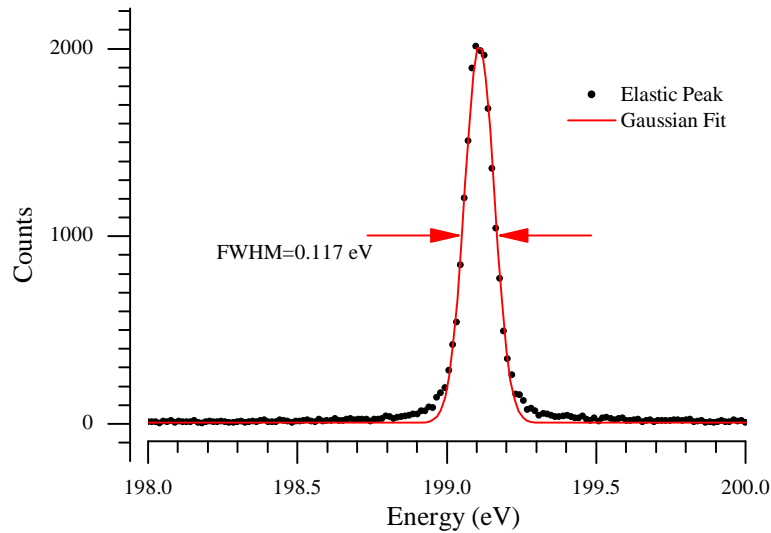


**Figure 6.9:** The elastic peak recorded at 200 eV using the MEG and a 50  $\mu\text{m}$  monochromator exit slit, and the Gaussian fit to it.

Adjustments to the originally predicted resolving powers were required to account for the fact that since that original design was completed, the detector choice changed twice. Since it proved mechanically unfeasible, a 20  $\mu\text{m}$  CCD detector was abandoned early in the mechanical design process in favor of an asymmetric MCP detector with roughly 40-50  $\mu\text{m}$  x 80-100  $\mu\text{m}$  resolution that could be operated in either orientation. The need to improve the detector mounting and shielding lead to the abandonment of the asymmetric detector in favor of a square 80-100  $\mu\text{m}$  resolution MCP. The theoretical resolving power plotted in Figure 6.10 reflects this change. The energy range across which the theoretical resolving power is plotted indicates the true accessible range of each grating based on the current mechanical limits of the system. The MEG and HRHEG high energy limit continues well beyond the plotted area but their usefulness is limited much above the oxygen K-edge (525 eV).

The results obtained are reasonably consistent, but none of the gratings has, as yet, achieved the theoretically predicted performance. There are a variety of reasons for this. Each grating will have different levels of figure error, line density variations, and other aberrations. The current mechanical limits prevents the MEG from reaching ideal alignment which could be impacting its performance. This will be resolved when the remaining two

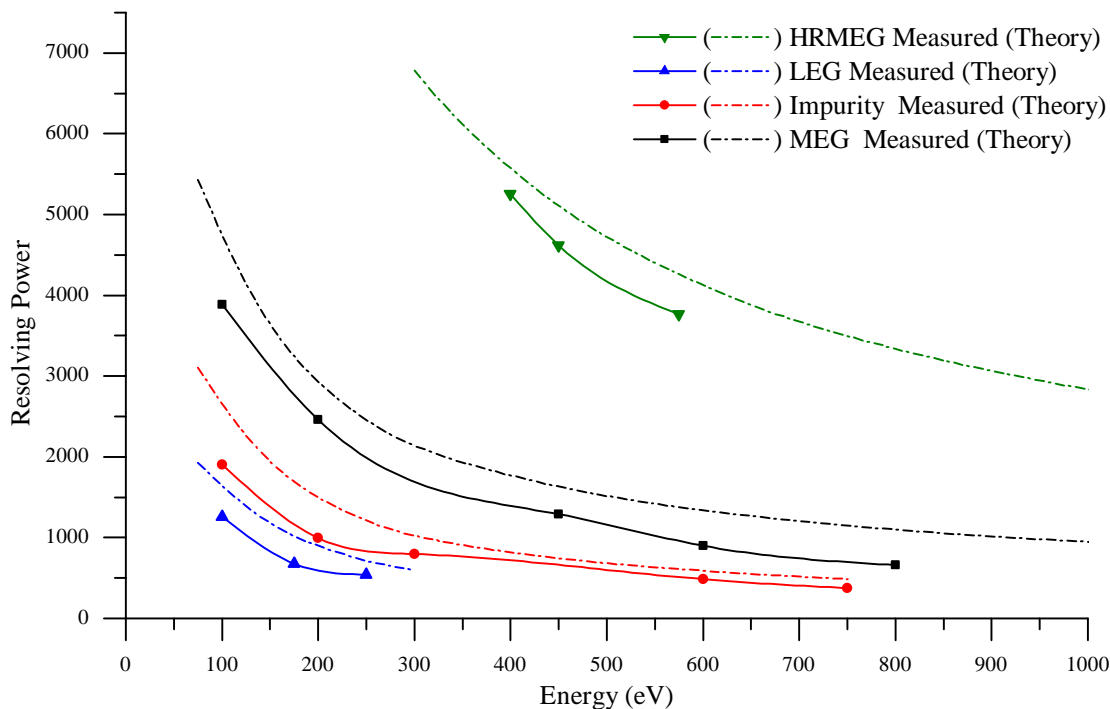


**Figure 6.10:** The resolution of the REIXS XES spectrometer in its current configuration as determined by FWHM measurements of elastic peaks from  $25 \mu\text{m}$  exit slit (see Appendix A). Predicted theoretical performance over the entire accessible energy range is plotted for comparison.

gratings are installed. Experiments conducted with a temporary entrance slit suggest that the current slitless configuration is impacting the resolving power as well (see Section 5.3.4). Efforts continue to improve the resolution, both by continued refinement of the spectrometer alignment as well as improvement to the beamline alignment to further optimized the spot size and profile. The reintroduction of a new entrance slit design is being considered, however the final results of beamline fine tuning will determine if this is required. In addition, the CLS is currently looking at reconfiguring the ring for a high tune operating mode<sup>69</sup> that has the potential to further reduce the beam spot size delivered by the REIXS beamline. The performance of all gratings is expected to continue to improve as beamtime is available for continued alignment, and with the complete and detailed resurvey that will take place during the installation of the remaining two gratings. Despite all this, the performance so far is excellent.

Two changes occur as the monochromator exit slit is opened. The incident bandwidth

increases, and so does the spot size on the sample (see Figure 6.11). Due to the current slitless configuration, the beam spot is the optical source of the spectrometer, so a larger beam spot means a lower spectrometer resolving power.

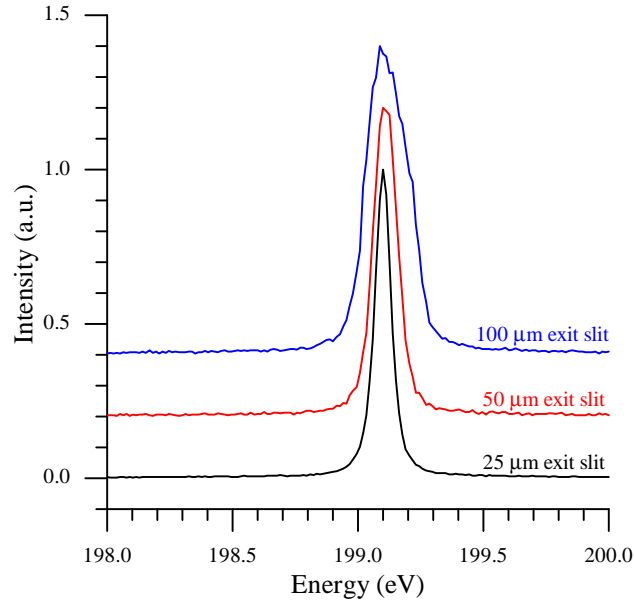


**Figure 6.11:** The effect of different monochromator exit slit sizes on the width of an elastic peak at the detector. The increase in peak width is due to both a larger beam spot (source size) and reduced incident resolution (i.e., the peak *is* broader).

For non-resonant emission measurements that rely on excitation energies well above the elemental edge, the incident bandwidth is unimportant and opening the slit as wide as possible without degrading the resolution beyond a desirable level is the key to maximizing throughput. For the vast majority of these non-resonant emission measurements, the natural line widths of the emitted spectra are wide enough that little impact is seen in the spectra when going from a 25  $\mu\text{m}$  to a 50  $\mu\text{m}$  exit slit, and going to a 100  $\mu\text{m}$  exit slit has only a small impact. The effective resolving power of the spectrometer for all four gratings with 25  $\mu\text{m}$ , 50  $\mu\text{m}$  and 100  $\mu\text{m}$  monochromator exit slits was measured at several energies (see Figure 6.12).

For some measurements, such as the broad features of a Si L-edge, a 500  $\mu\text{m}$  exit slit results in only a slight change in the recorded emission spectra (Figure 6.13).

For resonant excitation, a low incident bandwidth is critical, making a small monochromator exit slit desirable. This would make the use of the highest possible efficiency grating,

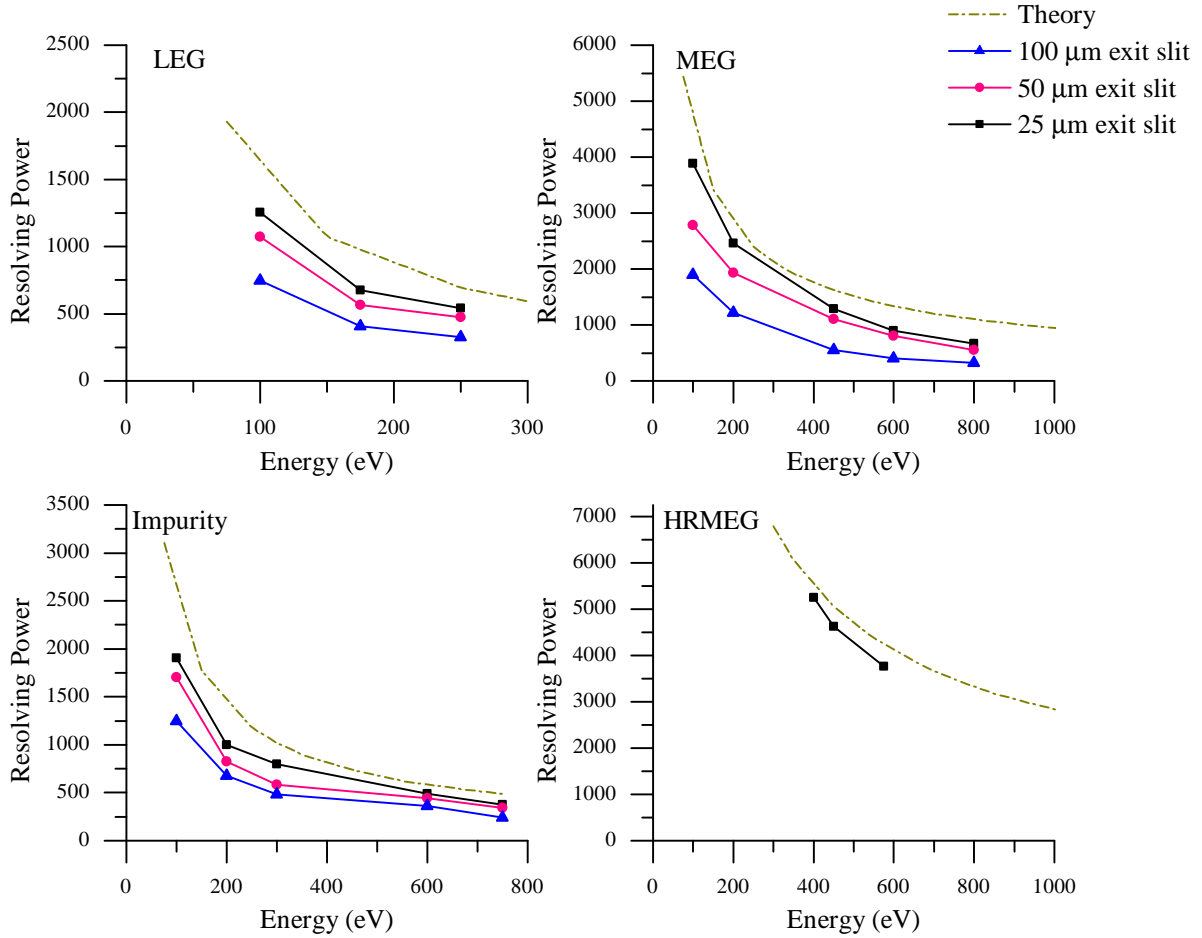


**Figure 6.12:** The resolution of the spectrometer for different monochromator exit slits. The monochromator contribution to the line widths has been removed, the change is only due to the change in source size.

with an acceptable resolution, ideal. This is exactly the case for the measurements shown in Figure 6.7. The problem with this approach is that RIXS spectra tend to have much sharper features than non-resonant emission spectra making very high resolution also desirable. In fact, high resolution RIXS measurements were the motivation behind including the 3<sup>rd</sup> order gratings in the design. There is no way around this unfortunate trade off. Higher resolution will always come at the cost of lower flux, and the only option is to minimize noise levels and maximize stability to allow for the use of very long accumulation times to achieve acceptable spectra when such high resolution measurements are required.

Compounding this challenge is the fact that the monochromator exit slit size will impact higher resolution gratings more than low resolution gratings. This can be understood by

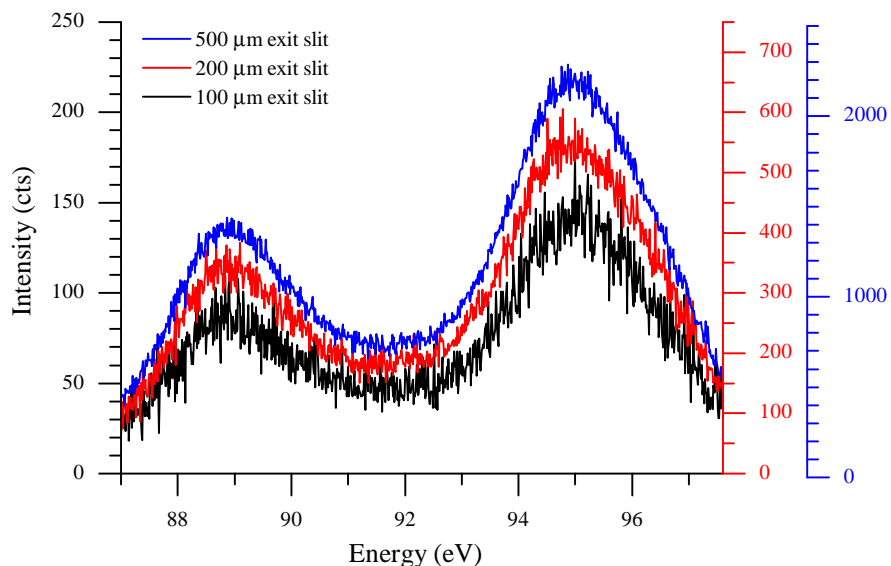


**Figure 6.13:** A series of SiO<sub>2</sub> emission spectra collected at three different monochromator exit slit sizes. Each spectrum was accumulated for the same length of time. The natural line width of the features is so much larger than the resolution at this energy that the only noticeable difference is the improved statistics with a large slit and more flux.

studying Figure 6.14, which shows that for the lower resolution impurity grating, the total resolution of the system is determined almost entirely by the spectrometer resolution, meaning that opening the monochromator exit slit will increase the source size but the change in incident bandwidth will not have a significant impact.

For a high resolution grating, particularly the HRMEG, which is approaching the resolution of the monochromator, increasing the exit slit size will not only increase the slit size but will also result in the monochromator bandwidth dominating the total resolution. There is no avoiding this. Operating slitless is already the ideal case for this type of measurement. A spectrometer entrance slit will fix the source size at the cost of flux so, as is usually the case, flux must be traded for improved resolution (Figure 5.44).

### 6.3.2 Efficiency and Flux

It is difficult to quantify the efficiency of a spectrometer due to the lack of a monochromatic source of well known intensity to compare the flux at the detector to. Even using a photodiode or channeltron to measure the total fluorescence signal from a sample will include a

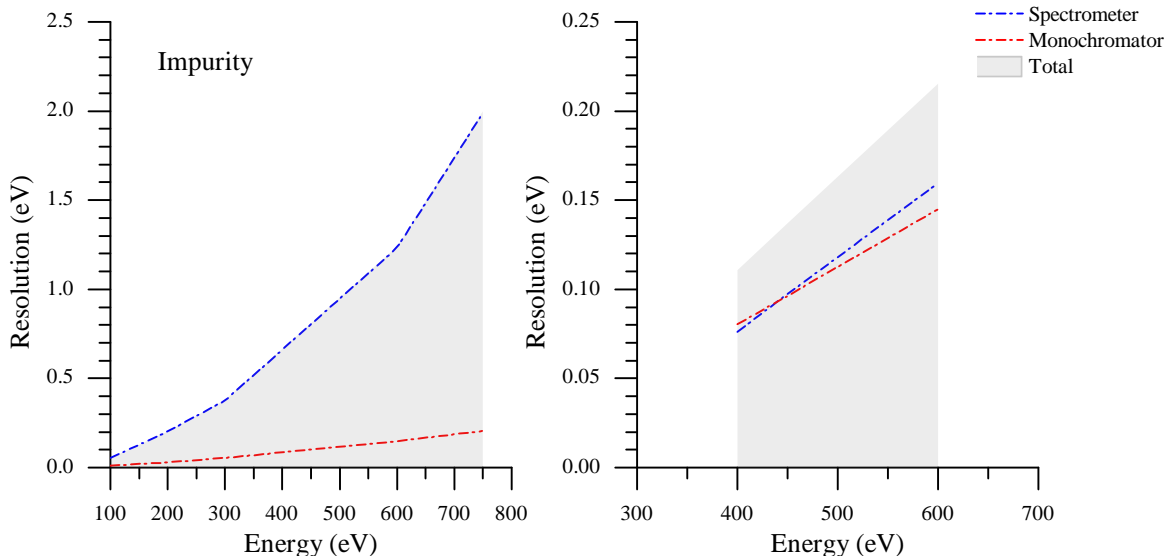


**Figure 6.14:** The contributions to the total system resolution from the monochromator and spectrometer for the highest and lowest resolution gratings.

large number of photons outside the bandwidth of the spectrometer, that vary with incident energy, adding a non-uniform background that cannot be factored out. Sharp monochromatic elastic peaks are far too sensitive to incidence angle to be used for this purpose. A second spectrometer with a known efficiency looking at the same sample could be used, but such an approach is not practical. A Silicon Drift Detector (SDD) may serve this purpose, if available and if the quantum efficiency was well known. Measurements of this type may be attempted in the future.

The absolute efficiency is not an important quantity, strictly speaking, as the fluorescence yield of a particular sample is rarely known before a measurement is attempted. This makes calculating expected count rates for a measurement impossible. During an experiment, the only use for spectrometer efficiency data is to aid in the selection of the grating most suited to a particular measurement. With that in mind, using one grating as a reference with a ‘known’ efficiency of ‘1’ allows the determination of the relative efficiency of different gratings with respect to each other. The impurity grating, with the highest average efficiency is taken as this reference and the other gratings are compared to it at a number of emission edges (Figure 6.15). There are still some complexities that are overlooked, such as difference in background noise and stray light levels due to the different mechanical configurations, but

these are relatively minor contributors to the count rate in most cases.

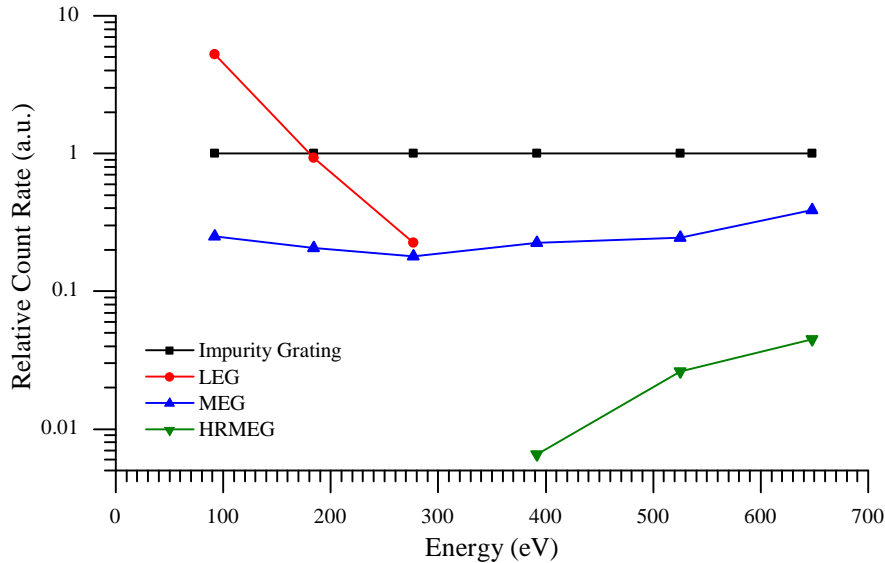


**Figure 6.15:** The flux at the detector for a number of emission edges relative to that delivered by the impurity grating.

This measurement takes into account the complete efficiency of the spectrometer and is not influenced by the performance of the beamline. Its utility is in the ability to compare the true expected relative flux to the resolving power (Figure 6.10) for the different grating choices available. It includes not only the diffraction efficiencies for the gratings that were measured directly (Figures 5.2-5.4), but also detector quantum efficiency and the geometric efficiency of the spectrometer, which differs for each grating and energy.

In terms of absolute performance, it is difficult to do much better than the qualitative comparisons to a similar instrument already given in Section 6.2.2.

By way of a verification of expected performance, known beamline flux from Figure 2.14 ( $\sim 10^{12}$ ), typical fluorescence yields ( $\sim 0.01 - 0.1$ )<sup>70</sup>, the measured gratings diffraction efficiency ( $\sim 0.1 - 0.3$ ), approximate detector quantum efficiency ( $\sim 0.3$ ) and known spectrometer acceptance angles ( $\sim 10^{-7} - 10^{-6}$ ) can be used to make an order of magnitude estimate of the expected count rates. This is of limited use due to the wide range of variables and number estimates involved, but when carried out it yields  $\sim 10^1 - 10^3$  for the first order gratings and  $\sim 10^0 - 10^2$  for the third order gratings which is in good agreement with the observed count rates.

## **Part III**

### **Conclusion**

# CHAPTER 7

## CONCLUSION

### 7.1 The Design

The optical design for this spectrometer was based on the proven, solid performance of Rowland circle geometry, with an added novel approach to achieve higher resolution by deliberate optimization of higher diffraction orders. Consideration and calculation of both the resolution and diffraction efficiency allow for a careful balance between these two key factors to be maintained.

The mechanical design to support this optical system was far from trivial. The combined requirements of the standard and high resolution gratings results in an unusually long required range of motion. There were significant oversights made during the design process, partially due to the rushed nature of its completion and partially due to attempts to simplify an already complex mechanical system. This resulted in an extended construction and commissioning process that has only recently born fruit.

### 7.2 Construction and Commissioning

The construction and commissioning of this instrument was far from smooth. Numerous delays and setbacks were encountered along the way due to initial design oversights, complications and delays with procurement, and unforeseen difficulties associated with novel applications of existing systems. In spite of all the issues encounter, very little in the way of performance had to be sacrificed in the course of devising solutions to the encountered problems. The only significant loss was the ability to rotate the detector to select a higher resolution mode. This change had an upside, however, since the detector head was changed

to a symmetric sensor increasing the active area and helping to compensate for lower available flux. While the process took longer than expected (and is still outstanding, awaiting the remaining optics), it has been remarkably successful.

## 7.3 Performance

Because the endstation is located at a smaller synchrotron facility, there are inherent limitations on its overall performance as compared to similar systems at other facilities. In spite of this, careful design of the optics and adaption of the endstation to slitless operation to take full advantage the excellent beamline design has resulted in an instrument that is able to compete with the any in the world, and may even be superior in some respects. The calculations performed during the optical design of the endstation made it clear that the spectrometer on beamline 8.0.1 at the Advanced Light Source is one of the best general-use soft X-ray emission instruments in operation and is being operated at one of the best facilities in the world for the soft X-ray energy range. The results presented in Section 6 show that our instrument does quite well when compared to the spectrometer on beamline 8.0.1 of the ALS.

The novel third order gratings provide resolving powers that were unheard of at the time of their design. Since then, an extremely high resolution instrument, the SAXES spectrometer, has come online at on the ADDRESS beamline of the Swiss Light Source<sup>71</sup> that exceeds that resolving performance by a significant margin. This massive instrument is more than twice the size of the REIXS XES endstation and has produced some impressive RIXS measurements<sup>72</sup>. The REIXS XES endstation will not be able to match the resolution of SAXES, but the third order gratings will provide access to many of the same experimental systems, in a smaller package and while still providing high performance non-resonant emission spectroscopy.

## 7.4 Future Development

The most pressing issue is the installation and commissioning of the remaining two gratings. Once that is complete, the endstation will be opened to peer-reviewed access. Further devel-

opment will need to be worked in around that user program which will slow it, but not stop it. The next significant upgrade to the endstation will be the addition of a silicon drift detector (SDD) to allow faster PFY and improved TFY measurements. A UHV compatible SDD detector is currently in development at the CLS and once complete, that system will be ported over to both REIXS endstations. If user interest is sufficient, the addition of a basic optical spectrometer for XEOL measurements will be added to the system. Work is continuing on the VLS spectrometer with the goal of using the lessons learned during to commissioning of the rest of the endstation to ensure a smooth commissioning of that instrument. There is a significant potential for improvement in functionality, usability and data quality through continued development of the Acquaman software suite, and this will be a top priority as resources become available. The main focus in the immediate future, however, will be the application of this instrument to research both through the support of this research group's efforts and through the development of an external user community. At the time of this writing, three publications have been submitted with data from this endstation and publication quality data has been successfully collected on several other projects (see Appendix B). The first external group to use the system successfully grew samples in the prep chamber and transferred them under vacuum to the endstation where they were measured. This is only the beginning of what will become a very successful and prolific research tool for the materials science community in Canada and around the world.

## REFERENCES

- [1] D Muir. Design of a high performance soft X-ray emission spectrometer for the REIXS beamline at the Canadian Light Source. Master's thesis, University of Saskatchewan, 2006.
- [2] M Boots. *Designing and optimizing gratings for soft X-ray diffraction efficiency*. PhD thesis, University of Saskatchewan, 2012.
- [3] M Boots, D Muir, and A Moewes. Optimizing and characterizing grating efficiency for a soft X-ray emission spectrometer. *Journal of Synchrotron Radiation*, 20(2):272, Mar 2013.
- [4] A Thompson, D Vaughan, et al. X-ray data booklet. Lawrence Berkeley National Laboratory, 2001. 2nd Edition.
- [5] FR Elder, AM Gurewitsch, RV Langmuir, and HC Pollock. Radiation from electrons in a synchrotron. *Physical Review*, 71(11):829, 1947.
- [6] DH Tomboulion and PL Hartman. Spectral and angular distribution of ultraviolet radiation from the 300-Mev cornell synchrotron. *Physical Review*, 102(6):1423, 1956.
- [7] JA Clarke. *The science and technology of undulators and wigglers*. Oxford University Press Oxford, 2004.
- [8] W Peatman. *Gratings, Mirrors and Slits*, chapter 3. Gordon and Breach Science, Australia, 1997.
- [9] K Kim. Characteristics of synchrotron radiation. In *AIP Conference Proceedings*, volume 184, page 565, 1989.
- [10] R Bartolini. Synchrotron radiation energy flux, April 2013. [http://en.wikipedia.org/wiki/File:Synchrotron\\_radiation\\_energy\\_flux.png](http://en.wikipedia.org/wiki/File:Synchrotron_radiation_energy_flux.png).
- [11] Canadian Light Source. Facility photos, April 2013. <http://www.lightsource.ca/media/photos/index.php>.
- [12] Canadian Light Source. Resource book, April 2013. <http://www.lightsource.ca/education/pdf/resourcebook.pdf>.
- [13] LO Dallin, I Blomqvist, M de Jong, E Hallin, DS Lowe, and RM Silzer. The canadian light source: An update. In *Particle Accelerator Conference, 2001. PAC 2001. Proceedings of the 2001*, volume 4, page 2680. IEEE, 2001.

- [14] E Hallin, M de Jong, T Ellis, W Thomlinson, and M Dalzell. Technical report: Canadian light source facility update. *Synchrotron Radiation News*, 19(6):7, 2006.
- [15] L Dallin, I Blomqvist, M De Jong, D Lowe, and M Silzer. The canadian light source. In *Proceedings of the Particle Accelerator Conference, 2003*, volume 1, page 220. IEEE, 2003.
- [16] L Dallin. Synchrotron light source magnets. Approved Document 5.2.31.2, Canadian Light Source Inc., February 2001.
- [17] DT Attwood. *Soft X-rays and extreme ultraviolet radiation: principles and applications*. Cambridge university press, 2000.
- [18] S Sasaki, K Kakuno, T Takada, T Shimada, K Yanagida, and Y Miyahara. Design of a new type of planar undulator for generating variably polarized radiation. *Nuclear Instruments and Methods in Physics Research Section A: Accelerators, Spectrometers, Detectors and Associated Equipment*, 331(1):763, 1993.
- [19] M Sigrist. Photon energy and polarization lookup tables for REIXS–EPU. Approved Document 30.2.25.2, Canadian Light Source Inc., September 2008.
- [20] M Sigrist. Magnetic design of a 75 mm APPLE II undulator. Approved Document 6.2.25.3, Canadian Light Source Inc., April 2006.
- [21] F He. Preliminary design report for the resonant elastic and inelastic soft X-ray scattering (REIXS) beamline. Approved Document 30.2.69.1, Canadian Light Source Inc., June 2006.
- [22] F He. Technical specification for the REIXS beamline vacuum components. Approved Document 30.8.33.1, Canadian Light Source Inc., September 2006.
- [23] M Itou, T Harada, and T Kita. Soft X-ray monochromator with a varied-space plane grating for synchrotron radiation: design and evaluation. *Applied optics*, 28(1):146, 1989.
- [24] H Rabus, F Scholze, R Thornagel, and G Ulm. Detector calibration at the PTB radiometry laboratory at BESSY. *Nuclear Instruments and Methods in Physics Research Section A: Accelerators, Spectrometers, Detectors and Associated Equipment*, 377(2):209, 1996.
- [25] M Krumrey, E Tegeler, Jo Barth, M Krisch, F Schäfers, and R Wolf. Schottky type photodiodes as detectors in the vuv and soft X-ray range. *Applied optics*, 27(20):4336, 1988.
- [26] J Barth, E Tegeler, M Krisch, and R Wolf. Characteristics and applications of semiconductor photodiodes from the visible to the X-ray region. In *Soft X-Rays Optics and Technology*, page 481. International Society for Optics and Photonics, 1986.
- [27] Opto Diode Corp. Axuv100g datasheet, April 2013. <http://www.optodiode.com/pdf/AXUV100G.pdf>.

- [28] EM Gullikson, R Korde, LR Canfield, and RE Vest. Stable silicon photodiodes for absolute intensity measurements in the vuv and soft X-ray regions. *Journal of Electron Spectroscopy and Related Phenomena*, 80:313, 1996.
- [29] CT Chen and F Sette. Performance of the dragon soft X-ray beamline. *Review of Scientific Instruments*, 60(7):1616, 1989.
- [30] HA Rowland. The concave diffraction grating. *Philosophical Magazine*, 13:469, June 1882.
- [31] T Harada and T Kita. Mechanically ruled aberration-corrected concave gratings. *Applied Optics*, 19(23):3987, 1980.
- [32] BJ Brown and IJ Wilson. Holographic grating aberration correction for a rowland circle mount. *Journal of Modern Optics*, 28(12):1587, 1981.
- [33] Quantar Technology Inc. *3300 Series Open-Face MCP/RAE Sensors Installation and Maintenance Manual*, 2000.
- [34] Harvard-Smithsonian Center for Astrophysics. Microchannel plate principles, April 2013. <http://ihea-www.cfa.harvard.edu/HRC/mcp/mcp.html>.
- [35] Quantar Technology. 3300/2400 operation manual. Technical report, October 2000. Rev E.
- [36] Quantar Technology. 2401b position analyzer manual. Technical report, October 2006. Rev G.
- [37] PA Redhead. Modeling the pump-down of a reversibly adsorbed phase. I. Monolayer and submonolayer initial coverage. *Journal of Vacuum Science & Technology A: Vacuum, Surfaces, and Films*, 13(2):467, 1995.
- [38] G Lee. Materials for ultra-high vacuum. Technical report, Fermi National Accelerator Lab., Batavia, IL (USA), 1989.
- [39] Y Ishikawa, Y Koguchi, and K Odaka. Outgassing rate of some austenitic stainless steels. *Journal of Vacuum Science & Technology A: Vacuum, Surfaces, and Films*, 9(2):250, 1991.
- [40] JF O'Hanlon. *A Users Guide to Vacuum Technology, 3rd Edition*. John Wiley & Sons, 2003.
- [41] M Wong. Review of papers regarding vacuum system and materials, March 2013. [http://home.fnal.gov/~mlwong/outgas\\_rev.htm](http://home.fnal.gov/~mlwong/outgas_rev.htm).
- [42] N Yoshimura, T Sato, S Adachi, and T Kanazawa. Outgassing characteristics and microstructure of an electropolished stainless steel surface. *Journal of Vacuum Science & Technology A: Vacuum, Surfaces, and Films*, 8(2):924, 1990.

- [43] N Yoshimura. Water vapor permeation through viton o ring seals. *Journal of Vacuum Science & Technology A: Vacuum, Surfaces, and Films*, 7(1):110, 1989.
- [44] AD Chew. Mechanical vacuum pumps. *CAS CERN Accelerator School, vacuum in accelerators: proceedings*, 3:43, 2007.
- [45] P Danielson. Knowing your effective pumping speed. *A Journal of Practical and Useful Vacuum Technology*, 2001.
- [46] RJ Elsey. Outgassing of vacuum materials I: A paper in our education series: The theory and practice of vacuum science and technology in schools and colleges. *Vacuum*, 25(7):299, 1975.
- [47] P Hofmann. <http://philiphofmann.net/>, March 2013.
- [48] G Levi. Combination of turbomolecular pumping stages and molecular drag stages. *Journal of Vacuum Science & Technology A: Vacuum, Surfaces, and Films*, 10(4):2619, 1992.
- [49] Dynapumps. Ion vacuum pumps, March 2013. <http://www4.nau.edu/microanalysis/Microprobe-SEM/Instrumentation.html>.
- [50] JH Wittke. Microprobe-sem instrumentation, March 2013. <http://www4.nau.edu/microanalysis/Microprobe-SEM/Instrumentation.html>.
- [51] Omega Engineering, Inc. High pressure & vacuum, March 2013. [www.omega.com/literature/transactions/volume3/high3.html](http://www.omega.com/literature/transactions/volume3/high3.html).
- [52] Operating Manual. Programming reference, models RGA100, RGA200, and RGA300 residual gas analyzer, 1996.
- [53] A Hunt, D Muir, and A Moewes. Studying 4d–4f transitions in Er using resonant inelastic scattering. *Journal of Electron Spectroscopy and Related Phenomena*, 144:573, March 2005.
- [54] JM Hollas. *Modern Spectroscopy, 4th Ed.* Wiley, 2004.
- [55] S Hüfner. *Photoelectron spectroscopy: principles and applications.* Springer, 2003.
- [56] JJ Sakurai. *Advanced quantum mechanics*, 1967.
- [57] O Fuchs, L Weinhardt, M Blum, M Weigand, E Umbach, M Bar, Clemens Heske, Jonathan Denlinger, YD Chuang, Wayne McKinney, et al. High-resolution, high-transmission soft X-ray spectrometer for the study of biological samples. *Review of Scientific Instruments*, 80(6):063103, 2009.
- [58] Physik Instrumente GmbH, Jan 2013. <http://www.physikinstrumente.com>.
- [59] T Pirling, G Bruno, and P J Withers. SALSA-A new instrument for strain imaging in engineering materials and components. *Materials Science and Engineering: A*, 437(1):139, 2006.

- [60] JH Underwood, EM Gullikson, M Koike, PJ Batson, PE Denham, KD Franck, RE Tackaberry, and WF Steele. Calibration and standards beamline 6.3.2 at the advanced light source. *Review of Scientific Instruments*, 67(9):3372, 1996.
- [61] NKS Lee, GH Yu, JY Chen, and A Joneja. Effect of mechanical alignment system on assembly accuracy. *Journal of Manufacturing Science and Engineering*, 125(3):595, 2003.
- [62] J Hoagland. Avoiding the ‘vertical load mistake’, December 2001. <http://www.isa.org>.
- [63] F He. Resonant elastic and inelastic soft X-ray scattering (REIXS) beamline conceptual design report. Approved Document 30.2.1.1, Canadian Light Source Inc., November 2005.
- [64] R Green. *Transition Metal Impurities in Semiconductors: Induced Magnetism and Band Gap Engineering*. PhD thesis, University of Saskatchewan, 2013.
- [65] MM van Schooneveld, R Kurian, Am Juhin, Kejin Zhou, Justine Schlappa, Vladimir N Strocov, Thorsten Schmitt, and Frank MF de Groot. Electronic structure of CoO nanocrystals and a single crystal probed by resonant X-ray emission spectroscopy. *The Journal of Physical Chemistry C*, 116(29):15218, 2012.
- [66] Argonne National Laboratory. Experimental physics and industrial control system home page, May 2013. <http://www.aps.anl.gov/epics/>.
- [67] Spallation Neutron Source. edm home page, May 2013. <http://ics-web.sns.ornl.gov/edm/>.
- [68] M Boots, D Chevrier, D Hunter, et al. The acquaman repository on github, May 2013. <https://github.com/acquaman/acquaman>.
- [69] L Dallin, T Summers, and D Bodnarchuk. Optimizing beam brightness at the canadian light source. In *Particle Accelerator Conference, 2007. PAC. IEEE*, page 920. IEEE, 2007.
- [70] JH Hubbell, PN Trehan, N Singh, B Chand, D Mehta, ML Garg, RR Garg, S Singh, and S Puri. A review, bibliography, and tabulation of K, L, and higher atomic shell X-ray fluorescence yields. *Journal of physical and chemical reference data*, 23(2):339, 1994.
- [71] G Ghiringhelli, A Piazzalunga, C Dallera, G Trezzi, L Braicovich, T Schmitt, VN Strocov, R Betemps, L Patthey, X Wang, et al. Saxs, a high resolution spectrometer for resonant X-ray emission in the 400–1600. *Review of scientific instruments*, 77(11):113108, 2006.
- [72] Th Schmitt, VN Strocov, K Zhou, Je Schlappa, C Monney, U Flechsig, and L Patthey. High-resolution resonant inelastic X-ray scattering with soft x-rays at the adress beamline of the swiss light source: Instrumental developments and scientific highlights. *Journal of Electron Spectroscopy and Related Phenomena*, 2013.

**Part IV**  
**Appendix**

# APPENDIX A

## RESOLVING POWER MEASUREMENTS

The resolving power of the spectrometer was determined by measuring a series of elastic peaks at different energies with each grating. The measurements are not always uniformly spaced due to difficulties in finding clean elastic peaks near emission edges. This is particularly difficult at and above the oxygen K-edge (525 eV) since oxygen is present in or on most available materials. As many energy points were taken as possible for each grating within the available experiemntal time.

In theory, the line width should be a function of the spectral width of the incident photons and the resolution of the spectrometer. Since both of these contributions are fit very well by Gaussian profiles, the resulting measured peaks will be convulsions of the two Gaussian contributions. Since the theoretical resolution of the beamline has been confirmed by gas phase absorption measurements, it can be taken as a known value and used to extract the contribution of the spectrometer in the recorded peak widths:

$$\sigma_{\text{spec}} = \sqrt{\sigma_{\text{total}}^2 - \sigma_{\text{mono}}^2} \quad (\text{A.1})$$

Applying the Rayleigh criterion, the resolution ( $\Delta E$ ) of the instrument is the FWHM of the monochromatic peak width which, for a Gaussian distribution, is:

$$\Delta E = \text{FWHM} = 2\sqrt{2 \ln 2} \sigma \quad (\text{A.2})$$

The following tables list the FWHM of the Gaussian profiles fit to the measured peaks, the known monochromator resolution, the resolution of the spectrometer resulting from the deconvolution:

$$\Delta E_{\text{Spec}} = \sqrt{\text{FWHM}^2 - \Delta E_{\text{mono}}^2} \quad (\text{A.3})$$

and the resulting measured resolving power of the spectrometer at each energy,  $E$ :

$$RP_{\text{spec}} = \frac{E}{\Delta E_{\text{Spec}}} \quad (\text{A.4})$$

## A.1 LEG Measurements

**Table A.1:** Measured resolving power of the LEG for a 25  $\mu\text{m}$  exit slit.

Energy (eV)	FWHM (eV)	$\Delta E_{\text{Mono}}$ (eV)	$\Delta E_{\text{Spec}}$ (eV)	$\text{RP}_{\text{Spec}}$
100	0.0803	0.0101	0.0797	1255
175	0.2600	0.0233	0.2590	676
250	0.4654	0.0398	0.4636	539

**Table A.2:** Measured resolving power of the LEG for a 50  $\mu\text{m}$  exit slit.

Energy (eV)	FWHM (eV)	$\Delta E_{\text{Mono}}$ (eV)	$\Delta E_{\text{Spec}}$ (eV)	$\text{RP}_{\text{Spec}}$
100	0.0951	0.0193	0.0931	1074
175	0.3120	0.0448	0.3087	567
250	0.5347	0.0764	0.5292	472

**Table A.3:** Measured resolving power of the LEG for a 100  $\mu\text{m}$  exit slit.

Energy (eV)	FWHM (eV)	$\Delta E_{\text{Mono}}$ (eV)	$\Delta E_{\text{Spec}}$ (eV)	$\text{RP}_{\text{Spec}}$
100	0.1395	0.0383	0.1342	745
175	0.4393	0.0886	0.4303	407
250	0.7850	0.1512	0.7702	325

## A.2 Impurity Grating Measurements

**Table A.4:** Measured resolving power of the Impurity grating for a 25  $\mu\text{m}$  exit slit.

Energy (eV)	FWHM (eV)	$\Delta E_{\text{Mono}}$ (eV)	$\Delta E_{\text{Spec}}$ (eV)	$\text{RP}_{\text{Spec}}$
100	0.0534	0.0101	0.0525	1907
200	0.2027	0.0285	0.2007	996
300	0.3790	0.0524	0.3753	799
600	1.2416	0.1481	1.2327	487
750	1.9988	0.2070	1.9881	377

**Table A.5:** Measured resolving power of the Impurity grating for a 50  $\mu\text{m}$  exit slit.

Energy (eV)	FWHM (eV)	$\Delta E_{\text{Mono}}$ (eV)	$\Delta E_{\text{Spec}}$ (eV)	$\text{RP}_{\text{Spec}}$
100	0.0563	0.0193	0.0529	1891
200	0.2477	0.0547	0.2416	828
300	0.5268	0.1005	0.5171	580
600	1.3945	0.2842	1.3652	439
750	2.2170	0.3972	2.1811	344

**Table A.6:** Measured resolving power of the Impurity grating for a 100  $\mu\text{m}$  exit slit.

Energy (eV)	FWHM (eV)	$\Delta E_{\text{Mono}}$ (eV)	$\Delta E_{\text{Spec}}$ (eV)	$\text{RP}_{\text{Spec}}$
100	0.0889	0.0383	0.0802	1247
200	0.3132	0.1082	0.2939	681
300	0.6505	0.1988	0.6194	484
600	1.7617	0.5623	1.6695	359
750	3.2386	0.7859	3.1418	239

### A.3 MEG Measurements

**Table A.7:** Measured resolving power of the MEG for a 25  $\mu\text{m}$  exit slit.

Energy (eV)	FWHM (eV)	$\Delta E_{\text{Mono}}$ (eV)	$\Delta E_{\text{Spec}}$ (eV)	$\text{RP}_{\text{Spec}}$
100	0.0276	0.0101	0.0257	3885
200	0.0863	0.0285	0.0814	2457
450	0.3611	0.0962	0.3480	1293
600	0.6841	0.1481	0.6678	898
800	1.2294	0.2280	1.2081	662

**Table A.8:** Measured resolving power of the MEG for a 50  $\mu\text{m}$  exit slit.

Energy (eV)	FWHM (eV)	$\Delta E_{\text{Mono}}$ (eV)	$\Delta E_{\text{Spec}}$ (eV)	$\text{RP}_{\text{Spec}}$
100	0.0408	0.0193	0.0360	2781
200	0.1171	0.0547	0.1035	1931
450	0.4487	0.1846	0.4090	1100
600	0.7952	0.2842	0.7427	808
800	1.5091	0.4376	1.4442	554

**Table A.9:** Measured resolving power of the MEG for a 100  $\mu\text{m}$  exit slit.

Energy (eV)	FWHM (eV)	$\Delta E_{\text{Mono}}$ (eV)	$\Delta E_{\text{Spec}}$ (eV)	$\text{RP}_{\text{Spec}}$
100	0.0652	0.0383	0.0528	1894
200	0.1966	0.1082	0.1642	1218
450	0.8949	0.3653	0.8169	551
600	1.6080	0.5623	1.5065	398
800	2.6115	0.8658	2.4638	325

## A.4 HRMEG Measurements

Resolving power measurements for the HRMEG with a monochromator exit larger than  $25 \mu\text{m}$  were not feasible by this technique because the spectrometer resolution exceeds the monochromator resolution, complicating the deconvolution.

**Table A.10:** Measured resolving power of the HRMEG for a  $25 \mu\text{m}$  exit slit.

Energy (eV)	FWHM (eV)	$\Delta E_{\text{Mono}}$ (eV)	$\Delta E_{\text{Spec}}$ (eV)	$\text{RP}_{\text{Spec}}$
400	0.1109	0.0806	0.0761	5256
450	0.1369	0.0962	0.0974	4619
575	0.2064	0.1389	0.1527	3767

## APPENDIX B

# SUBMITTED PUBLICATIONS WITH DATA FROM THE REIXS XES SPECTROMETER

### **Magnesium Double Nitride $\text{Mg}_3\text{GaN}_3$ as New Host Lattice for $\text{Eu}^{2+}$ -Doping - Synthesis, Structural Studies, Luminescence and Band-Gap Determination**

Hintze, Frauke; Johnson, Neil; Seibald, Markus; Muir, David; Moewes, Alexander; Schnick, Wolfgang

Published August 28, 2013: *Chemistry of Materials*, 25 (20), pp 40444052

**Abstract:** The double nitride  $\text{Mg}_3\text{GaN}_3$  and binary nitride  $\text{Mg}_3\text{N}_2$  were synthesized from the elements by reaction with  $\text{NaN}_3$  in Na-flux. Reactions were carried out at 760 °C in weld shut Ta-ampoules.  $\text{Mg}_3\text{GaN}_3$  was obtained as single crystals (space group  $\bar{R}3m$  (no. 166),  $a = 3.3939(5)$  and  $c = 25.854(5)$  Å,  $Z = 3$ ,  $R1 = 0.0252$   $wR2 = 0.0616$  for 10 refined parameters, 264 diffraction data). This double nitride consists of an uncharged three dimensional network of  $\text{MgN}_4^-$  and mixed (Mg/Ga) $\text{N}_4$ -tetrahedra which share common corners and edges. First-principles DFT calculations predict  $\text{Mg}_3\text{GaN}_3$  to have a direct band gap of 3.0 eV, a value supported by soft X-ray spectroscopy measurements at the N K-edge.  $\text{Eu}_{2+}$ -doped samples show yellow luminescence when irradiated with UV to blue light ( $\lambda_{max.} = 578$  nm, FWHM = 132 nm). Doped samples of  $\text{Mg}_3\text{GaN}_3:\text{Eu}_{2+}$  also show luminescence at room temperature when excited with UV to blue light. The maximum intensity of this emission band is found at 589 nm (FWHM = 145 nm).

---

### **Large Scale Production of Photoactive Few-layer-thick Carbon Nitrides Nanosheets Via Facile Liquid Ammonia-Assisted Lithiation Route**

Yin, Ying; Han, Jiecai; Zhou, Jigang; Muir, David; Sutarto, Ronny; Zhang, Zhihua; Jian, Jikang; Liu, shengwei; Song, Bo

Submitted August 18, 2013: *Nano Letters*

**Abstract:** Two-dimensional (2D) nanosheets have attracted tremendous attention because they bring in unusual physical and chemical properties as a result of unique surface atomic geometry and electronic structure. Herein, we report for the first time a simple, high efficient and large scale route to prepare the ultrathin few-layer-thick graphite-phase  $\text{C}_3\text{N}_4$  (g- $\text{C}_3\text{N}_4$ ) nanosheets via a liquid ammonia-assisted lithiation method from bulk g- $\text{C}_3\text{N}_4$ . A significant feature of this route is that the lithium intercalation process can be “viewed” from the obvious color change from deep blue to colorless, while the lithium intercalation rate can be “tuned” by adjusting the shaking speed. More significantly, this approach can be also widely applied to synthesize other 2D layered structure materials. Compared with bulk g- $\text{C}_3\text{N}_4$ , ultrathin g- $\text{C}_3\text{N}_4$  nanosheets with a thickness of about 2.5 nm, shows unique fine structures and intriguing electronic and optical properties, which at least contribute to a

remarkably improved photocatalytic performance, demonstrating this metal-free nanosheets is a promising candidate for photocatalytic application.

---

### **Effect of thermal annealing of sputtered ZnO cathode interfacial layer on the photovoltaic performances of inverse organic solar cells**

Jouane, Youssef; Colis, Silviu; Schmerber, Guy; Bazylewski, Paul; Chang, Gap Soo; Dinia, A.; Chapuis, Yves-Andre

Submitted July 2013: *The Journal of Physical Chemistry*

**Abstract:** The influence of post-annealing treatment of rf-magnetron sputtered zinc oxide (ZnO) on the efficiency of inverted organic solar cells (OSCs) has been investigated. ZnO layer is deposited at room temperature as interfacial layer between the indium tin oxide (ITO) cathode and organic active layer. We find that the annealing temperature strongly impacts the structural properties of ZnO films. Even low annealing temperature (around 180 °C) can lead to an improvement of the cell efficiency. The structural and morphological changes in ZnO help straighten the current-voltage characteristics of OSCs. Thus the short circuit current and efficiency are improved up to 10.8 mA/cm<sup>2</sup> and 3% upon annealing at 500 °C, respectively.